Preliminary Design of Commercial Aircraft from the Academic Perspective

A THESIS

SUMMITED TO THE FACULTY OF THE GRADUATE SCHOOL

OF THE UNIVERSITY OF MINNESOTA

BY

Leonardo Dong Le

IN PARTIAL FULFILLMENT OF THE REQUIREMENTS

FOR THE DEGREE OF

MASTER OF SCIENCE

William L. Garrard, Advisor

May 2012

Acknowledgements

I would like to thank the Aerospace Engineering and Mechanics department of the College of Science and Engineering of the University of Minnesota, Twin City campus. The campus has been my home for almost seven years. The memories that I have had on this campus in those years are unforgettable. These memories are the materials that have contributed to define who I am. Thanks to you, all the instructors and staffs who have been working very hard to create such a friendly and motivated learning environment. The Aerospace Engineering and Mechanics department has been my second family since the sophomore year of my Bachelor's degree education. I would like to thank all the staffs of the department for their help and understanding to me in all those years. I want to take this opportunity to express my gratitude to the professors of the department for their interesting lessons and valuable guidance.

Especially, I would like to express my special gratitude to my advisor, Professor William L. Garrard for everything that he has done for me throughout this long journey. Thanks to his academic guidance, his financial assistance, and his emotional support for enabling me to finish this thesis. Thanks to the members of my thesis committee for their willingness to review my thesis! I also would like to thank the Minnesota Space Grant Consortium Fellowship Program in providing me a financial support throughout my Master's degree education!

To my family, Susan, Tom, Kat, and Duy: You are the infinite unconditional love and countless support for me. Besides being my parents and my siblings, you are the encouragement for me to overcome challenges and to continue my education. I thank you by all of my heart!

To my friends, Jenny, Woody, and Pat, I would like to thank you for your love, your support, and the friendship that have helped me throughout this journey!

Dedication

To my mother, Susan Le

To my father, Tom Le

To my sister, Katherine M. Le

And

To my brother, Duy Le

Abstract

We have developed a preliminary design method for commercial aircraft in academic perspective. There are four main phases in this design method. They are (1) determining design objectives and requirements, (2) statistically estimating of takeoff weight, required sea level static (SLS) thrust, and wing reference area, (3) performing a trade study to locate the optimal design point and the design region, and (4) conceptualizing the model based on the optimal design point.

Based on historical data of jet transports and the Federal Aviation Regulation (FAR) rules, we established a guideline to determine the design objectives and requirements for a commercial aircraft. We also used the historical data to formulate statistical equations to estimate the takeoff weight, the require SLS thrust, and the wing reference area. We utilized the knowledge of aircraft flight mechanics into a comprehensive comparison among the design requirements in order to sketch the design region and to locate the optimal design point. Finally, we used computer aid design (CAD) softwares to conceptualize the model based on the optimal design point.

We implemented the method into designing a wide-body commercial aircraft. Inspiring by the blended-wing-body (BWB) concept, we designed jet transport whose fuselage was shaped by the MS(1)-0317 airfoil and was blended with an Eppler 407 wing. The aircraft was sized for 200 passengers and to cruise at Mach 0.85 at the initial cruise altitude (ICA) of 38,000 ft over a 3,000-nmi range. The results show that the vehicle has an overall lift-to-drag ratio of 24, a takeoff weight of 203,096 lb, a required SLS thrust of 38,759 lb per engine, and a wing reference area of 2,338 ft^2. Through the design of this aircraft, we learned that the improvement in fuel consumption of an aircraft through enhancing its aerodynamic efficiency is remarkable. From the practical perspective, this type of wide-body concept has more potential to be developed into production than the current BWB concept.

Table of Contents

List of Tables

List of Figures

List of Symbols

Abbreviations

Terminology

AC: aerodynamic center

AIM: aeronautical information manual

AoA: angle of attack

BTOFL: balance takeoff field length

BWB: blended wing body

CAD: computer aid design

CG: center of gravity

Eng: engine

EF: engine failed (same for subscript)

FAA: Federal Aviation Administration

FAR: Federal Aviation Regulation

FL: flight level

FTO: final takeoff (same for subscript)

HL: hinge line (same for subscript)

HT: horizontal tail (same for subscript)

ICA: initial cruise altitude

Int.: initial

Max or Max.: maximum

MFW: maximum fuel weight

Min or Min.: minimum

MLW: maximum landing weight

MSL: mean sea level

MTW: maximum takeoff weight

LD: landing

L2D: lift-to-drag

Unit

deg or °: angle degree

ft: foot

fpm: foot per minute

hr: hour

in.: inch

°K: kelvin degree

kn: knot

lb: pound

mn: minute

nmi: nautical mile

sec or s: second

Sub-script

app: approach

crs: cruise

e: empty

f: fuel, force, final

m: mass or intermediate

max: maximum

min: minimum

nom: nominal

pax: passenger

pld: payload

r: root

ref: reference

LE: leading edge (same for subscript)

LO: liftoff (same for subscript)

LRC: long range cruise

OEW: operating empty weight

SFC: specific fuel consumption

SLS: sea level static

TE: trailing edge (same for subscript)

TO: takeoff

TOGW: takeoff gross weight

TSFC: thrust specific fuel consumption

VT: vertical tail (same for subscript)

R: rotation

s: stall

t: thrust or tip

tk: takeoff

w: wing

Symbols

a: lift slope or temperature rate of change

A_n: Fourier's Series coefficient

AR: aspect ratio

b: span

c or C: chord length

c': extended chord length by control surf.

c_{HT}: horizontal tail volume coefficient

c_{VT}: vertical tail volume coefficient

$\bar{c}_w$: wing's mean aerodynamic chord length

C_d: drag coefficient of infinite wing

C_D: drag coefficient of finite wing

C_{D_i}: induced drag coefficient

C_{D_o}: zero-lift drag (parasite drag)

C_l: lift coefficient of infinite wing

C_L: lift coefficient of finite wing

C_m: moment coefficient of infinite wing

R: universal gas constant

Re: Reynolds number

S: wing area

t: time

T: thrust or temperature

t_N: rotation time in takeoff

V: speed

V_∞: free stream velocity

V_1: decision-making speed

V_2: obstacle-clearance speed

w: induced velocity

W: weight

W_o: brake-released weight

α: geometric angle of attack

α_o: effective angle of attack

α_a: absolute angle of attack

C_M: moment coefficient of finite wing

$C_{M_{ac}}$: moment coefficient at AC

C_t: thrust specific fuel consumption

d: distance

D: drag

e: Oswald factor

E: endurance or loitering time

g or g_o: gravitational acceleration

G: climb gradient

h: altitude

L/D: lift-to-drag ratio

L: lift or length

L_{HT}: horizontal tail moment arm

L_{VT}: vertical tail moment arm

M_∞: free stream Mach number

n: load factor or chord length factor

p: passenger count

r or R_a: range

α_i: induced angle of attack

α_{LO}: zero-lift angle of attack

β: Biot-Savart angle

ρ: air density

σ: air density fraction

γ: flight path angle

ϕ: roll angle or span efficiency

λ: taper ratio

θ: spanwise position relative angle

φ: induced angle factor

τ: airfoil maximum thickness

δ: induced drag factor

δ_f: flap deflection angle

δ_s: slat deflection angle

Λ: sweep angle

$\Gamma(y)$: spanwise circulation function

Ψ: weight fraction for L2D calculation

$\forall$: average

Chapter 1 Introduction

1.1 Needs of New Commercial Aircraft Concepts

The economy crisis and the fuel crisis have threatened the survival of many airline companies around the world. The situation has brought the competition between Airbus and Boeing up to a higher level than ever. Within the first decade of the 21th century, the world has witnessed the births of a giant Airbus A380 and the most sophisticated modern jet transport, Boeing 787. The strategy of each company has shown clearly in these aircraft. Airbus is seeking payload efficiency, while Boeing is looking for high performance efficiency. However, both companies have two common goals that are to increase airliner companies' profitability and to improve passenger comfort.

In the academic world, aeronautics research has focused on alternative structural materials and on improving the efficiency of the propulsion system. On the other hand, aerodynamic research for commercial aircraft has been slow since the conventional aircraft configuration has worked so well. In 1994, Boeing and NASA introduced a new commercial airplane concept called blended-wing-body (BWB). The original BWB study showed the configuration was lighter, had higher aerodynamic efficiency, and had lower fuel consumption compared to the conventional configuration [1]. The concept has brought new challenges to aerodynamicists, structural engineers, propulsion engineers, and flight mechanics engineers. Since then, Boeing and NASA have constantly made efforts in studying this new concept; and the X-48 BWB is the state of the art BWB research.

1.2 Related Work

Inspired by the BWB concept, a group of students at the University of Minnesota took on a project to design a commercial BWB aircraft in the fall of 2009. The design objectives were to learn how to design a commercial airplane and to study the feasibility of the BWB concept in commercial transport. We were asked to design a new BWB model to replace the Boeing 767 Family. This means the Boeing 767 Family's characteristics are our design requirements and objectives. The challenges are (1) the new model must have the performance better than or equal to the Boeing 767 performance and (2) it must be able to operate in a conventional airport.

We began to size our new model based on the Boeing 767 performance characteristics. The goals and the achievements are compared in the Table 1.1. In this project, we used a back-of-the-envelope method to size the characteristics of the aircraft model. First, we used the Breguet range equation to estimate the takeoff weight based on the assumptions of the maximum landing weight (MLW) is 296,000 lb (the same as the MLW of the Boeing 767), the specific fuel consumption (SFC) is 0.54 $lb_f/(lb_t*hr)$ (the SFC of the current propulsion system on the market), and the cruise lift-to-drag ratio is 26. The result is shown in Fig. 1.1(a). Once we obtained the maximum takeoff weight (MTW), we combined the sizing method that is described in Chapter 7 of [2] with the approach speed constraint and the wing span limit to find the required thrust and the wing platform area. The method is illustrated in Fig. 1.1(b). Hence, a complete set of performance characteristics were calculated and listed in Table 1.2.

In the BWB concept, the entire passenger cabin is completely inside the wings. This is a unique characteristic of the BWB concept, and it is a big challenge in designing the passenger cabin. Based on the wing platform area, we designed a passenger compartment layout for three classes and a pressure vessel to contain the compartment. Combining the spatial constraint with the available wing area, we designed the passenger compartment as a pod in which all cross sections are ellipses.

Table 1.1: Comparing goal and achievement of BWB design		
Parameter	*Goal*	*Achieved*
Payload (tri-class)	174 – 245 seats	191 seats
Operational Range	6,000 nmi	6,500 nmi
Long-Range-Cruise Mach	0.85	0.85
Takeoff Distance @ Sea-Level	< 8,000 ft	4,000 ft
Service Ceiling	35,000 ft	35,000 ft
Time to Climb	< 30 mn	28 mn
Approach Speed	< 135 kn	110 kn
Wing Span Limit	< 156 ft	156 ft

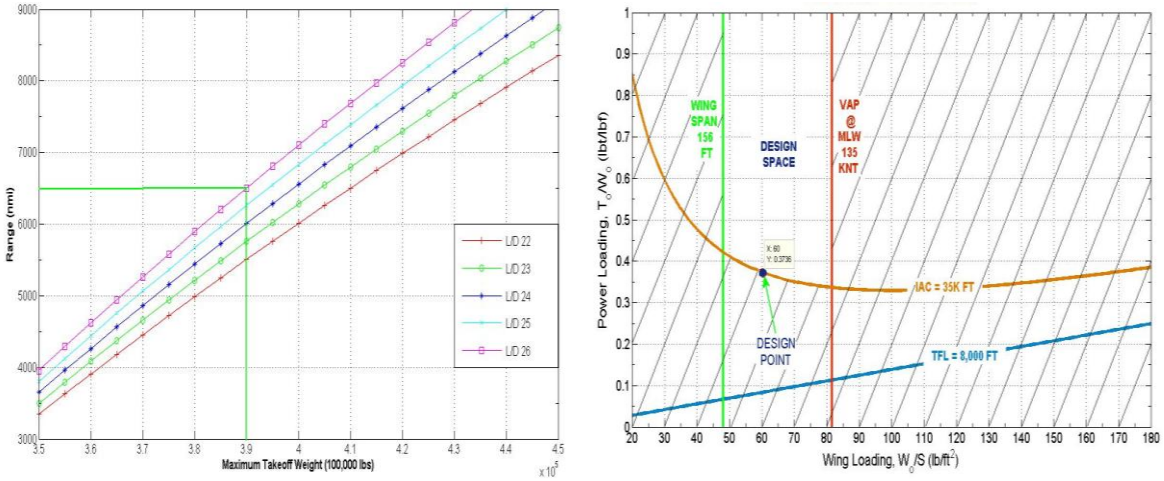

(a) **(b)**

Figure 1.1: (a) MTW estimation; (b) Sizing method for BWB model.

The result is shown in Fig. 1.2 by courtesy of Ben Simmer. Complying with the FAA safety rules and the airliner's seating standard, the pressure vessel can fit 191 seats for three classes in a volume of 81 ft long by 39 ft wide and 18 ft tall. The passenger seat layout is shown in Fig. 1.3 by courtesy of Jared Siegel.

Table 1.2: Performance characteristics of BWB model			
Parameter	*Value*	*Parameter*	*Value*
MTW	390,000 lb	Wing Loading	60
MLW	296,000 lb	Thrust Ratio	0.3736
MFW(max. fuel weight)	94,000 lb	Wing Platform Area	6,500 ft^2
L/D_{crs}	26	Required Thrust	145,704 lb
$C_{Lmax + flap}$	1.7	Min. Time to Climb	10.5 mn
C_{Do}	0.02	Max. Time to Climb	28 mn
AR	3	Takeoff Speed	207 ft/s
Oswald (e)	0.85	Takeoff Distance	4,000 ft
$K = 1/(\pi eAR)$	0.1248	SFC	0.54 $lb_f/(lb_t*hr)$
Leading Edge Sweep	40 deg	Taper Ratio	0.1
Loiter Time	30 mn	Mean Aerodynamic Chord	52 ft

Figure 1.2: Podded pressure vessel for BWB model (by courtesy of Ben Simmer).

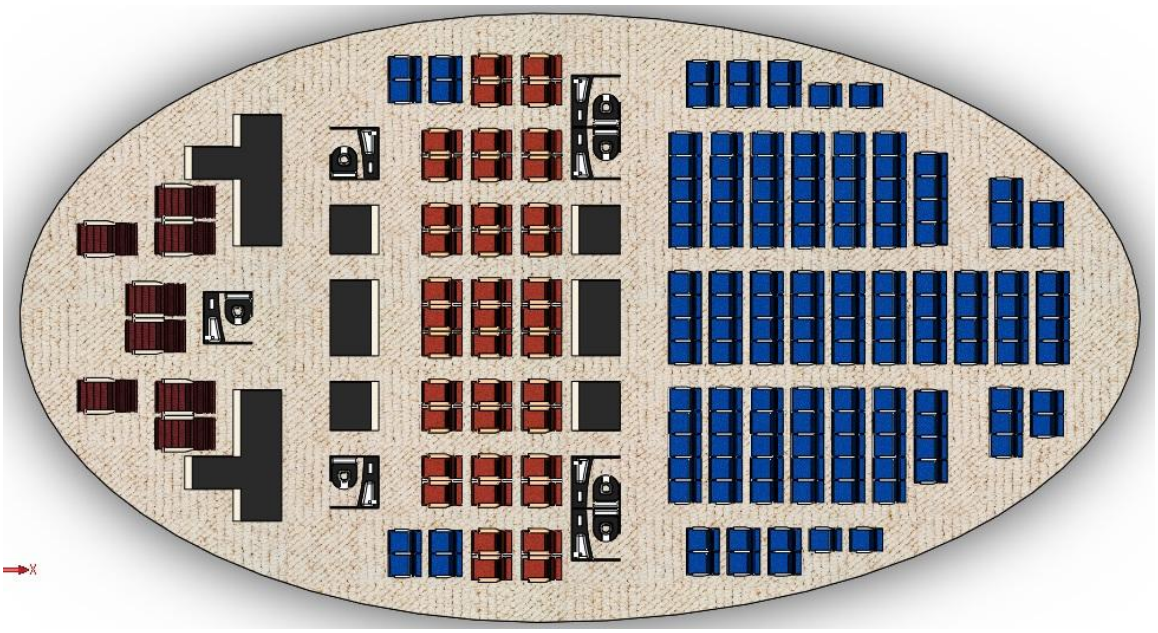

Figure 1.3: Layout of passenger accommodations for BWB model (by courtesy of Jared Siegel).

After incorporating all components together, we obtained a conceptual design of the BWB model as shown in Fig. 1.4 by courtesy of Christopher Geis. This model has several critical issues that degrade its feasibility. The first issue is the hoop stress on the pressure vessel. This type of podded pressure vessel does not handle the pressure stress as well as the tubed vessel does. The second issue is that there is so much wasted space in the aircraft. The third issue is the high emergency egress density. There are total of 6-type-A exits on the aircraft. Because of the high occupant density and the complex passenger layout, six exits are still not enough to evacuate all passengers in case of emergency. The emergency evacuation scheme is illustrated in Fig. 1.5 by courtesy of Derek Dahl.

The fourth problem is that there is not a window for each row of passengers. The number of seats per row is very high compared to the number of seats per row of a conventional aircraft. However, there are only several windows in the front of the vehicle. The entire economy class section does not have any window. The high occupant density combined with no outside view can cause claustrophobia to the passengers in the middle columns of

the section. The fifth issue of this configuration is its phenomenal wide body. The outer passengers will experience very strong centrifugal forces in yaw and roll maneuvers.

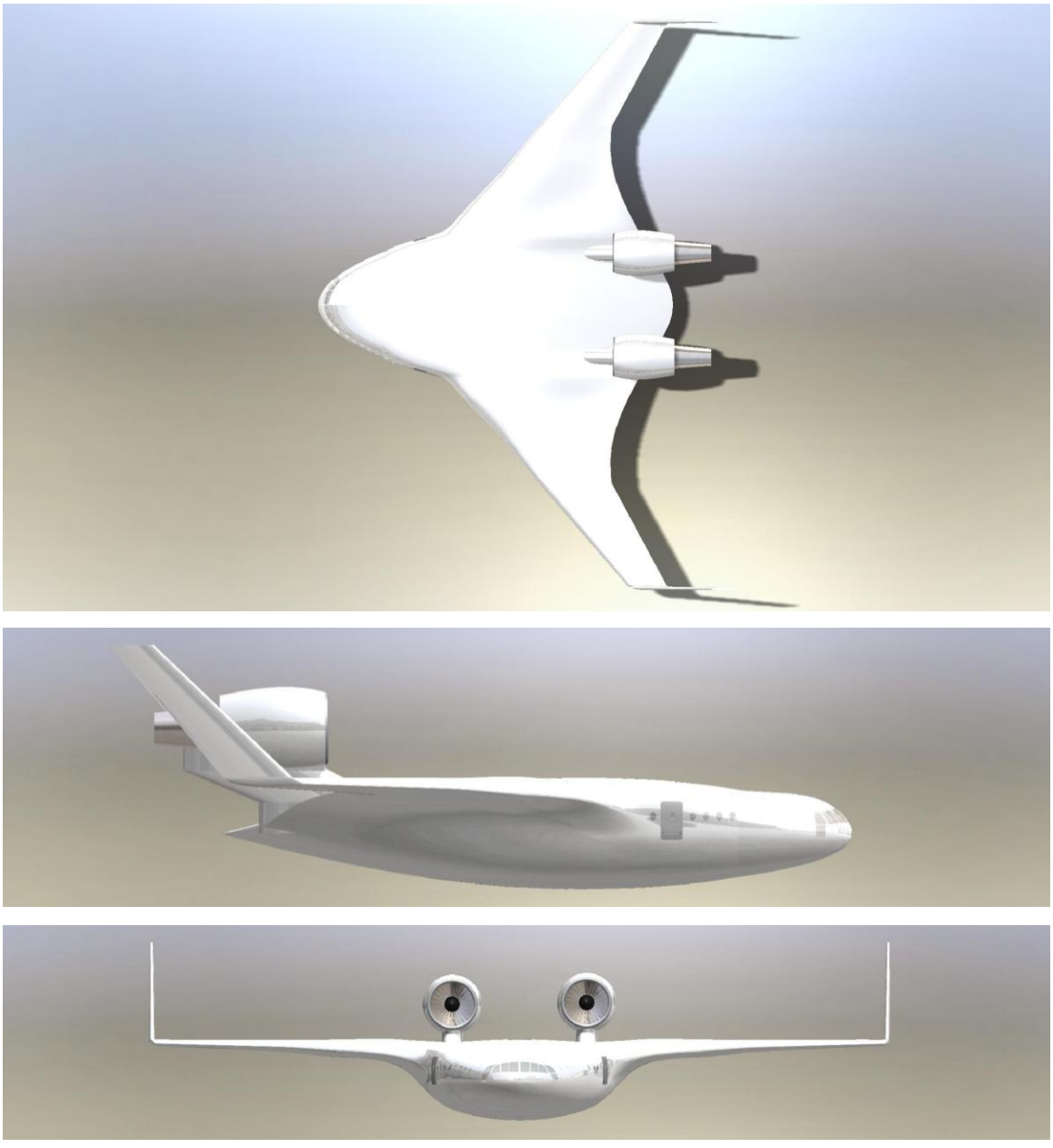

Figure 1.4: The conceptual design of the BWB model (by courtesy of Christopher Geis).

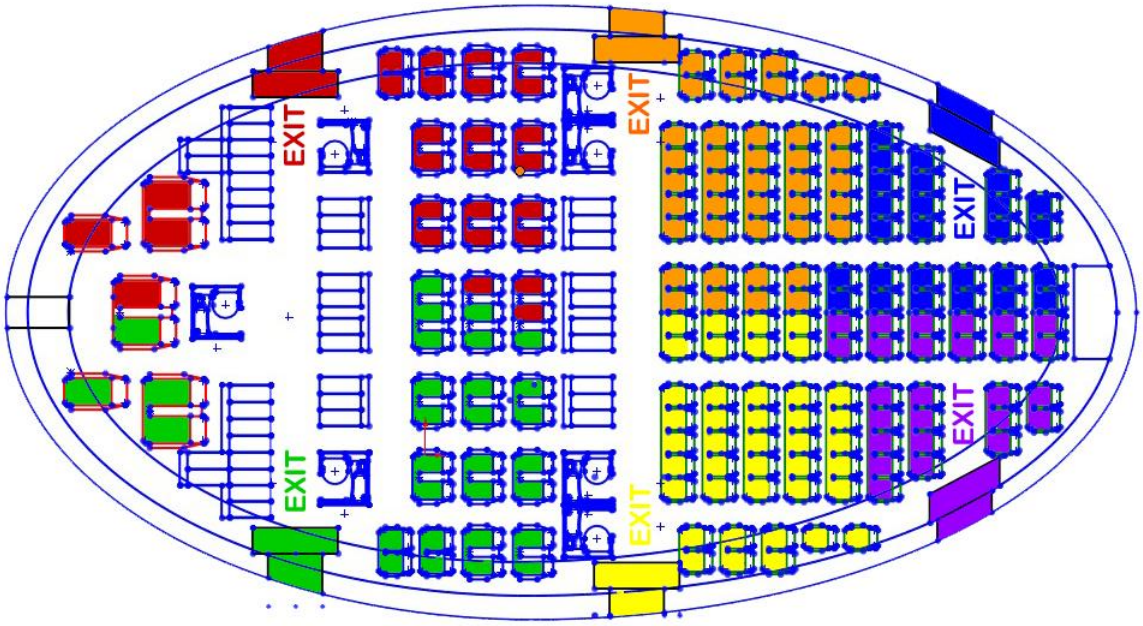

Figure 1.5: Emergency exit scheme for the BWB model (by courtesy of Derek Dahl).

Nonetheless, when riding on this aircraft the passenger will experience very weak centrifugal forces during pitch maneuver due to its short length. In addition, the model has a tremendous improvement on aerodynamic efficiency because there is not any skin friction drag on the fuselage. Hence, the vehicle will save a large amount of fuel consumption. This is the key advantage of the BWB concept. The comparison of the BWB model to similar conventional aircraft is shown in Table 1.3. Through this project, we realized that we need a better sizing method to make further analyses on performance characteristics, propulsion system, structural design, as well as other aspects of the vehicle. Moreover, if we treat the passenger compartment as a separate part of the wing area and size the wing platform area based on the 191-seat payload, we would reduce the wasted space significantly. Thus this document presents a new aircraft preliminary sizing method and applied it to the design of modified aircraft.

Table 1.3: Comparing the BWB model to conventional aircraft			
Parameter	*Boeing 767-200ER*	*Airbus A330-200*	*BWB*
Passenger Count	181 (3-Class)	253 (3-class)	191 (3-class)
Range	6,385 nmi	6,750 nmi	6,500 nmi
Wingspan	156 ft 1 in.	197 ft 10 in.	156 ft
Fuel Weight	162,000 lb	248,000 lb	94,000 lb
Cruise Speed	Mach 0.80	Mach 0.82	Mach 0.85

1.3 Aircraft Preliminary Design from the Academic Perspective

Designing and building an aircraft is a very long and expensive process. In the aerospace industry, it takes aircraft builders 10 years on average to design and to build a new conventional commercial airplane with ready tools and based on the old models. For example, the Airbus A380 program ran from 1988 to 2005, when the first test flight was successfully made. According to USA Today [3], the total cost of the program was $17.06 billion. Another example is the Boeing 787 program, which ran from the late 1990's until 2010 and cost $32 billion (by the Seattle Times [4]).

On the other hand, a senior design project lasts from 16 weeks to 35 weeks in the academic world. Thus the students do not have luxuries such as Airbus or Boeing to complete a detailed design of a new model or a new concept. However, they must estimate the primary design parameters like maximum takeoff weight, required thrust, and the minimum wing platform area. For higher level work, the accuracy of these estimations is even more essential. For instance, to analyze and to compare the climb performance of a BWB model to a conventional aircraft, the primary parameters of the BWB model must be known accurately in order to yield reliable results. Therefore, a logical preliminary sizing method for academic uses is developed in this thesis. With this sizing method, users will be able to estimate the primary parameters of an aircraft from a typical set of design objectives such as: the number of passengers or payload, the

operating range, the flight scheme, and requirements such as: the takeoff field length, the approach speed, the climb gradient, and the rate of climb at the beginning of cruise.

1.4 Preliminary Design of a Wide-Body Aircraft Concept

In addition to the preliminary sizing method, this thesis also demonstrates the application of the primary parameters into a conceptual design of a wide-body commercial aircraft. Unlike the conventional wide-body aircraft, this concept has the fuselage is made out of an airfoil without any modification on the airfoil. Based on the idea of the BWB concept, the airfoil-fuselage will be semi-blended with a low aspect ratio wing to create a smooth transition between the fuselage and the wing. A semi-blend means the entire fuselage is not completely buried inside the wing. The advantage of this concept is the small skin friction drag and the extra free lift from the fuselage, compared to the conventional configuration wide-body aircraft. Hence, the vehicle's aerodynamic efficiency will be improved. However, its aerodynamic efficiency will be lower than the BWB concept due to the uncompleted blend. On the other hand, the conception offers a window at each row of passenger seats, lower emergency egress flow rate, less unusable space, and smaller centrifugal forces in yaw and roll maneuvers.

1.5 Scope of this Work

We have presented the motivation for conceptual commercial aircraft research in the academic world. We have summarized the related work and the encourage lesson to continue working on this project. We have introduced the reason for the need of aircraft preliminary sizing in academic works. We have also described the new commercial aircraft concept as the goal of our design example. However, let us take this chance to specify the areas, which this work will focus on. We also would like to outline the thesis through each chapter.

Chapter 2 shows how to establish a set of requirements to design a new commercial aircraft model. An academic aircraft design project is different from an industrial project since there is not any customer asking for specific requirements nor do we design for any

specific market trend. Rather, we want to test the aerodynamic efficiency, to study the structural feasibility, and to analyze the performance characteristics of a new concept. Thus we need to set up the design requirement reasonably. These requirements are limited only to commercial aircraft. This chapter also presents the statistical estimations for the primary parameters of an aircraft using historical data of commercial aircraft and business jet.

Chapter 3 illustrates the trade study in aircraft preliminary sizing. This can be considered as the optimal estimation for the primary parameters of a new model. The method shows how to compare the typical flight mechanics design constraints for a commercial airplane. Then it lets us choose a minimum wing area and a minimum required thrust, which satisfy all the constraints.

Chapter 4 demonstrates a process on design a wide-body commercial aircraft. In this chapter, we show how to select the airfoil for the fuselage and the airfoil for the wing of this type of aircraft. Then we establish the design requirements. Finally, we perform the preliminary sizing, which includes the statistical estimations and a trade study, to determine the primary parameters for the model.

Chapter 5 presents the conceptual design of the wide-body commercial aircraft model that was numerically designed in Chapter 4. Here, we limit the design details to the physical layout of the vehicle. We leave the internal structure (the airframe) for detailed design. In this chapter, we show how to design the fuselage, the wings, the tails, and the reasons for the locations of the engines and the arrangement of the landing gear.

Chapter 2 Design Requirements and Statistical Estimations of Primary Parameters

2.1 Introduction

In order to design an aircraft, the designers must know the purposes of the vehicle. These purposes could be one or combination of the following categories: commercial jet, civil cargo, bomber, military cargo, fighter jet, and scientific research vehicle. Once the purposes of the vehicle are determined, the designers will be able to establish a set of requirements. That is a set of questions like: What is the payload? What is the flight envelope? What is the FAA or FAR certification target? In the industrial world, these questions are usually asked by the customers or by the company's development target. They are often responded to straightforward and solid answers. In the academic world, both questions and answers are flexible; and sometimes they can also be controversial topics. In this presentation, we are studying new concept for a commercial jet transport. Therefore, the vehicle's purpose is to serve as a commercial airliner. The flight requirements are set based on the historical data of the commercial jets and the FAR rules.

Once the vehicle's type and the flight requirements are set, the designers can estimate the takeoff weight of the vehicle. The vehicle's takeoff weight can be estimated based on the number of passengers and the operational range. Then the designers must also answer the question: for a given takeoff weight, what are a reasonable wing platform area and a required thrust to ensure that the aircraft can fly? The wing platform area and the required thrust are approximated in the forms of wing loading ratio and thrust-to-weight ratio at this stage of the design process. These ratios are statistically estimated based solely on the vehicle's takeoff weight. This chapter will cover the survey, the establishment of the design requirement, the takeoff weight estimation, and the wing loading ratio and the thrust-to-weight ratio estimations.

2.2 Aircraft Requirement Surveys

2.2.1 Range and Passenger Capacity

Gathering information from a wide range of commercial airplanes [5] that have been in service such as Airbus series, Boeing series, DC series, Embraer ERJ series, Fokker series, and McDonnell Douglas series, we found a linear correlation between the passenger capability and the operational range of the airplanes. Figure 2.1 shows the trend of the number of passengers in a range from 100 passengers at 1,000 nautical miles (nmi) to 500 passengers at 8,000 nmi.

The scatter plot allows us to classify the aircraft into three subgroups. The short range airplanes carry less than 200 passengers and travel from 1,000 to 3,000 nmi. The airliners that can carry from 200 to 300 passengers and fly in the range from 3,000 to 6,000 nmi belong to the medium group. The long range group is the home of those can take more than 300 passengers and cruise beyond the 6,000-nmi range. Among these three groups, the short range group has the highest population. It is understandable for the fact that most of aircraft have been designed for the short range size and used as the baseline model in the series. The majority of the airliners in the medium and the long range cruise are developed from the short range group.

Learning from history, we should target our first model in the short range population. Most of these short range jet transport aircraft serve as regional airliners. The geographical distance between New York City and San Francisco is about 2,250 nmi. Based on these facts, we decide to set the first two design requirements as following: (1) passenger capacity is 200 persons and (2) cruising range is 3,000 nmi. Having set the payload and the range, we need a few more characteristics like cruise speed, cruise altitude, approach speed, climb time, and takeoff field length to completely describe a conceptual aircraft model.

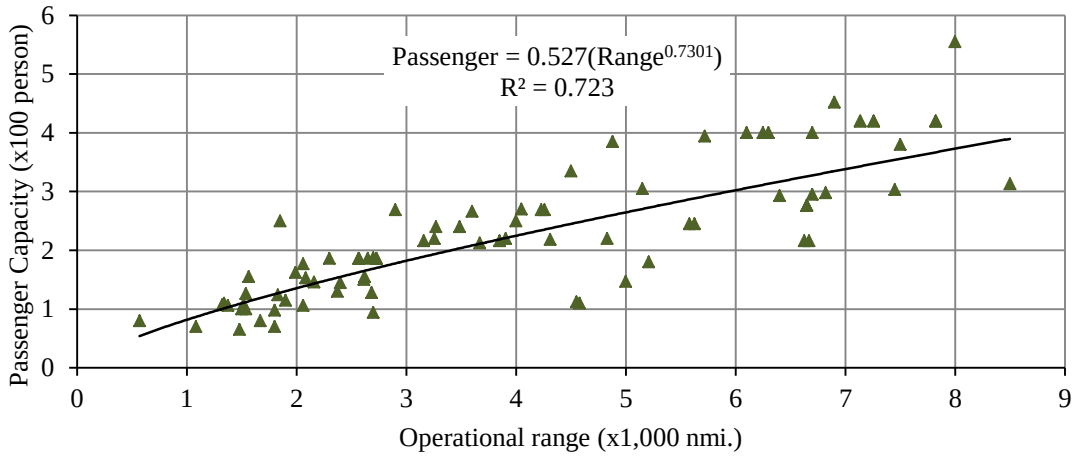

Figure 2.1: Trend of passenger capability with operational range for Jet transport.

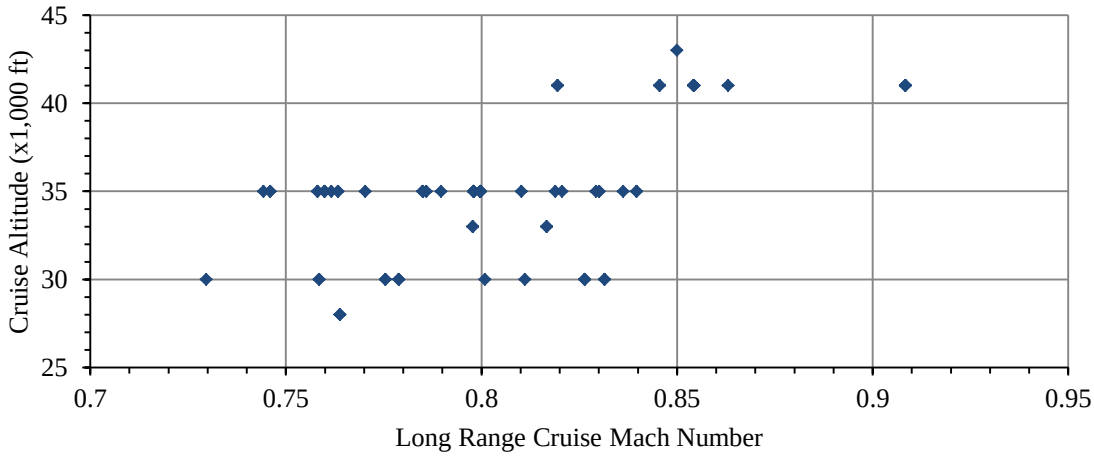

Figure 2.2: Jet transport cruise altitude and long range cruise Mach.

2.2.2 Cruise Altitude and Cruise Mach

In order to determine these flight characteristics, we need more information from the data used in Fig.1. From the database, we also extract the cruise speeds and the cruise altitudes of these airplanes, and we plot them in Fig. 2.2. The trend shows these jet transports cruise at speeds in a range from Mach 0.73 to Mach 0.91 at a flight level (FL) from 25,000 ft to 45,000 ft. The majority of these aircraft operate at 35,000 ft flight level (FL 350) at a cruising speed ranging from Mach 0.75 to Mach 0.85. Thus, it is reasonable for

us to set our third and fourth design requirements as: 3) long range cruise (LRC) Mach 0.8 at 4) initial cruise altitude of FL 350.

2.2.3 Takeoff Field Length

The US Federal Aviation Regulations Part 25 (FAR 25) §111 defines the takeoff path as the traced line of the aircraft from the standing start point on the runway to the point at which the aircraft is 115 ft above the runway surface [6]. Section 113 defines the takeoff distance on a dry runway as the horizontal distance along the takeoff path from the start of takeoff to the point at which the airplane is 35 ft above the takeoff surface. In this same section, the takeoff run is the horizontal distance from the start to the point at which the liftoff speed is reached and the point at which the airplane is 35 ft above the runway surface. FAR defines liftoff speed is the speed at which the airplane first time becomes airborne in the takeoff process. Boeing 747-400 makes a takeoff within 12,000 ft FAR takeoff runway length with brake release gross weight of 800,000 lb on a runway at 6,000 ft altitude standard day. With a payload that is less than half of the Boeing 747-400, we can set the design balance takeoff field length (BTOFL) to be 8,000 ft on a runway at 6,000 ft above sea level.

2.2.4 Time to Climb and Approach Speed

Aeronautical Information Manual (AIM) Chapter 13 classifies the airspace from the surface to 10,000 ft MSL as class B airspace, the nation's busiest airspace [7]. Meanwhile, FAR 91 rules that no person may operate an aircraft below 10,000 ft MSL at a speed faster than 250 knots or more than 200 knots in the class B airspace. There are two points we can draw out from these rules. One is the aircraft must be able to climb out of the class B airspace as fast as possible to avoid traffic congestion. Two is the approach speed must be lower than the allowable speed. Therefore, the maximum time to climb must be less than 30 minutes and the maximum approach speed must be less than 130 knots.

2.3 Statistical Estimation of Takeoff Weight

2.3.1 Takeoff Weight Definition

The MTW is the weight of the aircraft at the beginning of its flight mission. It is the weight of the aircraft at the standing point on the runway in the takeoff phase. This weight is built up by three components: the empty weight, the payload, and the fuel weight.

$$W_0 = W_{pld} + W_f + W_e \tag{2.1}$$

where W_0 is the MTW (refer to Fig. 2.6) it is the aircraft weight at station zero in the flight plan), W_{pld} is the payload, W_f is the fuel weight, and W_e is the empty weight.

2.3.2 Initial Guess of Takeoff Weight

The initial takeoff weight of the aircraft is estimated based on the number of passengers and the range. The number of passengers defines the payload and the volume to hold the payload. The range defines the fuel weight and the volume of the fuel tanks. The volume of the passenger compartment and the volume of the fuel tank define the empty weight of the aircraft. Therefore, it is necessary to formulate a takeoff weight equation as a function of the passengers and the range. Using the same data in Fig. 2.1, we plot the takeoff weight of the aircraft corresponding to their passenger capacities and their operational ranges in Fig. 2.3. The surface fit of the plot is presented in Fig. 2.4. The fitting surface of the data shows that the takeoff weight is linearly related to the range and nonlinearly related to the passenger capacity. Let p be the number of passengers; and let r be the operational range (nmi). The polynomial least square surface function that estimates the takeoff weight a jet transport based on the passenger capacity and the operational range is given by:

$$W_o = 5.614p^2 - 360p - 0.1632pr + 72.43r - 9{,}638 \tag{2.2}$$

2.3.3 Payload Estimation

The payload is determined from the passenger capacity and the FAR flight crew accommodation. The rule requires at least two flight crew to operate an aircraft: a captain pilot and a co-pilot (FAR 125 §263). Recently, the regulation has changed due to security enforcement. It requires a law officer to travel with the crews for regional service as well as the transoceanic flight [6]. Also in transoceanic flights, a flight engineer is required to help the crews with technical trouble shooting. The rule can be summarized in Table 2.1.

According to the FAR 125 §269, if the total number of the passengers is more than 100, it requires the service provider to have two flight attendants plus one additional flight attendant for each 50 passengers above 100 passengers. For example, a 200-passenger airliner needs 4 flight attendants. Let x be the number of passengers and y be the number of flight attendants. The number of flight attendants is calculated by:

$$y = 2 + \frac{x - 100}{50} \tag{2.3}$$

Table 2.1: FAR 125 § 263 - Flight crew member regulation

Flight Range	*Number of Crew*
Minimum	2
Regional	3
Transoceanic	4

The FAR 119 §3 prescribes the average weight for each flight crewmember and flight attendant by gender. In this project, we take the average weight for both categories in both genders by 180 lb plus 30 lb of personal luggage and miscellaneous. In the same method, we determine the average weight of each passenger is 180 lb plus 70 lb of baggage and 30 lb of onboard luggage and miscellaneous supplements. Let z be the number of flight crew. Then the total payload can be calculated at this stage of the design by:

$$W_{crew} = (y + z) \cdot 210\ lb \tag{2.4}$$

$$W_{pax} = x \cdot 280\ lb \tag{2.5}$$

$$W_{pld} = W_{crew} + W_{pax} \tag{2.6}$$

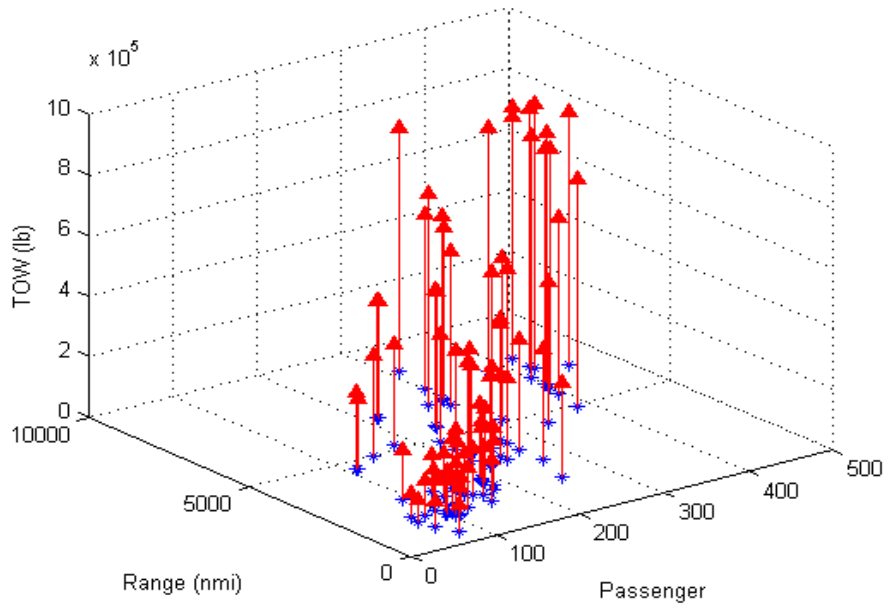

Figure 2.3: Takeoff weight of jet transport vs. passenger & range.

2.3.4 Empty Weight Estimation

Once the takeoff weight is determined, the empty weight can be calculated using the historical data trend of the commercial aircraft empty weights. From the trend, we find the empty weight is correlated with takeoff weight by a power function. The data is plotted in Fig. 2.5 with the fitting curve using the least square method. It is more convenient to write the empty equation in the rational form. Both versions of this formula are presented here:

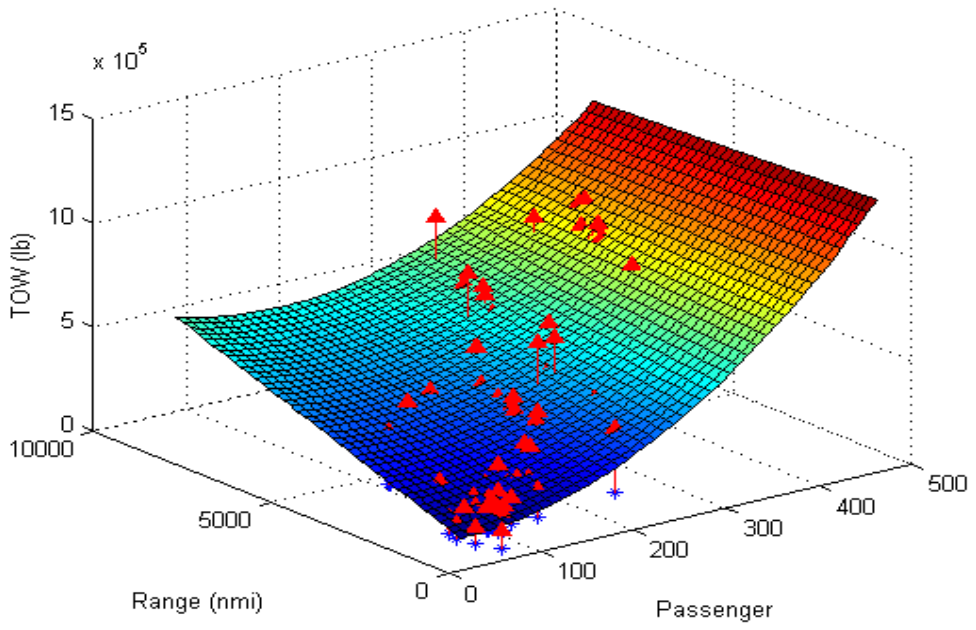

Figure 2.4: Takeoff weight surface of jet transport.

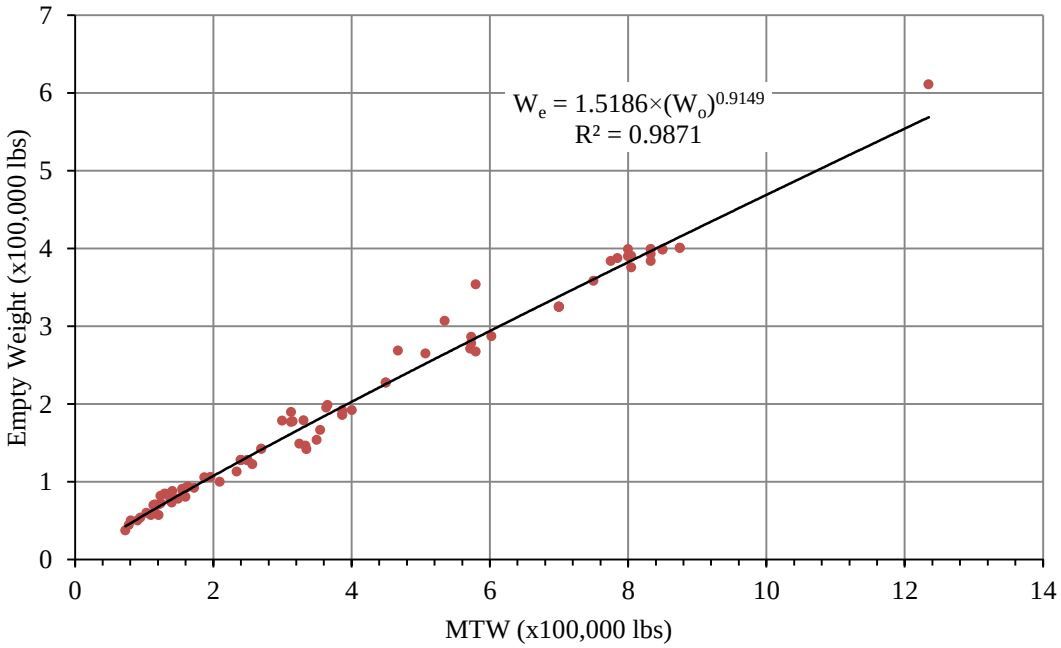

Figure 2.5: Empty weight of commercial aircraft.

$$W_e = 1.5186 \times W_0^{0.9149} \quad (lb) \tag{2.7a}$$

or

$$\frac{W_e}{W_0} = 1.5186 \times W_0^{-0.085} \tag{2.7b}$$

2.3.5 Fuel Weight Estimation

The second component of the MTW is the fuel weight. The fuel weight is calculated based on the flight mission of the aircraft. Longer range requires more fuel and larger volume of the fuel tanks. In fact the flight mission is also an important guideline in the aircraft performance analysis. At this point we need to set up a brief flight mission in order to estimate the fuel weight. A conceptual sketch of the flight mission is presented in Fig. 2.6. A typical flight mission for a commercial jet-transport has the main flight mission and the reserve. The simplest structure of the main flight mission includes: takeoff, climb to the cruise altitude and accelerate to the cruise speed, cruise to the destination, descent to the loiter altitude, loiter, and land. The reserve is designed for emergency situation and airport traffic congestion. In this flight mission, we designed the reserve for the case of missed approach. After failing the first attempt to land, the vehicle climbs back the divert altitude and cruises to nearby airport. At the end of diversion, the aircraft descends for landing. For the second landing, loitering is optional.

According to Raymer [8], we can calculate the fuel weight fraction for each phase of the flight mission. Except for the cruise, divert, and loiter phases, all other phases can be approximated fraction using the empirical estimations. For example, the fuel weight fraction for the climb stage after takeoff is written as W_2/W_1, and the fraction for the takeoff stage is W_1/W_0. Then weight fraction at the beginning of cruise (station 2) to the total takeoff weight is product of the weight fractions of the climb phase and the takeoff phase – that is W_2/W_0. A generalized formula for the weight fraction at i^{th} station is W_i/W_{i-1}. The empirical initial estimations of these stages are obtained from [8] and are summarized in Table 2.2.

For the cruise segment, the weight fraction W_3/W_2 is calculated by re-arranging the Breguet range equation into a weight-fraction equation [8]. It is the exponential function of the ratio of the product of the range and the engine's thrust specific fuel consumption (TSFC) to the product of the cruise aerodynamic efficiency and the cruise speed.

$$\frac{W_3}{W_2} = exp\left[-\frac{R_a C_{t\_crs}}{V_{crs}\frac{L}{D}\Big|_{max}}\right] \tag{2.8}$$

where R_a is the range (ft), C_{t_crs} is the engine's cruise TSFC $\left(\frac{lb_m}{sec \cdot lb_f}\right)$, V_{crs} is the cruise speed (ft/sec), and $\frac{L}{D}\Big|_{max}$ is the maximum aerodynamic efficiency.

For the loiter segments, the weight fraction W_5/W_4 and W_{10}/W_9 are calculated by re-arranging the endurance equation into a weight-fraction formula [8]. It is an exponential function of the ratio of the product of the endurance and the engine's takeoff TSFC to the maximum aerodynamic efficiency. Let E_i be the loiter endurance (sec) and C_{t_tk} be the engine's takeoff TSFC, the weight fraction is given by:

$$\frac{W_i}{W_{i-1}} = exp\left[-\frac{E_i C_{t\_tk}}{\frac{L}{D}\Big|_{max}}\right] \tag{2.9}$$

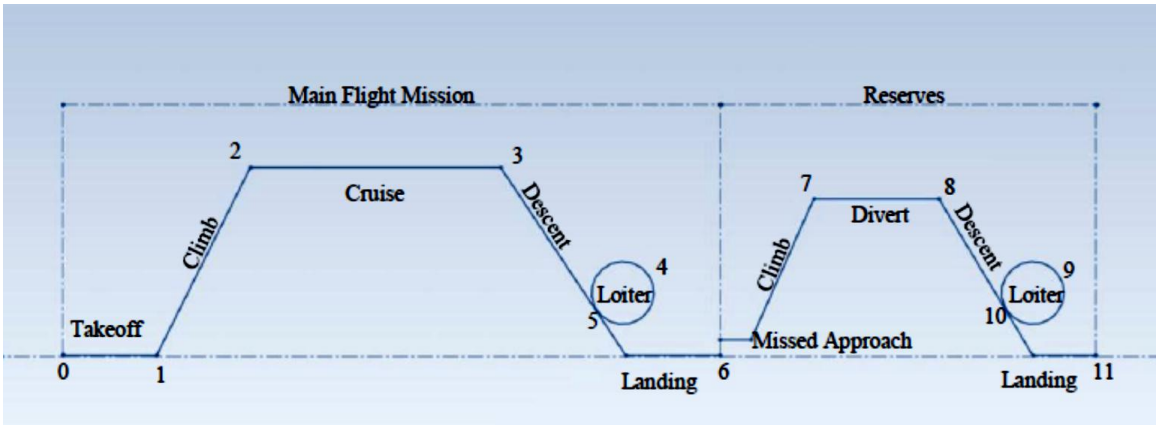

Figure 2.6: Typical flight mission of commercial jet transport.

For the divert segment, the fuel weight fraction can be estimated by two different approaches: the range equation or the endurance equation. If we want to reserve the fuel for diverting over a range, we need to define the diverting altitude and the diverting speed in order to apply Eq. (2.8) in calculating the W_8/W_7 weight fraction. The most convenient flight condition for diverting over a range is the condition the same as the cruising condition. If we want reserve the fuel for diversion in a period of time, we use Eq. (2.9) with a specific diverting endurance and the engine's cruise TSFC. In this presentation, the fuel fraction for diversion is calculated for a fixed endurance at the cruise condition.

Table 2.2: Empirical mission fuel weight fraction estimation

Mission segment	W_i/W_{i-1}
Engine Start, Taxi, and Takeoff (W_1/W_0)	0.97 – 0.99
Climb and Accelerate (W_2/W_1)	$1.0065 - 0.0325M_{crs}$
Cruise (W_3/W_2)	$exp\left[-\frac{R_a C_{t\_crs}}{V_{crs}\frac{L}{D}\Big\vert_{max}}\right]$
Descent to Loiter (W_4/W_3 , W_9/W_8)	0.99 – 0.995
Loiter (W_5/W_4 , W_{10}/W_9)	$exp\left[-\frac{E_i C_{t\_tk}}{\frac{L}{D}\Big\vert_{max}}\right]$
Missed Approach and Re-climb (W_7/W_6)	$1.0065 - 0.0325M_{crs}$
Divert (W_8/W_7)	$exp\left[-\frac{E_d C_{t\_crs}}{\frac{L}{D}\Big\vert_{max}}\right]$ or $exp\left[-\frac{R_d C_{t\_crs}}{V_{crs}\frac{L}{D}\Big\vert_{max}}\right]$
Approach and Land (W_6/W_5 , W_{11}/W_{10})	0.992 – 0.997

The reason for making the distinction between the takeoff TSFC and the cruise TSFC of the turbofan engines is because their differences are relatively large. The historical data in Fig. 2.7 (obtained from [9] and [10]) indicates the takeoff TSFC is approximately half of

the cruise TSFC. The mean values of the cruise TSFC is 0.63 $\left(\frac{lb_m}{hr \cdot lb_f}\right)$ while the mean value of the takeoff TSFC is 0.38 $\left(\frac{lb_m}{hr \cdot lb_f}\right)$.

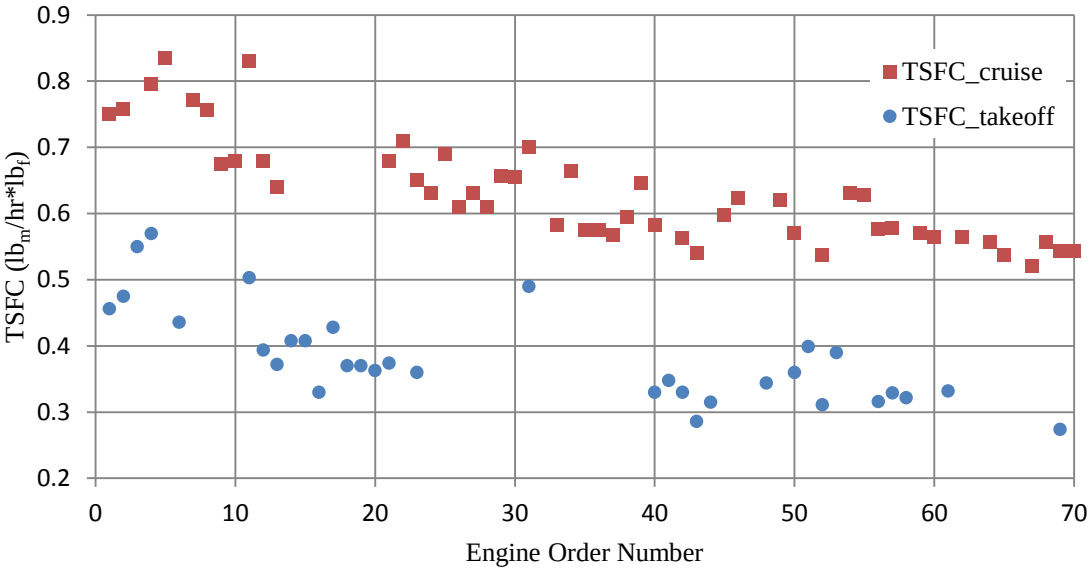

Figure 2.7: Thrust specific fuel consumptions of jet engines.

Once all the weight fractions of the entire flight plan are estimated, the weight ratio of the aircraft at the end of the flight mission to the beginning of the mission is calculated by:

$$\frac{W_{11}}{W_0} = \frac{W_1}{W_0}\frac{W_2}{W_1}\frac{W_3}{W_2}\frac{W_4}{W_3}\frac{W_5}{W_4}\frac{W_6}{W_5}\frac{W_7}{W_6}\frac{W_8}{W_7}\frac{W_9}{W_8}\frac{W_{10}}{W_9}\frac{W_{11}}{W_{10}} \tag{2.10}$$

The difference between the aircraft's initial weight and its final weight in a certain flight plan is the consumed fuel weight. Since the flight mission in Fig. 2.6 already includes the reserve, thus the fuel weight to the takeoff weight ratio is determined by:

$$\frac{W_f}{W_0} = 1 - \frac{W_{11}}{W_0} \tag{2.11}$$

2.3.6 Estimation of Required Maximum Lift-to-Drag Ratio

In order to evaluate Eq. (2.10), we must know all the parameters in Table 2.2. The range, the cruise Mach number, the cruise altitude, and the endurance are set by the designers. The TSFCs can be found from a specific engine or from the historical record as in Fig. 2.7. However, the maximum lift-to-drag ratio is a bit trickier to assign. If the wing airfoil is already designed before the preliminary sizing is performed, the designer simply uses the wing airfoil lift-to-drag ratio to evaluate Eq. (2.10). If the airfoil will be designed after the preliminary sizing, the designer should make a reasonable guess on the maximum lift-to-drag ratio based on all the information up to this stage.

If the aircraft flew all the way to the station 11 in the flight mission sketched in Fig. 2.6, it would consume all of its usable fuel. According to Boeing [11], this W_{11} weight is called the minimum landing weight. That is the sum of the payload and the operating empty weight (OEW). If the aircraft made a landing at the station 6 (the end of the main flight mission), its weight at this stage is called the maximum landing weight. That is the sum of the payload, OEW, and the reserved fuel weight. In designing an aircraft, one of our goals is to ensure that the aircraft can land successfully at the maximum landing weight. Therefore, when estimating the required maximum aerodynamic efficiency, we should not use the entire flight mission in the sketch on Fig. 2.6. Instead, we estimate the aerodynamic efficiency based only on the main flight mission. Then we use the estimated aerodynamic efficiency to calculate the reserved fuel weight.

The maximum aerodynamic efficiency is estimated by the following formula:

$$\left.\frac{L}{D}\right|_{max} = -\frac{1}{\ln \Psi}\left(\frac{R_a C_{t\_crs}}{V_{crs}} + E_i C_{t\_tk}\right) \tag{2.12}$$

where

$$\Psi = \frac{\frac{W_6}{W_0}}{\left(\frac{W_1}{W_0}\right)\left(\frac{W_2}{W_1}\right)\left(\frac{W_4}{W_3}\right)\left(\frac{W_6}{W_5}\right)} \tag{2.13}$$

All the weight fractions in Eq. (2.13) are smaller than 1. Thus the natural log of Ψ is negative. As a result, the minus sign in Eq. (2.12) makes the lift-to-drag ratio positive. The magnitude of ln Ψ increases as the weight fraction Ψ decreases. Thus smaller weight fraction Ψ will lead to the lower lift-to-drag ratio and vice versa. Inside the parentheses, the high TSFCs, the larger range, and the longer endurance require a higher aerodynamic efficiency. If the aircraft cruises faster, the aerodynamic efficiency is smaller and vice versa. However, flying at a higher cruise speed requires more thrust. Moreover, the commercial jet's cruise speed is constrained by the critical Mach number.

Please consult Appendix A for the detailed derivation of Eqs. (2.12 – 13). All parameters inside the parentheses of Eq. (2.12) are known. All the weight fractions in the denominator of Eq. (2.13) are known up to this stage of the design process. Therefore, the numerator of the fraction on the right hand side of Eq. (2.13) must be known in order to evaluate Eq. (2.12). The $\frac{W_6}{W_0}$ weight fraction can be computed in the following procedures:

- Substitute the given passenger capacity and the known operating range into Eq. (2.2) to obtain W_0.
- Apply the newly calculated W_0 into Eq. (2.7a) to obtain the empty weight.
- Use the operating range and the passenger capacity to estimate the payload.
- Add the payload to the empty weight to determine the landing weight.

Note that the last bullet contains an assumption that the aircraft does not carry any extra fuel for reserves. When the aircraft made a landing at the station 6 in the flight mission above, the engines have already consumed all usable fuel. This assumption can lead to confusion in determining the existence of the empty weight. To avoid such confusion, let us discuss these possibilities in detail.

In the first case, the empty weight that is given by Eq. (2.7a) is fixed for the rest of the sizing process. Now we can simply calculate the reserved fuel weight using the estimated maximum aerodynamic efficiency. Adding this reserved fuel weight to the takeoff weight from the first bullet will give us a grand total takeoff weight of the aircraft. However, this

type of solid empty weight sizing cannot be guaranteed by Eq. (2.7a). The source of the data that constitutes Eq. (2.7a) does not indicate that those empty weights are the allowable maximum empty weights of the aircraft. The allowable maximum empty weight is determined by the structural sustainability and the airworthiness of the aircraft. It will be known after the detailed design has been finalized. Moreover, the takeoff weight of an aircraft can be known only when it successfully takes off on a runway. The empty weight and the takeoff weight of an aircraft during the preliminary sizing are very fluid. Therefore, we must address the second case where the empty weight varies with the takeoff weight.

When adding the extra fuel weight for the reserves, we have established a new takeoff weight of the aircraft. We must ensure that the aircraft is capable of carrying this extra weight of fuel. Inasmuch as the takeoff weight is changed, the empty weight must be recalculated. So far, the empty weight is estimated based on only the takeoff weight up to this stage. Therefore, fluid empty weight sizing helps us tracking the proportions among the weight components correctly at this stage of the design.

Even if we do not add extra fuel weight for the reserves and the lift-to-drag ratio is chosen independently from the flight plan, we still want to compute the weight components proportionally, so that the sum of these weight components will be the takeoff weight. By doing so, we are iteratively calculating the takeoff weight which is discussed in the next section. Even if after the detailed design was completed; the allowable maximum empty weight was determined; the maximum range was known, the takeoff weight iteration would be still essential in determining the weight components and the takeoff weight of the aircraft.

For instance, the takeoff weight contour of the Boeing 777-200LR model in Fig. 2.10 shows that at a certain range, the takeoff weight varies as the OEW plus the payload changes. Similarly, at a fixed OEW plus the payload, the takeoff weight varies as the range changes. Thus it is necessary to calculate the takeoff weight iteratively based on the fuel weight ratio and the empty ratio during the preliminary design.

2.3.7 Takeoff Weight Iteration

The payload is calculated independently from the initial guess of the takeoff weight. If the maximum lift-to-drag ratio is chosen based on a specific airfoil that was assigned prior to the weight calculation, the fuel weight would be estimated independently from the initial guess of the takeoff weight. Otherwise, if the lift-to-drag ratio is calculated through the procedures in the previous section, the fuel weight fraction will be affected by the initial guess of the takeoff weight. The empty weight is calculated based on the initial guess through Eq. (2.7a – b). As a result, we must compute the takeoff weight iteratively. Combining Eqs. (2.1), (2.7b), and (2.11), we write the formula for the takeoff weight in the following form:

$$W_0 = \frac{W_{pld}}{1 - \frac{W_f}{W_0} - \frac{W_e}{W_0}} \tag{2.14}$$

The takeoff weight formula in Eq. (2.14) implies that the takeoff weight is a function of itself.

2.4 Statistical Estimations of Required SLS Thrust and Wing Reference Area

2.4.1 Statistical Estimation of Required SLS Thrust

The historical trend of the SLS thrust correlates with the MTW is shown in Fig. 2.8. From the plot in Fig. 2.8, we find the curve for the required thrust as a function of the takeoff weight using the least square method. The formula is:

$$T_{SLS} = 0.2662 \times W_{tk} + 6{,}838 \quad (lb) \tag{2.15a}$$

or

$$\frac{T_{SLS}}{W_{tk}} = 0.2662 + \frac{6{,}838}{W_o} \tag{2.15b}$$

2.4.2 Statistical Estimation of Wing Reference Area

Similar to the required thrust, the historical data shows that the trend of the wing platform area for jet transports is a power function of the MTW. Figure 2.9 shows the data trend of wing reference area and the MTW for jet transport by fitting a curve to the data, we write the wing reference area function in the following form:

$$S_{ref} = 0.0554 \cdot W_{tk}^{0.8475} \quad (ft^2) \tag{2.16a}$$

or

$$\frac{W_{tk}}{S_{ref}} = 18.051 \cdot W_{tk}^{0.1525} \tag{2.16b}$$

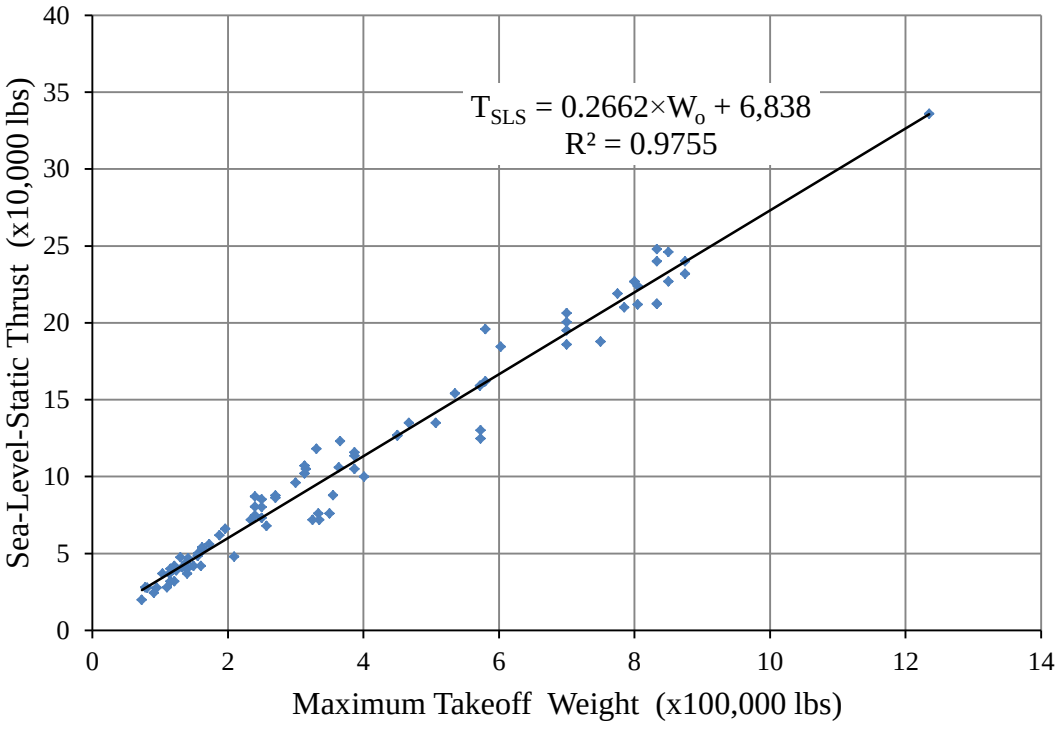

Figure 2.8: Sea level static thrust vs. MTW of jet transport.

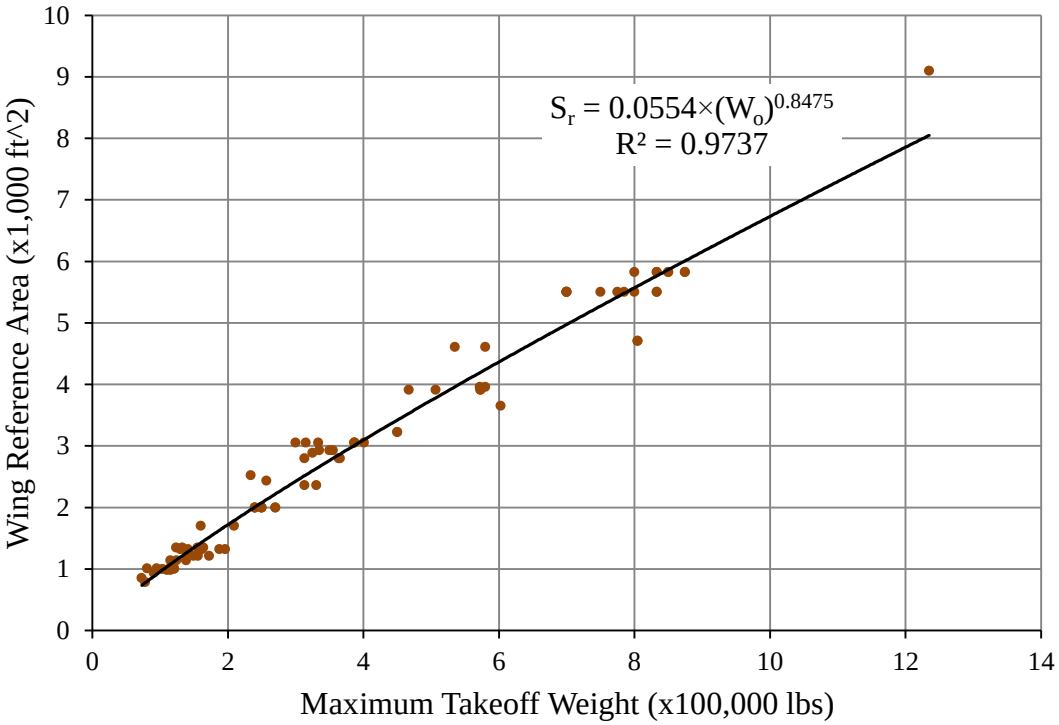

Figure 2.9: Wing platform area vs. MTW of jet transport.

2.5 Example 1: Statistically Estimate the Primary Parameters of the Boeing 777-200ER/LR Model

2.5.1 Estimating the Takeoff Weight

According to Boeing [11], the Boeing 777-200LR model which is powered by two GE90-100 Series Engines has the maximum design taxi weight of 768,000 lb. Each engine (specifically the GE90-110B model) produces 110,000 lb maximum continuous sea level static thrust. The aircraft model has two typical seating capacities: the two-class layout can hold 279 seats and the three-class layout can hold 301 seats. In order to make an initial sizing example and to make a comparison between the sizing results to the actual model's parameters, we need to know more specific details of the takeoff weight and the

range of the aircraft. Thus we refer to the information in Fig. 2.10 (a courtesy graph from Boeing [11]) for the range and the takeoff weight of the aircraft.

Based on the chart in Fig. 2.10, the "brake release gross weight" is equivalent to our MTW in Eq. (2.1). Boeing defines the operating empty weight (OEW) as the aircraft's weight without the usable fuel and the payload. Thus, the quantity on the vertical axis of the graph in Fig. 2.10 is the sum of the payload and the empty weight according to our weight definition in Eq. (2.1). In most cases, we also consider this sum of weights as the maximum landing weight (MLW) of the aircraft. Let us assume that a 301-seat Boeing 777-200LR has the OEW plus the payload equals 350,000 lb and a 5,000-nmi-range. We read its MTWO is approximately 505,000 lb from the chart in Fig. 2.10. With the same number of passengers and the same range, Eq. (2.10) yields an estimation of the aircraft's takeoff weight at 507,170 lb. The difference is about 0.4% relative to the MTWO that is read from Boeing's chart (Fig. 2.10). Notice that the fuel weight, the empty, and the payload in our calculations might differ from Boeing's calculation mainly due to the difference in the flight mission and the assumptions in calculating the empty weight. We shall discuss this matter in details in the next few sections.

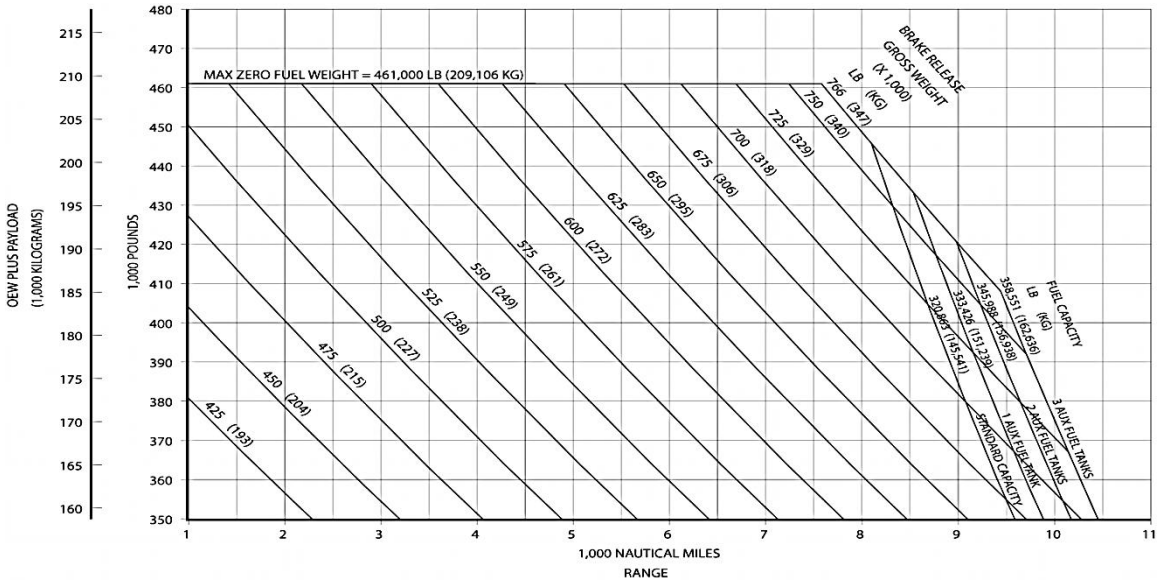

Figure 2.10: Boeing 777-200LR/GE90-100: range – weight chart.

2.5.2 Payload Calculation

Even though the estimation from Eq. (2.10) is highly accurate, it does not provide details about the payload, the empty weight, and the fuel weight of the aircraft. As a designer, we must provide these three weight components. They are the essential details which describe an aircraft. It is difficult to know the exact values of the weights at the preliminary sizing stage. However, we must at least provide their approximations. A 5,000-nmi-range is long enough for the aircraft to fly from Seattle to Tokyo. Thus a 5,000-nmi-range is classified as a transoceanic range. Therefore, the number of flight crew has 4 members. Since the number of passengers is 301 people, we assign 6 flight attendants to accompany the crew using Eq. (2.2). Applying Eqs. (2.3 – 5), we calculate the total payload at 86,380 lb.

2.5.3 Estimating the Required Aerodynamic Efficiency

Table 2.3: Performance Characteristic of Boeing 777-200ER/GB90-85B (2ERGB)

Parameter	*Value*	*Parameter*	*Value*
Wing Span	199 ft 11 in	2ERGB Max Wing Loading	125.95 lb/ft^2
Aspect Ratio	8.7	2ERGB Max T_{SLS}/W_{TK} Ratio	0.29 lb_f/lb_m
Wing Reference Area	4,605 ft^2	Cruise Mach	0.84
2ERGB OEW	317,300 lb	2ER Approach Speed	138 kn
2ER Max Fuel Weight	299,490 lb	2ERGB Initial Cruise Altitude	36,600 ft
2ERGB Max TO Weight	580,000 lb	2ERGB TO Field Length	8,250 ft
2ER Max LD Weight	460,000 lb	2ERGB LD Field Length	5,300 ft
Note: "TO" – Takeoff; "LD" – Landing			

The information about the Boeing 777-200LR model's performance is necessary for good estimation of its aerodynamic efficiency. The following parameters are either the general parameters of the Boeing 777 family or the exclusive parameters of the Boeing 777-200ER/GE90-85B Engine Series (2ERGB). We found the Boeing 777-200ER model and

the Boeing 777-200LR model are very similar. These numbers are collected from the Jane's Information Group [12] and are reported Table 2.3.

In order to calculate the maximum aerodynamic efficiency, we need the TSFC of the GE90-115B engine. For simplicity, we assume the cruising TSFC to be 0.65 $\left(\frac{lb_m}{hr \cdot lb_f}\right)$ and the takeoff TSFC to be 0.4 $\left(\frac{lb_m}{hr \cdot lb_f}\right)$ based on Fig. 2.7. Let set the first loitering endurance to be 20 minutes. Based on these parameters, the initial estimation of the required maximum aerodynamic efficiency of the aircraft is determined at 20.

2.5.4 Takeoff Weight Iteration

Table 2.4: Takeoff weight iteration for the Boeing 777-200LR

$W_{tk,guessed}$	W_{pld}	W_{empty}	W_{fuel}	$W_{tk,computed}$
507,170	86,380	306,832	224,756	617,968
617,968	86,380	284,845	212,188	583,413
583,413	86,380	290,953	215,680	593,012
593,012	86,380	289,197	214,676	590,253
590,253	86,380	289,697	214,962	591,039
591,039	86,380	289,554	214,880	590,814
590,814	86,380	289,595	214,903	590,878
590,878	86,380	289,583	214,897	590,860
590,860	86,380	289,587	214,899	590,865
590,865	86,380	289,586	214,898	590,864
590,864	86,380	289,586	214,898	590,864

Once the maximum aerodynamic efficiency is known, we can compute the fuel weight for the reserves and the fuel weight-to-takeoff weight fraction of the entire flight mission. In this example, we set the diversion endurance to be 30 minutes and the second loitering endurance to be 10 minutes. In addition, the $\frac{W_e}{W_0}$ weight ratio must be known in order to

evaluate Eq. (2.14). This weight ratio is computed by using the initial guess takeoff weight that is determined by Eq. (2.2). The computation results are shown in Table 2.4.

2.5.5 Calculations of the Required SLS Thrust and the Wing Reference Area

Furthermore, we should compare the calculations of the required thrust and the wing platform area by Eq. (2.15a) and Eq. (2.16a), respectively. The results are compared in Table 2.5. The documented takeoff weight is determined based on the OEW at 317,300 lb plus the payload at 86,380 lb giving the total of 403,680 lb. In the documented row, the thrust-to-weight ratio, the wing loading, and the wing reference area are quoted from [12]. The documented SLS thrust per engine is calculated by multiplying the takeoff weight with the thrust-to-weight ratio.

Table 2.5: Comparison between statistical sizing results and documented values of the Boeing 777-200LR

Source	$W_{pld} + W_e$	W_{tk}	$\frac{T_{SLS}}{W_{tk}}$	T_{SLS}/Eng	$\frac{W_{tk}}{S_{ref}}$ (lb/ft^2)	S_{ref}
Documented	403,680 lb	580,000 lb	0.29	84,100 lb	125.95	4,605 ft^2
Int. Estimation	375,966 lb	590,864 lb	0.28	82,063 lb	136.98	4,314 ft^2

2.6 Summary

The historical data survey is a feasible method to study the design requirements of an aircraft. In the case when the designers want to develop a current model into a new one, or when the design target is a conventional or unconventional concept, this survey method is an appropriate starting point of a design project. Our project is designing an unconventional conceptual commercial aircraft. We mainly want to study how to improve the aircraft's efficiency by introducing a new concept. Thus the historical data and the FAR rules are very helpful in determining the design requirements.

The results of our calculations for the basic parameters of the Boeing 777-200ER/GE94-100 Engine Series Model show that the statistical equations are accurate enough so that we can rely on these equations for our design. These calculations are based on only the statistical data and fitted curves. The statistical data represents a wide range of different aircraft. Thus we should expect uncertainties in our estimations. The numerical results show that our estimations for the required SLS thrust per engine and the wing reference area are underestimated, even though the takeoff weight is overestimated. However, the documented parameters are not the absolute measurements either. If we knew how Boeing or the Jane's Information Group calculated the payload and know the flight mission scheme of the Boeing 777-200LR model, we would obtain better estimations.

Since the design requirements are also set based on the FAR rules, we want to ensure that our basic parameters satisfy these rules. We are going to introduce another sizing method in the next chapter. It is a typical trade study in designing a new aircraft. The method will be more sophisticated than the statistical estimations that are presented in this chapter because it will include all the constraints from the design requirements.

Chapter 3 Trade Study in Aircraft Preliminary Sizing

3.1 Introduction

We have been able to set up the design requirements for a new vehicle's concept in Chapter 2. We have utilized these requirements as our guidelines to design the vehicle. We have determined the takeoff weight, the required SLS thrust, and the wing reference area at the end of Chapter 2. However, we are still not able to ensure that these three basic parameters satisfy all the requirements. In this chapter, we are going to determine the optimal design point of the aircraft so that the thrust, the wing area, and the takeoff weight will satisfy all the requirements. These requirements make up constraints which challenge the designers throughout the preliminary design. These constraints are (1) the takeoff ground roll distance, (2) the takeoff climb gradients, (3) the maximum bank angle, (4) the initial cruise capability, (5) the time to climb, (6) the approach speed limit, and (7) the wing span limit.

Even though the results from initial estimation in the previous chapter do not guarantee that they will satisfy all the requirements, it does not mean the work done in that chapter is worthless. In a vast plane of possibilities, there is a tiny area for an optimal design point to exist. It will very difficult for us to locate a single point in an infinite positive thrust-wing area plane. Sometimes, it is impossible to sketch these contours when the ranges of thrust and wing area are too large. The initial estimations in Chapter 2 have guided us to the site where the optimal design point exists. The computation example at the end of this chapter will illustrate the present method and will portray the helpfulness of the initial estimations.

3.2 Takeoff Ground Roll Distance

In the main flight mission of Fig. 2.6, there are four important phases. They are (1) the takeoff phase, (2) the climbing phase, (3) the cruising phase, and (4) the landing phase. Each of these phases has a set of requirements that are mandated either by the

development plan or by the FAR rules. Each of these requirements is a constraint on the others. Our optimal design point is a combination of the minimal thrust and the smallest wing area that satisfy all the requirements.

Let us begin the discussion at the takeoff phase. The FAR 25 describes the takeoff flight path for jet transport is the path that is traced out by the aircraft from the starting point to the point at which the aircraft is 1,500 ft above the surface of the runway. A complete takeoff procedure contains two phases. The first part is called ground roll phase in which the aircraft accelerates from its standing point to the point it reaches the liftoff speed, V_{LO}. This is the moment where the aircraft is airborne for the first time in the flight mission. The second phase is called the takeoff climb where the aircraft accelerates from the rotational speed, V_R, to the final takeoff speed, V_{FTO}. The entire takeoff path is shown in Fig. 3.1 (there is no scale in this figure).

In this section, we focus on the ground roll distance. For a given weight W and a specific wing, we must determine the thrust T and the wing area S so that the aircraft can lift off after it has run within a finite distance d_{TO} on the runway. There is an elegant derivation and analysis of the formula for calculating the ground roll distance in [2]. In this presentation, we borrow the simplified version of ground distance formula from [2]. It is written as:

$$d_{TO} = \frac{1.21}{g\rho C_{L,TO}} \frac{W/S}{T/W} + 1.1 V_s t_N \tag{3.1}$$

where g is the gravitational acceleration, ρ is the air density, $C_{L,TO}$ is the takeoff maximum lift coefficient of the wing, t_N is the rotational time, and V_s is the stall speed. For simplicity of equations, we dropped all the subscripts of weight, thrust, and wing area quantities in these general sections. The stall speed of an aircraft is defined as the minimum speed that keeps the vehicle airborne. It is formulated as:

$$V_s = \sqrt{\frac{2}{\rho} \frac{1}{C_{L,TO}} \frac{W}{S}} \tag{3.2}$$

Note that the constant 1.1 in Eq. (3.1) is the ratio of V_{LO} to V_s; and 1.21 is the square of 1.1. The first term of Eq. (3.1) is the accelerated distance from V = 0 to V_R; the second term in Eq. (3.1) is the distance during the rotational maneuver. A wing with a high maximum takeoff lift coefficient requires a short distance to lift off. If everything is fixed, the increasing in thrust requires the decreasing in wing area to keep the same lift off distance and vice versa. If an aircraft has larger wing reference area, it would lift off at a shorter distance on the runway. Similarly, providing stronger thrust will help the aircraft lift off at shorter ground roll distance. Eq. (3.1) is derived based on the assumption that the speed of the vehicle during the entire acceleration is constant. This constant speed is the mean value of V_{LO}. Similarly, we should implement Eq. (3.1) with the vehicle's mean weight during the takeoff phase.

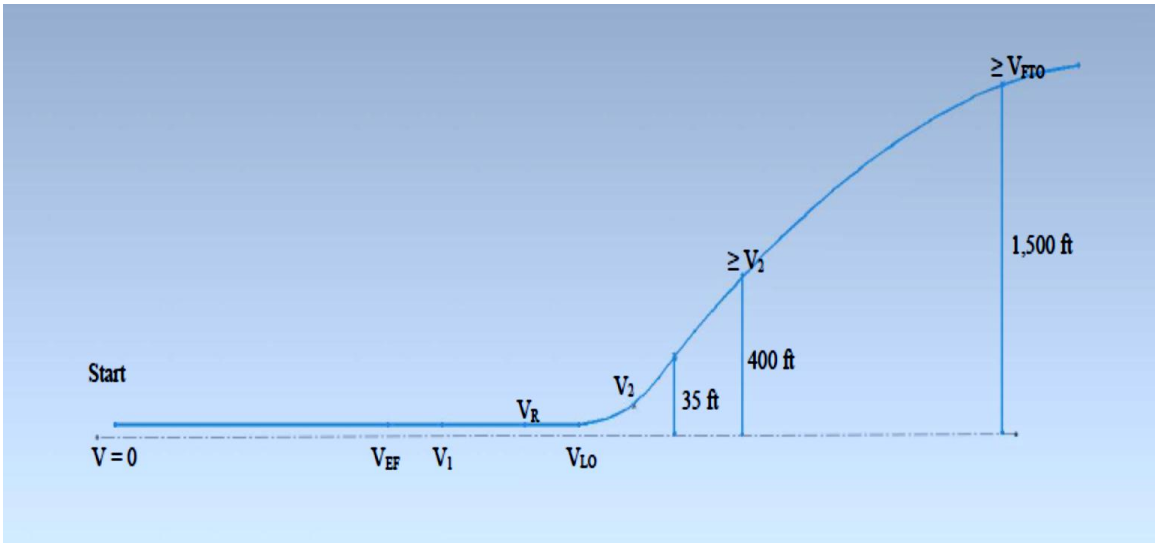

Figure 3.1: FAR takeoff path of commercial jet transport.

3.3 Takeoff Climb Gradients

In the second phase of the takeoff, the biggest concern for the designers is the climb capability of the vehicle. As soon as the vehicle is airborne, it must climb over an obstacle and keep accelerating until it reaches 1,500 ft above the runway surface and flies at the final takeoff speed. This capability is measured by the climb gradients of the vehicle. This takeoff climb phase has three segments where the requirements of each

segment are set by FAR 25. There is a summary of the FAR rule in Appendix F of [8]. In this section, we briefly underline the key requirements of the rule.

The first segment is the period when the vehicle completes the rotation and the transition. In terms of the speed, it is the stage where the vehicle accelerates from V_R to V_2. During this climb segment, the average speed of the vehicle is assumed to be the liftoff speed, V_{LO}. The flaps are set to the takeoff positions; the landing gear is still down; and the steady climb gradient is required to be positive. The climb gradient is defined as the ratio of the rate of climb to the reference speed. In this case the reference speed is liftoff speed, V_{LO}.

The second segment of the takeoff climb is the stage where the airplane keeps accelerating beyond the V_2 speed, clears the obstacle, and climbs up to 400 ft above the runway surface. FAR has a guideline for this climb segment as following: the flaps are at the takeoff positions; the landing gear is up; the steady climb gradient is 2.4 %; and the reference speed is V_2.

The third takeoff climb segment is the stage where the aircraft accelerates to the final takeoff speed, V_{FTO}, and it clears the 1,500 ft mark as a requirement to complete the takeoff procedure. The configuration for this final stage is prescribed as all flaps and landing gear is up; the steady climb gradient is 1.2 %; and the reference speed is $1.25V_S$, where V_S is the stall speed.

The last bit of this discussion is the definition of the reference speed at each stage. The definitions of the takeoff speeds by FAR 25 are little complicated and not easy to digest. In fact, taking the stall speed as the base-speed and let every other speed be the references of the stall speed yield substantially accurate results. More importantly, the stall speed is the minimum speed to keep an airplane airborne. Therefore, the stall speed is the most appropriate reference speed. A summary of the takeoff climb and the reference speeds are tabulated in the Table 3.1 (for more details on the reference speeds please consult [13]).

Table 3.1: FAR takeoff climb configuration in each segment				
Takeoff Climb	*G (%)*	*Speed*	*Flap Position*	*Landing Gear*
First Segment	0.5	$V_{LO} = 1.1V_S$	Takeoff	Down
Second Segment	2.4	$V_2 = 1.2V_S$	Takeoff	Up
Third Segment	1.2	$V_{FTO} = 1.25V_S$	Up	Up

It would be easier to discuss the formula of the climb gradient with a free body diagram (FBD) of an aircraft in steady flight. The FBD is sketched in Fig. 3.2 with an assumption that the jet thrust vector coincides with the longitudinal axis of the aircraft. In doing so, the flight path angle is automatically offset and the thrust vector is parallel and opposite to the drag force.

The rate of climb of the vehicle is defined as the vertical component of the vehicle's velocity. The formula for the rate of climb that is borrowed from [2] is written as:

$$Vsin\gamma = V\left[\frac{T}{W} - \frac{1}{2}\rho V^2 C_{Dmin}\left(\frac{W}{S}\right)^{-1} - \frac{W}{S}\frac{2K}{\rho V^2}\right] \tag{3.3}$$

with the assumption that $cos\gamma = 1$, and where C_{Dmin} is the minimum drag coefficient of the drag polar, and $K = \frac{1}{\pi eAR}$.

The definition of the climb gradient from [8] is the tangent of the climb angle. That is the ratio of the vertical component of the velocity to the horizontal component of the velocity. Let G be the climb gradient.

$$G = tan\gamma = \frac{Vsin\gamma}{Vcos\gamma} \tag{3.4}$$

We have already assumed that $cos\gamma = 1$ in the rate of climb equation. Thus the climb gradient is approximately given by:

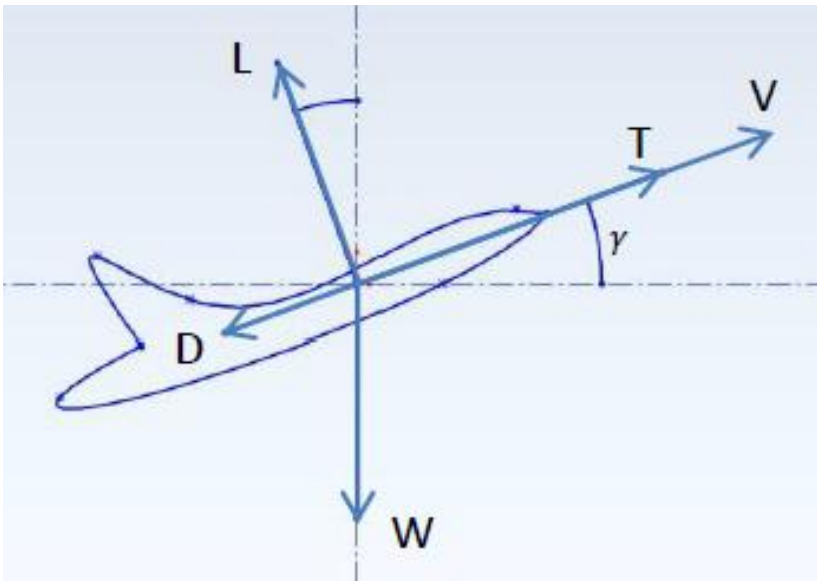

Figure 3.2: Free body diagram of an aircraft in climbing flight.

$$G = \left[\frac{T}{W} - \frac{1}{2}\rho V^2 C_{Dmin}\left(\frac{W}{S}\right)^{-1} - \frac{W}{S}\frac{2K}{\rho V^2}\right] \times 100\% \tag{3.5}$$

where 100% converts the climb gradient from the rational form to the percentage form. Looking Eq. (3.5), we see that a wing that has small C_{Dmin} and small K will offer the airplane a high climb gradient. In order to have a small K, the wing must have a large aspect ratio and the aircraft must have high Oswald efficiency factor.

Obviously, Eq. (3.5) indicates that having higher thrust-to-weight ratio will offer larger climb gradients. On the other hand, traveling at higher speed will decrease the climb gradient. However, the effect of the wing loading on the aircraft climb gradient is not obvious. Let us graphically analyze this effect through the climb gradient of the Boeing 777-200LR model in the first takeoff climb segment. The climb gradient contours in Fig. 3.3 show that the climb gradient isoclines are the lines with positive slopes. Along an isocline, the increasing in thrust must be compensated by the increasing in wing area. To illustrate the velocity's effect on the climb gradient, we sketch two contours Fig. 3.3(a – b). The contours show that increasing the speed twice causes the climb gradient drops by 15%.

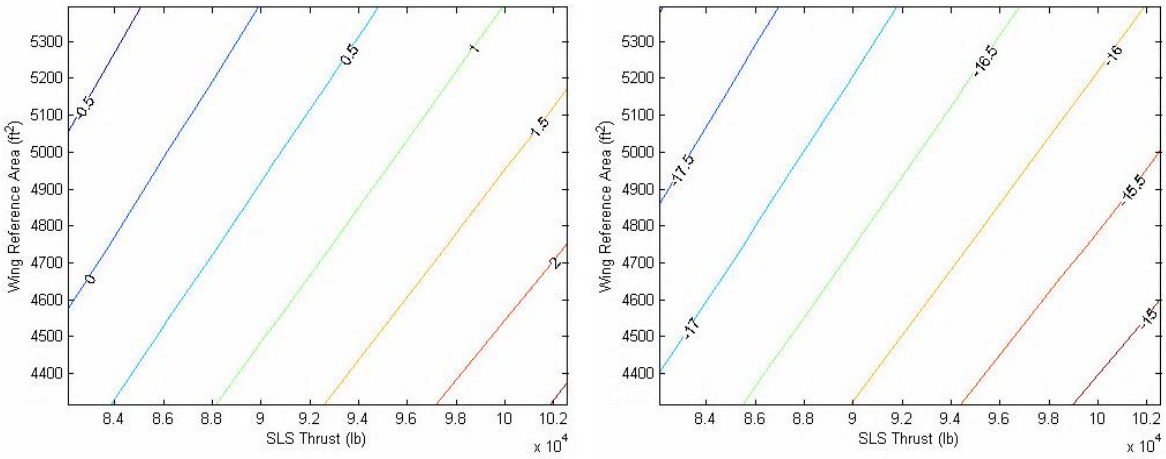

(a): climbing at speed of V **(b): climbing at speed of 2V**

Figure 3.3: Climb gradient contours of Boeing 777-200LR during takeoff climb.

3.4 Maximum Roll Angle at the End of Takeoff Climb

After finishing takeoff, an aircraft usually turns its nose toward the destination before beginning to climb and cruise out. Thus we should check the maximum roll angle of the aircraft at the end of takeoff climb. The roll angle ϕ of an aircraft is defined as the arccosine of the reciprocal of its load factor n. The load factor is the ratio of the lift force to the weight of the aircraft.

$$\phi = arccos\frac{1}{n} \tag{3.6}$$

where

$$n = \frac{L}{W} \tag{3.7}$$

The equations of motion of an aircraft in climbing flight and level flight are different mainly because of the existence of the climb angle in the climbing flight. The rolling maneuver at the end of takeoff climb is different from the level turning maneuver. Nonetheless, the assumption of thrust equals drag is acceptable for steady climb; and the climbing flight of most commercial jet transport is considered as steady climb. Thus our sizing for the turning capability of a commercial jet transport based on the analysis of a

level turning maneuver is still acceptable. Note that for fighter jets, the level rolling maneuver analysis would be biased because most fighter jets are required to climb more rapidly and aggressively. Thus steady climb assumption would be inappropriate. A detailed derivation for the load factor of an aircraft can be found in [2]. In this presentation, we use the final version of the formula for our analysis. It is:

$$n = \sqrt{\frac{\frac{1}{2}\rho V^2}{K(W/S)}\left[\frac{T}{W} - \frac{1}{2}\rho V^2 \frac{C_{Dmin}}{W/S}\right]} \tag{3.8}$$

Surprisingly, the altitude, the minimum drag coefficient, the thrust-to-weight ratio, and the wing loading slightly affect the roll angle. The roll angle is very sensitive to the speed of the aircraft. Flying at a higher speed will allow the aircraft to bank at a larger roll angle. Normally, the banking angle requirement for the commercial aircraft is not as important as for the fighter jets because a sharp and quick turn is a top priority in dogfight. On the other hand, turning slowly in a steady climb is an important criterion to ensure a smooth ride on the commercial jets.

3.5 Time to Climb to Initial Cruise Altitude

When the nose is pointed toward the destination, the pilots begin to take the aircraft up to the cruising altitude. During the climbing flight, a commercial aircraft is asked to meet three main criteria. One is the aircraft must climb as quickly as it can to avoid causing a traffic jam within airspace B (below 10,000 ft). Two is the aircraft is restricted to a speed limit of 250 knots within the airspace B. Three is the aircraft must also accelerate during the climbing flight so that when it reaches the initial cruise altitude, its speed is equal to the long range cruise (LRC) Mach number.

Due to overlapping among the constraints, an appropriate climbing scheme is very necessary in order to design the aircraft satisfactorily. A typical climbing scheme for civil aircraft can be found in [14]. We are presenting the simplest scheme in our discussion here. The climbing path is sketched in Fig. 3.4. The scheme shows that from 1,500 ft, the

aircraft climbs as fast as it can to 10,000 ft. As soon as it reaches 10,000 ft, the aircraft begins to accelerate as fast as it can. The reasons for choosing to accelerate at the edge of the airspace B are because the air is still dense enough for the jet engines to save fuel at this altitude and the pilots do not violate the air traffic rules.

The detailed derivation of the equation of motion for the accelerated climb is presented in [2] using the energy method. In this presentation, we implement the simplified version of the accelerated rate of climb.

$$\frac{dh}{dt} + \frac{V}{g}\frac{dV}{dt} = V\left[\frac{T}{W} - \frac{1}{2}\rho V^2 C_{Dmin}\left(\frac{W}{S}\right)^{-1} - \frac{W}{S}\frac{2K}{\rho V^2}\right] \tag{3.9}$$

where $\frac{dh}{dt}$ is the rate of climb and $\frac{dV}{dt}$ is the acceleration. The right hand side of Eq. (3.9) has the same characteristics as the right hand side of Eq. (3.3). In case of steady climb, $\frac{dV}{dt} = 0$ transforms Eq. (3.9) back to Eq. (3.3).

$$\frac{dh}{dt} = V\left[\frac{T}{W} - \frac{1}{2}\rho V^2 C_{Dmin}\left(\frac{W}{S}\right)^{-1} - \frac{W}{S}\frac{2K}{\rho V^2}\right] \tag{3.10}$$

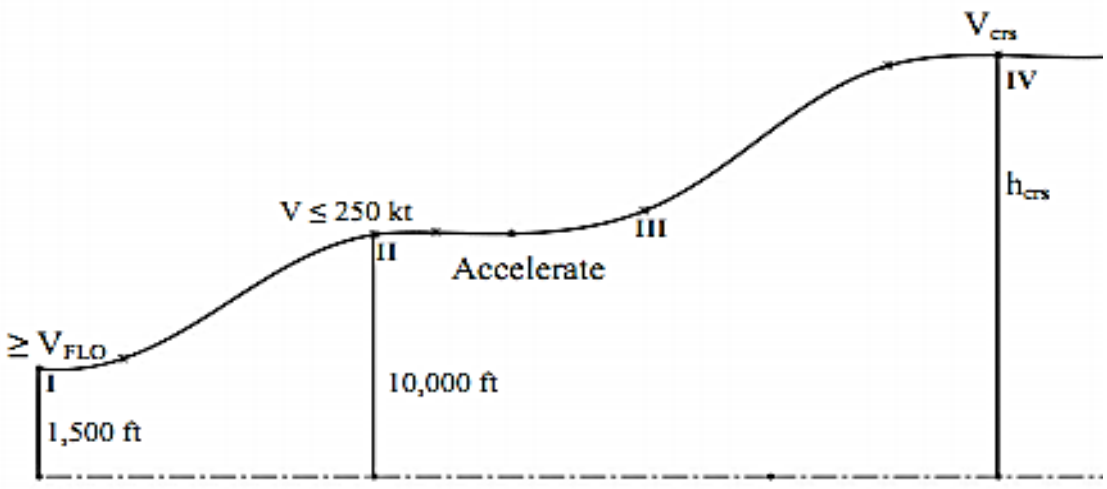

Figure 3.4: Typical climb scheme of civil aircraft.

In case of level acceleration, $\frac{dh}{dt} = 0$ yields the formula for acceleration.

$$\frac{dV}{dt} = g\left[\frac{T}{W} - \frac{1}{2}\rho V^2 C_{Dmin}\left(\frac{W}{S}\right)^{-1} - \frac{W}{S}\frac{2K}{\rho V^2}\right] \tag{3.11}$$

We assumed steady climb and level acceleration in our calculation for the time to climb. According to our climb scheme in Fig. 3.4, the time to climb from the end of takeoff to the initial cruise altitude is the sum of three time segments.

3.5.1 Time to Climb out of Airspace B

In the first climb segment, the aircraft climbs from 1,500 ft above the runway at V_{FTO} to 10,000 ft at 250 knots. With the assumption of steady climb, we use Eq. (3.10) to calculate the first time segment. Since Eq. (3.10) is written in the differential form, we have to integrate it in order to find the expression for the time to climb. In this equation, the thrust, the air density, the weight, and the speed are the functions of altitude. Thus it is difficult to evaluate the integral. A simplest alternative is dividing the altitude difference by the average rate of climb [14].

Let h_{tk} be the altitude of the runway from sea level. The initial altitude at the beginning of climb is $h_i = h_{tk} + 1{,}500\ ft$. The intermediate climb altitude is 10,000 ft, $h_m = 10{,}000\ ft$. The final climb altitude is the cruise altitude, $h_f = h_{crs}$. The average rate of climb in the first climb segment and the time to climb are calculated in the following steps:

The steady rate of climb at h_i:

$$\left.\frac{dh}{dt}\right|_{h_i} = V\left[\frac{T}{W} - \frac{1}{2}\rho V^2 C_{Dmin}\left(\frac{W}{S}\right)^{-1} - \frac{W}{S}\frac{2K}{\rho V^2}\right]\Bigg|_{h_i, V_{FTO}} \tag{3.12a}$$

The steady rate of climb at h_m:

$$\left.\frac{dh}{dt}\right|_{h_m} = V\left[\frac{T}{W} - \frac{1}{2}\rho V^2 C_{Dmin}\left(\frac{W}{S}\right)^{-1} - \frac{W}{S}\frac{2K}{\rho V^2}\right]\Bigg|_{h_m,250kt} \tag{3.12b}$$

The average rate of climb in the first segment:

$$\forall \left.\frac{dh}{dt}\right|_1 = \frac{1}{2}\left(\left.\frac{dh}{dt}\right|_{h_i} + \left.\frac{dh}{dt}\right|_{h_m}\right) \tag{3.12c}$$

The time to climb in the first segment:

$$\Delta t_1 = \frac{h_m - h_i}{\forall \left.\frac{dh}{dt}\right|_1} \tag{3.13}$$

3.5.2 Time to Accelerate from 250 knots to V_m

When the aircraft is out of the airspace B and its speed has reached 250 knots, the pilots will accelerate the aircraft until it reaches an allowable flight speed V_m in knots at 10,000 ft. We use the same averaging method in the previous section to calculate the time to accelerate. The following equations are used to calculate the average acceleration.

$$\left.\frac{dV}{dt}\right|_1 = g\left[\frac{T}{W} - \frac{1}{2}\rho V^2 C_{Dmin}\left(\frac{W}{S}\right)^{-1} - \frac{W}{S}\frac{2K}{\rho V^2}\right]\Bigg|_{h_m,250kt} \tag{3.14a}$$

$$\left.\frac{dV}{dt}\right|_2 = g\left[\frac{T}{W} - \frac{1}{2}\rho V^2 C_{Dmin}\left(\frac{W}{S}\right)^{-1} - \frac{W}{S}\frac{2K}{\rho V^2}\right]\Bigg|_{h_m,V_m} \tag{3.14b}$$

$$\forall \frac{dV}{dt} = \frac{1}{2}\left(\left.\frac{dV}{dt}\right|_1 + \left.\frac{dV}{dt}\right|_2\right) \tag{3.14c}$$

The time to accelerate:

$$\Delta t_2 = \frac{V_m - 250\ kt}{\forall \frac{dV}{dt}} \tag{3.15}$$

3.5.3 Time to Climb to Initial Cruise Altitude and to Accelerate to Cruise Speed

In the last climb segment, the aircraft climb from 10,000 ft at V_m to the initial cruise altitude at V_{crs}. We use the same method as presented in §3.5.1. The final time to climb segment is given by:

$$\Delta t_2 = \frac{h_{crs} - h_m}{\forall \frac{dh}{dt}\Big|_2} \tag{3.16}$$

where

$$\forall \frac{dh}{dt}\Big|_2 = \frac{1}{2}\left(\frac{dh}{dt}\Big|_{h_m, V_m} + \frac{dh}{dt}\Big|_{h_{crs}, V_{crs}}\right) \tag{3.17}$$

3.6 Initial Cruise Capability

After climbing, the aircraft reaches the initial cruise altitude. It begins to cruise out to the destination at the designated cruise speed. At this stage, we want to know whether the aircraft is capable to cruise. Thus the initial cruise capability needs to be examined. The initial cruise capability of the commercial aircraft is the requirement for the aircraft to have a steady rate of climb of 300 fpm while it is flying at the cruise speed at the initial cruise altitude [14]. Thus we can implement Eq. (3.3) or Eq. (3.10) with the cruising conditions to examine the initial cruise capability of a commercial aircraft. Of course, we will expect the similar contours like the climb gradient contours in Fig. 3.3.

3.7 Approach Speed

At the end of cruise, the aircraft descends and approaches the runway to make a landing. The designers must size the aircraft's wing reference area so that it can make a safe landing. A safe landing is usually measured by the approach speed. The approach speed of a commercial airplane is normally defined as 30% higher than its stall speed at landing conditions. Therefore, the approach is written as:

$$V_{app} = 1.3 \times \sqrt{\frac{2}{\rho}\frac{1}{C_{L,max}}\frac{MLW}{S}} \tag{3.18}$$

where MLW is the maximum landing weight of the vehicle.

A small approach speed helps the aircraft avoiding suffer from a strong impact between the landing gear and the ground. A small approach speed will ensure the vehicle being able to stop before running out of the runway. Moreover, when an aircraft approaches a runway, it is required to fly under 250 knots again. Thus, the approach speed is usually small. In real life flight, the pilots can use flares or reversed thrust to decelerate the aircraft while approaching a runway. These options are not considered in our discussion here. In our case, we also assume the thrust is very small, almost zero. Therefore, we force the aerodynamics of the wings to help the vehicle gliding toward the runway.

In order to glide at a slower speed, the vehicle must glide at a lower altitude, at lighter *MLW*, and must have higher maximum approach lift coefficient and larger wing reference area. We want to size the aircraft for the worst case scenario. That is when the aircraft approaches a runway that is very high above sea level at the heaviest *MLW*. According to our designated flight mission in Fig. 2.6, the heaviest *MLW* is the weight at station 5.

3.8 Wing Span

The last constraint in the trade study sizing is the wing span limit. This constraint is optional in the study in some respects. Nonetheless, it serves as a key requirement in airport operation. Let imagine that two aircraft are taking off or landing at the same time on two parallel runways. If their wing spans are too long, the wing tip vortices will overlap each other and disaster will occur. When an aircraft parks near a terminal to dock with a passenger bridge, the available space between two stations is the limit of its wing span. Thus we include the wing span limit in this presentation. The wing span limit is sized based on aspect ratio and the wing reference area.

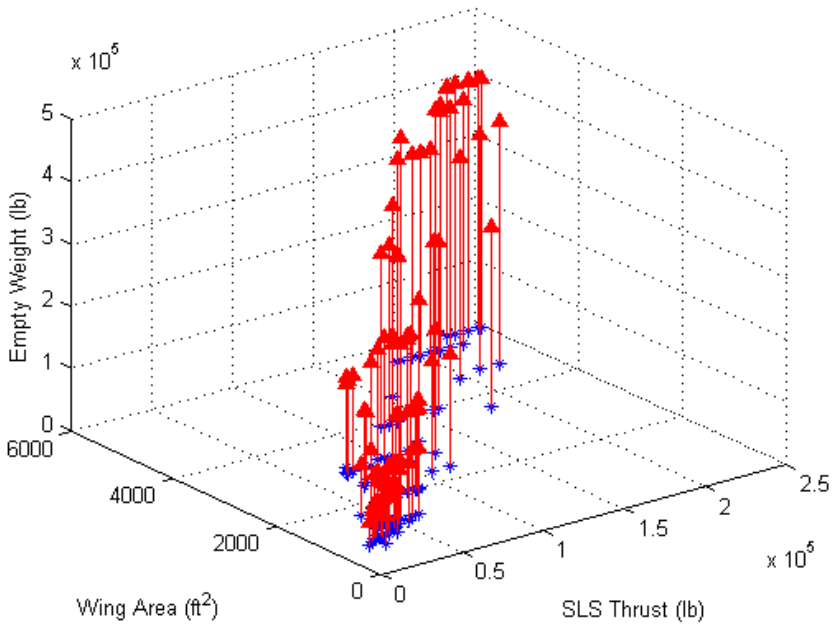

Figure 3.5: Empty weight of jet transport vs. SLS thrust & wing reference area.

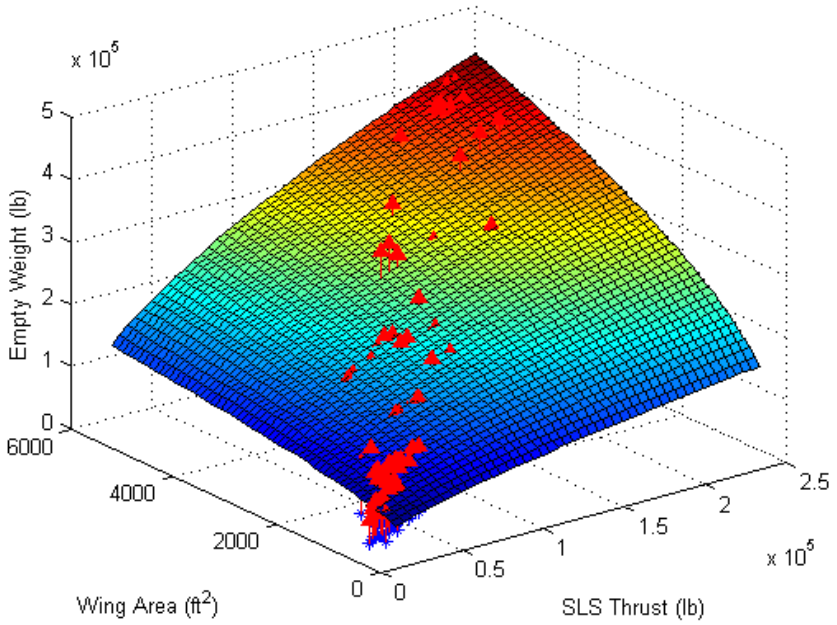

Figure 3.6: Empty weight surface of jet transport.

For an aspect ratio *AR* and the wing reference area *S*, the wing span limit *b* is given by:

$$b = \sqrt{AR \cdot S} \tag{3.19}$$

3.9 Empty Weight Surface

So far up to this point, we have covered all the essential requirements to ensure that the aircraft can carry out this designated flight mission. All the equations discussed above are straight forward. However, they must be implemented with care in order to size the aircraft correctly. Except for the wing span limit, all other equations involve with the weight, the thrust, and the wing reference area of the aircraft. In fact, the weight is a function of thrust and wing reference area.

The total weight of the aircraft includes the payload, the fuel weight, and the empty weight. Among these three weight components, the empty weight is directly associated with the size of the wing reference area and the amount of required thrust. The larger wing reference area will come with a larger structure weight. The stronger thrust will come with heavier engines, the structural weight of the engine mounts, and the engine accessories. Thus we need a function to estimate the empty weight based on the thrust and the wing reference area. Using the historical data of the empty weight of the commercial aircraft, we found:

$$W_e = 6.796\left(T_{sls}^{0.5654}\right)\left(S_{ref}^{0.4623}\right) \tag{3.20}$$

Then the takeoff weight is estimated by:

$$W_o = \frac{W_{pld} + W_e}{1 - \frac{W_f}{W_0}} \tag{3.21}$$

By keeping the fuel-to-takeoff weight fraction in Eq. (3.21), we ensure having enough fuel for the aircraft to accomplish the flight mission. For a given fixed range, when empty

weight increases, the fuel weight must also increase to cover the same range. The historical data and the fitting surface are presented in Figs. 3.5 – 6, respectively.

3.10 Pertinent Air Density Fraction and Weight Fraction

Making careful observations on these sizing equations, we see that the wing reference area interval stays constant throughout the flight plan; and it is independent of the altitude. On the other hand, the weight of the vehicle varies throughout the flight mission. The thrust interval varies with altitude. In order to create a meaningful trade study, we must use the takeoff weight as the reference weight and the SLS thrust as the reference thrust. It would be very convenient to have an equation to relate an available thrust at any altitude to the SLS thrust. The two quantities are related through the air density. It can be found in [15] as:

$$T = \frac{\rho}{\rho_{sl}} T_{sls} = \sigma_{(h)} T_{sls} \tag{3.22}$$

where T is the available thrust at altitude h, T_{sls} is the SLS thrust, ρ is the air density at altitude h, and ρ_{sl} is the sea level air density. The air density ratio function $\sigma_{(h)}$ is derived by using the standard atmosphere. The detailed derivation is provided in the Appendix B. The final version of the function is presenting below:

$$\sigma_{(h)} = \begin{cases} \left[1 - \left(6.875 \times 10^{-6} \frac{1}{ft}\right) h\right]^{4.25}, & 0 \le h \le 36{,}000\ ft \\ 0.298 \times e^{\left[1.729 - \left(4.804 \times 10^{-5} \frac{1}{ft}\right) h\right]}, & 36{,}000\ ft < h \le 82{,}000\ ft \end{cases} \tag{3.23}$$

3.11 Example 2: Determine the Optimal Design Point of the Boeing 777-200LR Model

Now, we are ready to apply the trade study into determining the optimal design point the Boeing 777-200LR Model. Its performance characteristics are listed in Table 2.3. The statistical takeoff weight, the initial required SLS thrust, and the initial wing reference area were calculated in Example 1 of §2.5. The initial thrust and wing area are our bases

in the trade study. We should vary the thrust and the wing area in a small neighborhood around these bases. In this example, we set the wing reference area as $S_{ref} \in [1,\ 1.25] \times 4{,}314\ ft^2$. For the thrust range, we must reduce the initial required SLS thrust to a half in order to account for the case of a single engine failure (the aircraft has two engines). Thus we set the SLS thrust range as $T_{sls} \in [1,\ 1.25] \times 82{,}063\ lb$. We assume the Oswald factor of the entire aircraft is 0.85, $e = 0.85$. The clean maximum lift coefficient, the maximum lift coefficient without aids from flap or slat, is 1.5, $C_{L,max-clean} = 1.5$. The clean minimum drag coefficient is 0.015, $C_{D,min-clean} = 0.015$.

3.11.1 Takeoff Ground Roll Distance

In takeoff ground roll distance estimation, we want to size the aircraft for the worst case scenario when the runway is high above sea level. In this example, we consider the Denver International Airport, whose runway is 6,000 ft above sea level, $h_{tk} = 6{,}000 ft$. The flap is set to the takeoff configuration so that the maximum lift coefficient is 1.75, $C_{L,max-tk} = 1.75$. During the takeoff ground run, the weight of the vehicle drops from W_o at the beginning of the run to W_1 at the end of the takeoff. Thus we use the average weight of W_o and W_1 as the weight during the takeoff run. The contour of Eq. (3.1) is shown in Fig. 3.7.

3.11.2 Takeoff Climb Gradients

The flaps are deployed during takeoff climb to increase the lift coefficient. Meanwhile, they cause more drag and decrease the Oswald factor. In the first and the second climb segments, the flaps are set to the takeoff configuration. In the third segment, the flaps are pulled up. Thus the increments in maximum lift coefficient during the first and the second climb segments are the same, but there is not any increment in maximum lift coefficient in the third climb segment. On the other hand, the landing gear is down only during the first segment. Combining with the flaps, the first segment has the highest minimum drag increment, and then the second segment and the third segment have no

minimum drag increment. The Table 3.2 lists all the necessary parameters for sketching the climb gradient contours in three segments. The contours are shown in Figs. 3.8 – 10.

3.11.3 Maximum Roll Angle

At the end of takeoff climb, the aircraft's weight is W_1 according to the flight mission in Fig. 2.6. It is flying at a speed of $1.25V_s$ and 1,500 ft above the runway's surface. The maximum roll angle contour is shown in Fig. 3.11.

3.11.4 Time to Climb to Initial Cruise Altitude

When the nose is pointing to the destination, the aircraft will rapidly climb out the airspace B in the conditions at the end of the takeoff climb. In the time to climb sizing, the worst case scenario is the climb from sea level. Thus the conditions at the end of takeoff climb in this case are at sea level rather than at Denver runway. At the edge of the airspace B, the speed of the vehicle reaches 250 knots; and its weight fraction is 0.965

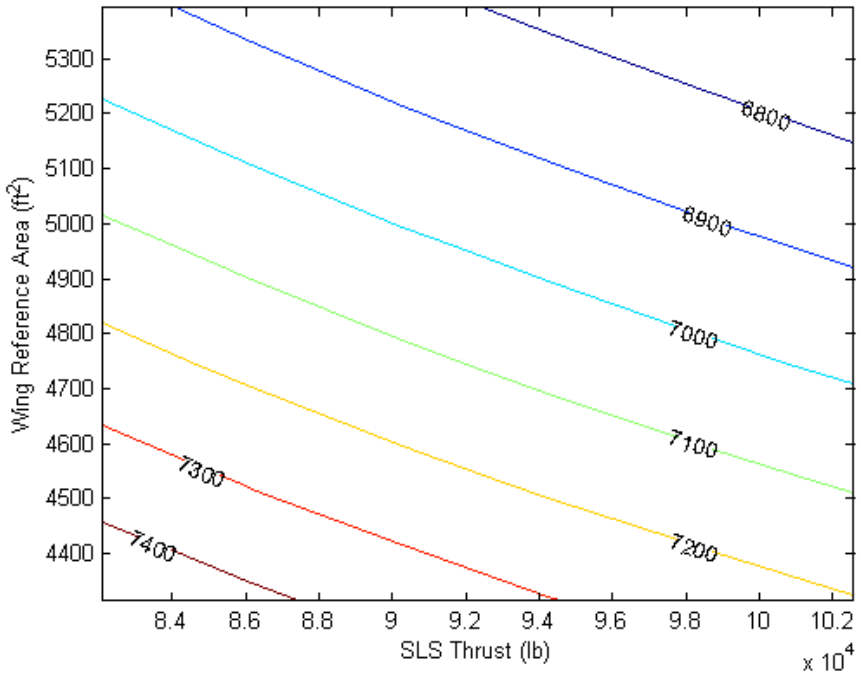

Figure 3.7: Takeoff ground roll distance of Boeing 777-200LR.

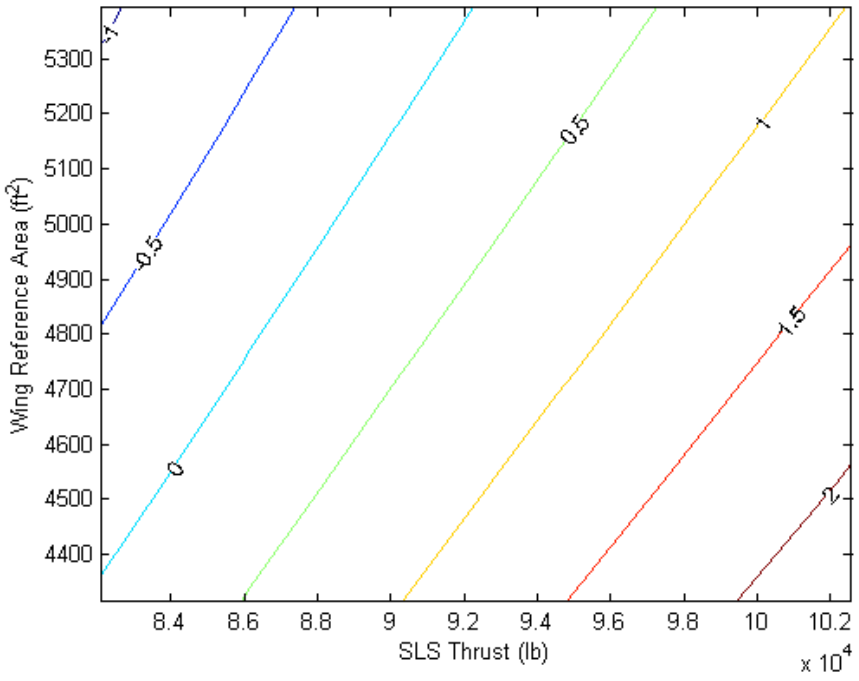

Figure 3.8: Climb gradient in takeoff climb segment 1 of Boeing 777-200LR.

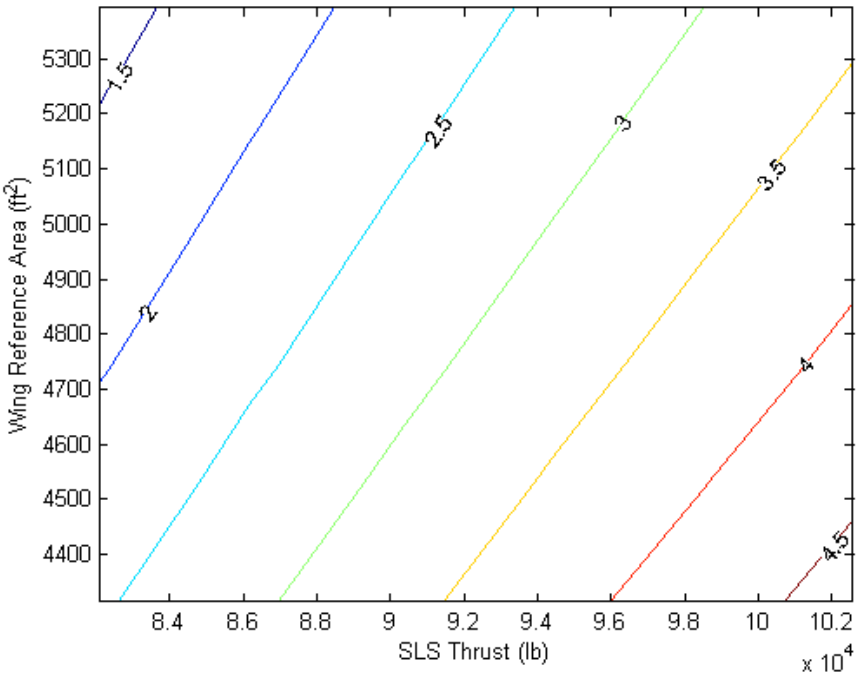

Figure 3.9: Climb gradient in takeoff climb segment 2 of Boeing 777-200LR.

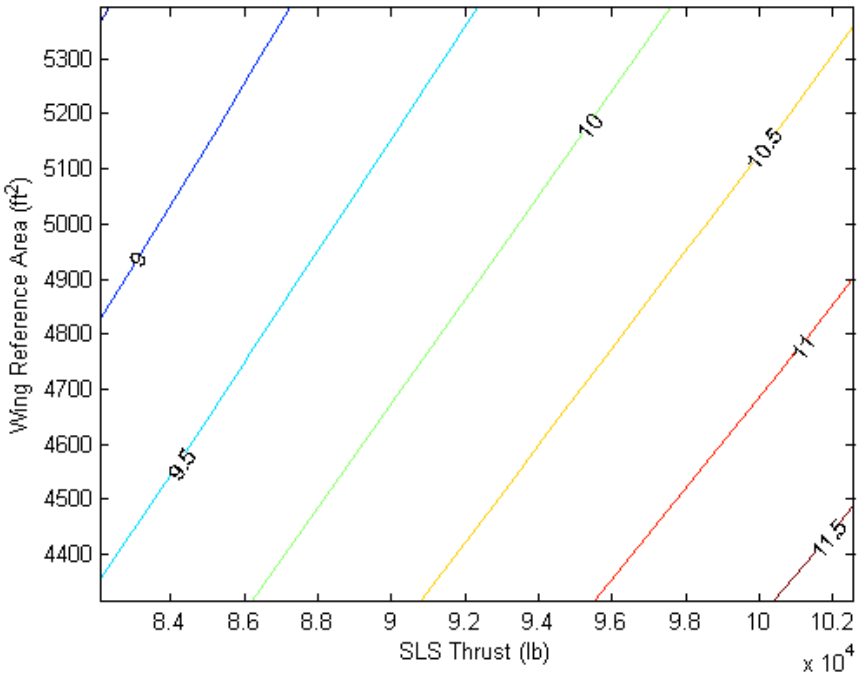

Figure 3.10: Climb gradient in takeoff climb segment 3 of Boeing 777-200LR.

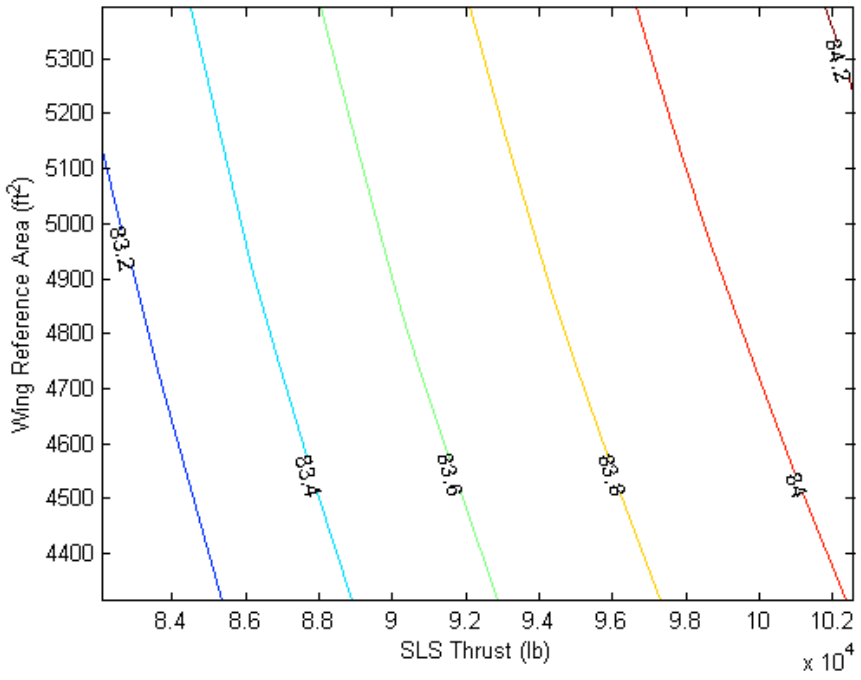

Figure 3.11: Maximum roll angle of Boeing 777-200LR.

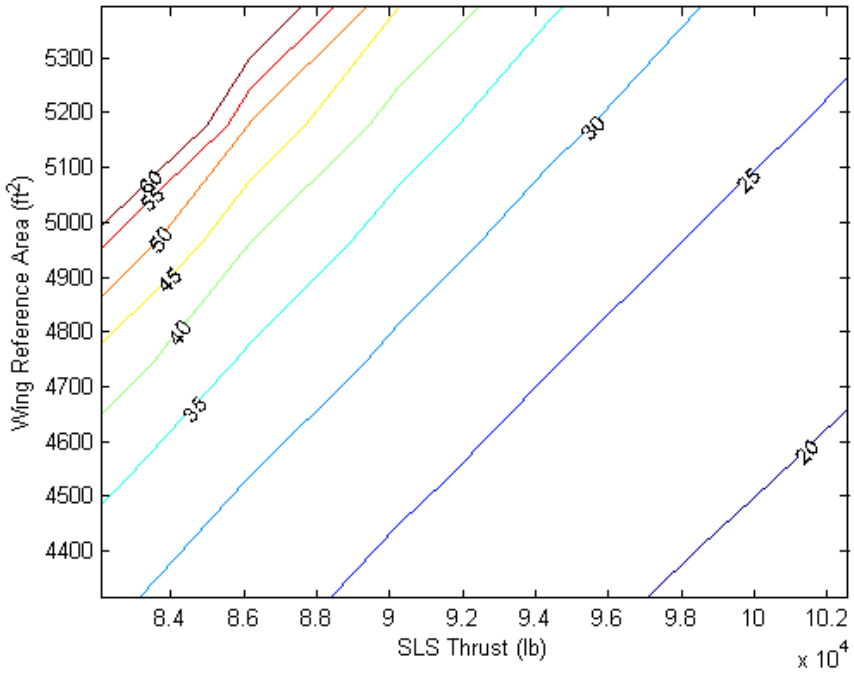

Figure 3.12: Time to climb of Boeing 777-200LR.

Table 3.2: Aerodynamics and Altitude Increments during Takeoff Climb			
Parameters	*Segment 1*	*Segment 2*	*Segment 3*
$\%e$	95	95	100
$\Delta C_{L,max}$	0.25	0.25	0
$\Delta C_{D,min}$	0.12	0.08	0
$\Delta h\ (ft)$	35	400	1,500

relative to the takeoff weight. Then the vehicle accelerates to 400 knots while maintaining the same altitude at 10,000 ft. At the end of acceleration, the fuel weight fraction is 0.955, relative to the takeoff weight. Finally, the aircraft climbs to the initial cruise altitude at 36,600 ft and accelerates to the cruise speed of Mach 0.84. Table 3.3 summarizes the climbing phase of the main flight mission. The time to climb contour is shown in Fig. 3.12.

Table 3.3: Summary of climbing in the main flight mission of Boeing 777-200LR				
Parameters	*Station I*	*Station II*	*Station III*	*Station IV*
Altitude (ft)	1,500	10,000	10,000	36,600
Speed	$1.25V_s$	250 kn	400 kn	0.84 Mach
W_i/W_o	W_1/W_o	0.965	0.955	W_2/W_o

3.11.5 Initial Cruise Capability

Sizing for the initial cruise capability is fairly straight forward. Based on the definition of the initial cruise capability in §3.6, we simply calculate the steady rate of climb of the aircraft in the cruising conditions, and then size accordingly. The initial cruise capability contour of the Boeing 777-200LR model is shown in Fig. 3.13.

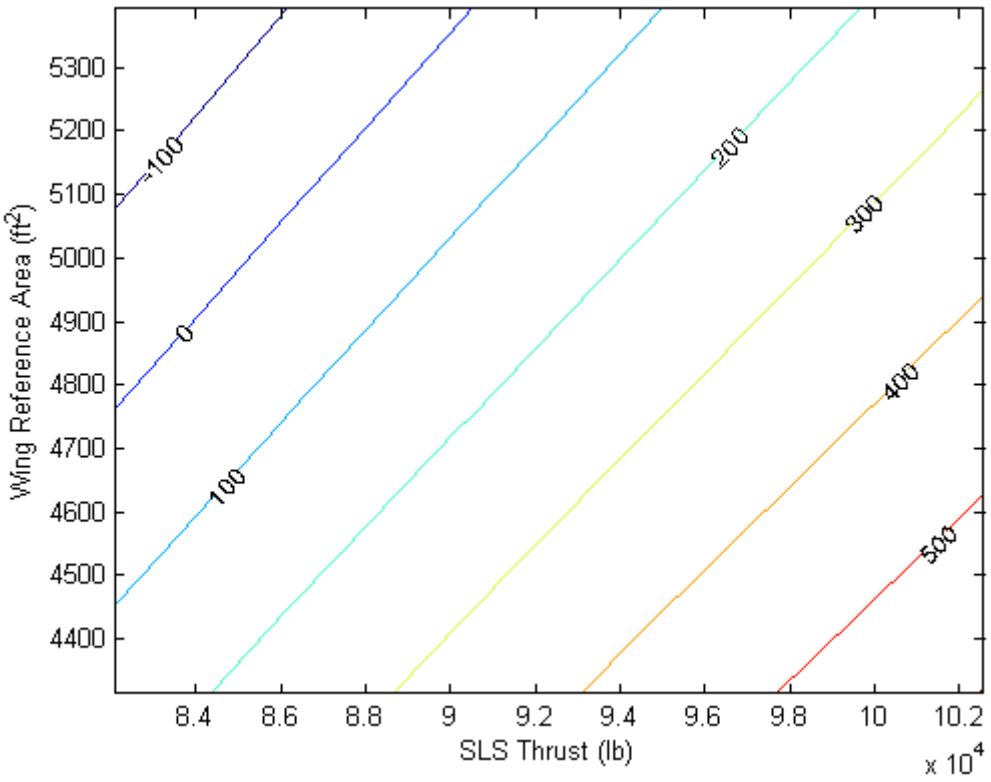

Figure 3.13: Initial cruise capability at 36,600 ft of Boeing 777-200LR.

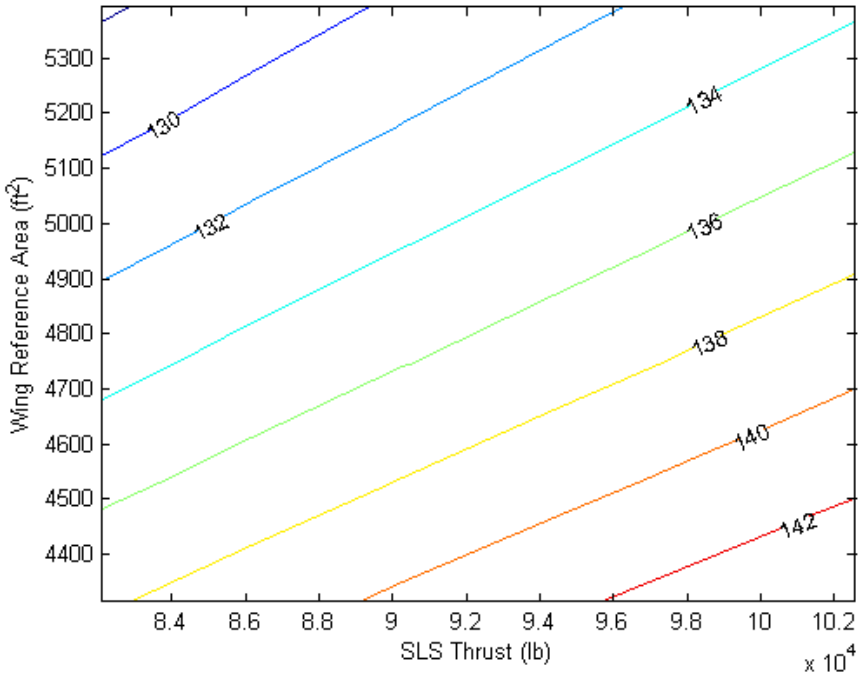

Figure 3.14: Approach speed of Boeing 777-200LR.

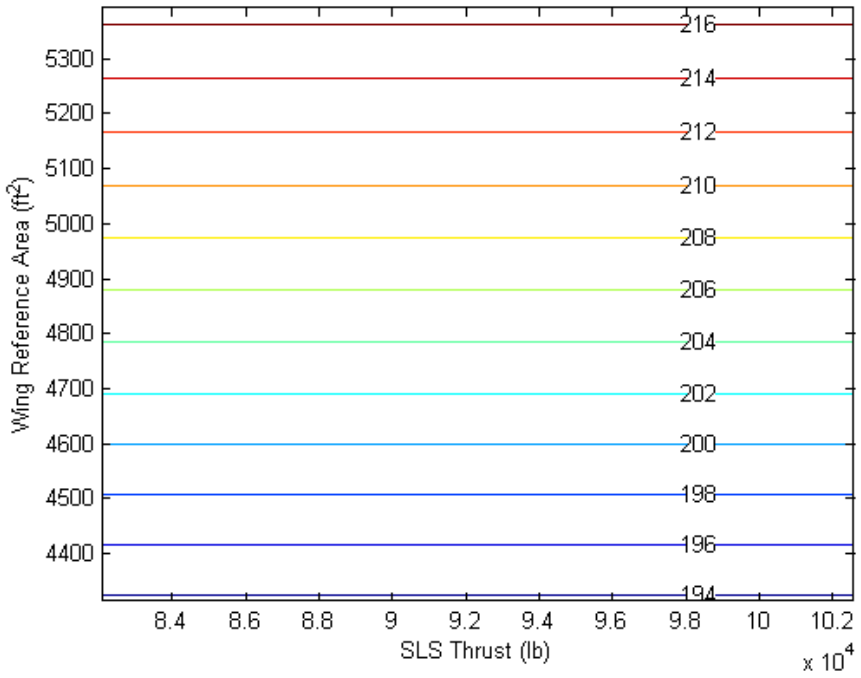

Figure 3.15: Wing span of Boeing 777-200LR.

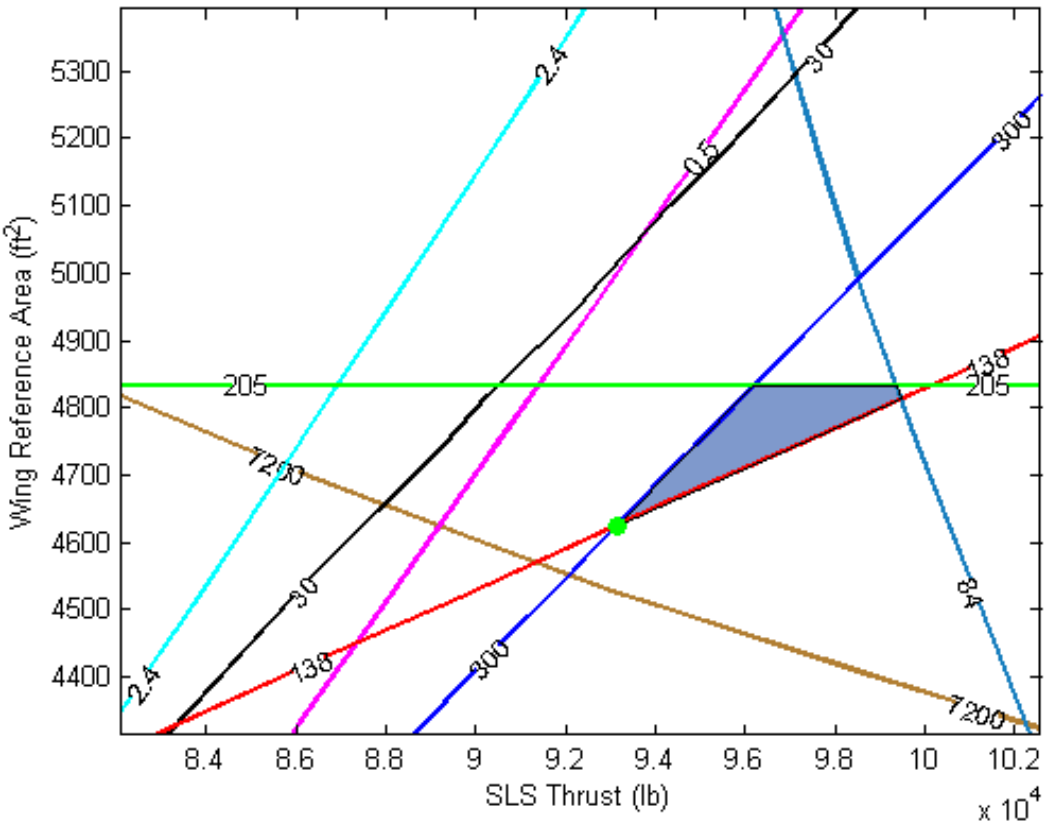

Figure 3.16: Design region and optimal design point of Boeing 777-200LR.

3.11.6 Approach Speed and Wing Span

According to the flight mission in Fig. 2.6, station 5 is the beginning of the approach for landing. In Eq. (3.18), if the approach-speed, the lift coefficient, and the weight are constant, decreasing the air density (approach at higher altitude) leads to the increasing in the wing reference area, and vice versa. In this example, we size for the aircraft approach to the Denver runway as the worst case scenario. We assume the approaching configuration of the flaps can generate a maximum lift coefficient of 2.165. The approach speed limit contour of the Boeing 777-200LR model is shown in Fig. 3.14. For the wing span limit contour, we simply evaluate Eq. (3.19). The contour is shown in Fig. 3.15.

3.11.7 Design Point Determination

Once all the requirement contours are sketched, we match them together in one contour to determine the design point. When matching the contours together, we select one appropriate isocline for each constraint. These isoclines are determined by the set of requirements that is the result of the surveys in §2.2. In this example, the requirements are determined by the information about the Boeing 777 family. They are presented below:

- Takeoff ground roll distance is less than 7,200 feet.
- Climb gradient in takeoff climb segment 1 is greater than 0.5%.
- Climb gradient in takeoff climb segment 2 is greater than 2.4%.
- Climb gradient in takeoff climb segment 3 is greater than 1.2%.
- Maximum roll angle at the end of takeoff is less than 84 degrees.
- Time to climb is less than 30 minutes.
- Initial cruise capability is 36,600 ft where the steady rate of climb is greater 300 fpm.
- Approach speed is less than 138 knots.
- Wing span is limited to 205 feet.

The combination of all constraints is shown in Fig. 3.16. The allowable possibilities are enclosed inside the shaded area on the graph. Within this area, the optimal design point is the green vertex on the graph. It is the optimal design point because it requires the least SLS thrust per engine and wing reference area to satisfy all the requirements. Figure 3.17 shows the takeoff weight contour of the model on top of the design point. This figure is the completion of the trade study; it tells us the takeoff weight, the required SLS thrust, and the necessary wing reference area of the model. Table 3.4 compares the model's basic design parameters from documents, initial estimations, and the trade study.

Table 3.4: Comparison between sizing results and documented values of the Boeing 777-200LR						
Source	$W_{pld} + W_e$	W_{tk}	$\frac{T_{SLS}}{W_{tk}}$	T_{SLS}/Eng	$\frac{W_{tk}}{S_{ref}}$	S_{ref}
Documented	403,680 lb	580,000 lb	0.29	84,100 lb	125.95 lb/ft^2	4,605 ft^2
Int. Estimation	375,966 lb	590,864 lb	0.28	82,063 lb	136.98 lb/ft^2	4,314 ft^2
Trade Study	303,231 lb	476,554 lb	0.39	93,137 lb	103.05 lb/ft^2	4,625 ft^2

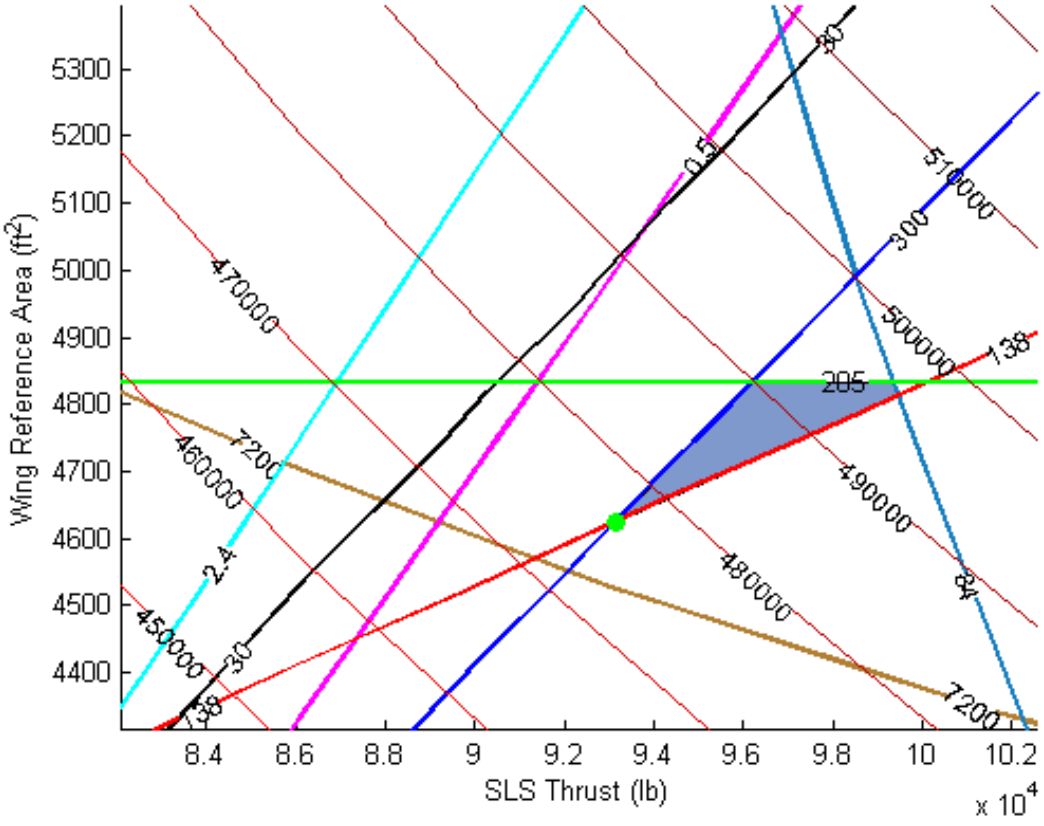

Figure 3.17: Takeoff weight contour of Boeing 777-200LR.

3.12 Summary

3.12.1 Discussion

The results from the trade study have strength and weakness. The required SLS thrust per engine and the wing reference area are higher the documented values. The required SLS thrust per engine is 110.75% of the documented SLS thrust per engine. The sizing wing reference area is 100.43% of the documented wing reference area. This means both results from our trade study are overestimated. On the other hand, the results from the initial estimations are underestimated. The confident level in estimation of SLS thrust per engine is lower than that in the estimation of the wing reference area. It is acceptable to have the basic parameters overestimated in the preliminary sizing. Nonetheless, the thrust-to-weight ratio and the wing loading are very far away from the trends. They raise a concern in our method.

The weight estimations in the trade study are much lower than the initial estimations and the documented values. Even though the takeoff weight is much underestimated, we overestimated the SLS thrust and the wing reference area. This phenomenon is the contradiction in our estimation. Observing the results closely, we see that the thrust-to-weight ratio and the wing loading are higher and lower than the main streams, respectively. The explanations for these differences are the weights of the vehicle.

The documented values in Table 3.4 were obtained from [12] which are different from the standard values of the Boeing 777-200LR model found in [11]. According to the Jane's Information Group [12], the Boeing 777-200 LR model has the operational empty weight plus the payload of equal to 403,680 lb and the takeoff weight of 580,000lb. The group uses the wing reference area of 4,605 square feet to calculate the wing loading, 125.95 pounds per square foot. And then the group uses the maximum SLS thrust of the engine is 84,100 lb to calculate the thrust-to-takeoff weight ratio, 0.29 pound thrust per pound mass.

According Boeing [11], this aircraft model has the operational empty weight plus the payload varying from 350,000 lb to 460,000 lb (see Fig. 2.10). According to Fig. 2.10, if the operational empty weight plus the payload of the aircraft was 403,680 lb and flew 5,000-n mile, its takeoff weight would be 575,000 lb. Comparing to the documented values, the Jane's Information Group [12] have estimated the weight accurately. However, we found the Boeing 777-200LR model is powered by two GE90-110B engines; each engine generates 110,000 lb thrust [11]. If we followed the Boeing document, the required SLS thrust estimation in our trade study would be underestimated. From this comparison, we have realized that it is very difficult to obtain an accurate set of weight data. As in the document from Boeing [11] declares that the weights in their document are the standard weights. These numbers can greatly vary due to different practices among airliners. Thus we accept the uncertainty in our weight functions. Hence we accept the existence of uncertainty in the results of our trade study.

Nevertheless, the numerical solutions of this preliminary sizing are not completely off scale. If we compare the trade study's takeoff weight result to the Boeing 777-200 High Gross Weight Airplanes (HGWA), we would conclude that it is very accurate. According to the range chart in Fig. 3.18 [16], a 300,000 lb OEW plus payload aircraft has the takeoff weight of 450,000 lb to cover a range of 5,000 nmi. The root cause for the great change in the empty weight and the takeoff weight in this step comes from Eq. (3.20) and Eq. (3.21). Thus the results are still acceptable because the weight equations in this method are mainly based on the statistical data. Moreover, the information from [16] and [11] shows that the available SLS thrust per engine and the wing reference area of a certain model are fixed. However, the takeoff weight and the payload fluctuate widely. As a result, the existences of uncertainties in our calculations are inevitable.

3.12.2 Conclusion

The results from the trade study demonstrate the necessity of the trade study in the preliminary sizing in aircraft design. The trade study's estimations for SLS thrust and wing reference area are higher than those from the initial estimations. They mean the

initial estimations would not satisfy all the requirements that ensure the aircraft can fly safely. However, the variances of the trade study results from the initial estimations are relatively small. The example shows that the initial estimations serve as the base lines of the trade study. Without the initial estimations, it will be very difficult to find correct location the design point.

Beside the effects from the weight functions, the aerodynamics of the wing also contributes to the uncertainty of the results. The aerodynamic coefficients in the example in this chapter are set based on the common values. All the increments in all aerodynamic coefficients in the example are guesses. The Appendix D of this thesis shows how to approximate the increments in aerodynamic coefficients of an airfoil due to high lift devices. The entire preliminary sizing which includes the work from Chapter 2 and Chapter 3 is summarized in the road map at the end of this chapter.

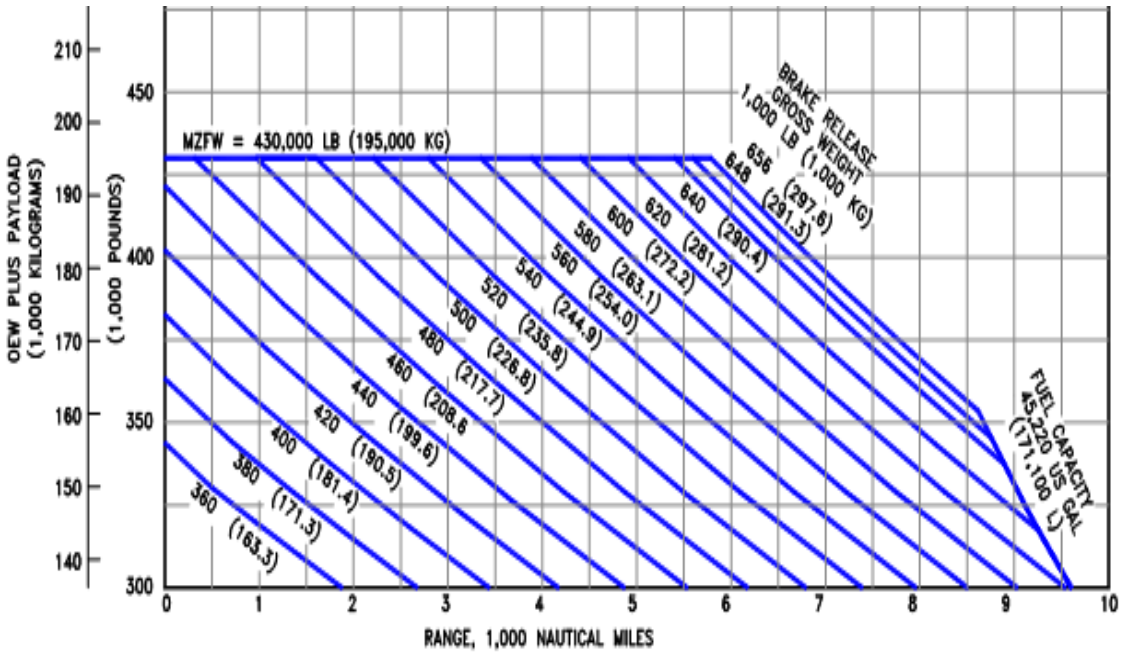

Figure 3.18: Boeing 777-200(HGWA): range – weights chart.

PRELIMINARY SIZING ROAD MAP

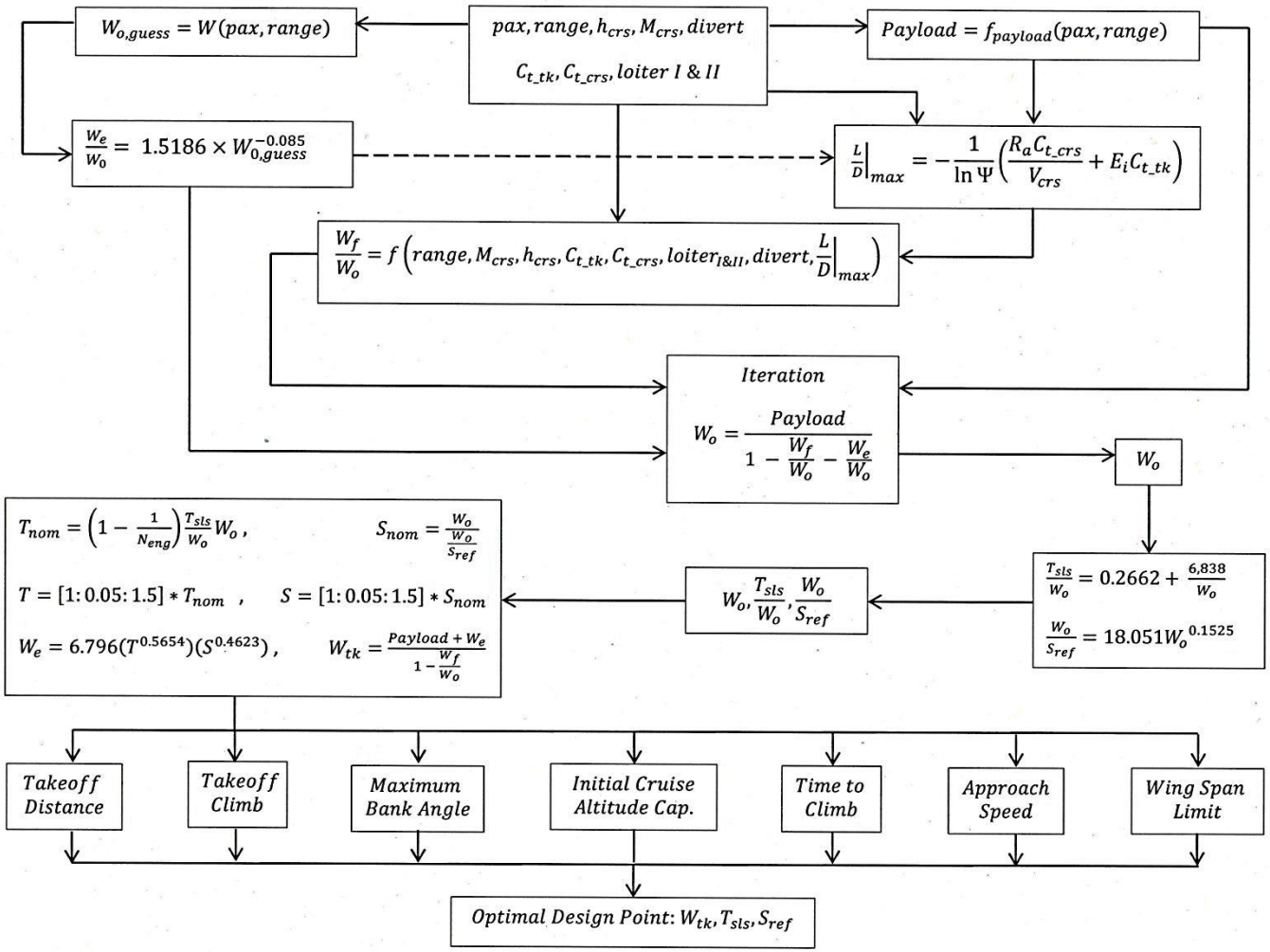

Chapter 4 Designing a Wide-Body Aircraft Model

4.1 Introduction

In the previous chapters, we have presented all the necessary tools for the preliminary sizing a new commercial aircraft concept. In a preliminary sizing for a conventional aircraft, the designers must know the performance requirements for the new concept in order to apply those statistical equations. In the lesson that we learned from the previous design in Chapter 1, we realized that beside the performance requirements, knowing the airfoil of the wing prior to the preliminary sizing is an advantage in sizing a blended-wing-body (BWB) aircraft.

Indeed, carefully selecting an airfoil before sizing this type of aircraft is a priority because the airfoil is the core in designing a BWB aircraft. Even though, we are not designing a pure BWB aircraft in this study, carefully selecting an airfoil is still the keystone of the design. In this design, we are going to wrap a wide fuselage of a conventional aircraft into an airfoil. Then, we blend this airfoil shape fuselage to the wing with hope to minimize drag of the entire aircraft. We mainly want to design a new aircraft concept with higher performance though aerodynamic efficiency enhancement. In this chapter, we will show the criteria for selecting an airfoil candidate and the preliminary sizing of the new commercial aircraft concept.

4.2 Airfoil for the Fuselage

There have been many groups around the globe studying the aerodynamic characteristics of airfoils that are specifically designed for flying wing aircraft. The UIUC applied aerodynamics group [17] has found and suggested many airfoils for this type of aircraft. The common characteristics of these airfoils are: (1) trailing edge concaves up (reflex); (2) leading edge radius is relatively small; (3) moderate lift-to-drag ratio; and (4) low parasite drag coefficient. High lift-to-drag ratio combined with less parasite drag gives

enormous advantages in improving the overall aerodynamic efficiency of the aircraft. The reflex airfoil helps improve the aircraft stability by limiting the moment coefficient.

In designing a blended wing body aircraft, choosing the airfoils is a difficult challenge. Similar to conventional aircraft, airfoils play several important roles in the aerodynamic efficiency of the aircraft. The difference is that the entire body of a blended wing body is made out of different airfoils. In each of these parts of the aircraft (1) passenger compartment, (2) intermediate wing, and (3) outer wing require a unique airfoil for both aerodynamics and space utility. All airfoils in this chapter are retrieved from the airfoil database of [18].

For the passenger compartment, we focus on space utility. We need a high thickness to chord ratio and relatively constant chordwise thickness. Since the lift from this segment is free comparing to the tube fuselage of conventional aircraft, any lift coefficient will be accepted. However, higher lift coefficient at 0-deg angle of attack (AoA) will be considered first because the chord line of the airfoil will be the entire passenger floor. We do not want the flight attendants to push the food carts uphill or downhill. Thus we will lean toward better aerodynamic performance at 0-deg AoA. Another important feature is that the moment coefficient must be small in the neighborhood around 0-deg AoA. The neutral moment of the airfoil helps in balancing the aerodynamic stability of the aircraft.

In the following figures, we show a number of airfoils whose aerodynamic characteristics are well matched to our criteria. These airfoils' aerodynamic parameters are collected from the simple 2-D potential flow simulations at Reynolds number of $6x10^6$, Mach number of 0.1, and sea level conditions. All estimations are computed by using the JavaFoil tool obtained from MH-Aerotools website whose uniform resource locator is listed in [19]. Since our decision leans toward aerodynamic performance at 0-deg AoA, it is reasonable to consider the airfoils' characteristics at 0-deg AoA first.

These airfoils have the same geometry, their thicknesses are relatively constant along the chord length; the maximum thicknesses are well above 15% chord. Figure 4.1 shows the

comparison in the maximum thickness of the selective airfoils. The maximum thicknesses of the NASA airfoils are higher than that of the MH airfoils. The lift coefficients at the 0-deg AoA of both NASA airfoils are approximately 50% higher than the lift coefficients of the MH airfoils.

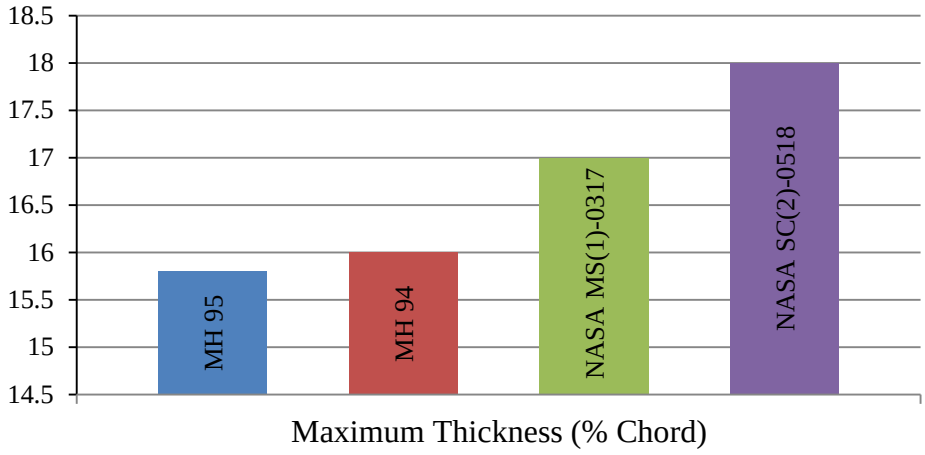

Figure 4.1: Maximum thicknesses of airfoils for the fuselage.

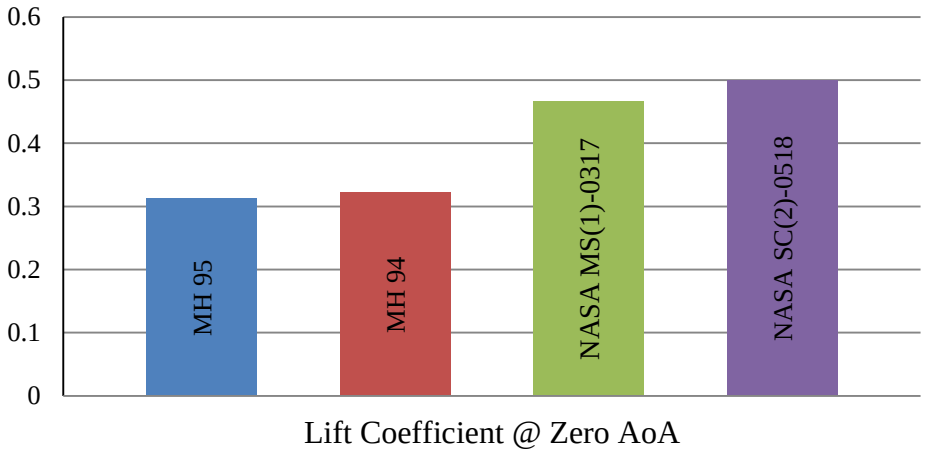

Figure 4.2: Lift coefficients at 0-deg AoA of airfoils for the fuselage.

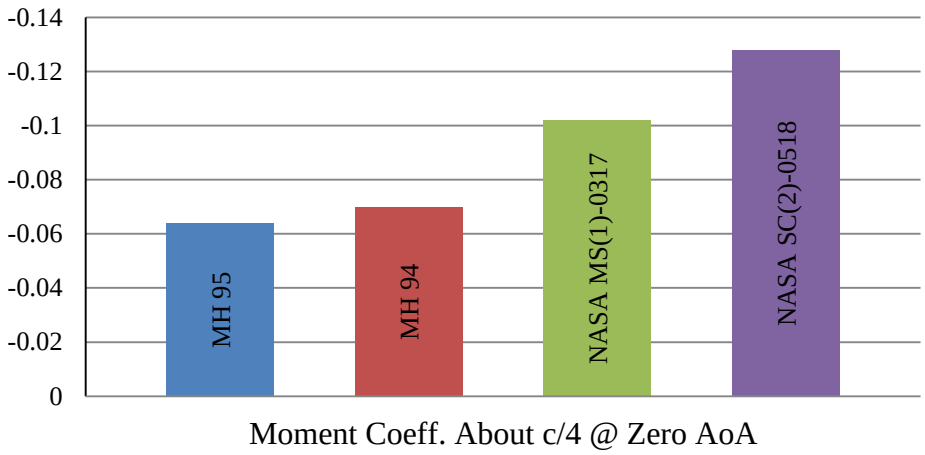

Figure 4.3: Moment coefficients at 0-deg AoA of airfoils for the fuselage.

However, the moment coefficients at 0-deg AoA of the MH airfoils are closer to zero than the moment coefficients of the NASA airfoils. Making the selection at this point based on the three characteristics is insufficient because the choice in favor of the lift coefficient over the moment coefficient will require more work in balancing the aircraft. If we sacrifice the lift and favor the small moment coefficient, we would not ensure that the aircraft meets the required aerodynamic efficiency. Thus Figs. 4.4 – 5 compare the drag coefficients and the lift-to-drag ratios of these airfoils.

The drag coefficient comparison in Fig. 4.4 shows that the NASA MS (1)-0317 and the MH 95 airfoils have the smaller drag at 0-deg AoA. Obviously, this results in better aerodynamic efficiencies of the both airfoils than the other airfoils in Fig. 4.5. They both exceed the required lift-to-drag ratio of 30. Because one of our goals is to improve the aerodynamic efficiency, we eliminate the MH 94 and the NASA SC (2)-0518 at this point. The consequence of eliminating these poor aerodynamic performance airfoils is the loss of maximum thickness by 1%. However, we gain back a 50% increase in lift-to-drag from sacrificing 1% of the maximum thickness.

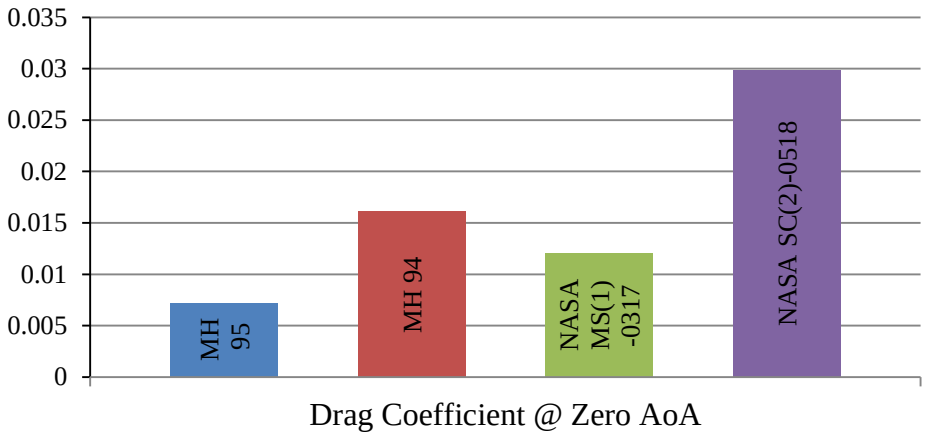

Figure 4.4: Drag coefficients at 0-deg AoA of airfoils for the fuselage.

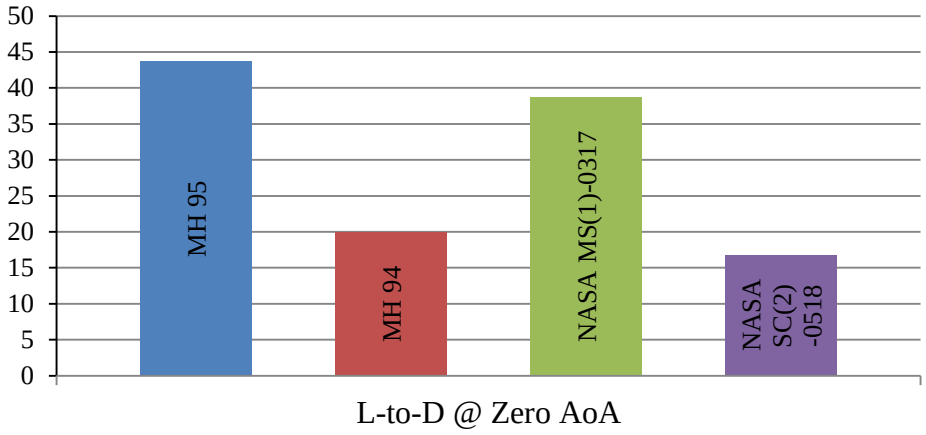

Figure 4.5: Lift-to-drag at 0-deg AoA of airfoils for the fuselage.

Choosing the MH 95 airfoil cost us 1.2% in thickness loss. The need for space is crucial in the fuselage design. If we let the main wing take care of the aerodynamic efficiency, the better choice for us in the fuselage airfoil selection will be the NASA MS (1)-0317. However, the quarter chord moment of this airfoil is almost twice as high as that of the MH 95 airfoil. We can try to balance the aircraft by arranging the configuration and by a control system. Therefore, our first consideration for the fuselage airfoil is the NASA MS (1)-0317. The aerodynamic characteristics of the NASA MS(1)-0317 airfoil are described in Figs. 4.6 – 9.

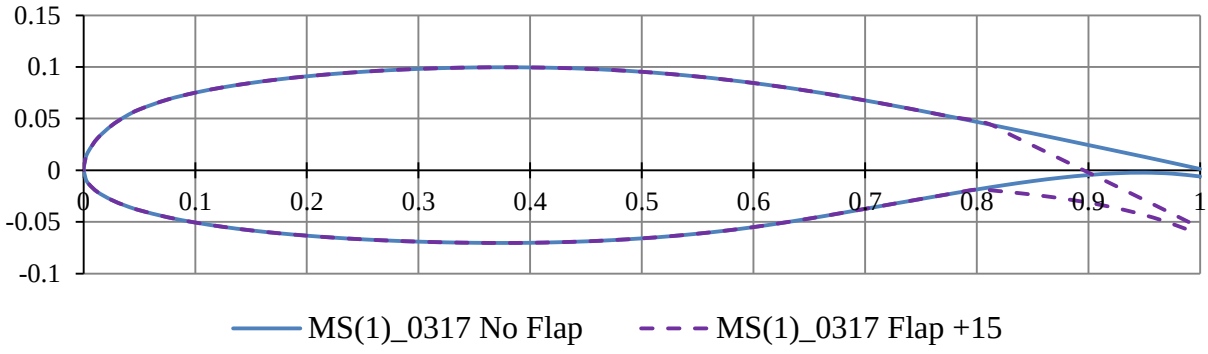

Figure 4.6: 2-D sketch of the NASA MS(1)-0317 airfoil.

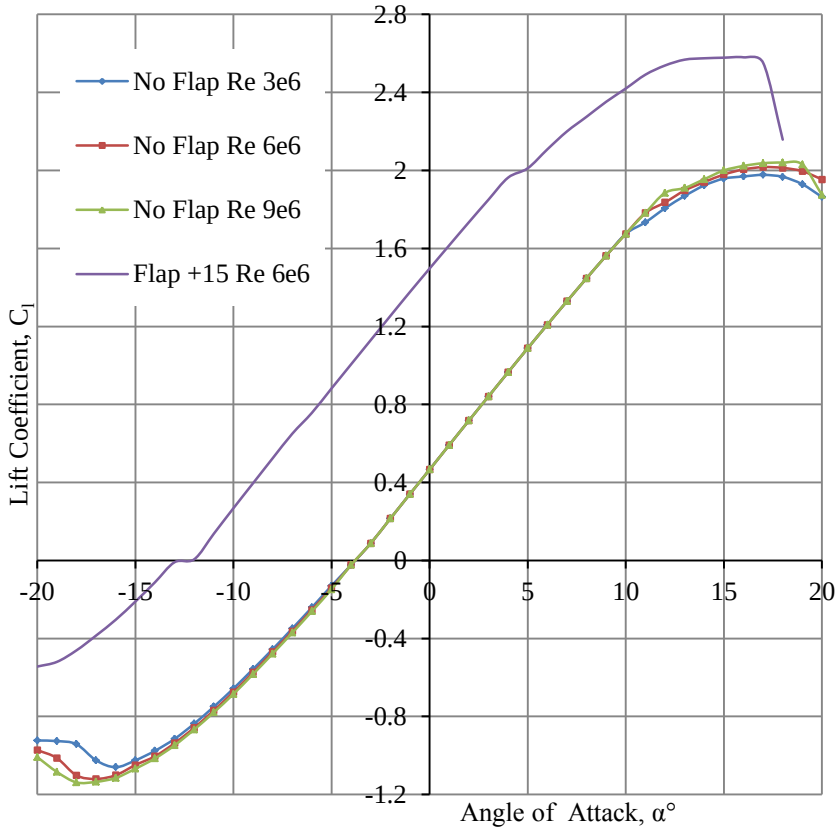

Figure 4.7: Lift curves of the NASA MS(1)-0317 airfoil.

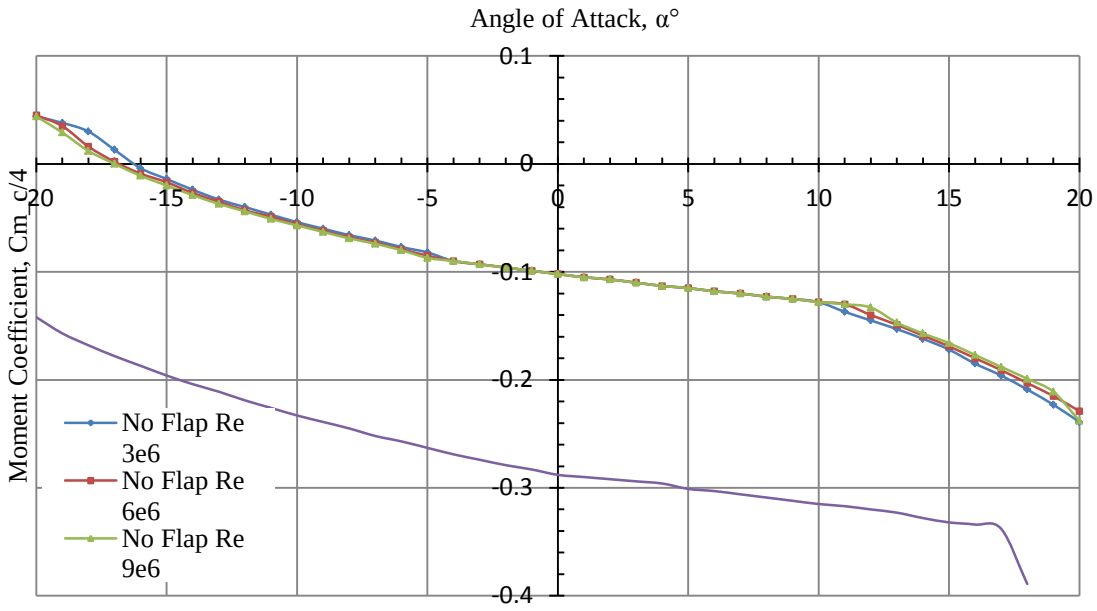

Figure 4.8: Quarter-chord moment curves of the NASA MS(1)-0317 airfoil.

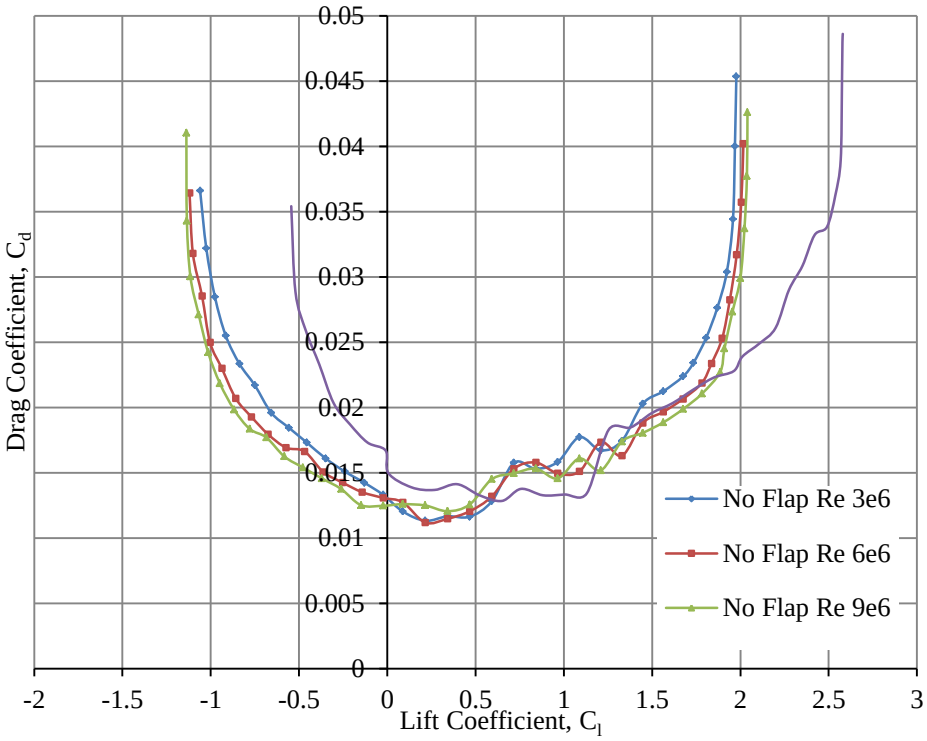

Figure 4.9: Drag polar diagram of the NASA MS(1)-0317 airfoil.

4.3 Airfoil for the Blending Section

The blending section connects the passenger compartment and the main wing. This blending section will also be the house of the engines, the landing gear, and maybe the fuel tanks. We also consider the space for the windows of the passenger compartment in the fuselage. Thus we need a moderate thickness airfoil for this section. From the aerodynamic perspective, we need a high lift coefficient at 0-deg AoA, small minimum drag coefficient, small AoA at maximum lift-to-drag ratio, and small moment coefficient.

It is important to have high aerodynamic efficiency at small AoA for two reasons. This section plays a similar role as the fairing section of a conventional aircraft. The flow over the wing is disturbed and slowed down due to skin friction at the joint between the fairing and the fuselage. Thus if the blending section has a high aerodynamic efficiency airfoil, it will automatically counteract the negative effects. The small AoA condition limits the offset angle between the engine thrust vector and the aircraft velocity. The parallelism of the velocity vector and the thrust vector saves a portion of the thrust loss during cruise. We obtained the aerodynamic data of the well-matched airfoils by deploying the JavaFoil for the same type of estimation in the fuselage section. From an investigation of seventeen airfoils, we have come up with the final four whose aerodynamic performances are most matched to the guidelines. Figures 4.10 – 16 show the comparisons and the approach in selecting the airfoil for the blending section.

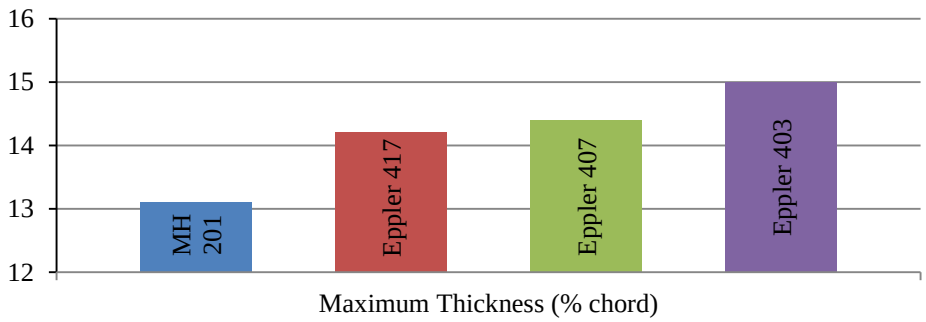

Figure 4.10: Maximum thickness of airfoils for blending.

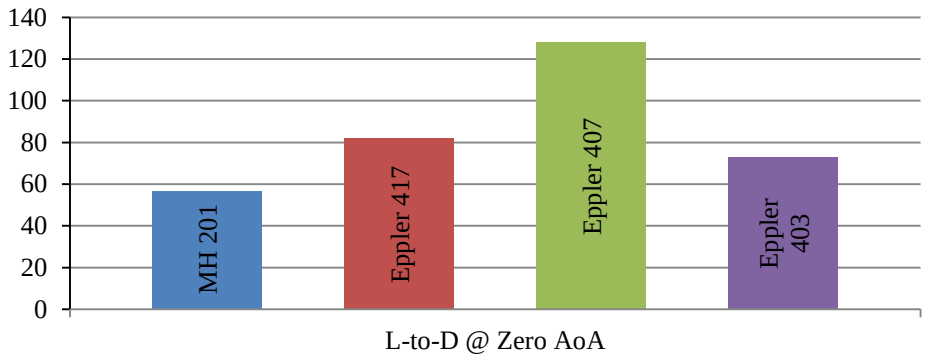

Figure 4.11: Lift-to-drag ratios at 0-deg AoA of airfoils for blending.

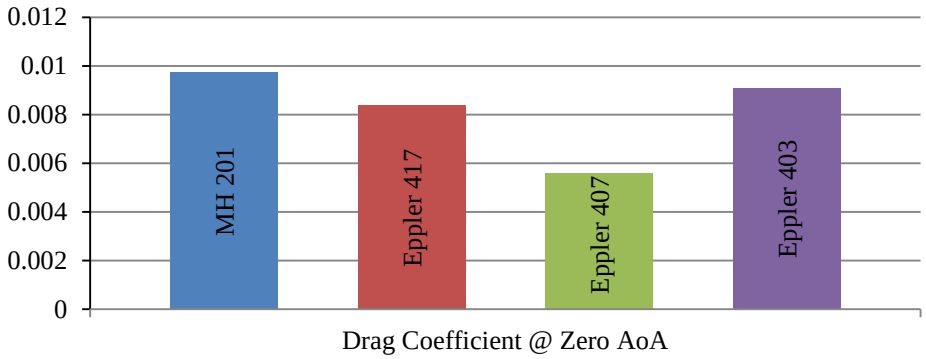

Figure 4.12: Drag coefficients at 0-deg AoA of airfoils for blending.

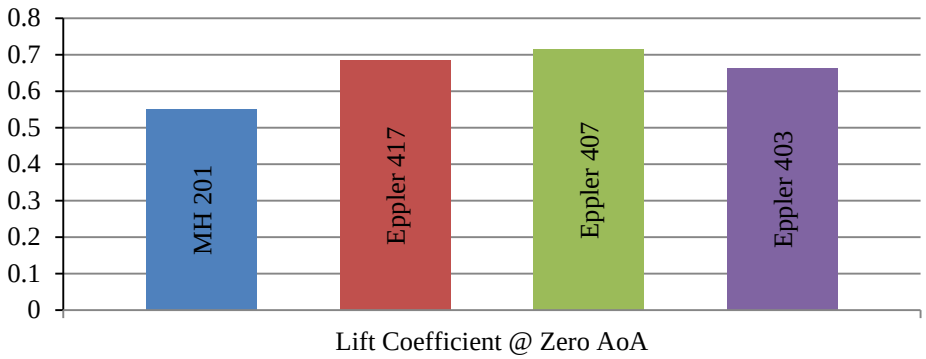

Figure 4.13: Lift coefficients at 0-deg AoA of airfoils for blending.

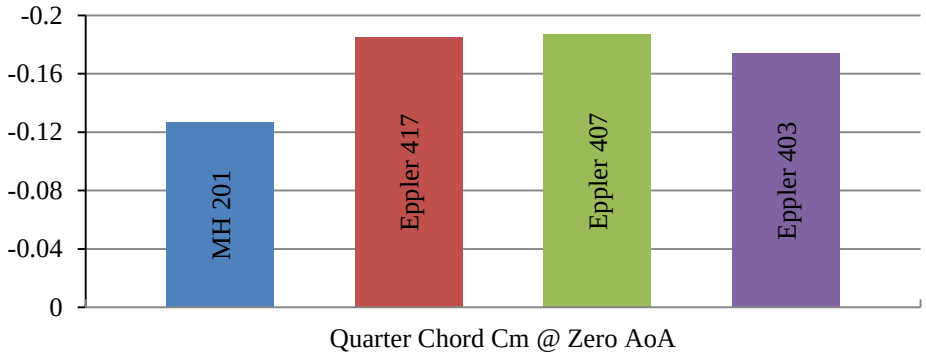

Figure 4.14: Quarter-chord moment coefficients at 0-deg AoA of airfoils for blending.

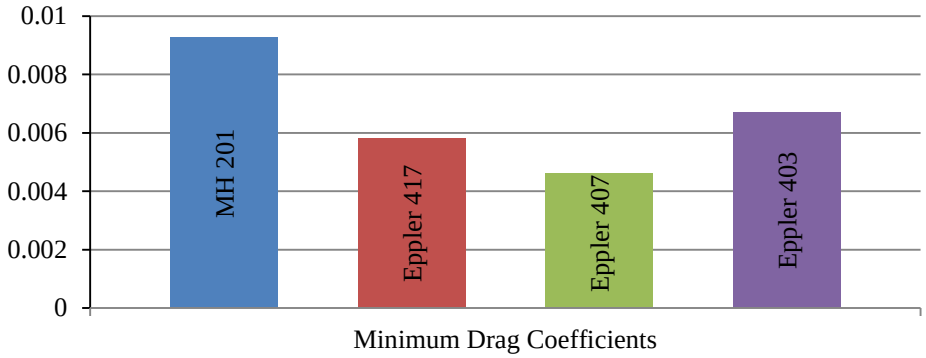

Figure 4.15: Minimum drag coefficients of airfoils for blending.

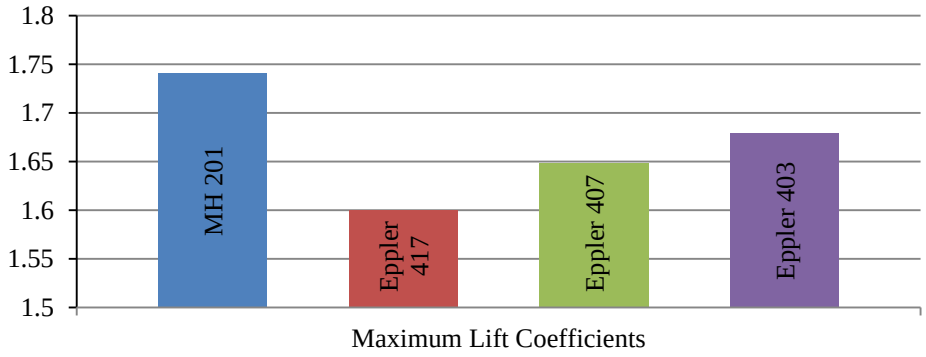

Figure 4.16: Maximum lift coefficients of airfoils for blending.

The maximum thickness comparison in Fig. 4.10 shows that all the candidates for the blending section have their maximum thickness less than that of the fuselage airfoil. From the aerodynamic efficiency perspective, the Eppler 407 and Eppler 417 are the advanced airfoils. They both have high lift coefficients and low drag coefficients at 0-deg AoA. The lift-to-drag ratio comparison in Fig. 4.11 shows that Eppler 407 is the best choice in terms of aerodynamic efficiency. Nevertheless, the high lift coefficient comes with high quarter chord moment coefficient. In conventional aircraft design, the high moment coefficient is an advantage in stabilizing the aircraft as long as the coefficient is negative. In flight control, it is not preferable due to the limited static margin of the blended wing body configuration. However, at this stage of the design process we do not known all the details of the aircraft's configuration. Thus we assume that the negative effect of a large negative moment coefficient is not important.

The comparison in the minimum-drag coefficients between the airfoils (Fig. 4.15) shows that the Eppler 407 has the smallest minimum-drag. On the other hand, the investigation of maximum-lift coefficient (Fig. 4.16) shows that the MH 201 has the highest maximum-lift coefficient. The maximum-lift coefficient of the Eppler 407 is approximately 0.1 less than that of the MH 201. However, the minimum-drag coefficient of the MH-201 is twice the minimum-drag coefficient of the Eppler 407. The MH 201 has the lowest aerodynamic efficiency at 0-deg AoA. Trading the largest negative quarter chord moment coefficient with the highest aerodynamic efficiency and the best minimum-drag coefficient, we consider the Eppler 407 as the first trial airfoil for the blending section. The aerodynamic characteristics of the Eppler 407 airfoil are illustrated in Figs. 4.17 – 20.

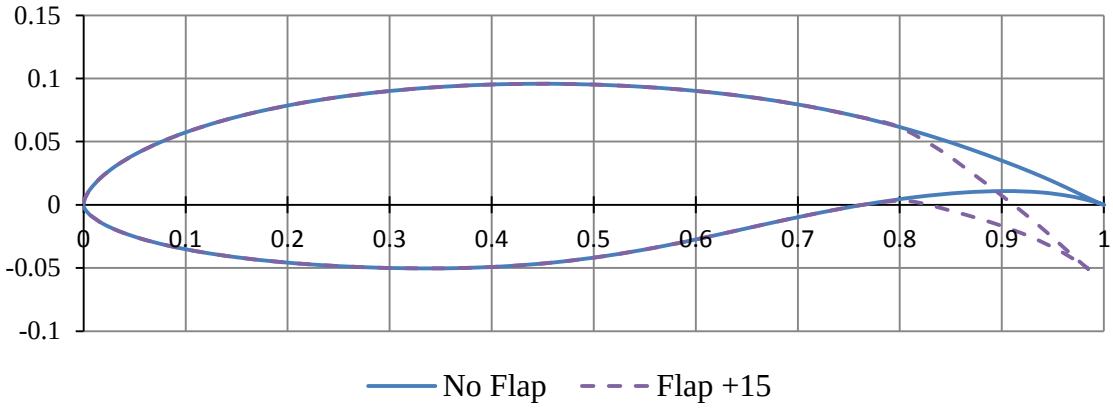

Figure 4.17: 2-D Sketch of the Eppler 407 airfoil.

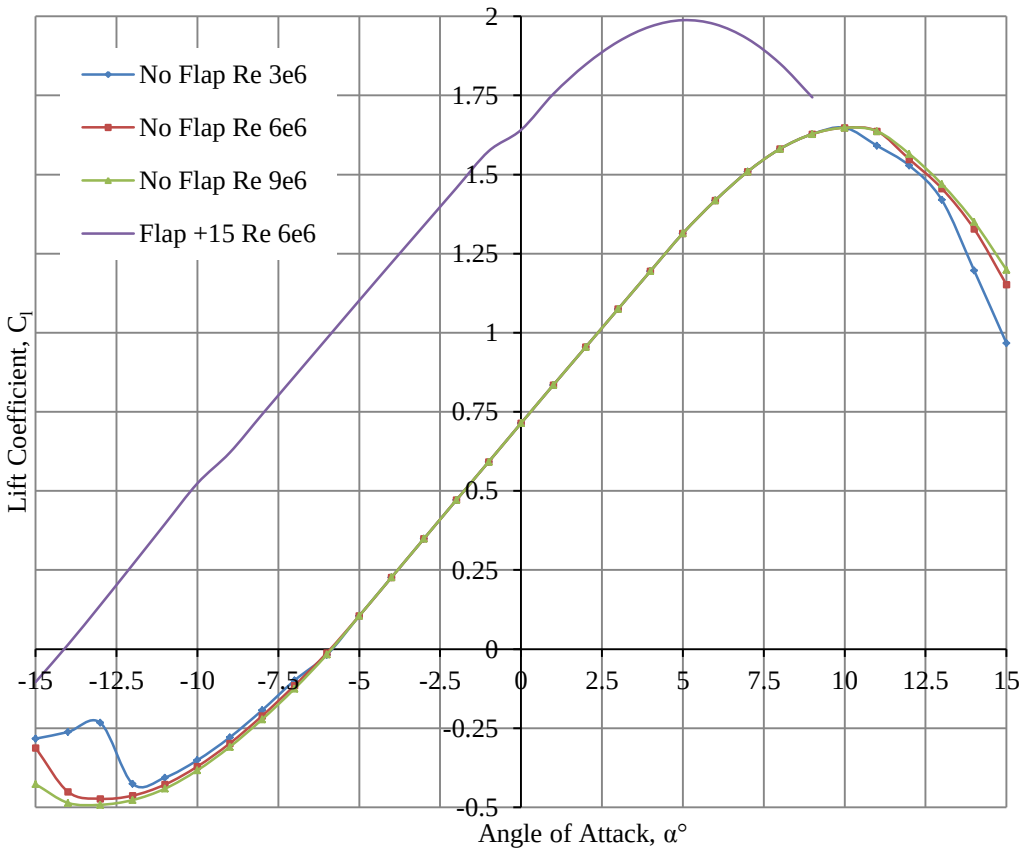

Figure 4.18: Lift curves of the Eppler 407 airfoil.

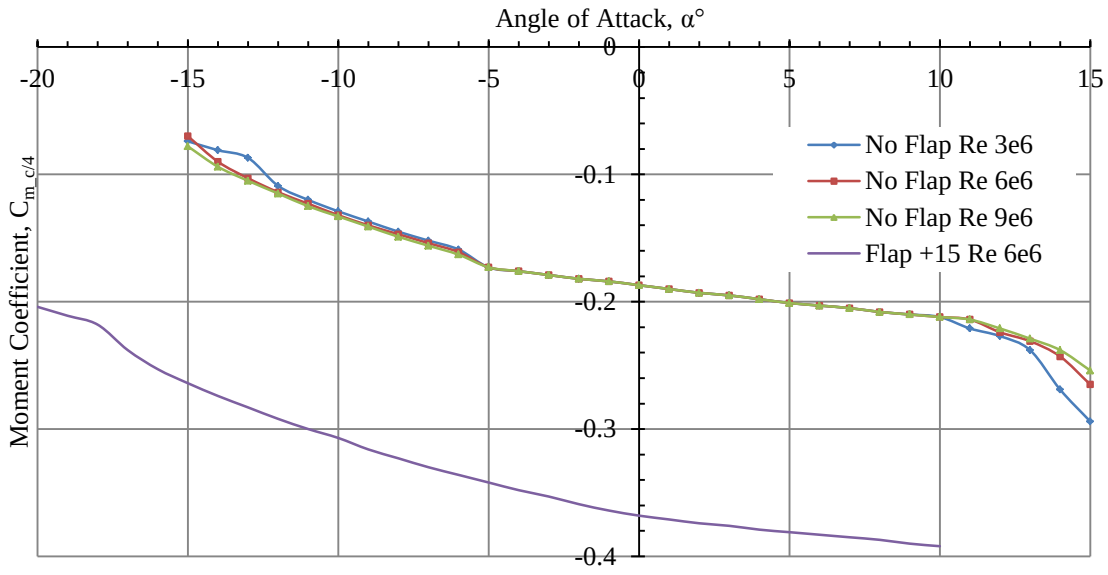

Figure 4.19: Quarter-chord moment curves of the Eppler 407 airfoil.

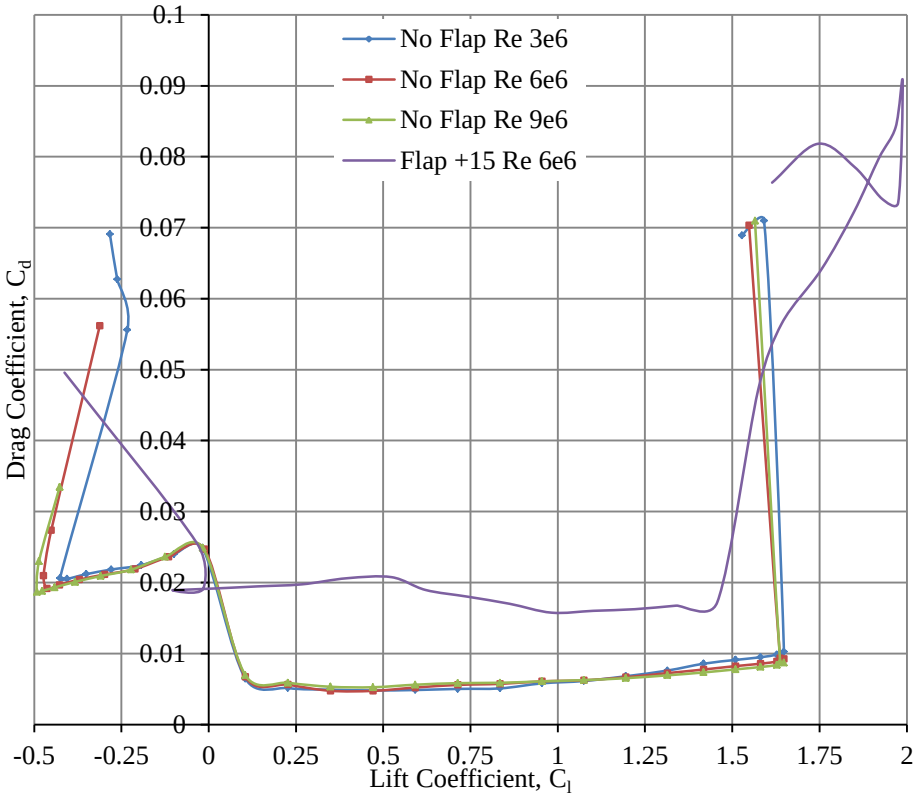

Figure 4.20: Drag polar diagram of the Eppler 407 airfoil.

4.4 Airfoil for the Wing

4.4.1 Study on Reflex Airfoils

The wing plays the main aerodynamic role of the entire aircraft. This section provides most of the lift and the aerodynamic efficiency for the aircraft. If we choose to cruise at the maximum lift-to-drag ratio, we will need an airfoil with a high maximum lift-to-drag while still maintain a moderate lift. Beside the high lift-to-drag ratio, we want the wing to be thin with a small minimum-drag coefficient. The study shows that the blending section and the wing both need reflex camber airfoils (airfoils with "S-shape" camber lines) for maintaining stability [8]. Based on these guidelines, we investigated a wide range of airfoils by utilizing the JavaFoil and applying the same conditions as used in the previous two sections. The twelve prominent candidates are shown in the following comparisons.

All airfoils in these comparisons share a common geometrical characteristic that is the "S-shape" camber line. The estimations show that the majority of these airfoils have small positive quarter chord moment coefficients at 0-deg AoA (Fig. 4.21). Except the MH-22 airfoil, the moment coefficients of all other airfoils are within the [-0.005, 0.01] range. The MH-62 airfoil has a zero moment coefficient at 0-deg AoA. Such small moment coefficient at 0-deg AoA is ideal for an aircraft with a small static margin.

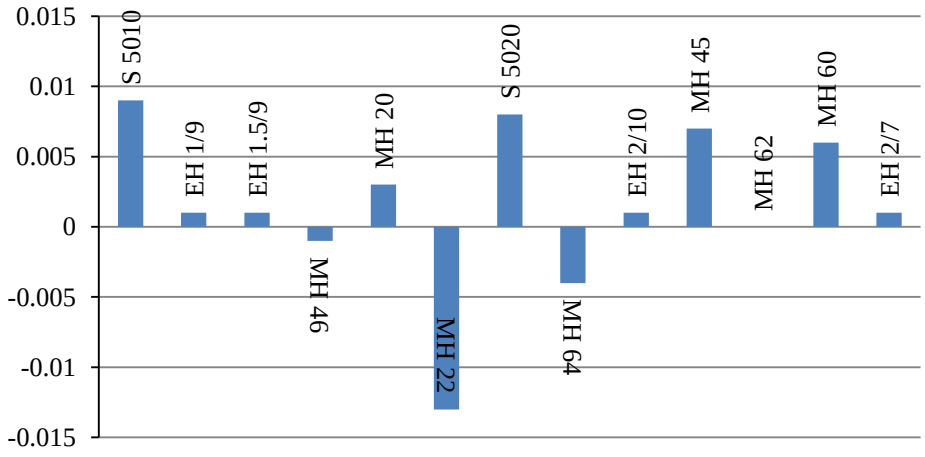

Figure 4.21: Quarter-chord moment coeffs. at 0-deg AoA of reflex airfoils.

Another advantage of these airfoils is that their minimum-drag coefficients are relatively small in comparison to other airfoils. Figure 4.22 shows the S-5010, EH 1/9, and EH 1.5/9 airfoils have highest minimum-drag coefficients, which are approximately 0.012. On the other hand, the MH-22 and MH-20 have the lowest minimum drag coefficients as small as 0.004. Obviously, the small drag coefficient leads to higher aerodynamic efficiency. Figure 4.23 compares the maximum lift-to-drag ratios of the selected airfoils. It shows that most of these airfoils have the aerodynamic efficiencies well above 30. The lowest maximum lift-to-drag ratio is about 78; and the highest one is about 187. The majority of the maximum lift-to-drag ratios are above 100. The small positive quarter-chord moment coefficient, the low minimum drag, and the high aerodynamic efficiency are all advantages that we are looking for our design. However, there are a few crucial drawbacks in these airfoils.

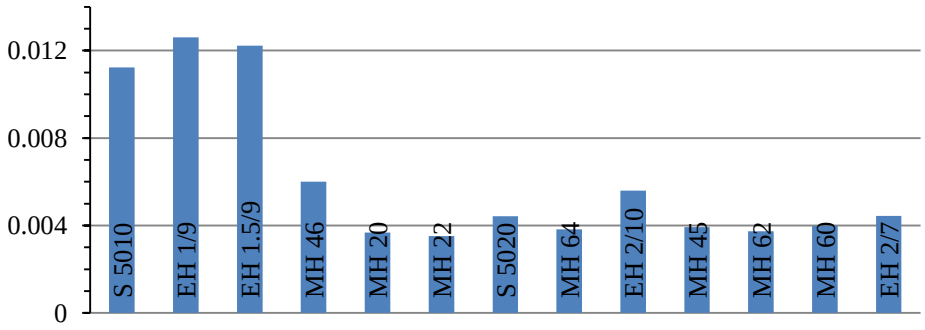

Figure 4.22: Minimum drag coefficient of reflex airfoils.

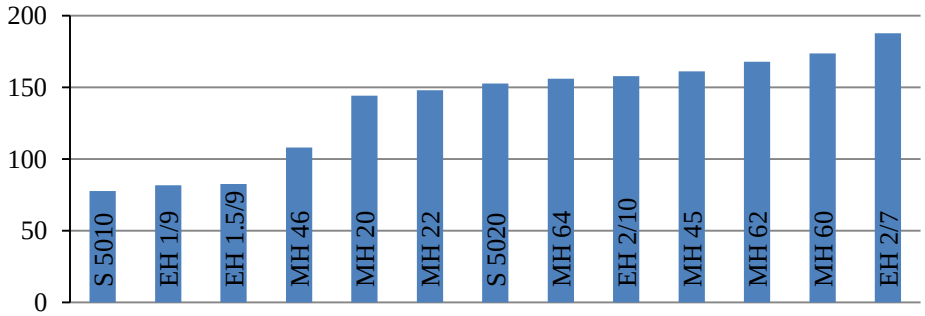

Figure 4.23: Maximum lift-to-drag ratios of reflex airfoils.

The first drawback of these "S-shape" airfoils is the low lift coefficients. Figure 4.24 shows that the maximum-lift coefficients of these airfoils are within the neighborhood of unity. The MH-22 has the lowest maximum-lift coefficient approximately 0.78. The S-5020 has a maximum-lift coefficient about 1.2 which is the highest maximum-lift coefficient in the group. The rest of the airfoils have maximum-lift coefficients in the [1 – 1.2] range. A lower lift coefficient wing requires higher thrust and larger wing reference area to lift up a fixed weight.

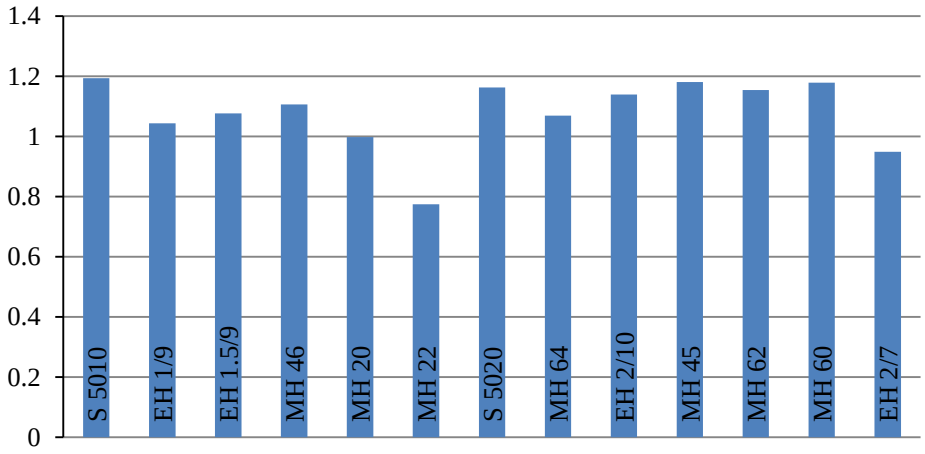

Figure 4.24: Maximum lift coefficient of reflex airfoils.

4.4.2 Choosing the Eppler 407 Airfoil for the Wing

Normally, the cruise speed is high enough so that the lift coefficient is not required to be higher than unity. Therefore, the low maximum-lift coefficient is not an issue in cruising flight. However, the low lift coefficient at the 0-deg AoA is a problem in cruising flight. It means we have to cruise at high AoA in order to achieve the desired lift coefficient. High AoA during cruise is not preferable in commercial airplanes. We could use the flap during cruise to increase the lift coefficient at 0-deg AoA. Even so, the flap deflection increases the drag and decrease the moment coefficient. We may choose to offset the main wing's AoA relative to the fuselage. This option might solve our problem that is caused by the insufficiency of lift coefficient. Nevertheless, in practice most wings are

often twisted in the nose-down fashion along the spanwise direction (washout) to avoid early stall and aeroelastic effects. In our case, we may want to twist the wing in the nose-up fashion along the spanwise direction. Twisting the wing can become a difficult problem in climbing flight due to the limited stall angle.

The small stall angle combined with the high AoA at maximum lift-to-drag ratio is another weakness of these reflex camber airfoils. The comparison between the maximum aerodynamic efficiency angle and the stall angle is illustrated in Figure 4.25. It shows that the majority of these airfoils have the two angles close to each other. It means in order to achieve the maximum aerodynamic efficiency the wing must be flown at an AoA in the neighborhood of the stall angle. This is risky in cruising flight because in doing so we shrink the safety margin and increase the chance of stall.

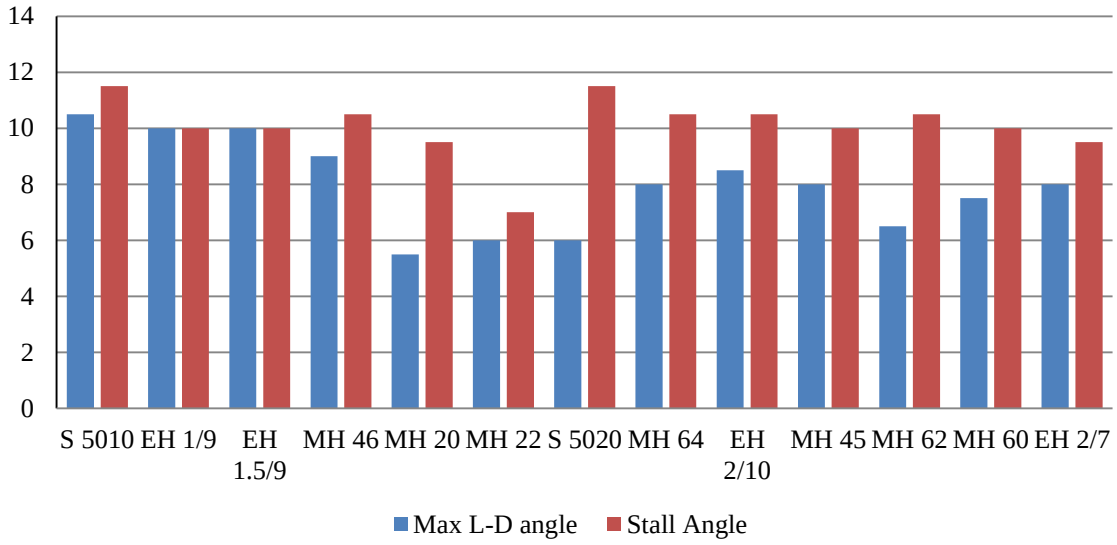

Figure 4.25: Max. lift-to-drag ratio AoA vs. stall AoA of reflex airfoils.

There are only three airfoils whose differences between the maximum lift-to-drag angle and the stall angle are greater than 3 degrees. They are MH-20, S-5020, and MH-62. Figure 4.26 shows the comparison on the stall angle and the maximum aerodynamic efficiency angle of these airfoils. Figure 4.27 compares the differences between the maximum lift coefficient and the lift coefficient at maximum lift-to-drag coefficient. The

low drag coefficient and the small positive quarter chord moment coefficient are the desirable features for our design concept in theory. However, the small lift coefficient and the limited stall angle can cause crucial issues. The disadvantages of these airfoils make them unfeasible in our design. Moreover, we should keep our estimation as simple and clean as possible at this stage of the design process. The simplest way is to use the same airfoil for the entire configuration design. However, we should accommodate the space for the passenger compartment's windows. Therefore, we seek another airfoil with smaller thickness. An alternative is to make the main wing out of the airfoil that was selected for the blending section. The selection of the Eppler 407 airfoil for the wing will simplify the configuration drawing. It also makes the aerodynamic estimation easier. Once we finished sizing and had the configuration sketch, we will be able to optimize the airfoil again.

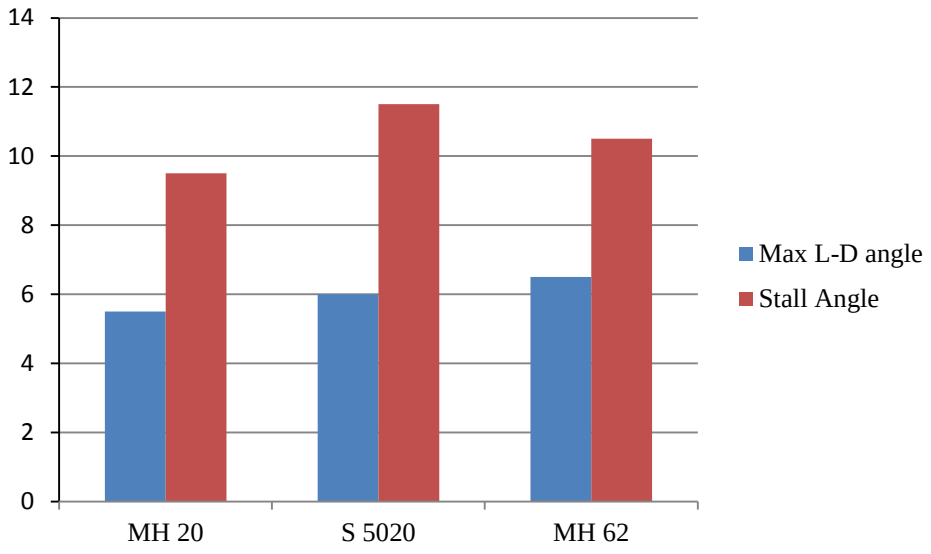

Figure 4.26: Comparison between max. lift-to-drag ratio AoA and stall AoA of the three best reflex airfoils.

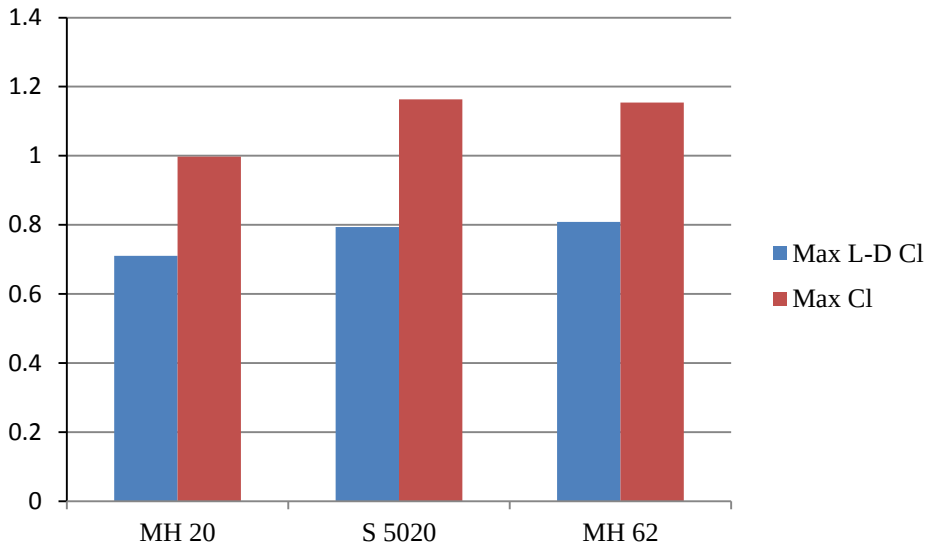

Figure 4.27: Comparison between maximum lift coeff. and max-lift-to-drag-ratio lift coeff. of the three best reflex airfoils.

4.5 Aerodynamic Characteristic of a Finite EPPLER 407 Wing

For our design, the NASA MS1-0317 will be used to build the aircraft's fuselage. Therefore, its wing section will have a very low aspect ratio. For this reason, we do not calculate its finite aerodynamic characteristic. Meanwhile, the Eppler 407 will be the main wing and the blending section. Thus the aspect ratio will be higher at these sections. Moreover, in the preliminary stage, we should simplify all calculations by assuming the main source of lift is the main wing. Let consider the platform of the wing is straight with the aspect ratio $AR = 5$, the tapper ratio $\lambda = 0.4$, and the half-chord sweep angle $\Lambda_{c/2} = 40°$. The airfoil of the wing is Eppler 407 whose maximum thickness is $\tau_{o,max} = 15\%$. The aerodynamic coefficients of the airfoil are collected from a flow at $M_\infty = 0.1$ and $Re = 6 \times 10^6$ at sea level condition. The aerodynamic coefficients of the wing in the incompressible flow at $M_\infty = 0.1$ and subsonic compressible flow at $M_\infty = 0.8$ are shown in Figs. 4.28 – 30. Appendix C of this thesis provides a detailed approach to convert the aerodynamic coefficients of an infinite wing to the aerodynamic coefficients of a finite wing. Please consult Appendix C for details of how to specifically choose the taper ratio and sweep angle corresponding to the aspect ratio of a finite wing.

For the sea level condition, incompressible flow at Mach 0.1 and Reynolds number at 6 million, the maximum lift coefficient without flap or slat is 1.521 at 19° stall angle. The minimum drag coefficient is 0.0076 at the lift coefficient of 0.1201 equivalently at the -4° AoA. The maximum lift-to-drag ratio is 30.5192 at the lift coefficient of 0.3843 and at the 0° AoA.

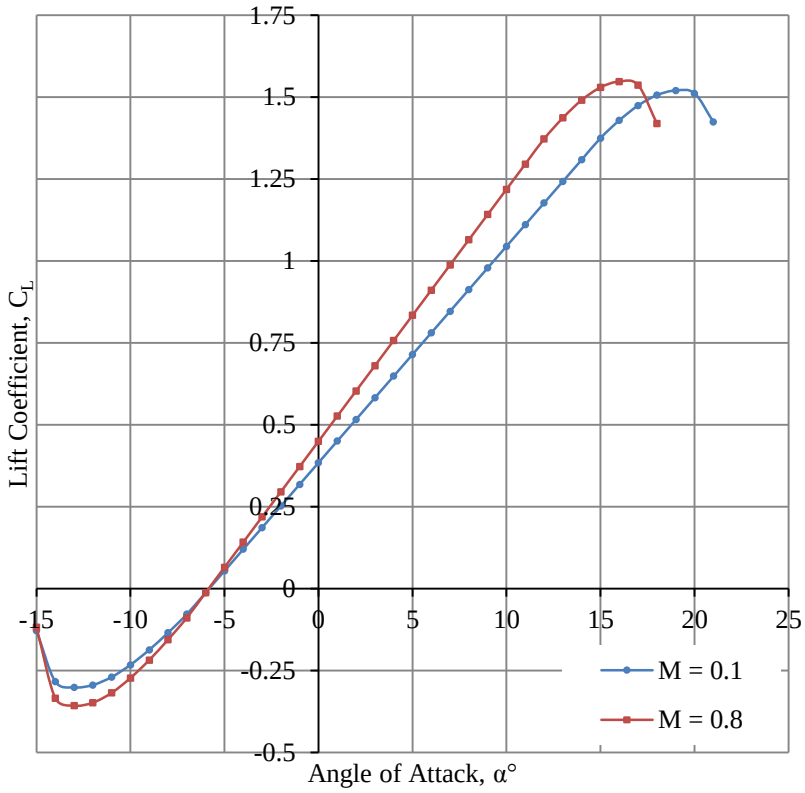

Figure 4.28: Lift curves of the Eppler 407 straight wing with

$$\boldsymbol{AR = 5, \lambda = 0.4, \Lambda_{c/2} = 40°, Re = 6 \times 10^6.}$$

Likewise, in the sea level condition, subsonic compressible flow at Mach 0.8 and Reynolds number at 6 million, the maximum lift coefficient without flap or slat is 1.548 at 16° stall angle. The minimum drag coefficient is 0.0077 at the lift coefficient of 0.142 corresponding to a -4° AoA. The maximum lift-to-drag ratio is 30.5854 at the lift coefficient of 0.3727 corresponding to -1° AoA. The span efficiency of the wing is 0.9942.

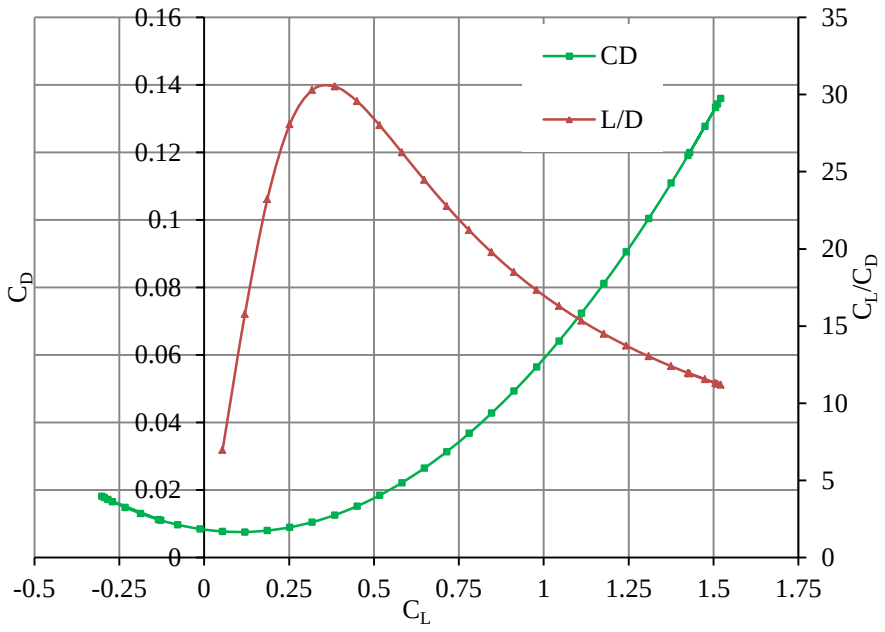

Figure 4.29: Drag polar and lift-to-drag ratio of the Eppler 407 straight wing with $AR = 5, \lambda = 0.4, \Lambda_{c/2} = 40°, Re = 6 \times 10^6, M_\infty = 0.1$.

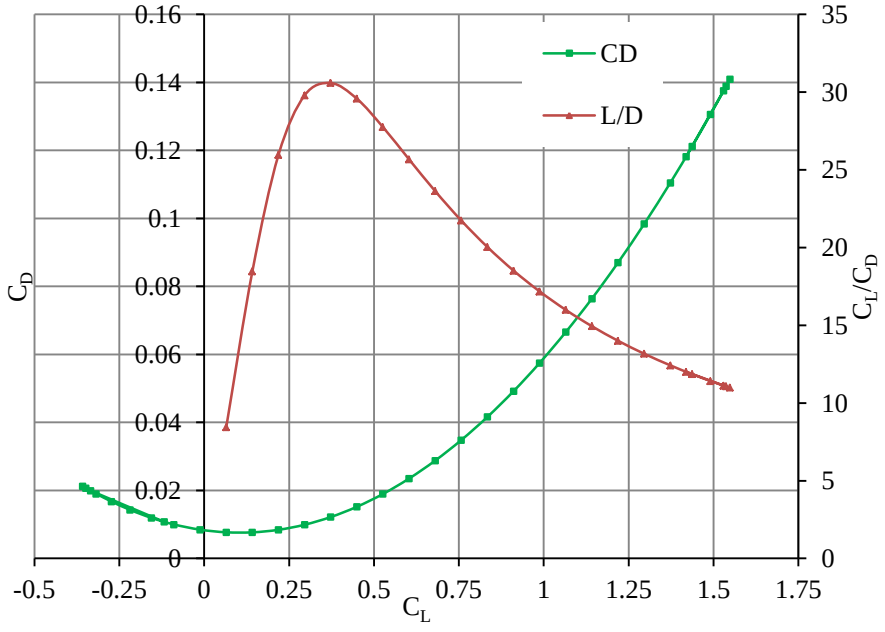

Figure 4.30: Drag polar and lift-to-drag ratio of the Eppler 407 straight wing with $AR = 5, \lambda = 0.4, \Lambda_{c/2} = 40°, Re = 6 \times 10^6, M_\infty = 0.8$.

4.6 Preliminary Sizing for a Wide-Body Aircraft with a Standard Aerodynamic Efficiency

Once the airfoils are selected, the aerodynamic limits of the wing are known. Now, we can apply the preliminary sizing that was presented in Chapter 2 and Chapter 3 to determine to the takeoff weight, the required SLS thrust, and the wing platform area of a conceptual unconventional commercial airplane. For comparison purpose, we size the new model in two trials. In the first trial, we size the aircraft with a standard efficiency that is determined by Eq. (2.12). Then in the second trial, we make our estimations based on the aerodynamic efficiency of the EPPLER 407 wing.

4.6.1 Basic Requirements for the Aircraft from Surveys

Following the federal rules and using historical data trends in §2.2, we have found a guideline to establish the design criterions as in the following summary:

- Commercial jet transport vehicle.
- Payload is 200 passengers.
- Operating range is 3,000 nmi.
- Long range cruise speed is Mach 0.85 at the initial cruise altitude of 38,000 ft.
- Time to climb from the runway to the initial cruise altitude is less than 20 minutes.
- Maximum approach speed is less than 130 knots.
- Take-off distance is less than 7,000 ft on a runway at 6,000 ft above sea-level on a standard day.

These requirements serve as the design target from the conceptual design phase through the preliminary design phase. They are the basic principles in defining performance characteristics of an aircraft. The maximum takeoff weight (MTW) is the most important parameter in designing an aircraft and plays a crucial role in shaping the wings and sizing the power plants. Due to its importance, the MTW is the first parameter which must be estimated before anything else can be calculated.

4.6.2 Flight Mission and Initial Estimations

The fuel weight fractions of the flight mission in Fig. 4.31 are prescribed in Table 2.2. Beside the basic requirements in §4.6.1, we need the loiter endurances and the divert endurance to completely describe the flight mission. In addition, we need the TSFCs for cruise and takeoff flights to make the initial estimations of the weight components. The endurances and the TSFCs are listed in Table 4.1.

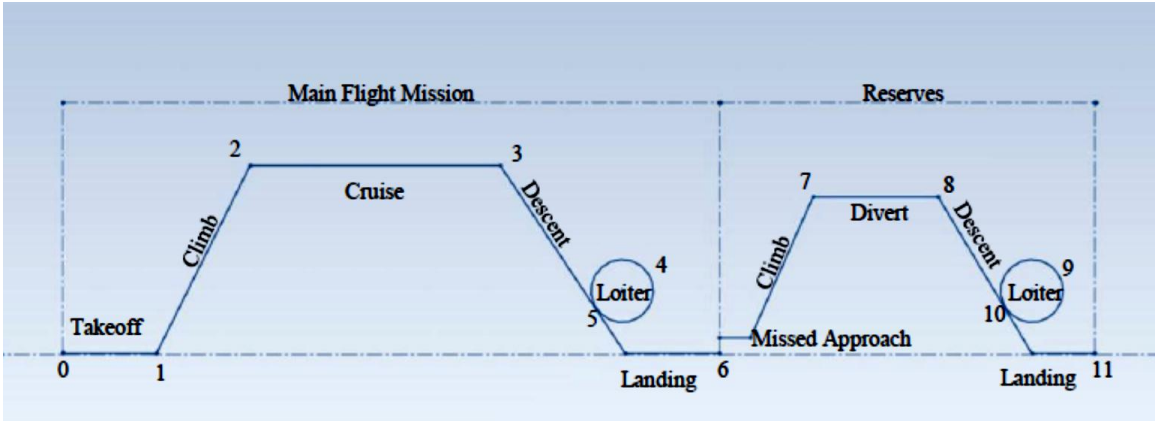

Figure 4.31: Typical flight mission of jet transport.

Table 4.1: Endurances and TSFCs in the flight mission of the wide-body model

Parameter	*Value*	*Parameter*	*Value*
First Loiter Endurance	20 mn	Takeoff TSFC	0.40 1/hr
Divert Endurance	30 mn	Cruise TSFC	0.65 1/hr
Second Loiter Endurance	10 mn	Standard Maximum L/D	18

Applying all the known quantities into Eq. (2.12), we found the required maximum lift-to-drag ratio for the model is 18 (we abbreviate to L2D18). We call this lift-to-drag ratio the standard aerodynamic efficiency in our study. Following the standard aerodynamic efficiency estimation is the iterative weight component estimations. These iterations are shown in Table 4.2.

4.6.3 Optimal Design Point Determination

Once the takeoff weight of the vehicle is known, we are ready to carry out the trade study to determine the required SLS thrust and the wing reference area. Before showing the result, we briefly introduce the design parameters that were used in the trade study. The first set of these parameters are the aerodynamic coefficients of the wing. The airfoil of the wing is the EPPLER 407 airfoil whose finite properties are computed in §4.5. The wing's aerodynamic characteristics that are altered by Fowler flaps and Handley Page slats are shown in Table D.10. Table 4.3 lists the specific aerodynamic coefficients that were used in the trade study. Note that the Oswald factor and the Span Efficiency factor are different. The Oswald factor is more accurate than the Span Efficiency factor in aircraft design (see Appendix C for detailed explanation).

Table 4.2: Takeoff weight iteration of the wide-body L2D18 model (in lb)

$W_{tk,guessed}$	W_{pld}	W_{empty}	W_{fuel}	$W_{tk,computed}$
262,292	57,470	162,114	89,101	308,686
308,686	57,470	153,907	85,771	297,148
297,148	57,470	155,761	86,524	299,755
299,755	57,470	155,333	86,350	299,153
299,153	57,470	155,431	86,390	299,291
299,291	57,470	155,409	86,380	299,259
299,259	57,470	155,414	86,383	299,266
299,266	57,470	155,413	86,382	299,265
299,265	57,470	155,413	86,382	299,265

The second set of parameters includes the speeds, the altitudes, and the weight fractions at critical stations throughout the main flight mission. Table 4.4 lists the parameters for takeoff ground roll, level turning at the end of takeoff climb, initial cruise, and landing. Table 4.5 sets the parameters for takeoff climb gradient estimations. We assume the vehicle's weight throughout the takeoff climb is fairly constant. Thus we set its weight to W_1 for the entire takeoff climb.

Table 4.3: Aerodynamic characteristic of the EPPLER 407 wing			
Parameter	*Value*	*Parameter*	*Value*
Aspect Ratio	5	Taper Ratio	0.4
Half-Chord Sweep	40°	Maximum Thickness	0.15c
Span Efficiency, ϕ	0.9942	Oswald Factor, e	0.9
Mach 0.1 $C_{L,max}$	1.52	Mach 0.8 $C_{L,max}$	1.55
Mach 0.1 $C_{D,min}$	0.0076	Mach 0.8 $C_{D,min}$	0.0077
Mach 0.1 L/D	30.52	Mach 0.8 L/D	30.59
Takeoff $C_{L,max}$	1.75	Approach $C_{L,max}$	2.5
Takeoff Climb 1 $\Delta C_{L,max}$	0.75	Takeoff Climb 1 $\Delta C_{D,min}$	0.06
Takeoff Climb 2 $\Delta C_{L,max}$	0.75	Takeoff Climb 2 $\Delta C_{D,min}$	0.05
Takeoff Climb 3 $\Delta C_{L,max}$	0	Takeoff Climb 3 $\Delta C_{D,min}$	0

Table 4.4: Altitude, weight, and speed at critical stations of the main flight mission				
Parameter	*Takeoff*	*Turning*	*Initial Cruise*	*Landing*
Altitude (ft)	6,000	7,500	38,000	6,000
Weight (lb)	$\frac{1}{2}(W_0 + W_1)$	W_1	W_2	W_5
Speed	$0.707V_{LO}$	$1.25V_s$	Mach 0.85	V_{app}

Table 4.5: Altitude, speed, and Oswald factor during takeoff climb			
Parameter	*Segment I*	*Segment II*	*Segment III*
Altitude (ft)	6,035	6,400	7,500
Speed	$1.1V_s$	$1.2V_s$	$1.25V_s$
Oswald Factor	$0.95e$	$0.95e$	e
Climb Gradient (%)	≥ 0.5	≥ 2.4	≥ 1.2

Table 4.6 prescribes the altitude, the weight, and the speed of the vehicle at critical stations in the climb from end of takeoff climb to the initial cruise altitude. Note that we size for the climb from sea-level to the initial cruise altitude as the worst case scenario, rather than from the takeoff runway to the initial cruise altitude.

Table 4.6: Altitude, weight, and speed at critical stations in climb

Parameter	*Station I*	*Station II*	*Station III*	*Station IV*
Altitude (ft)	1,500	10,000	10,000	38,000
Weight (lb)	W_1	$0.965W_{tk}$	$0.955W_{tk}$	W_2
Speed	$1.25V_s$	250 knot	400 knot	Mach 0.85

Remember that the air density must be set corresponding to the altitude of the vehicle during the entire flight mission. As the stall speed of the vehicle is defined by Eq. (3.2), we must calculate it corresponding to the weight of the vehicle in each phase of the flight mission. The results are shown graphically in Fig. 4.32 and numerically in Table 4.7, respectively.

Table 4.7: Summary of preliminary sizing results of the wide-body L2D18 model

Initial Estimation		*Trade Study's Results*	
Parameter	*Value*	*Parameter*	*Value*
Thrust Ratio	0.289	Thrust Ratio	0.382
Wing Loading (lb/ft^2)	123.481	Wing Loading (lb/ft^2)	89.782
Payload (lb)	57,470	Payload (lb)	57,470
Empty Weight (lb)	155,413	Empty Weight (lb)	111,452
Fuel Weight (lb)	86,382	Fuel Weight (lb)	68,544
Takeoff Weight (lb)	299,265	Takeoff Weight (lb)	237,466
SLS Thrust (1xEng) (lb)	43,251	SLS Thrust (1xEng) (lb)	45,318
Wing Reference Area (ft^2)	2,424	Wing Reference Area (ft^2)	2,645

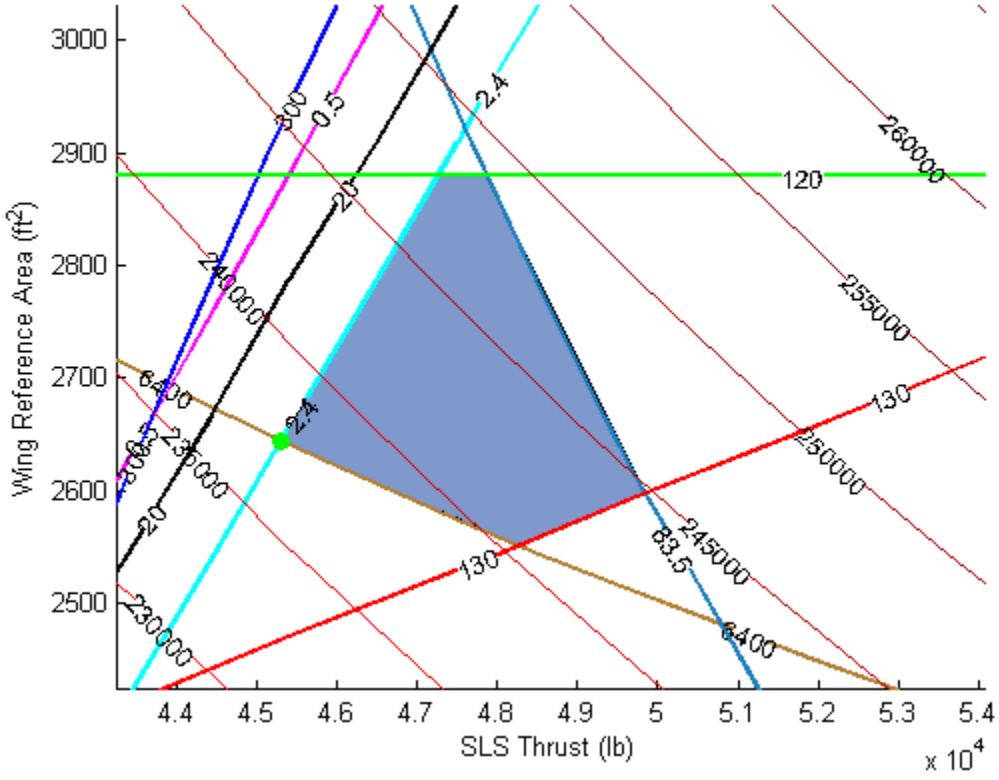

Figure 4.32: Design region & design point of the wide-body L2D18 model.

4.7 Preliminary Sizing for a Wide-Body Aircraft with an Advanced Aerodynamic Efficiency

Previously, we sized the model based on a standard aerodynamic efficiency, which is the required maximum lift-to-drag ratio for the aircraft to accomplish the flight mission with a given amount of fuel. We determined the required maximum lift-to-drag ratio for the model is 18. On the other hand, our wing model has a much higher aerodynamic efficiency than the requirement. If we deduct 20% efficiency of the wing to account for the combination of the wing and the fuselage, the aircraft would have a lift-to-drag ratio of 24 (L2D24). Keeping all the parameters the same as before and changing only the aerodynamic efficiency, we obtained different sizes for the model. Table 4.8 shows the

iteration of the initial estimation. Table 4.9 summarizes the results from the trade study. The new design point is sketched in Fig. 4.33.

Table 4.8: Takeoff weight iteration of the wide-body L2D24 model (in lb)

$W_{tk,guessed}$	W_{pld}	W_{empty}	W_{fuel}	$W_{tk,computed}$
262,292	57,470	129,916	59,990	247,376
247,376	57,470	132,056	60,675	250,201
250,201	57,470	131,636	60,541	249,647
249,647	57,470	131,718	60,567	249,755
249,755	57,470	131,702	60,562	249,734
249,734	57,470	131,705	60,563	249,738
249,738	57,470	131,705	60,563	249,737

Table 4.9: Summary of preliminary sizing results of the wide-body L2D24 model

Initial Estimations		*Trade Study's Results*	
Parameter	*Value*	*Parameter*	*Value*
Thrust Ratio	0.294	Thrust Ratio	0.382
Wing Loading (lb/ft^2)	120.121	Wing Loading (lb/ft^2)	86.858
Payload (lb)	57,470	Payload (lb)	57,470
Empty Weight (lb)	131,705	Empty Weight (lb)	96,374
Fuel Weight (lb)	60,563	Fuel Weight (lb)	49,252
Takeoff Weight (lb)	249,738	Takeoff Weight (lb)	203,096
SLS Thrust (1xEng) (lb)	36,659	SLS Thrust (1xEng) (lb)	38,759
Wing Reference Area (ft^2)	2,079	Wing Reference Area (ft^2)	2,338

4.8 Summary

Through the aerodynamic analyses of the airfoils, we found the reflex airfoils have some crucial disadvantages. These disadvantages make the airfoils unfeasible for the design.

Instead, we select the Eppler 407 airfoil for the blending section and the wing of the aircraft. On the other hand, we will use the NASA MS(1)-0317 airfoil for the fuselage section. Since the fuselage is not the main source of lift and its aspect ratio is very small, we do not specifically estimate its aerodynamic characteristics at this stage. The main wing is very important at this stage. Thus, we have specifically estimated its aerodynamics based on the particular assumptions about the wing platform as untwisted, aspect ratio at 5, taper ratio at 0.4, and half-chord sweep 40 degrees.

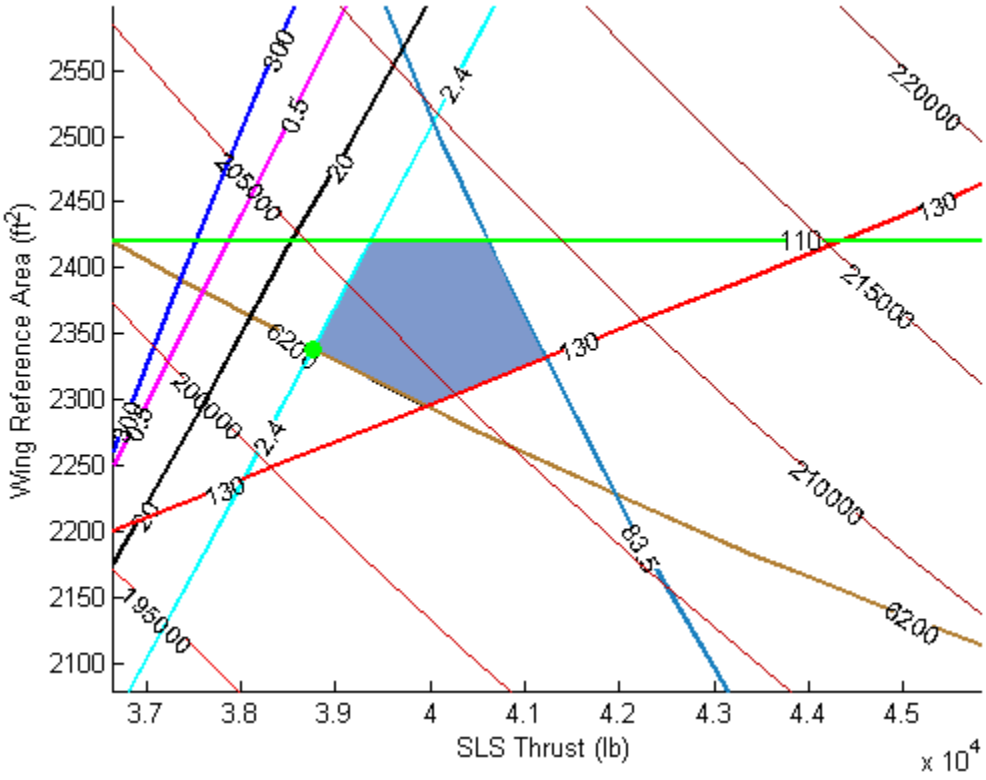

Figure 4.33: Design region & design point of the wide-body L2D24 model.

The trade study's results show that improving the aerodynamic efficiency of the wing leads to a tremendous operational efficiency of an aircraft in terms of fuel weight and structure weight. The results in Table 4.10 show that for the same payload and range, both models operate at the same conditions, the Wide-Body L2D24 requires only 72% fuel weight of the Wide-Body L2D18. The Wide-Body L2D24 model needs only 88.4%

the wing reference area and 85.5% SLS thrust of the Wide-Body L2D18 model. The smaller thrust saves fuel and structural weight for the fuel tank. The smaller wing platform area reduces the empty weight. Both of these two factors lead to the smaller takeoff weight of aircraft. In addition, the Wide-Body L2D24 can lift off after rolling 6,200 ft on the runway, which is 200 ft shorter than the rolling distance for the Wide-Body L2D18.

Table 4.10: Comparing trade study results of wide-body L2D18 to wide-body L2D24

Parameter	*L2D18 Model*	*L2D24 Model*
Thrust Ratio	0.382	0.382
Wing Loading (lb/ft^2)	89.782	86.858
Payload (lb)	57,470	57,470
Empty Weight (lb)	111,452	96,374
Fuel Weight (lb)	68,544	49,252
Takeoff Weight (lb)	237,466	203,096
SLS Thrust (1xEng) (lb)	45,318	38,759
Wing Reference Area (ft^2)	2,645	2,338

However, the design space (the shaded area in Figs. 4.32 – 33) of the Wide-Body L2D24 is much smaller than that of the Wide-Body L2D18. Even when we removed the span limit constraint on the L2D24 model, its design space is still smaller than the design space of the L2D18 model. The design space represents the future development possibility of the model. Nevertheless, it does not mean having a higher aerodynamic efficiency reduces the design possibility of the model. The design space of the L2D24 model is smaller than the design space of the L2D18 because the constraints of the L2D24 model are much more difficult to achieve than those for the L2D18 model. If we set the ground roll distance constraint for the L2D24 model to 6,400 ft and the span limit to 120 ft like those for the L2D18 model, the L2D24 model's design space would be a lot bigger than the design space of the L2D18 model. For the comparison purpose, the stretched design space of the L2D24 model is shown in Fig. 4.35.

From the Breguet range equation in Eq. (2.8), we realize there are two options to reduce the fuel weight for traveling at the same speed in the same range. They are the TSFC and the aerodynamic efficiency. Reducing the TSFC is a time consuming route. A study that can be found in [20] shows the history of the engine fuel consumption improvement over the last five decades. The TSFC of all engines in the study were calculated at the same operating condition: uninstalled Mach 0.8 at 35,000 ft. The evolution started from the turbojets in 1955 with TSFCs of 0.9 $lb_m/(hr*lb_f)$ to 0.8 $lb_m/(hr*lb_f)$ in 1960. From 1960 to 1970, the low bypass turbofan's TSFC dropped from 0.8 $lb_m/(hr*lb_f)$ to 0.65 $lb_m/(hr*lb_f)$. From 1970 to 1995, the first generation high bypass turbofan's TSFC got improved from 0.7 $lb_m/(hr*lb_f)$ to 0.55 $lb_m/(hr*lb_f)$. From 1995 to 2003, the second generation high bypass turbofan's TSFCs were reduced from 0.55 $lb_m/(hr*lb_f)$ to 0.52 $lb_m/(hr*lb_f)$. Figure 4.34 depicts the evolution in TSFC of jet engines. The fuel consumption reduction rate is slowing down. The history data indicates the engine's TSFC trend is approaching the asymptote. Thus reducing the engine's TSFC is not our main focus in this study.

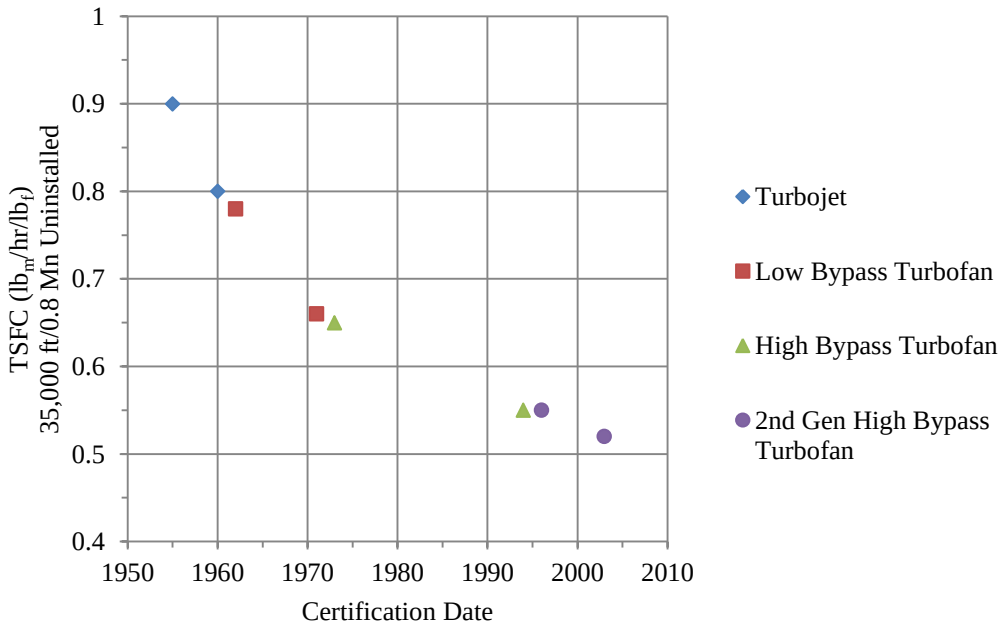

Figure 4.34: Evolution in TSFC of jet engines (source [20]).

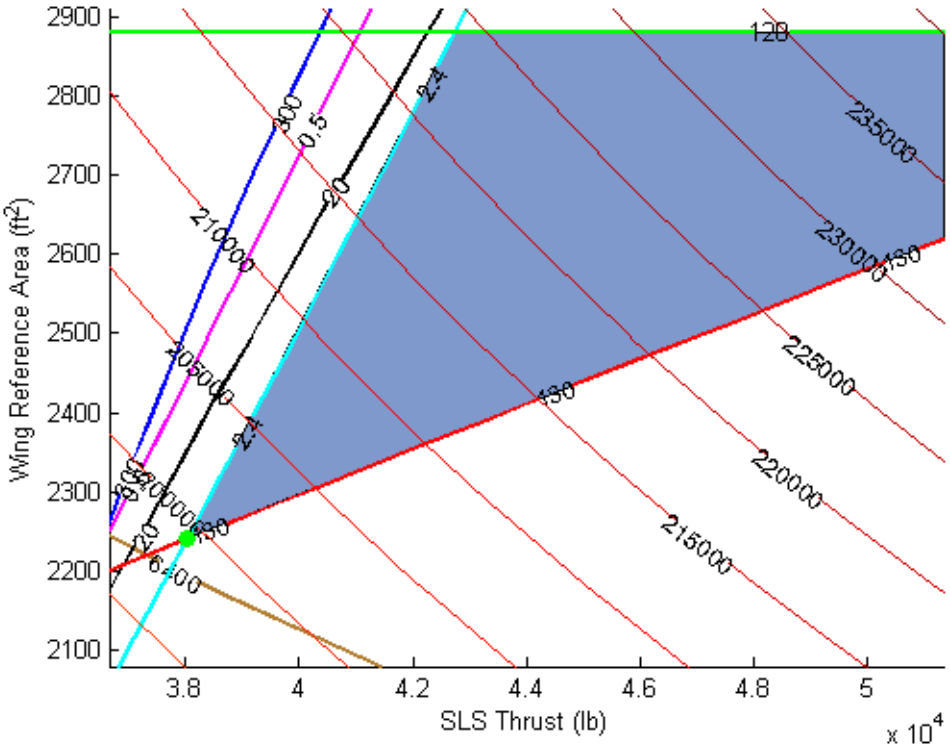

Figure 4.35: Stretched design region of the wide-body L2D24 model in the same constraints of wide-body L2D18 model.

Rather, we choose the aerodynamic efficiency improvement option. The original work focused on the blended wing body configuration. The study shows this type of aircraft has a very high aerodynamic efficiency due to blending the body into the wing. Ultimately, we eliminate the drag on the long fuselage. In contrast, the short and wide body causes problems in balancing the vehicle, emergency evacuation, and the passenger's riding quality. Thus in designing the Wide-Body model, we design the fuselage as a narrow airfoil separated from the wing. The restriction is that the shape of the entire fuselage must be identical to the shape of an airfoil. In doing so, we gain an extra lift and reduce the fuselage's drag. Moreover, we consider burying the engines inside the wings will reduce some drag from the engine mount pylons and the nacelles. Figure 4.36 contains initial sketches of the aircraft's configuration.

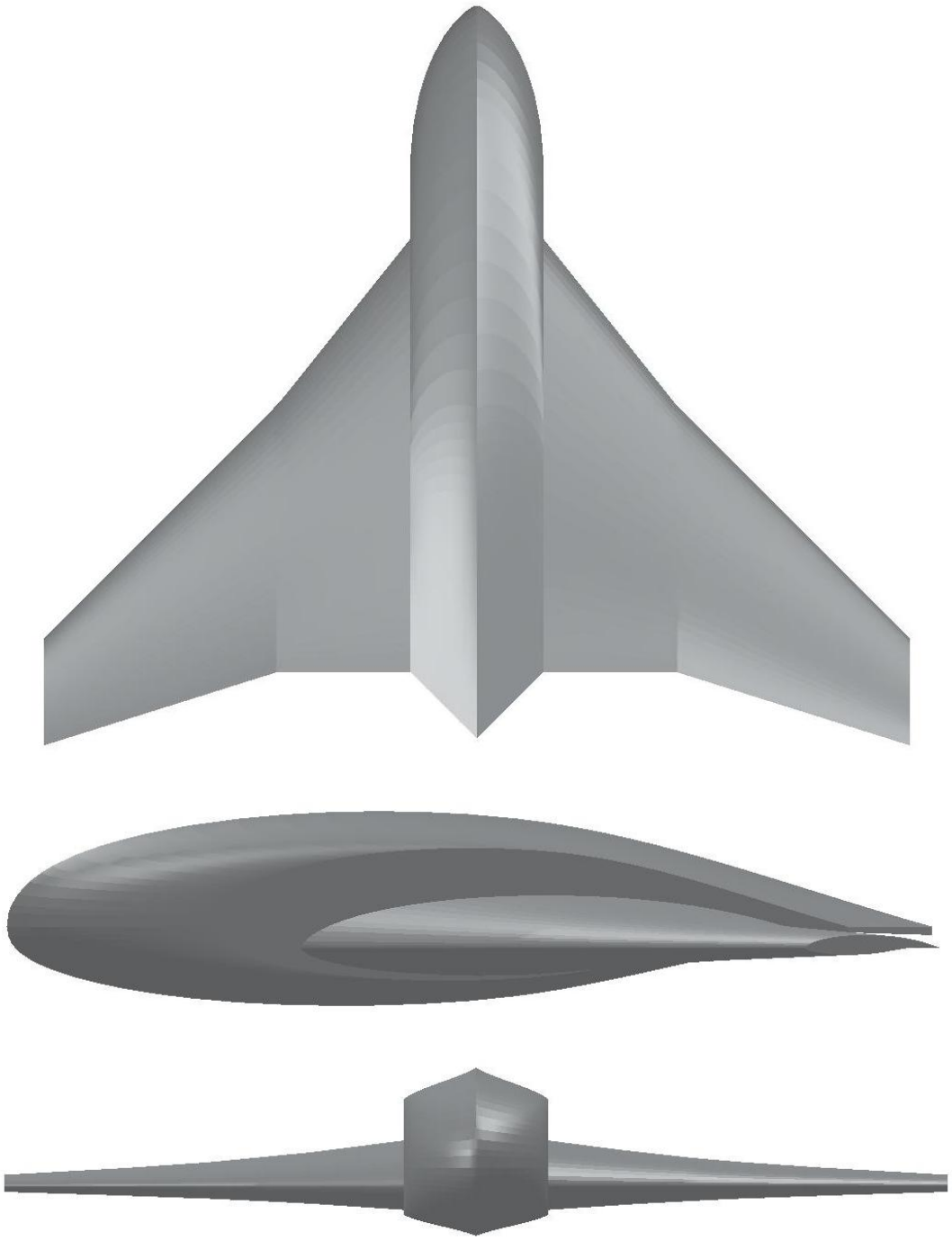

Figure 4.36: Conceptual sketch of the configuration of the wide-body aircraft.

Chapter 5 Conceptualizing a Wide-Body Aircraft Model

5.1 Introduction

So far we have made a significant achievement in preliminary design of a conceptual aircraft model by finishing the preliminary sizing. By the end of Chapter 4, we obtain the primary parameters: (1) the takeoff weight, (2) the SLS thrust per engine, and (3) the wing platform area of the new aircraft. The preliminary design does not stop there. Rather, the leading designers must show their team the basic layout of the vehicle. Therefore, they need to proceed further to the conceptual design of the fuselage, the wing, the tails, the positions of the engines, and the landing gear placements. This chapter will cover the entire conceptual design, as if it was the end of the preliminary design process.

5.2 Fuselage Designing

5.2.1 Layout of the Passenger Compartment

In the previous chapter, we have conceptualized the longitudinal (the y-axis of the body coordinate of a conventional aircraft) cross section of the fuselage as the MS(1)-0317 airfoil. Our main goal is to design a fuselage that can carry the entire payload without modifying the shape of the airfoil. Our major challenge is to design the passenger cabin based on the constraint of the chord length and the thickness of this airfoil. Because of this constraint, we lose two degrees of freedom in the fuselage design. These degrees of freedom are the length and the height of the fuselage. Thus, the width of the fuselage is the remaining degree of freedom.

Even though, the width is our degree freedom, we still do not fully control this variable due to safety rules and riding qualities. As a result, a careful design of the passenger cabin's layout is very important and needs to be done first. Our main concerns are the seat pitch and the number of seats abreast. At this stage of the design process, the

designers can use the reference seat pitch from [11] and the emergency egress rule from [8] to determine the passenger layout of the compartment.

In this design, we choose a 60-inch seat pitch and a 40-inch seat pitch for the business class and the economy class, respectively. A summary of the passenger emergency egress rule from [8] is quoted as "there should be no more than three seats accessed from one aisle." Thus, we choose eight seats abreast in a 1-2-2-2-1 pattern for the business class. Similarly, we choose twelve seats abreast in a 2-2-4-2-2 pattern for the economy class. Now, we have established the passenger distribution, the minimum length of the cabin, and the prediction for the width of the fuselage. A brief calculation of the minimum length of the passenger compartment is illustrated in Table 5.1.

Table 5.1: Passenger distribution and minimum length of the cabin

Class	*Seat/Row*	*Row*	*Total Seat/Class*	*Seat Pitch (in.)*	*Class Length (in.)*
Business	8	7	56	60	420
Economy	12	12	144	40	480
Total		19	200		900

5.2.2 Cross-section of the Passenger Compartment

The next step is designing the lateral cross section of the passenger cabin based on its layout. Strictly speaking, the cross section is determined by the seat width, the headroom, the aisle width, and the aisle height. For the business class, the seat width and the aisle width are set to 25 inches and 30 inches, respectively. For the economy class, both the seat width and the aisle width are set to 20 inches. For simplicity, a 75-inch-headroom is set for both business class and economy class. The aisle height is the last parameter to be determined. It varies across the cross section and depends on the shape of cross section. Figure 5.1 shows the initial proposal cross sections of the passenger cabin.

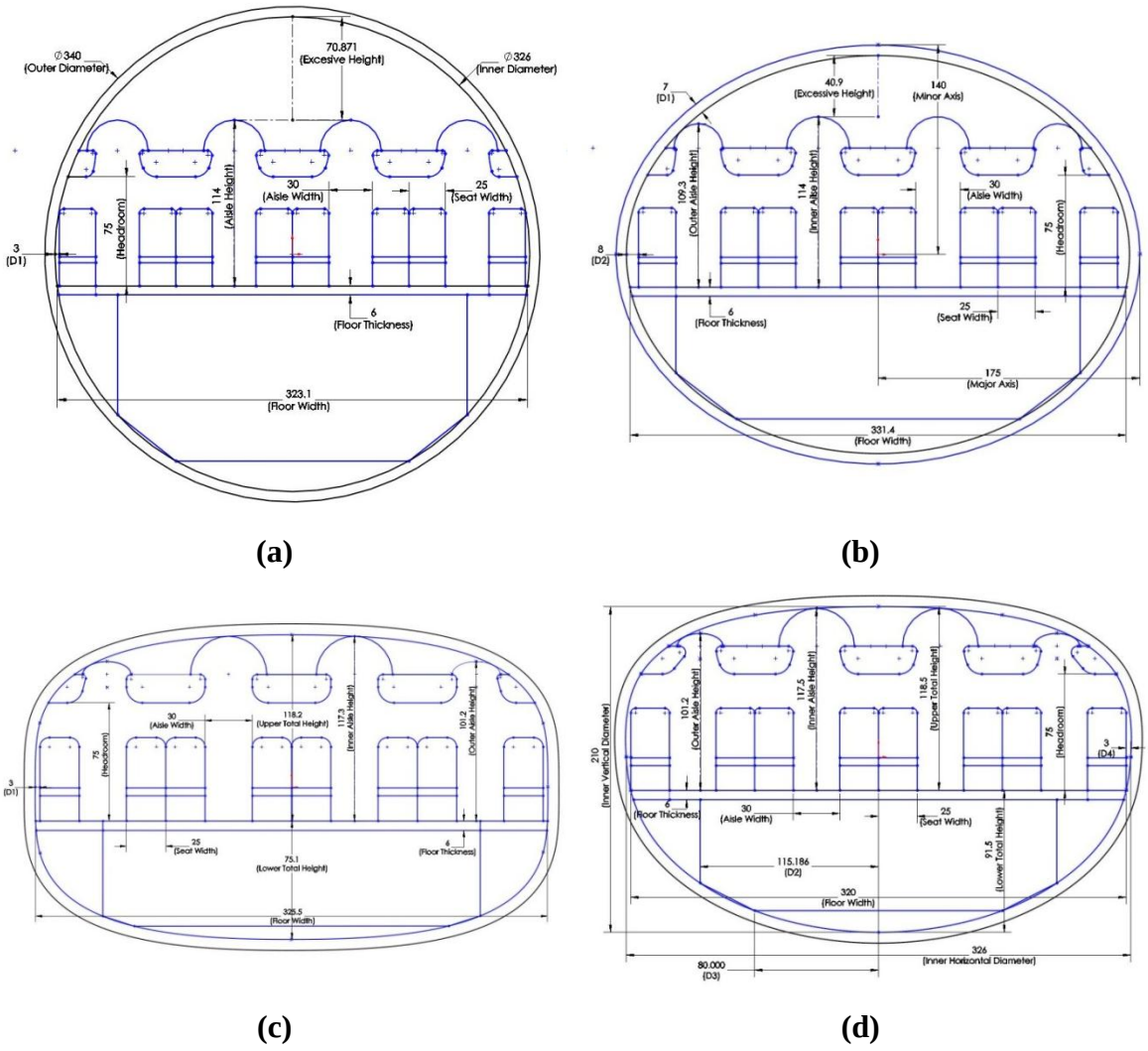

Figure 5.1: Proposal cross sections: (a) circular, (b) elliptical, (c) rectangular, and (d) combination of elliptical and rectangular (all dimensions are in inches).

All four cross sections are designed to house nineteen rows whose width is 320 in. wide. Among these cross sections, the circular cross section is the ideal shape for a pressurized vessel because of its uniform curvature. Thus hoop tress on its surface will be uniform as well. However, its excessive height above the passenger cabin is larger than all other cross sections in the group. The unusable height above the passenger cabin is 70.9 inches. The aisle height is 114 inches and stays constant across the seat row. The next candidate is the elliptical cross section whose excessive height is less than that of the circular cross section. The unusable height above the passenger cabin of the elliptical cross section is

40.9 inches. Nonetheless, it does not handle the internal pressure stress as well as the circular cross section does. In this case, the tensile stress is largest at the pivot of the minor axis and the compressive stress is largest at the pivot of the major axis. In the elliptical cross section, the outer aisle height is 109.3 inches. The inner aisle height is 114 inches and the pattern is symmetrical over the minor axis.

To minimize the unusable space above the passenger cabin, we designed an unconventional rectangular cross section for the pressure vessel. This type of cross section allows us to reduce the unusable height above the passenger cabin to zero. The inner aisle height is 117.3 inches and the outer aisle height is 101.2 inches. However, the hoop stress handling quality of this type of cross section is not as good as circular and elliptical. There are four pivots where the tensile stress concentrates at the top, bottom, and both sides of the section. Similarly, there are four pivots where the compressive stress is largest at the four corners of the cross section. Nevertheless, this type of cross section provides us the highest lift on the fuselage because of its flat surface on the top and the bottom of the cross section.

Finally, we designed an asymmetrical cross section to minimize the unusable height above the passenger cabin and to improve the ability to handle stress. We combine a semi rectangular section on the upper half with a semi elliptical section on the bottom half. In doing so, we sacrifice a portion of lift from the bottom surface. In return, we eliminate two compressive stress pivots and two tensile stress pivots. Meanwhile, we keep the unusable height at zero and obtain a 101.2-inch outer aisle height and a 117.5-inch inner aisle height. Moreover, we also enlarge the overhead closet for carry-on items with this combinational cross section. Thus we select this type of cross section for our design. The cross section has a 210-inch inner vertical diameter and a 326-inch inner horizontal diameter. The thickness of the cross section is 7 inches. The floor of the passenger cabin is 21.5 inches below the center line of the cross section. The leg room is 16-inch high; the seat back is 37-inch high; and the carry-on cabinet is 18-inch high. Table 5.2 summarizes

the dimensions of the cross section for both classes. Figure 5.2 shows the cross sections and the seat patterns for both classes.

Table 5.2: Summary of dimensions of the cross section					
Class	*Seat Width*	*Seat/Row*	*Aisle Width*	*Aisle/Row*	*Floor Width*
Business	25 in.	8	30 in.	4	320 in.
Economy	20 in.	12	20	4	320 in.
	Headroom	*Inner Aisle Height*		*Outer Aisle Height*	
Business	75 in.	117.5 in.		101.2 in.	
Economy	75 in.	111 in.		103.8 in.	
Passenger Compartment's Maximum Height				118.5 in.	
Cargo Compartment's Maximum Height				91.5 in.	
Inner Horizontal Diameter				326 in.	
Inner Vertical Diameter				210 in.	
Wall Thickness				7 in.	
Outer Horizontal Diameter				340 in.	
Outer Vertical Diameter				224 in.	

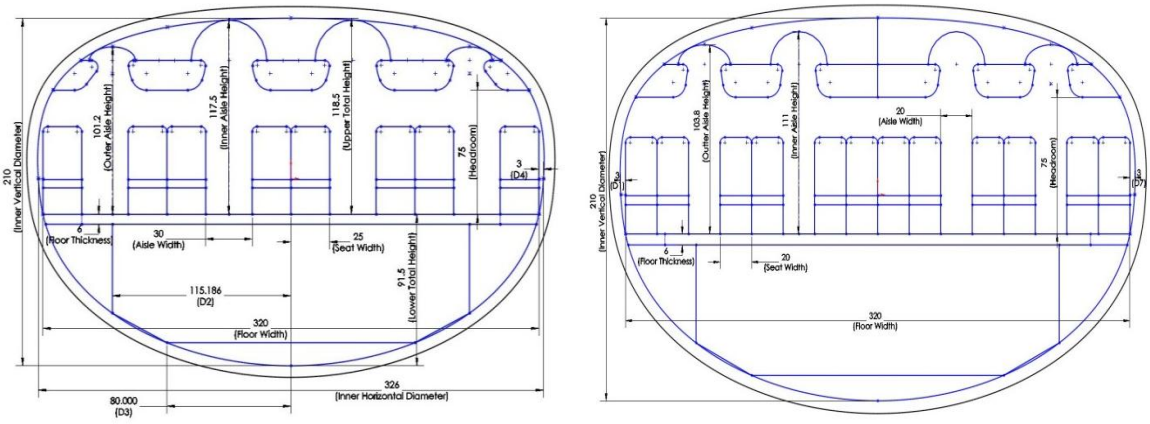

(a) **(b)**

Figure 5.2: Passenger cross sections of (a) business class and (b) economy class.

5.2.3 Sizing the Airfoil of the Fuselage

At this point, we have already established the length, the width, and the height of the passenger compartment. Now, we can size the airfoil that will be the longitudinal cross section of the fuselage. As mentioned earlier, the airfoil thickness is proportional to the airfoil chord length. The maximum thickness of the MS(1)-0317 airfoil is 17% of its chord length. If we size the airfoil by using the length of the passenger cabin, the height of the cabin will be dictated by the thickness of the airfoil and vice versa. Figure 5.3 illustrates this constraint in details. The symbols in the picture indicate that the length L_1 associates with the height h_1. Similarly, the length L_2 associates with the height h_2. As the height increases the length decreases and vice versa. Notice that the height is a function of the chordwise position. Likewise the length varies along the z-axis. Thus an appropriate assignment of the dimensions and their positions is very important for us to successfully size the fuselage airfoil, without wasting so much structural weight on the unusable space of the fuselage.

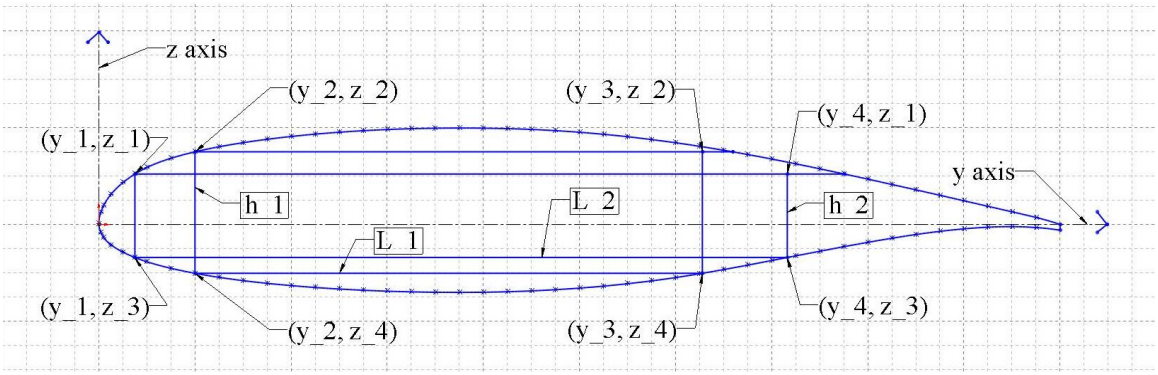

Figure 5.3: The MS(1)-0317 airfoil.

In this presentation, we sized the fuselage airfoil based on the height of the passenger cabin. The approach is quite simple and can be shown here in details. In the yz-coordinate, the position is measured in 0.025C unit, where C is the chord length. Let us consider the h_1-L_1 rectangular in Fig. 5.3. The height h_1 is located at $y_2 = 0.1C$ and $y_4 = 0.625C$ and ranging from $z_4 = -0.05C$ to $z_2 = 0.0725C$. By assigning the outer vertical

diameter (the maximum height) of the lateral cross section to h_1 we determine the chord length of the airfoil (or the total length of the fuselage). That is:

$$h_1 = z_2 - z_4 = 0.0725C + 0.05C = 0.125C = 224\ in. \tag{5.1}$$

Dividing Eq. (5.1) by 0.125, we obtain the fuselage length

$$C = \frac{224\ in.}{0.125} = 1{,}792\ in. \tag{5.2}$$

Now, we use the value of C to check whether L_1 is greater than or equal to the passenger compartment's minimum length.

$$L_1 = y_4 - y_2 = 0.625C - 0.1C = 0.525C = 940.8\ in. \tag{5.3}$$

L_1 is longer than the required length by 4.53%. The length of this fuselage is 149.333 ft. It is 60 ft shorter than the fuselage of the Boeing 777-200LR. The maximum height of the fuselage is 25.387 ft which is 5 ft higher than that of the Boeing 777-200LR. The width of the fuselage is 8.333 ft wider than the fuselage of the Boeing 777-200LR. Thus we are satisfied by these results. Figure 5.4 shows the side view of the fuselage with the seat row arrangement (all dimensions are in inches). Figures 5.5-9 show the fuselage in three dimensions.

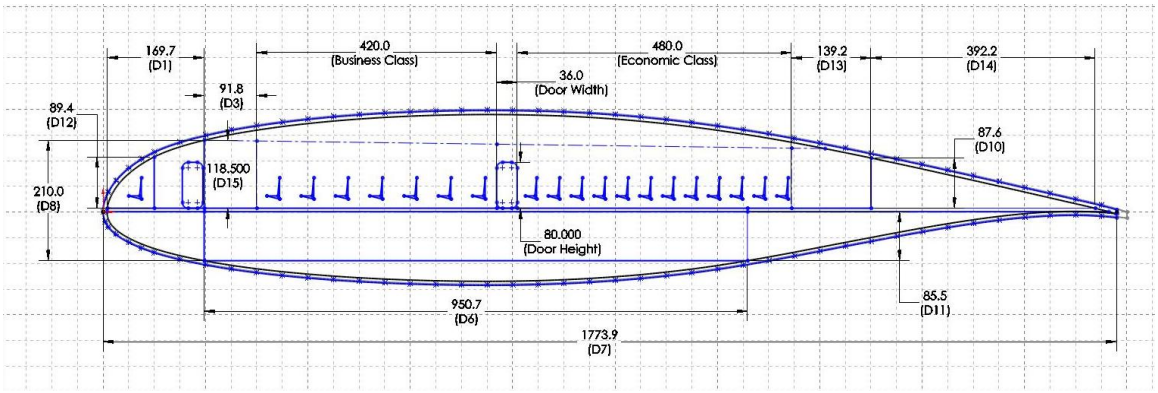

Figure 5.4: Side view of the fuselage with seat row arrangement.

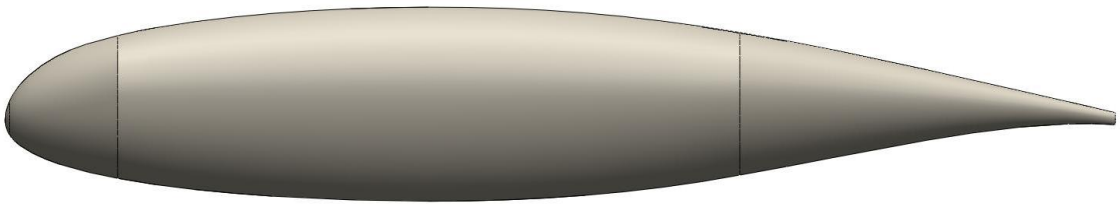

Figure 5.5: Side view of the lofted fuselage.

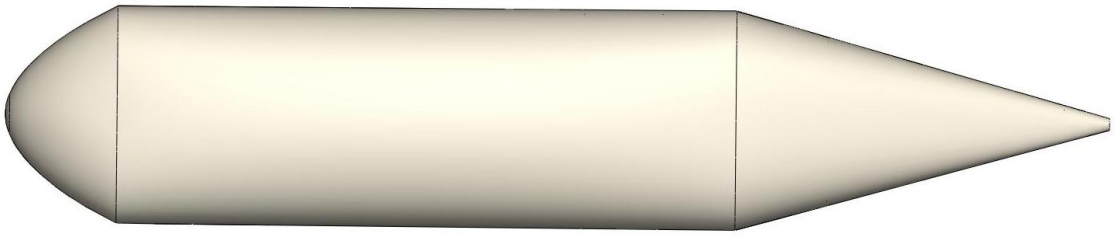

Figure 5.6: Top view of the lofted fuselage.

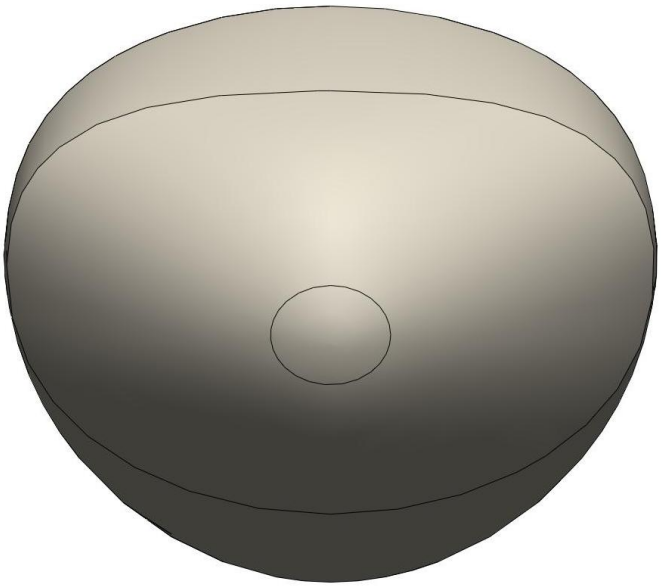

Figure 5.7: Front view of the lofted fuselage.

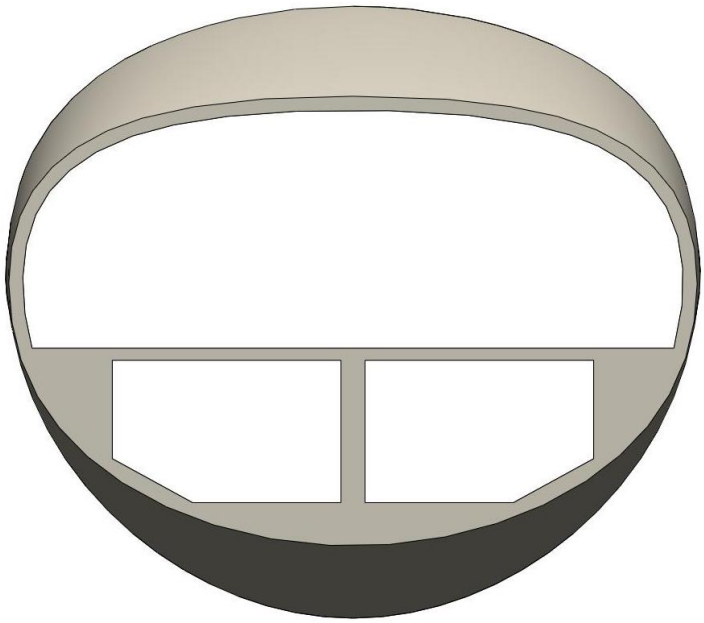

Figure 5.8: Front cross-sectional view of the lofted fuselage.

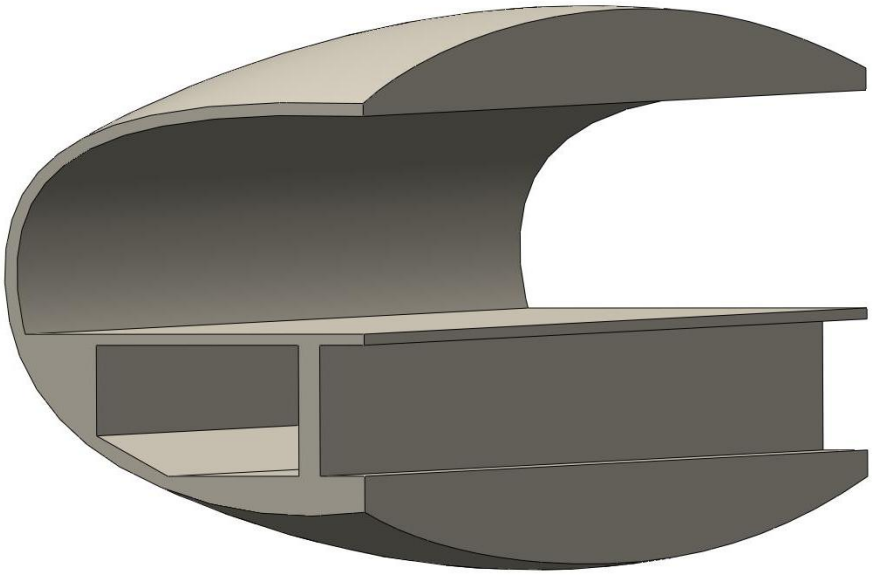

Figure 5.9: Side cross-sectional view of the lofted fuselage.

5.3 Wing Design

5.3.1 Main Wing

In this step, all necessary information is available from the previous chapter. We are going to sketch the geometry of the wing based on this information. Refer to Fig. 4.33, we select our design point at $(T_{SLS},\ S_{ref}) = (39{,}000\ lb,\ 2350\ ft^2)$ for some safety margins. Since the English unit system in SolidWorks is in IPS, we need to convert the wing area to square-inch for convenience. The equivalent wing platform area in square-inches is $338{,}400\ in.^2$. From the aspect ratio, we find the wing span is:

$$b = \sqrt{AR \cdot S_{ref}} = 108.397\ ft = 1{,}300.769\ in. \tag{5.4}$$

Now, we can find the root chord length and hence the tip chord length as well. The root chord length is given by:

$$C_r = \frac{2}{1+\lambda}\frac{S_{ref}}{b} = \frac{2}{1+0.4}\frac{338{,}400\ in.^2}{1{,}300.769\ in.} = 371.648\ in. \tag{5.5}$$

Hence the tip chord length is $C_t = 0.4C_r = 148.659\ in.$. Lastly, the wing sweeps 40° at half chord length. For the ease in sketching up the wing geometry, we convert the half chord sweep angle to the leading edge sweep angle by:

$$\tan\Lambda_{LE} = \tan\Lambda_{C/n} + \frac{4}{nAR}\left(\frac{1-\lambda}{1+\lambda}\right) = \tan 40° + \frac{4}{2\cdot 5}\frac{1-0.4}{1+0.4} = 1.01053 \tag{5.6}$$

where n is the dividing factor. For example, n is equal to 2 for the half-chord sweep angle (please consult Appendix D.5 for detailed derivation). Thus the leading edge sweep angle is 45.3°. In addition, implementing the method found in [8], we determine the mean aerodynamic chord length and the aerodynamic center (AC) of the wing. Figure 5.10 illustrates the wing geometry the mean aerodynamic chord length. Figure 5.11 shows the lofted wing with curvatures on the leading edge (LE) and trailing edge (TE) to enhance the aerodynamic efficiency by making an elliptical lift distribution on the wing.

5.3.2 Blending Section

In our design, the blending section plays a very important role. First and foremost, the blending section houses the main (rear) landing gear. Since the passenger compartment is tightly fit inside the fuselage, there is not any room left for us to fit the main landing gear into the fuselage when retracted. In addition to the main landing gear, the blending section will also provide room for other sub-systems like the mechanical systems, electrical systems, and air conditioning system. Secondly, we would like to have space to bury the engines inside the root of the wing. Finally, we want to have a smooth integration of the fuselage and the wings so that we eliminate the sharp corners at the roots of the wings, and hence we minimize the drag. Based on the sizes of the rear landing gear and the engines, we sketch the blending sections as the grey areas in Fig. 5.12.

5.3.3 Engine Placement

As we mentioned earlier, the second reason for the existence of the blending section is to bury the engines inside it. There are several reasons for us to consider burying the engines inside the blending wing sections. First of all, we are trying to design a vehicle that will achieve a very high aerodynamic efficiency. For a particular aircraft, the aerodynamic efficiency of the vehicle is limited by the maximum lift-to-drag ratio of its wing. In reality, combining a fuselage and a wing together degrades the aerodynamic efficiency of the vehicle due the skin friction on the surface of the fuselage. Thus flying wing is considered as the most aerodynamic efficient aircraft. Because of the issues of the blended-wing-body model that were discussed in Chapter 1, we rather design a wide-body aircraft in this presentation than a blended-wing-body aircraft. Even though we have designed the fuselage whose longitudinal cross section is the MS(1)-0317 airfoil, we still have to deduct 20% of the aerodynamic efficiency of the wing to account for the uncompleted blend. In the sense of blended-wing-body concept, a completed blend is defined as the fuselage (or the pressure vessel) is absolutely inside the wings.

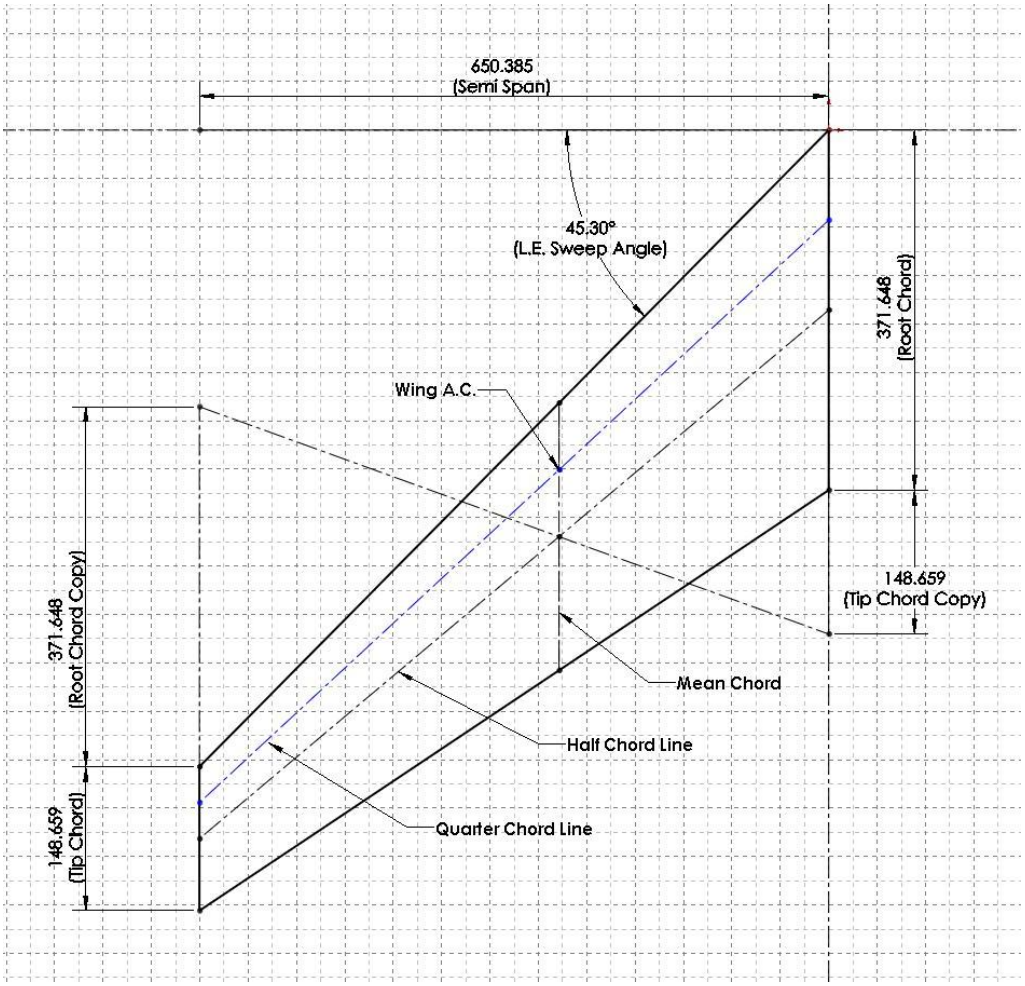

Figure 5.10: Geometry of the wing platform.

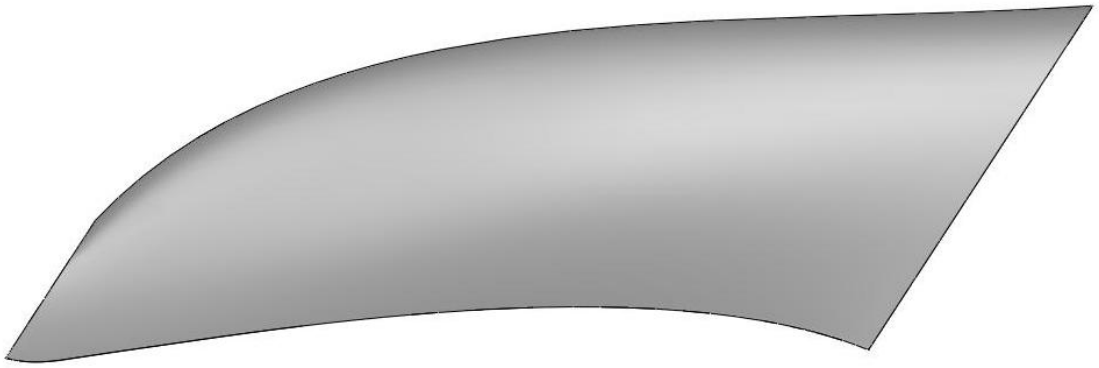

Figure 5.11: Lofted wing with curvatures on LE and TE.

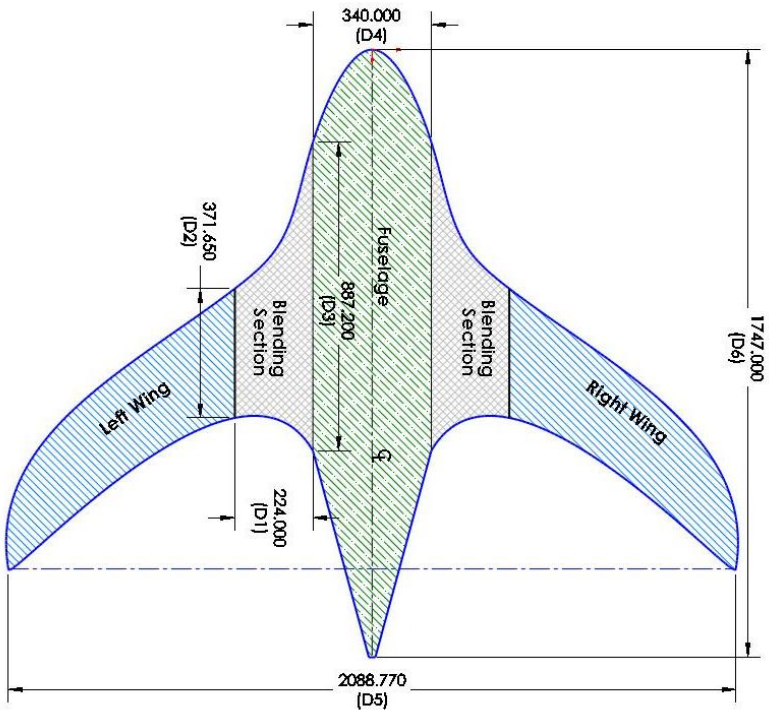

Figure 5.12: Top view of the integrated fuselage, blending section, and wing body.

Secondly, mounting an engine on a wing also degrades the efficiency of the wing. Normally, the engines are mounted beneath the wings of most modern commercial jets. Such design causes the lost in lift of the wing sections where the engines are mounted. This is because the jet-stream of the engine disturbs the flow on the lower surface of the wing section, where the engine is mounted. In addition, there is a turbulent flow behind the nacelle and the pylon of an engine. All of these disturbances in the flow underneath the wings contribute to the reduction in lift of the wings. Besides losing lift, there is an increase in drag due to the skin friction on the outer surface of the nacelle and the pylon. Therefore, locating the engines inside the wings will improve the aerodynamic efficiency of the vehicle.

Nonetheless, burying the engines inside the wings will cause other issues. Let us make a brief analysis designing of the internal engine mounted section of a wing. First, we need some information about the size of the engine to design the internal structure of this

section of the wing. Our design point indicates each engine must provide at least 39,000 lb of SLS thrust. Based on this number, we searched the market for engines that produce SLS thrust around the 39,000 lb. The results are listed in Table 5.3.

Table 5.3: Sizes of turbofan engine candidates for the wide-body model

Engine	*Max Diameter*	*Length*	*Dry Weight (lb)*	*SFC*	*SL Max Power (lb)*
CF6-6	105 in.	188 in.	8,176 – 8,966	0.35	41,500
RB211-535E4	74.1 in.	117.9 in.	7,264	0.607	40,100 – 43,100
PW2000	78.5 in.	141.4 in.	7,300	0.33	38,400 – 43,734

These engines are used to power the Boeing 757 aircraft. The sizes in Table 5.3 are the geometries of the core engines. After installed, with the nacelle, the diffuser, and the nozzle the engine can be 210-inch long and 106-inch wide to account for the engine accessories (these measurements are based on the geometry of the engines on the aircraft found in [21]). Using the MS(1)-0317 airfoil and assigning its maximum thickness to 106 inches, we find the chord length is 565 inches. Figure 5.13 illustrates the design of a straight air duct.

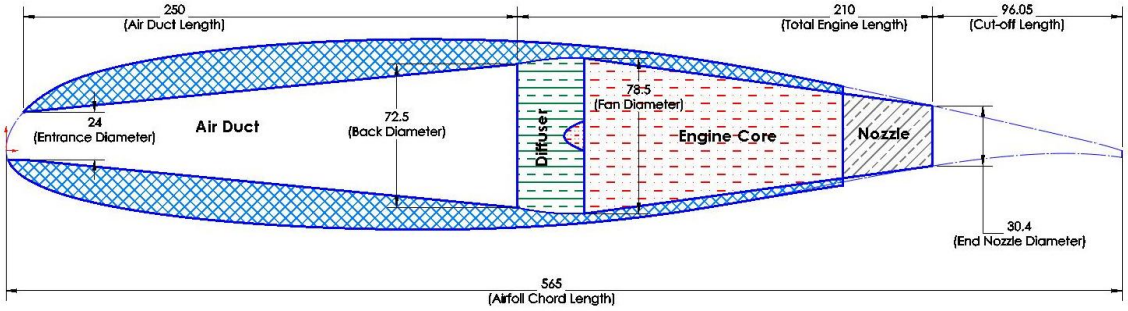

Figure 5.13: Straight air duct.

In the design, the engine is completely installed inside the airfoil. The entrance of the air duct is at the leading edge of the airfoil. The air duct is 250-inch long with a 24-inch entrance diameter and a 72.5-inch back diameter. This straight air duct is used to directly lead the free stream air to the diffuser of the engine. There is an advantage in use of a straight air duct because the air enters the entrance of the duct at the cruise speed.

However, the duct must go through the wing spar. From the structural perspective, this is a disadvantage of the design because drilling a cylinder through the spar will weaken it at this section. If we are not careful in the detailed design, the wing spar could experience structural failures.

Moreover, a diverging nozzle in a subsonic flow decelerates the air stream and degrades the propulsion efficiency of the engine. On top of this, the flow is turbulent at the end of the air duct. We do not want a turbulent flow enter the diffuser of the engine. Besides degrading the propulsion efficiency, the long air duct also experiences a large skin friction drag. The total surface area of the duct is $37{,}895.5\ in.^2$ where if the engine is hung outside, the total surface area of the nacelle would be $35{,}922.5\ in.^2$. In this case, we add more drag to the vehicle than it would be using external engines. There are four options for us to fix these issues. One is to move the engine forward. Two is using a turbojet engine instead of a turbofan engine. However, this option will come with higher noise level which is unfeasible for a commercial transport. Three is to develop a new type of propulsion system. Four is to design a different air duct.

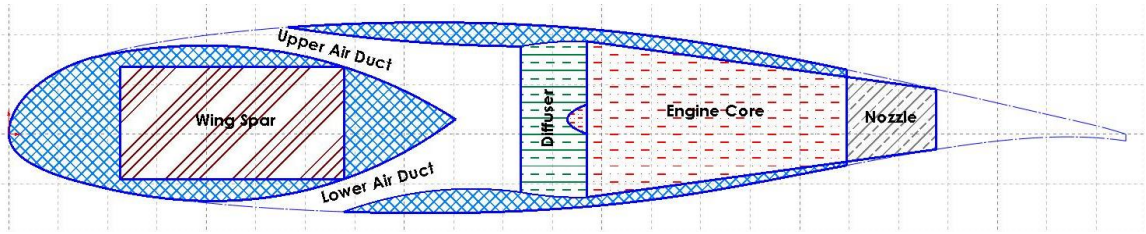

Figure 5.14: Split air duct.

Next, we introduce a split air duct design in Fig. 5.14. In this design, the duct sucks the air from the upper entrance and the lower entrance. This design shortens the length of the duct tremendously compared to the previous design. However, there is another issue with this design. There are two different streams of air entering the diffuser. While cruising at a transonic Mach number, the flow on the upper surface of the airfoil can accelerate beyond the sonic speed. Thus the upper duct can accelerate the air stream further. On the

other hand, the flow on the lower surface is subsonic. Thus the lower duct decelerates the air stream.

Also, if there are both subsonic flows on the top and the bottom surfaces of the airfoil, different diverging nozzles decelerate the flow at different rates. Thus it requires a very careful design in the air duct to bury the engines inside the wings. Moreover, burying the engines inside the wings will increase the complexity to the internal structures of the wings as we have seen so far in this discussion. Nevertheless, this does not mean that it is impossible to do so because most fighter jets have their engines located inside their wings. This includes the legendary blended-wing-body; the B-2 bomber has its engines buried inside its wings. In this case we need a deeper analysis of this issue which is left to further study. For simplicity, we choose to hang the engines beneath the wings and reduce the aerodynamic efficiency of the wing. We assume the above 20% deduction in the lift-to-drag ratio also accounts for the lost in efficiency that is caused by hangings the engines beneath the wings.

5.4 Initial Calculation of the Center of Gravity of the Aircraft

At this point, we already have enough information to sketch up the model without the landing gear and the tail. We are also ready to make the first calculation of the center of gravity (CG) of the aircraft and the payload. Figure 5.15 shows the 2D sketch the vehicle's layout with loads, no landing gear, and no tails. Note that there are many different CG locations in Fig. 5.15. Each load has its own CG. Thus, in this thesis, when we write CG alone, we mean the CG of a fully loaded vehicle. Otherwise, it will be specified with additional information on that CG. Table 5.4 illustrates the first calculation of the center of gravity. At this point, the CG is located at 834.074 inches behind the nose and 129.387 inches in front the AC. The pitching static margin is 41.86% of the mean chord length.

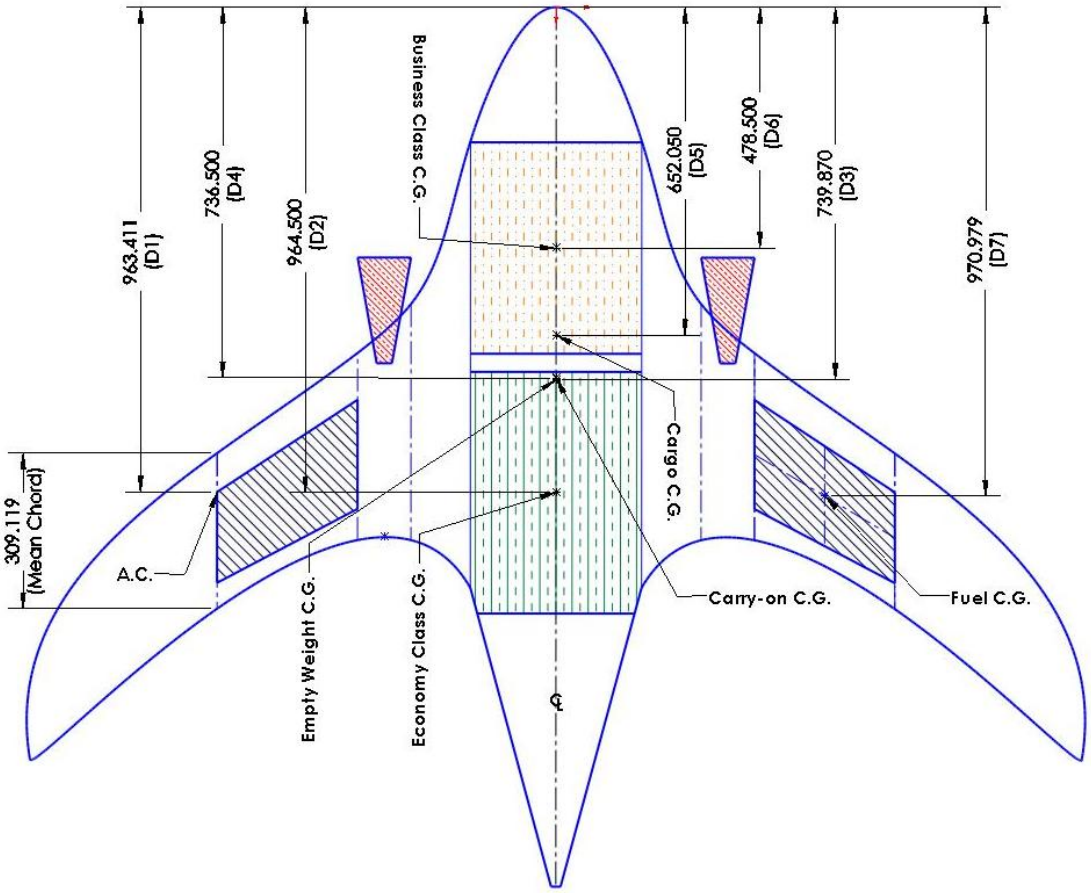

Figure 5.15: Load distribution on the vehicle without landing gear and tail.

5.5 Landing Gear Arrangement

5.5.1 Typical Requirements of a Landing Gear System

Knowing the center of gravity, we can proceed to design and to place a landing gear system. Since the model is already statically stable in pitching motion, the design for the landing gear is much easier. The current center of gravity is located at 834.074 inches behind the nose (, while the AC of the wing is at 963.461 in. behind the nose. The pitching static margin is 129.387 inches (equivalent to 41.86% of mean chord), which grants us a lot of freedom in arranging the landing gear.

There are several essential features that a landing gear system must have. The most important feature is to absorb the impact force as the vehicle touches down during landing. The second feature is to provide the aircraft a pitching angle of at least 10 degrees during takeoff and landing maneuvers. The third important feature is to help the aircraft balance during ground maneuvers. The fourth requirement is to provide the engines a ground clearance of at least 3 ft. In this presentation, we do not discuss the hydraulic system of the gear. Thus we skipped the first requirement and worked on the other three important requirements.

Table 5.4: The first calculation of the center of gravity

Component	*Weight (lb)*	*CG Position (in.)*	*Moment (lb-in)*
Business Class	10,980	478.5	5,253,930
Cargo	14,000	625.05	9,128,700
Carry-on	6,210	736.5	4,573,665
Economy Class	26,280	964.5	25,347,060
First Empty Weight	74,489.55	739.87	55,112,583.36
Fuel	49,252	971.0	47,823,692
Total	170,231.55		141,985,700.4
Center of Gravity	141,985,700.4 lb-in./170,231.55 in. = 834.074 in.		

5.5.2 Arranging a Landing Gear System in Pitching Motion Perspective

For this particular model, we find a convenient approach to design a landing gear system is to begin with the ground clearance. From an empirical equation for the size of the wheel found in [8], we calculate the diameter of the wheel as the following:

$$Dm_{wheel} = 1.63(W_{tk})^{0.315} = 1.63(203{,}096\ lb)^{0.315} \cong 77\ in. \tag{5.7}$$

Knowing the diameter of the wheel, we begin to locate the front landing gear based on the geometry of the fuselage. If we attach the front gear at 200 inches behind the nose, the height of the strut would be 175.794 inches. The height of the strut is shorter than the

distance between the gear and the nose. This means, we have enough room to store the gear after it is retracted. Thus we are satisfied with this position for the front gear. Figure 5.16 shows the side view of position of the gear.

Positioning the front gear is quite simple. In contrast, it is complicated to position the main gear. This carries about 90% of the weight [8]. Thus it has to be near the CG. Also, the main gear must be behind the CG to provide a pitching angle. Based on the geometry of the fuselage, attaching the vertical strut of the main gear at the mid-point between the CG and the AC is a good choice. At this position, the height of the strut is 192.024 inches. It allows the engine to clear the ground by 53.911 inches. At this position, the rear wheels of the main gear enable the aircraft to pitch at an angle as large as 18.22 degrees. In addition, to prevent the aircraft from tipping back on its tail, the off vertical angle is greater than the static tail-down angle [8] as shown in Fig. 5.16. Moreover, the main gear is nicely fit into the blending section along the y-axis of the body. Meaning, the main gear should be pulled forward when they are being retracted. Also at this position, the main strut of the main gear can be attached to the rear wing spar, which is a convenience for structural design later.

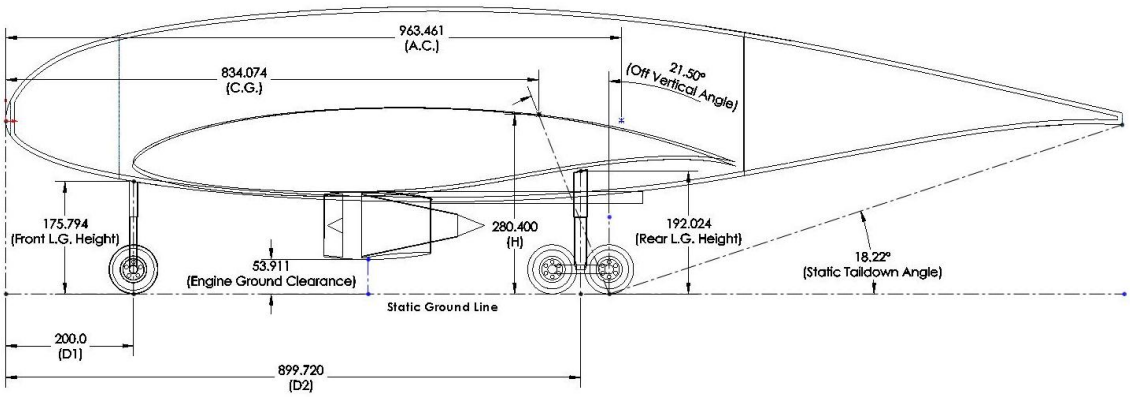

Figure 5.16: Side view of the position the landing gear without tail.

5.5.3 Arranging a Landing Gear System in Yawing Motion Perspective

Once the landing gear system satisfied the pitching requirements, we begin to position the main gear based on the yawing requirements, so that the aircraft can maneuver safely on the ground. The critical parameter in ground yawing motion is the overturn angle. To ensure the aircraft will not roll over during yawing at a sharp corner, the overturn angle must not be greater than 63 degrees [8]. Figure 5.17 illustrates the method to measure the overturn angle of tricycle landing gear arrangements. In both Figs. 5.16-17, the distance H is the height of the CG, which is measured from the static ground line. In this configuration, we attach the main strut of the rear landing gear to the blending section at a 230-inch lateral distance away from the center line. At this position, the overturn angle is 54.79 degrees, which yields a 13% safety margin for ground yawing maneuver. Note, we assume the vehicle is fully loaded in this calculation. If the vehicle is operating at the empty weight, its overturn angle would be 58.99 degrees. This is still under the safety threshold; therefore, we have convinced ourselves that this arrangement is feasible.

Table 5.5: The second calculation of the center of gravity

Component	*Weight (lb)*	*C.G. Position (in.)*	*Moment (lb-in)*
Business Class	10,980	478.5	5,253,930
Cargo	14,000	625.05	9,128,700
Carry-on	6,210	736.5	4,573,665
Economy Class	26,280	964.5	25,347,060
First Empty Weight	85,130.91	749.28	63,786,888.24
Fuel	49,252	971.0	47,823,692
Total	180,872.91		150,660,005.2
Center of Gravity	150,660,005.2 lb-in./ 180,872.91 in. = 832.961 in.		

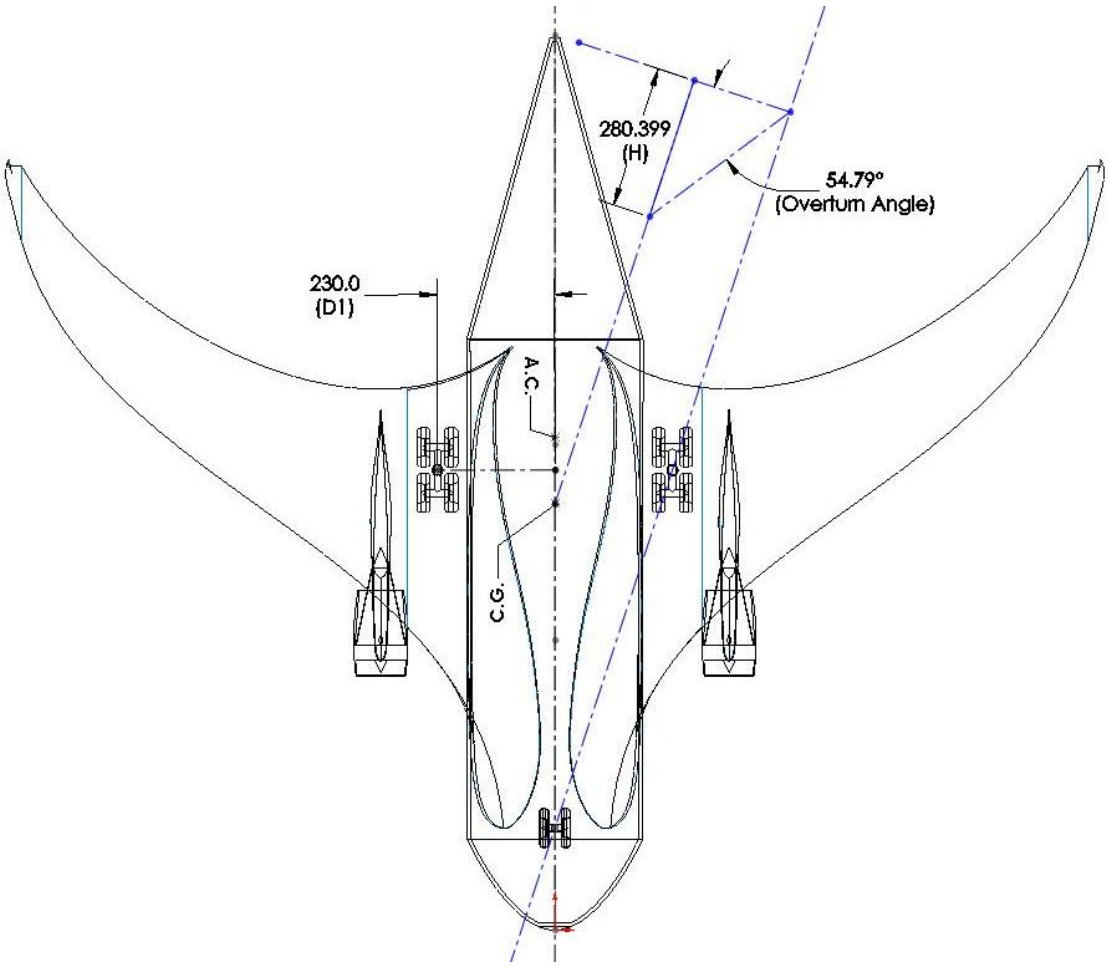

Figure 5.17: Top view of the position of the landing gear without tail.

5.5.4 The Second Calculation for the Center of Gravity

After attaching the landing gear, the empty weight increases by 10,641.4 lb, which makes the new empty weight to be 85,130.91 lb. Along with the increase in the weight, the CG of the empty airplane also moves backward by 9.41 inches and downward by 3.82 inches. Moving the CG of the empty weight backward shrinks the overturn angle of the empty aircraft. Thus it enlarges the overturn angle margin. On the other hand, it shrinks the off vertical angle. However, the CG of the new empty aircraft is still 84.794 inches in front of the fully loaded CG. Therefore, there is no need to re-measure the off vertical angle of the new empty weight.

The new CG of the entire aircraft without tails is calculated in Table 5.5. The new CG is now located at 832.961 inches behind the nose and 130.5 inches in front the AC. Since the CG of the entire aircraft is moved forward, both the off vertical angle and the overturn angle enlarge. For the off vertical angle, the enlargement is a good change. For the overturn angle, moving the CG forward is equivalent to shrinking its safety margin. Nonetheless, the new CG moves forward by only 1.113 inches from the old CG, the change in the overturn is insignificant. Therefore, there is no need to re-measure the new overturn angle of the fully loaded vehicle.

5.6 Tail Sizes and Designs

5.6.1 Horizontal Tail Size and Design

Once the CG is updated with the information of the landing gear, the tail design is much simpler. When designing the tails, we use the typical tail volume coefficients of similar types of aircraft. The horizontal tail volume coefficient is defined as:

$$c_{HT} = \frac{L_{HT} S_{HT}}{\bar{C}_w S_w} \tag{5.8}$$

where c_{HT} is the horizontal tail volume coefficient; S_{HT} is the horizontal tail platform area; $\bar{C}_w$ is the main wing's mean chord length; S_w is the main wing platform area (or reference area); and L_{HT} is the moment arm of the horizontal tail.

The moment arm of the horizontal tail is measured from the aerodynamic center of the main wing to the aerodynamic center of the horizontal tail. The typical c_{HT} can be found from [8]. For the jet transport, it is 1. To use Eq. (5.8) to compute the horizontal tail platform area, we need to know its moment arm. Raymer suggests the tail arm of the wing mounted engines aircraft is about 50 – 55% of the fuselage length [8]. We find the horizontal tail area is 108,849 $in.^2$ with the assumption the tail moment arm is 55% the fuselage length. Assuming the tail tapper ratio is 0.4, we design the horizontal tail as the sketch in Fig. 5.18.

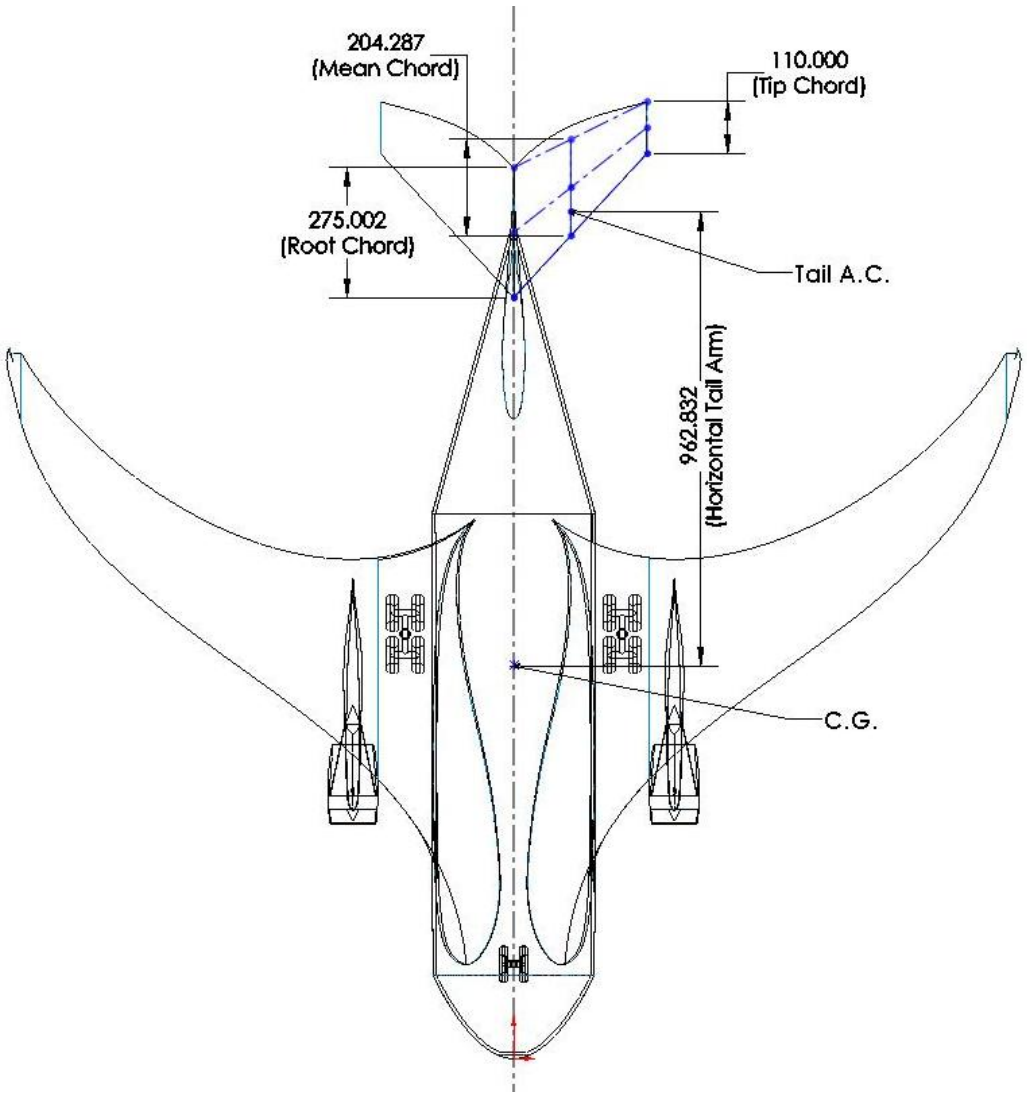

Figure 5.18: Design of the horizontal tail.

5.6.2 Vertical Tail Size and Design

Similarly to the horizontal tail, the vertical tail platform area is determined by its tail volume coefficient, which is given by:

$$c_{VT} = \frac{L_{VT} S_{VT}}{b_w S_w} \tag{5.9}$$

where c_{VT} is the vertical tail volume coefficient; S_{VT} is the vertical tail platform area; b_w is the main wing span; and L_{VT} is the vertical tail moment arm. For the vertical tail of a jet transport, the empirical tail volume is 0.09 [8]. Assuming the vertical tail arm is 45% of the fuselage length, we find its area is 30,150 $in.^2$. Consider the tail taper ratio is 0.1 and based on the fuselage geometry, we design the vertical tail as the sketch in Fig. 5.19.

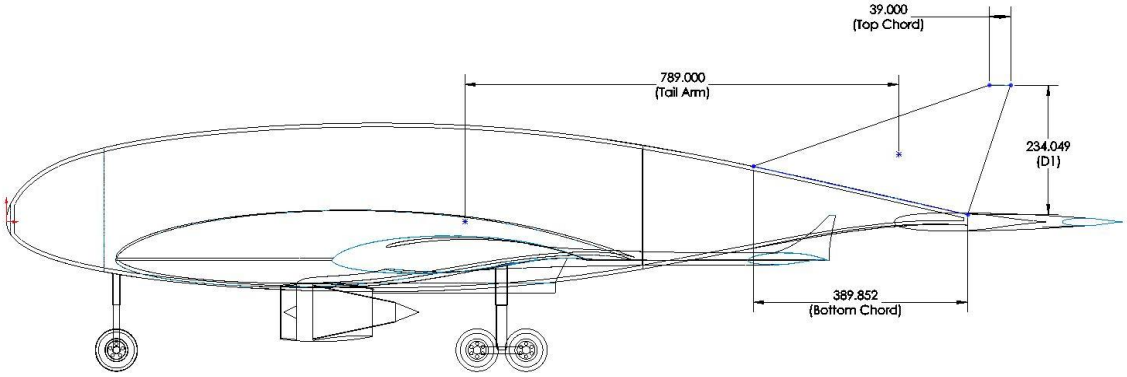

Figure 5.19: Design of the vertical tail.

5.6.3 The Third Calculation for the Center of Gravity

After adding the tail to the aircraft, the empty weight has increased by 6,500.54 lb that sums up to a 91,631.45-lb new empty weight. This new empty weight is 95% of the empty weight given by the results from the preliminary sizing in Chapter 4. If we include all other sub-systems of a complete aircraft, we would add about 10 – 15% of this new empty weight more to the vehicle. Based on these numbers, we can conclude that our design fits well with our initial estimation. Moreover, the drawing is not out of scale in comparison with similar aircraft. Thus we accept the drawing as the result of the preliminary design.

Besides, changing the empty weight, the tail also moves the empty weight CG backward to a point at 796.2 inches behind the nose. This makes the fully loaded CG becomes 853.003 inches behind the nose. The third CG calculation is done in Table 5.6. Since the

position of the CG changes significantly, we need to re-measure the off vertical angle and compare to the static tail-down angle. Figure 5.20 shows that the off vertical angle is till larger than the static tail down angle. Thus there is no need to make any change to the main gear.

Table 5.6: The third calculation of the center of gravity			
Component	*Weight (lb)*	*C.G. Position (in.)*	*Moment (lb-in)*
Business Class	10,980	478.5	5,253,930
Cargo	14,000	625.05	9,128,700
Carry-on	6,210	736.5	4,573,665
Economy Class	26,280	964.5	25,347,060
First Empty Weight	91,631.45	796.2	72,956,960.49
Fuel	49,252	971.0	47,823,692
Total	187,373.45		159,830,077.5
Center of Gravity	159,830,077.5 lb-in./ 187,373.45 in. = 853.003 in.		

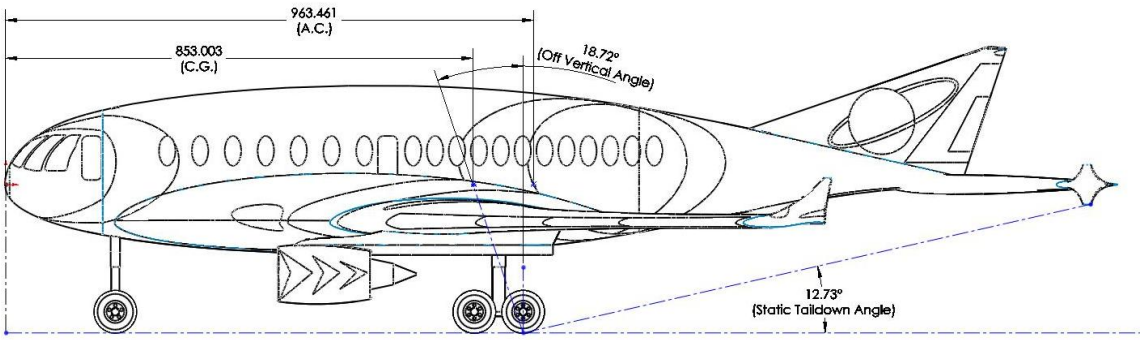

Figure 5.20: Re-calculation of the off vertical angle and the static tail-down angle.

5.7 Summary

Throughout this chapter, we have shown the advantages of the results obtained from the preliminary sizing in the previous chapter. We have utilized the weights, the wing reference area, and the required SLS thrust per engine to sketch and to loft the geometry of the model successfully. We have also demonstrated an approach to design a wide-body fuselage whose shape is an airfoil without modifying the airfoil at all. Even though we did not succeed in burying the engines inside the wings, we have been able to recognize the issues as well as possibilities for future studies. The conceptual model has been fully defined and sketched in Figs. 5.21 – 22, in which the CG and the AC are located. The model is statically stable in the pitching motion. Note that, further analysis and iterations are required in the detailed design and production process. This is a good point to finish the preliminary design of a conceptual commercial aircraft.

Figure 5.21: Isometric view of a wide-body commercial aircraft.

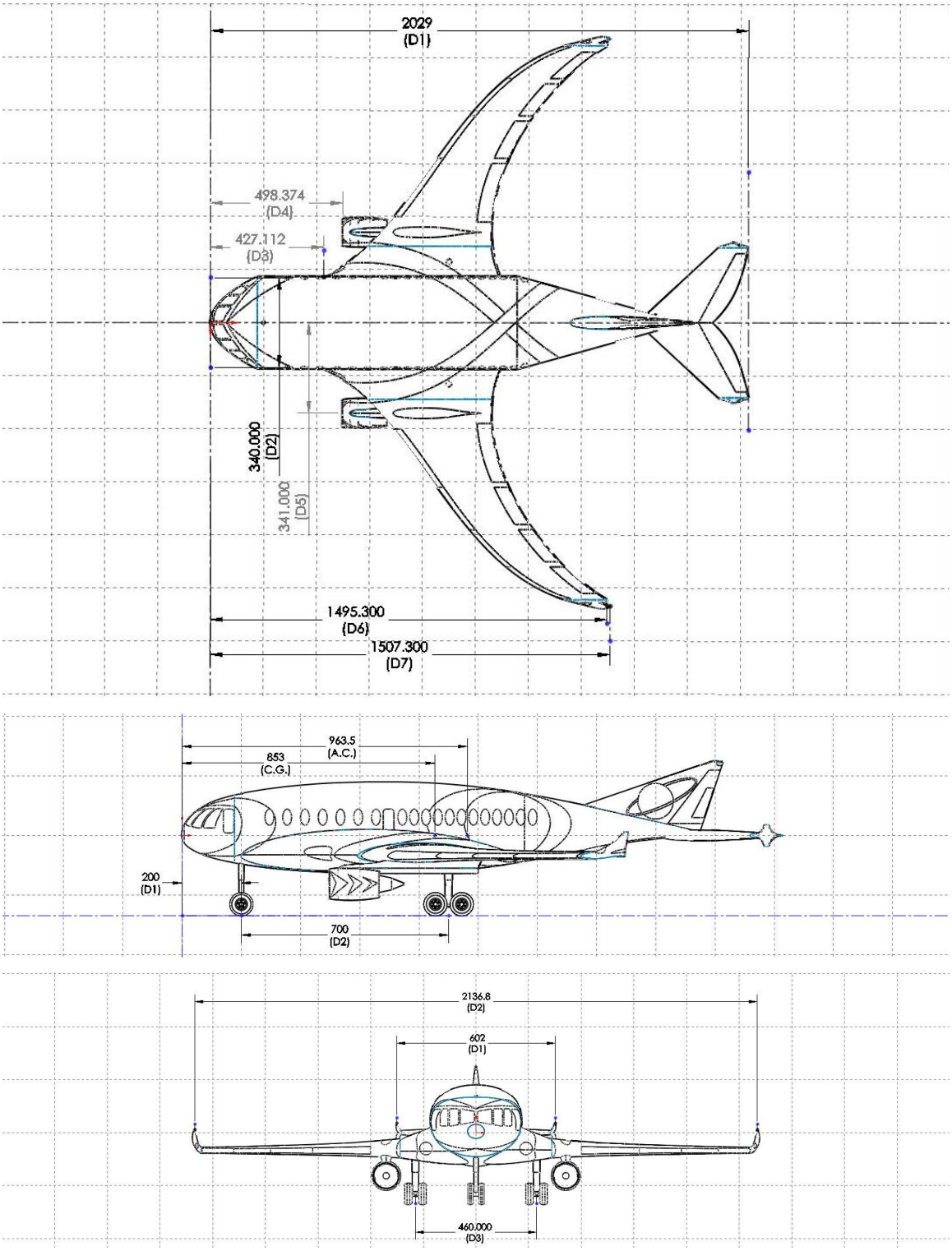

Figure 5.22: Conceptual model of a wide-body commercial aircraft.

Chapter 6 Conclusions and Future Work

6.1 Conclusions

6.1.1 Commercial Aircraft Design Requirement Setup Guidelines

Through this project, we established guidelines to setup the design requirements for a typical new commercial aircraft. Using historical data we determined the relationship between the passenger capacity and the operational range of the aircraft. From Fig. 2.1, we noticed that there is a very high population density of aircraft in the region of 1,000 – 4,000 nm and 100 – 300 passengers. We found other aircraft outside of this region are usually the derivative versions of those inside this region. It is recommend to begin with a small passenger capacity and a short range when develop a new model.

From the set of data, we also learned that most commercial aircraft cruise at 35,000 ft above sea level in range of cruise Mach number from 0.75 to 0.85 (see Fig. 2.2). Thus we suggest setting the initial cruise altitude for a new model at 35,000 ft and the cruise Mach number to 0.8.

Beside the historical data, we also found the FAR rules provide guidelines for the takeoff field length, the time to climb, the approach speed, the number of crew members, the number of flight attendants, and the loiter time. All of these parameters were discussed in Chapter 2 and Chapter 3 of this thesis.

6.1.2 Statistical Estimations of Primary Parameters

Based on the same data that was used to make the survey for the design requirements, we formulated the statistical estimation for the initial guess of the takeoff weight as a function of the passenger capacity and the operational range, Eq. (2.2). We also found the empty weight as a power function of the takeoff weight, Eq. (2.7). Similarly, we found the curves for the required SLS thrust and the wing platform area as functions of the

takeoff weight, Eq. (2.15) and Eq. (2.16), respectively. For convenience, the historical data that was used intensively throughout this project is provided in the Appendix E of this thesis.

Using the typical flight mission of the commercial aircraft, we determined the fuel weight for each segment of the flight mission in the form of the fraction of the takeoff weight. Then combining the fuel weight fraction for each segment, we calculated the total fuel weight for the entire flight mission.

6.1.3 Trade Study in Determining the Optimal Design Point

In Chapter 3, we employed the computational power of Matlab to sketch up the contours of all the design constraints in order to determine the optimal design point for a new model. In calculations of the takeoff ground roll distance and the takeoff climb gradients, we used FAR rules to determine the vehicle's speeds and altitudes for each phase of the takeoff. Knowing the typical climb path helped us calculate the time to climb from the end of takeoff to the initial cruise altitude. Using the historical data in Appendix E, we determined the surface of the empty weight as a function of the SLS thrust and the wing platform area, Eq. (3.20).

6.1.4 Selections of Airfoils for a Wide-Body Aircraft

Chapter 4 shows how to select the airfoil for the fuselage and the airfoil for the wing of the aircraft. We found the MS(1)-0317 airfoil and the Eppler 407 airfoil are appropriate for the fuselage and the wing, respectively. Appendix C shows how convert the aerodynamic coefficients of a 2D airfoil into the aerodynamic coefficient of a 3D wing. Appendix D demonstrates the calculations for the lift and drag increments of the Eppler 407 wing due to the deflections of flaps and slats.

We found an Eppler 407 wing whose aspect ratio is 5, taper ratio is 0.4, half chord sweep angle is 40 degrees, in a flow of Reynolds number of 6 million at Mach 0.8 sea level condition, has the maximum lift coefficient of 1.548 at an angle of attack of 16 degrees,

the minimum drag coefficient of 0.0077 at an angle of attack of -4 degrees. The wing's maximum lift-to-drag ratio is 30.585 at an angle of attack of -1 degrees (see Figs. 4.28 – 30).

6.1.5 Determining the Optimal Design Point for a Wide-Body Model By Implementing Preliminary Sizing

We determined the optimal design point and the design region for the wide-body aircraft model based on the following design requirements:

1. Commercial jet transport vehicle.
2. Payload is 200 passengers.
3. Operating range is 3,000 nmi.
4. Long range cruise speed is Mach 0.85 at the initial cruise altitude of 38,000 ft.
5. Time to climb from the runway to the initial cruise altitude is less than 20 minutes.
6. Maximum approach speed is less than 130 knots.
7. Take-off distance is less than 7,000 ft on a runway at 6,000 ft above sea-level on a standard day.

The results of the preliminary sizes were summarized in Table 4.10. In this study, we found the lift-to-drag ratio of 18 for the aircraft to accomplish the flight mission in Fig. 4.31 and Table 4.1. Since our wing model has a lift-to-drag ratio of 24, we found the model has less fuel consumption, smaller wing platform area, and requires less thrust than the model that has the lift-to-drag ratio of 18. Including the safety margins, we select the design point for our model as $(T_{SLS},\ S_{ref}) = (39{,}000\ lb,\ 2350\ ft^2)$.

6.1.6 Comparison between a Wide-Body Model and a BWB Model

Compared to the BWB model, the wide-body model has been sized in more constructive method. The confidence level of the preliminary sizing results for the wide-body model is higher than the results for the BWB model. With the wide-body concept, we have been

able to resolve the emergency egress issue and increase the number of windows. However, this concept must sacrifice some aerodynamic efficiency due to the drag on the fuselage even though the shape of the fuselage is an airfoil. In order to compare the aerodynamic characteristics between the two concepts, we need to carry out wind tunnel tests and fluid dynamic computations.

6.2 Future Work

6.2.1 Improving Accuracy of Preliminary Sizing Method

We made an example preliminary sizing for the Boeing 777 model and compared the results to the documented performance characteristics of this model in Chapter 2 and Chapter 3. Through this example, we saw a fluctuation of uncertainty in the results, where the statistical estimations of thrust and wing area are underestimated and the trade study estimations of those parameters are overestimated. Since our formulas that were used in the preliminary sizing were established based on historical data, we recognize the source of the uncertainty in our method is the inaccuracy of the data. For example, the takeoff weight and empty weight of the Boeing 777, which were obtained from [11], are the standard information. These weights vary with each airline due to their own business practices. Thus we could reduce the uncertainty in our formulas by improving the accuracy of the data.

The second source of uncertainty is the flight mission. In our calculation, we assumed the flight mission in Fig. 2.6 is the typical mission and applied to all commercial aircraft. However, each aircraft has its own designated flight mission based on the needs of the market. Moreover, the statistical fuel consumptions in Table 2.2, which were obtained from [8], are not verified. They could be inaccurate for all commercial aircraft. This source of uncertainty is inevitable since the flight mission is a design requirement rather than a standard scheme. The designers are not constrained to any particular flight mission.

The third source of uncertainty is the calculation of the time to climb. We know that aircraft climb and accelerate simultaneously in reality. Therefore, we must integrate Eq. (3.9) in order to estimate the time to climb accurately. In the future, we need to obtain the typical rate of climb and the acceleration of the majority commercial aircraft to integrate Eq. (3.9). In addition, knowing a more detailed climb path will also increase the accuracy in estimating the time to climb.

6.2.2 Build and Test the Wide-Boy Model in a Wind Tunnel

As we mentioned earlier, we need to test the design model in wind tunnel to verify the preliminary sizing results. It is important to obtain the aerodynamic characteristics of a new model before proceeding to the detailed design. The results of the conceptual design provide enough details of the vehicle to build its wind tunnel model. Alternatively, the designers can use computational fluid dynamics to obtain and to optimize the aircraft. Along with the aerodynamics, the structural designers can use the conceptual model to design the airframe and estimate the structural weight more realistically. Once these two tasks are done, building a wind tunnel model based the results of these tasks will provide us a more accurate model and hence better test results.

6.2.3 Further Study in Engine Placement

In future study, we should make a deeper analysis of engine placement. It would be a meaningful analysis on how the position of the engine affects its efficiency, noise level, and overall aerodynamics of the vehicle. We also would like to know whether a turbofan is our ultimate propulsion system.

6.2.4 Develop Iteration Method for Detailed Design

Lastly, we need to develop a method to iterate the calculation after having the aerodynamic coefficients and the structural weight of the vehicle updated. We need further analysis on the model's performance to determine the sensitivity of the aerodynamics of the vehicle. Ultimately, we want to know how to improve the aircraft' performance through improving its aerodynamic efficiency and flight trajectory.

Bibliography

1. Liebeck, R. H., "Design of the Blended Wing Body Subsonic Transport," *Journal of Aircraft*, Vol. 41, Jan. 2004, pp. 10 – 15.
2. Anderson, John D. Jr., *Aircraft Performance and Design*, McGraw-Hill, New York, NY, 1999.
3. Reuters/Airbus (2007, October 15). A380 by the numbers. USA Today. Retrieved April 26, 2012 from http://www.usatoday.com/travel/flights/2007-10-15-airbus-a380-facts_N.htm#uslPageReturn.
4. Gates, D. (2011, September 24). Boeing celebrates 787 delivery as program's costs top $32 billion. The Seattle Times. Retrieved April 26, 2012 from http://seattletimes.nwsource.com/html/businesstechnology/2016310102_boeing25.
5. Airliners Network, "Aircraft Technical Data and Specifications," Demand Media, Inc., Retrieved November 12, 2010 from http://www.airliners.net/aircraft-data.
6. FAA Regulations: Title 14 – Aeronautics and Space: Chapter I – Federal Aviation Administration, Department of Transportation, Part 25: Airworthiness Standards: Transport Category Airplanes, e-CFR, GPO Access, Retrieved May 20, 2011 from http://www.faa.gov/regulations_policies/faa_regulations.
7. Gleim, Irvin N., *FAR/AIM: Federal Aviation Regulation and Aeronautical Information Manual*, 2004 ed., Gleim Publications, Inc., Gainesville, FL, 2003.
8. Raymer, Daniel P., *Aircraft Design: A Conceptual Approach*, 4th ed., AIAA Education Series, Reston, VA, 2006.
9. Svoboda, Charlie, "Turbofan engine database as a preliminary design tool," *Aircraft Design* 3 (2000): 17 – 31.
10. Jenkinson, Lloyd R., Paul Simpkin, and Darren Rhodes, *Civil Jet Aircraft Design*, AIAA Education Series, Reston, VA, 1999. Retrieved September 15, 2011 from http://www.elsevierdirect.com/companions/9780340741528/appendices/default.html.

11. Boeing Commercial Airplanes, "777-200LR/-300ER/-Freighter Airplane Characteristic for Airport Planning: Airplane Description – Model 777-300ER General Dimensions," Boeing, 2009. Retrieved November 18, 2010 from http://www.boeing.com/commercial/-airports/acaps/777_2lr3er.pdf.
12. Jane's Information Group, *Jane's All the World's Aircraft 2003-2004*, 94th ed., Sampson Low, Marston & Co., London, UK, 2003.
13. Mair, W. Austyn and David L. Birdall, *Aircraft Performance*, Cambridge University Press, New York, NY, 1992.
14. Jenkinson, Lloyd R., Paul Simpkin, and Darren Rhodes, *Civil Jet Aircraft Design*, AIAA Education Series, Reston, VA, 1999.
15. Anderson, John D. Jr., *Introduction to Flight*, 5th ed., McGraw-Hill, New York, NY, 2005.
16. Boeing Commercial Airplanes, "777-200/-300 Airplane Characteristic for Airport Planning: Airplane Description," Boeing, 1998. Retrieved November 18, 2010 from http://www.boeing.com/commercial/airports/acaps/777_2lr3er.pdf.
17. UIUC Applied Aerodynamics Group: UIUC Airfoil Coordinates Database, Retrieved February 7, 2011 from http://www.aeillinois.edu/m-selig/ads/coord_database.html.
18. World of Krauss: Airfoil Investigation Database, Retrieved February 7, 2011 from http://www.worldofkrauss.com/foils/list.
19. Martin Hepperle Aerotools: JavaFoil – Analysis of Airfoils, Retrieved February 7, 2011 from http://www.mh-aerotools.de/airfoils/javafoil.htm.
20. United States Air Forces Scientific Advisory Board Study Committee, *Technology Options for Improved Air Vehicle Fuel Efficiency: Executive Summary and Annotated Brief*, SAB-TR-06-04, May 2006, Defense Technical Information Center, Retrieved February 23, 2012 from http://handle.dtic.mil-/100.2/ADA456127.
21. Boeing Commercial Airplanes, "757-200/300 Airplane Characteristic for Airport Planning: Airplane Description – Model 777-200 General Dimensions," Boeing, 2002. Retrieved March 10, 2012 from http://www.boeing.com/commercial/-airports/acaps/757_23.pdf.

22. Pope, A., *Basic Wing and Airfoil Theory*, Dover Publications, Inc., Mineola, NY, 2009 (originally published: McGraw-Hill, New York, 1951).
23. Kuethe, A. M. and Chow, C. Y., *Foundations of Aerodynamics: Bases of Aerodynamic Design*, 5th ed., John Wiley & Sons, New York, NY, 1998.
24. Glauert, H., *The Elements of Aerofoil and Airscrew Theory*, 2nd ed., Cambridge University Press, New York, NY, 1959.
25. Loftin, L. K., Jr., "Subsonic Aircraft: Evolution and the Matching of Size to Performance," NASA Reference Publication 1060, 1980.
26. Pepper, R. S., Dam, C. P., and Gelhausen, P. A.: "Design Methodology for High-Lift Systems on Subsonic Transport Aircraft," AIAA Paper 96-4056-CP, September 1996.
27. Lowry, J. G. and Polhamus, E. C., "A Method for Predicting Lift Increments Due to Flap Deflection at Low Angle of Attack in Incompressible Flow," NACA-TN-3911, 1957.
28. Riegels, F. W., *Aerofoil Sections: Results from Wind-Tunnel Investigations, Theoretical Foundations*, Butterworths, Inc., London, England, 1961.
29. Abbott, I. H. and Doenhoff, A. E., *Theory of Wing Sections*, Dover Publications, Inc., New York, New York, 1959.
30. Stinton, D., *The Design of the Airplane*, 2nd ed., AIAA, Reston, VA, 2001.
31. Weick, F. E. and Platt, R.C., "Wind-Tunnel Tests of the Fowler Variable-Area Wing," NACA-TN-419, 1932.
32. Wenzinger, C. J. and Shortal, J. A., "The Aerodynamic Characteristics of a Slotted Clark Y Wing as Affected by the Auxiliary Airfoil Position," NACA-TR-400, 1931.
33. Weick, F. E. and Platt, R. C., "Wind-Tunnel Tests on Model Wing with Fowler Flap and Specially Developed Leading-Edge Slot," NACA-TN-459, 1933.
34. Lowry, J. G., "Wind-Tunnel Investigation of an NACA 23012 Airfoil with Several Arrangements of Slotted Flaps with Extended Lips," NACA-TN-808, 1941.
35. Wentz, W. H. Jr. and Seetharam, H.C., "Development of a Fowler Flap System for a High Performance General Aviation Airfoil," NASA-CR-2443, 1974.

36. Wentz, W. H. Jr., “Wind Tunnel Tests of the GA(W) – 2 Airfoil with 20% Aileron, 25% Slotted Flap, 30% Fowler Flap, and 10% Slot-Lip Spoiler” NASA-CR-145139, 1977.
37. Schuldenfrei, M. J., “Wind-Tunnel Investigation of an NACA 23012 Airfoil with a Handley Page Slat and Two Flap Arrangements,” NACA-WRL-261, 1942.
38. Quinn, J. H. Jr., “Tests of the NACA 64_1A212 Airfoil Section with a Slat, a Double Slotted Flap, and Boundary Layer control by Suction,” NACA-TN-1293, 1947.
39. Axelson, J. A. and Stevens, G. L., “Investigation of a Slat in Several Different Positions on an NACA 64A010 Airfoil for a Wide Range of Subsonic Mach Numbers,” NACA-TN-3129, 1954.
40. Oswald, W. B., “General Formulas and Charts for the Calculation of Airplane Performance,” NACA-TR-408, 1932.

Appendix A. Derivation of Formula to Estimate Required Maximum Lift-to-Drag Ratio

Let us begin to formulate an equation to estimate the maximum aerodynamic efficiency for a typical flight mission in Fig. 2.6. Based on Eq. (2.10), the weight fraction of the weight at the end of the main fight mission, W_6, to the weight at the beginning of the flight mission, W_0, is given by:

$$\frac{W_6}{W_0} = \frac{W_1}{W_0}\frac{W_2}{W_1}\frac{W_3}{W_2}\frac{W_4}{W_3}\frac{W_5}{W_4}\frac{W_6}{W_5} \tag{A.1}$$

In this equation only $\frac{W_3}{W_2}$ and $\frac{W_5}{W_4}$ are depended on the maximum aerodynamic efficiency. Thus we can rearrange Eq. (A.1) in to the following form:

$$\frac{\frac{W_6}{W_0}}{\left(\frac{W_1}{W_0}\right)\left(\frac{W_2}{W_1}\right)\left(\frac{W_4}{W_3}\right)\left(\frac{W_6}{W_5}\right)} = \frac{W_3}{W_2}\frac{W_5}{W_4} \tag{A.2}$$

Let denote the left hand side of Eq. (A.2) as Ψ and substitute the expressions of $\frac{W_3}{W_2}$ and $\frac{W_5}{W_4}$ into Eq. (A.2). We obtained two new equations:

$$\Psi = \frac{\frac{W_6}{W_0}}{\left(\frac{W_1}{W_0}\right)\left(\frac{W_2}{W_1}\right)\left(\frac{W_4}{W_3}\right)\left(\frac{W_6}{W_5}\right)} \tag{A.3a}$$

$$\Psi = exp\left[-\frac{R_a C_{t\_crs}}{V_{crs}\frac{L}{D}\Big|_{max}} - \frac{E_i C_{t\_tk}}{\frac{L}{D}\Big|_{max}}\right] \tag{A.3b}$$

Taking the natural log on both sides of Eq. (A.3b), collecting $\frac{L}{D}\Big|_{max}$ term, and performing some algebra operations, we have the formula for the maximum aerodynamic efficiency:

$$\frac{L}{D}\Big|_{max} = -\frac{1}{\ln \Psi}\left(\frac{R_a C_{t\_crs}}{V_{crs}} + E_i C_{t\_tk}\right) \tag{A.4}$$

Appendix B. Derivation of Air Density Ratio Function in the Standard Atmosphere

There are two main regions in the atmosphere where the commercial aircraft often operates. In the first region (from sea level to 36,000 ft), the air temperature varies with altitude. Thus the governing equation is in term of temperature, that is:

$$\frac{\rho}{\rho_0} = \left(\frac{T}{T_0}\right)^{-\left(\frac{g_0}{aR}+1\right)} \tag{B.1}$$

And the temperature profile is a linear function of altitude.

$$T = T_0 + a(h - h_0) \tag{B.2}$$

where

$T_0 = 288.16° K$	sea level atmospheric temperature
$h_0 = 0\, m$	sea level altitude
$g_0 = 9.8\ \frac{m}{s^2}$	gravitational acceleration at sea level
$R = 287\ \frac{J}{kg \cdot K}$	universal gas constant
$a = -6.5 \times 10^{-3}\ \frac{^\circ K}{m}$	rate of change of temperature w.r.t. altitude
$\rho_0 = \rho_{sl} = 1.225\ \frac{kg}{m^3}$	sea level air density

Combining Eq. (B.1) and Eq. (B.2), we establish the air density ratio in the troposphere in the following form:

$$\sigma_1(h) = \frac{\rho}{\rho_{sl}} = \left[1 + \frac{a}{T_0}(h - h_0)\right]^{-\left(\frac{g_0}{aR}+1\right)} \tag{B.3}$$

Replacing the numerical values and simplifying Eq. (B.3) yields an approximated short form of the air density function as:

$$\sigma_1(h) \approx \left[1 - \left(2.256 \times 10^{-5} \frac{1}{m}\right) h\right]^{4.25} \tag{B.4}$$

In the English unit system:

$$\sigma_1(h) \approx \left[1 - \left(6.875 \times 10^{-6} \frac{1}{ft}\right) h\right]^{4.25} \tag{B.5}$$

In the second region (from 36,000 ft to 82,000 ft) the air temperature stays constant as we increase the altitude. Thus the air density ratio formula is different from that in the troposphere. Note that the atmospheric layer assignment that is discussed in this document is based on the 1976 standard atmosphere. Today, the atmosphere could be a lot different from the atmosphere in 1976 due to the change in the natural environment and the effects of human activities.

$$\frac{\rho}{\rho_1} = e^{-\frac{g_0}{RT}(h - h_1)} \tag{B.6}$$

where

$h_1 = 36{,}000\ ft$	stratosphere initial altitude
$T = 216.66\ °K = const$	stratosphere temperature (constant)
$\rho_1 = \rho_{sl}\sigma_1(h_1)$	stratosphere initial air density

We can write the air density at an altitude h in the stratosphere to the sea level air density ratio as a function of altitude as:

$$\sigma_2(h) = \frac{\rho}{\rho_{sl}} \approx 0.298 \times e^{\left[1.729 - \left(4.804 \times 10^{-5} \frac{1}{ft}\right) h\right]} \tag{B.7}$$

Appendix C. Aerodynamics of a Finite Wing

C.1 Introduction

When searching for an airfoil in an airfoil database, the information about that airfoil are the aerodynamic characteristics in two-dimensional flow. In reality, the streams of air that flow over a wing are always three-dimensional. In designing a wing for an aircraft, the three-dimensional aerodynamics of an airfoil is more useful. This discussion shows how to convert the aerodynamic coefficients of an infinite wing to the aerodynamic coefficients of a finite wing.

In a three-dimensional flow, beside generating lift and drag on the wing, the air flow also creates circulatory vortices at both ends of the wing. These vortices trail behind the wing and trace out U-shape vortex filaments. Aerodynamicists can calculate the lift and drag of a finite wing by combining the Prandtl lifting-line theory and the Helmoltz vortex laws [22]. In addition, these vortices also cause a downward velocity which is often called a downwash [23]. This downwash produces two additional aerodynamic quantities: induced angle of attack and induced drag. These two quantities are functions of the vortex strength and the geometry of the wing. The Biot-Savart law is the main tool for calculating the vortex strength. These theories and laws are not the subjects of our discussion. Thus, we will not explain them in detail. Rather, we will combine and rearrange the main points of these laws and methods into a coherent procedure to calculate the aerodynamic characteristics of a wing based on the aerodynamic profiles of its airfoil. Readers can find detailed discussions on this subject from [22] and [23].

C.2 Finite Wing Aerodynamics

The lift coefficient curve of a general airfoil is estimated by using the thin-airfoil theory. Disregarding the type of the airfoil, the lift coefficient curve (short name: lift curve) is constituted by two segments: a linear segment and a non-linear segment. The main purpose of this procedure is to transform the linear segment of the lift curve of an airfoil

into the linear segment of the lift curve of a wing. Figure C.1 graphically depicts the process which transforms the lift curve with slope a_o to the lift curve with slope a.

Thin-airfoil theory formulates the lift curve of an airfoil as a linear relation with the effective angle of attack α_o through a slope a_o.

$$C_l = a_o \alpha_o \tag{C.1}$$

If we take this airfoil to make an infinite-span wing, the wing would generate a higher lift coefficient $a_o \alpha_a$. However, a finite-span wing is more realistic than the infinite-span wing. The linear lift curve of a finite-span wing is predicted as a function of the absolute angle of attack α_a and the modified slope a.

$$C_L = a \alpha_a \tag{C.2}$$

Figure C.1 illustrates that the slope a is smaller than the slope a_o. In order to achieve the same lift coefficient as the airfoil does; the wing is required to pitch up by an extra angle of attack. This extra angle of attack is the difference between the absolute angle and the effective angle. It is often called the induced angle of attack. The following sections will discuss the derivation for the induced angle of attack and the modification of slope a_o to yield an appropriate estimation of slope a.

C.3 Incidence Angles

So far, we have already mentioned three different incidence angles. Before going to further discussion, we want to graphically describe these different incidence angles by introducing the cross-sectional view of a finite-span wing, which is shown in Fig. C.2. The angle α_{Lo} is the zero-lift angle. It is the angle at which the airfoil does not generate lift. In general this angle is negative for a positive cambered airfoil and zero for a symmetrical airfoil (un-cambered airfoil). The geometrical angle α is the angle between the flight path (direction of the free stream velocity) and the chord line of the airfoil.

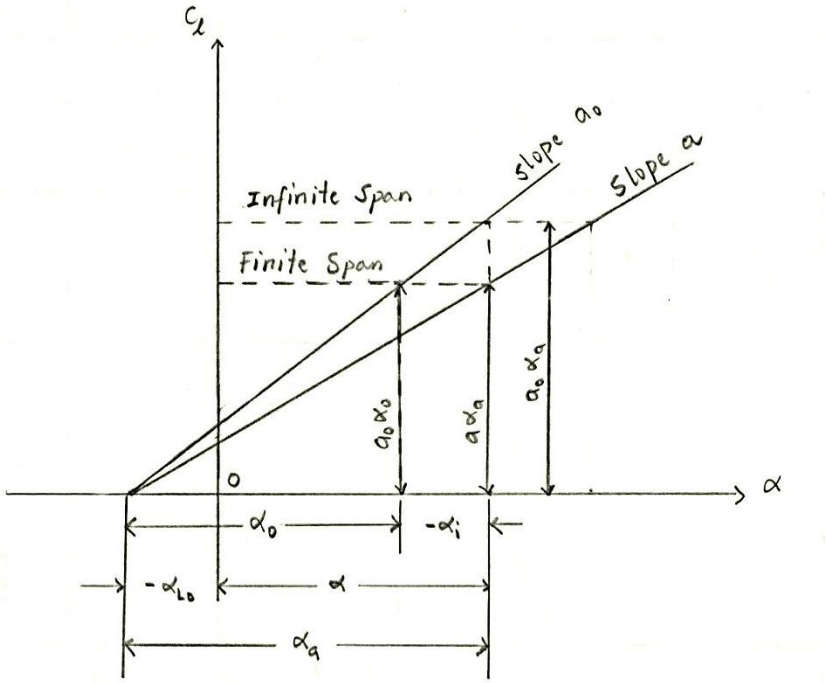

Figure C.1: Comparison of airfoil lift curve and wing lift curve.

The trailing vortex sheet behind the wing generates a downward velocity locally along the wing span. This velocity varies throughout the wing, whereas its maximum magnitude occurs at the wing tip and its minimum magnitude is found at the mid-span position. At a spanwise location on the wing this downward velocity alters the velocity field around the wing by combining with the free-stream velocity to create a relative velocity. In a three-dimensional flow the wing's airfoil actually experiences this relative wind rather than the free-stream wind. An angle between the flight path and the relative wind direction is defined as an induced angle of attack α_i. The effective angle of attack α_o is measured from the zero-lift line to the relative wind direction.

The absolute angle of incidence is defined as the sum of the effective angle and the induced angle. The relation among these incidence angles can be mathematically expressed in the following fashion:

$$\alpha_a = \alpha_o - \alpha_i \tag{C.3}$$

where $\alpha_i(y) = tan^{-1}\left[-\frac{w(y)}{V_\infty}\right]$.

In most cases the induced velocity is found very small relative to the free-stream velocity. The Taylor's series expansion on the arctangent for a small angle around the zero neighborhoods gives an approximation for the induced angle:

$$\alpha_i(y) \cong -\frac{w(y)}{V_\infty} \quad \text{for} \quad \frac{w(y)}{V_\infty} \ll 1 \tag{C.4}$$

Therefore, the expression of the absolute angle of attack can be rewritten in terms of the induced velocity, free-stream velocity, and the effective angle of attack.

$$\alpha_a \cong \alpha_o + \frac{w(y)}{V_\infty} \tag{C.5}$$

Surprisingly the most convenient approach in deriving an expression for the induced angle of attack is through the lift equation of the wing and the incidence angles relation. The following derivation will shows us a complete modification on a_o in order to obtain a. A three-dimensional view of a wing in a steady flow is shown in Fig. C.3. The Kutta-Joukowski theory of lift [22] for a three-dimensional wing with a finite span b and a spanwise circulation distribution $\Gamma(y)$ is given by:

$$L = \rho V_\infty \int_{-b/2}^{b/2} \Gamma(y) dy \tag{C.6}$$

where $\rho =$ free stream air density; $V_\infty =$ the free stream air velocity.

In order to evaluate the integral in Eq. (C.6), we must know the formula of $\Gamma(y)$. The simplest form of the circulation is the elliptic distribution. However, this type of distribution is often referred to the ideal case because it is difficult to design a wing platform in order to acquire an elliptic circulation distribution. In contrast, the circulation is arbitrarily distributed across the span but symmetrical about the mid-span. A raw

sketch of an arbitrary spanwise distribution of circulation is presented in Fig. C.4a. Generally, any arbitrary circulation distribution can be approximated as a Fourier's series. Let the spanwise location of an infinitesimal segment of circulation is represented as a trigonometric function $y = \frac{b}{2}\cos\theta$ (see Fig. C.4b). Then differentiate y with respect to θ, we get $dy = -\frac{b}{2}\sin\theta\, d\theta$.

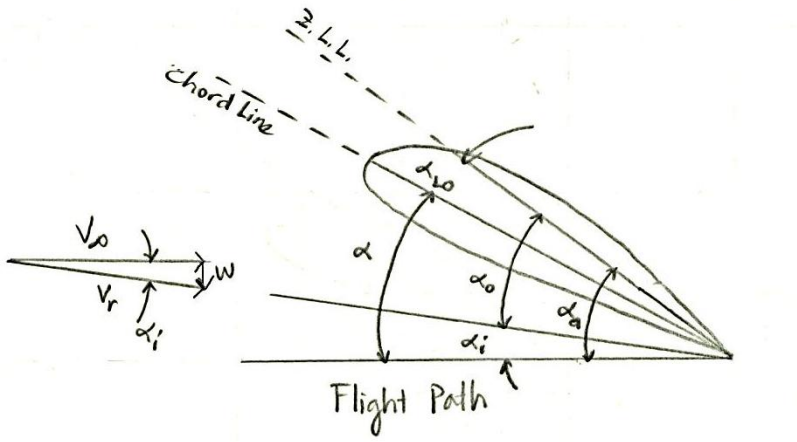

Figure C.2: Cross sectional view of a finite span wing.

The circulation distribution is a series of sine functions, that is:

$$\Gamma(\theta) = 4\frac{b}{2}V_\infty \sum_{n=1}^{\infty} A_n \sin n\theta \tag{C.7}$$

Substituting Eq. (C.7) into the lift equation (Eq. (C.6)) and changing the variable of the integral yields a new expression for lift that is evaluable.

$$L = -\rho V_\infty \int_\pi^0 4\frac{b}{2}V_\infty \sum_{n=1}^{\infty} A_n \sin n\theta \left(\frac{b}{2}\sin\theta\right) d\theta \tag{C.8}$$

which is simplified to:

$$L = \rho b^2 V_\infty^2 \int_0^\pi \sum_{n=1}^{\infty} A_n \sin n\theta \sin\theta\, d\theta \tag{C.9}$$

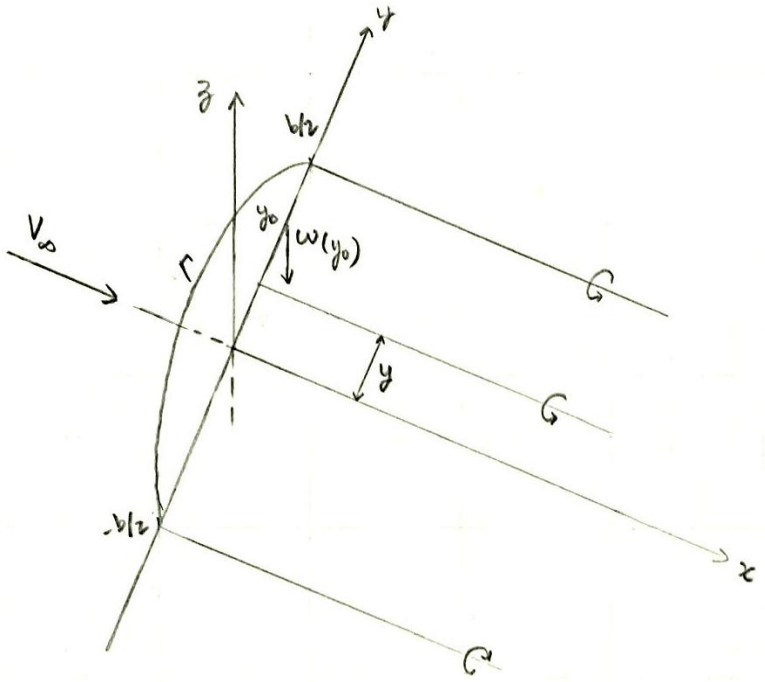

Figure C.3: Three-dimensional view of a wing in a steady flow.

The integral, $\int_0^\pi \sum_{n=1}^\infty A_n \sin n\theta \sin\theta \, d\theta = \begin{cases} \frac{\pi}{2} A_1, & n = 1 \\ 0, & \forall\, n \neq 1 \end{cases}$ vanishes for all values of n except for n equals unity. Thus the lift in Eq. (C.9) equals to:

$$L = \frac{\pi}{2} \rho b^2 V_\infty^2 A_1 \tag{C.10}$$

On the other hand, a wing whose platform area is S unit area and the lift coefficient is given by Eq. (C.2) will generate a lift:

$$L = \frac{1}{2} \rho V_\infty^2 S C_L \tag{C.11}$$

Combining Eq. (C.10) and Eq. (C.11) we obtain an expression for lift coefficient of a wing in three-dimensional flow. A wing's aspect ratio is defined as, $AR = \frac{b^2}{S}$. With this definition, we write the lift coefficient as a function of the aspect ratio and the first Fourier's series coefficient in the following form:

$$C_L = \pi A R A_1 \tag{C.12}$$

Comparing the result of lift coefficient in Eq. (C.12) to its prediction in Eq. (C.2), we see that the lift-slope of a wing is computed by:

$$a = \pi A R \frac{A_1}{\alpha_a} \tag{C.13}$$

So far we have not answered the main question on how to modify the lift-slope of an airfoil in two-dimensional flows to obtain the lift-slope of a wing that is made out of that airfoil in three-dimensional flows. The bridge that connects the two lift-slopes can be built through the relation between the incidence angles in Eq. (C.3). In Fig. C.1, the lift coefficient at the "finite span" dash line is generated by the airfoil with the a_o lift-slope through the α_o angle of attack. With the smaller lift-slope, the wing of the lift-slope a must pitch up to a higher angle of attack α_a by an extra angle $-\alpha_i$. This extra angle is the difference between:

$$\alpha_a - \alpha_o = \frac{C_L}{a} - \frac{C_l}{a_o} \tag{C.14}$$

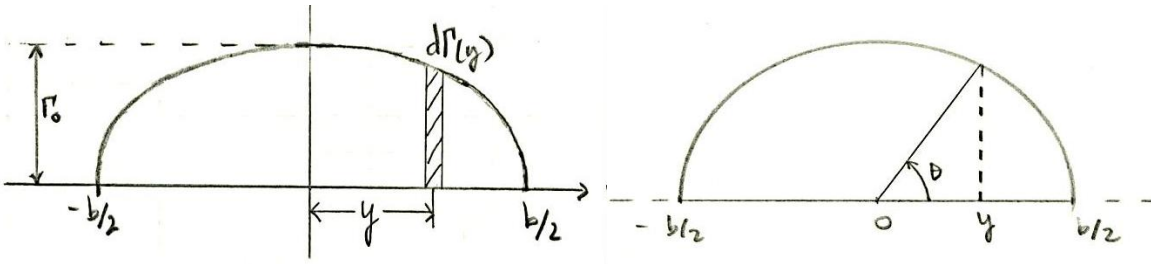

(a) **(b)**

Figure C.4: (a) Raw sketch of spanwise circulation distribution on a wing; (b) geometric function of the wing span.

Since the airfoil's lift coefficient is equal to the wing's lift coefficient, we rewrite Eq. (C.14) as:

$$\alpha_a - \alpha_o = C_L \left(\frac{1}{a} - \frac{1}{a_o}\right) \tag{C.15}$$

Substituting Eq. (C.13) into Eq. (C.15) and factoring $1/\pi AR$ out of the parentheses, we get

$$\alpha_a - \alpha_o = \frac{C_L}{\pi AR}\left(\frac{\alpha_a}{A_1} - \frac{\pi AR}{a_o}\right) \tag{C.16}$$

and by setting

$$1 + \varphi = \frac{\alpha_a}{A_1} - \frac{\pi AR}{a_o} \tag{C.17}$$

we obtain

$$\alpha_a - \alpha_o = \frac{C_L}{\pi AR}(1 + \varphi) \tag{C.18a}$$

which is equivalent to

$$\alpha_i = -\frac{C_L}{\pi AR}(1 + \varphi) \tag{C.18b}$$

Equation (C.18b) is the formula for the induced angle of a wing with an arbitrary circulation distribution. The quantity φ is referred as the induced angle factor. Generally, this quantity is small and positive. Therefore, it often tends to increase the induced angle. If all quantities in Eq. (C.17) are constant except the aspect ratio, the smaller aspect ratio wing will induce a higher angle. However, in the case where the aspect ratio is much greater than the airfoil's lift-slope the in induced angle factor will be negative. For the elliptic wing the induced angle factor will vanish.

C.4 Special Case: Induced Angle of an Elliptic Wing

The induced angle factor of an elliptic wing becomes zero for a reason. An elliptic wing is a wing whose platform can generate a spanwise lift distribution or a spanwise circulation distribution. Refer to Fig. C.4a, an elliptic circulation distribution takes in the form of a function of an ellipse:

$$\Gamma(y) = \Gamma_o \sqrt{1 - \left(\frac{2y}{b}\right)^2} \tag{C.19}$$

and

$$\frac{d\Gamma}{dy} = -\frac{\Gamma_o y}{\frac{b}{2}\sqrt{\left(\frac{b}{2}\right)^2 - y^2}} \tag{C.20}$$

Apply the circulation distribution in Eq. (C.19) to the lift equation in Eq. (C.6), then change the variable a described in Fig. C.4b, it gives:

$$L = \frac{b}{2}\rho V_\infty \Gamma_o \int_0^\pi sin^2\theta d\theta \tag{C.21}$$

Evaluate the integral, we get

$$L = \frac{\pi}{2}\frac{b}{2}\rho V_\infty \Gamma_o \tag{C.22}$$

Equate Eq. (C.22) to Eq. (C.21) and solve for the lift coefficient

$$C_L = \frac{\pi b \Gamma_o}{2SV_\infty} \tag{C.23}$$

Writing the lift coefficient in term of the wing aspect ratio, we get

$$C_L = \pi AR \frac{\Gamma_o}{2bV_\infty} \tag{C.24}$$

On the other hand, the induced angle of attack can be calculated directly through its definition that is given in Eq. (C.4). First, we calculate the magnitude of the downwash by applying the Bio-Savart law. A graphical illustration of the downwash calculation due to an infinitesimal trailing vortex filament is shown in Fig. C.5. According to the law, an increment velocity at point y_o on the wing induced by an infinitesimal element of circulation filament $d\Gamma$ at point (x, y) is given by:

$$dw(y_o, y) = \frac{d\Gamma}{4\pi}\frac{\cos\beta\, dx}{r^2} \tag{C.25}$$

The downwash at location y induced by the entire filament is computed by the integration:

$$w(y_o, y) = \frac{d\Gamma}{4\pi}\int_0^{\infty} \frac{\cos\beta\, dx}{r^2} \tag{C.26}$$

$$r = (y_o - y)\sec\beta\ ;\ \ x = (y_o - y)\tan\beta\ ;\ \ dx = (y_o - y)\sec^2\beta\, d\beta \tag{C.27}$$

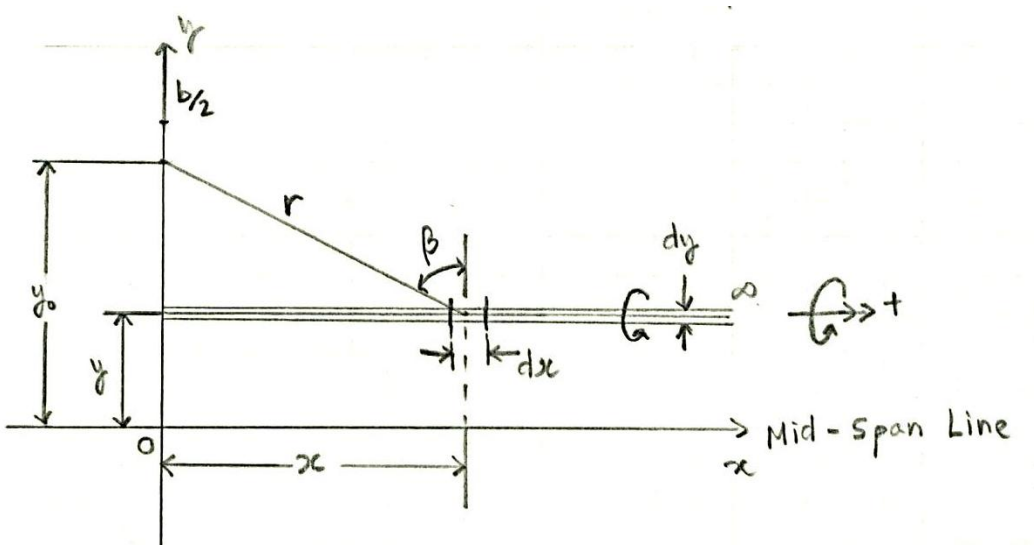

Figure C.5: Influence of a trailing vortex filament on a point of a wing.

That is:

$$w(y_o, y) = \frac{d\Gamma}{4\pi}\int_0^{\pi/2} \frac{\cos\beta\, d\beta}{(y_o - y)} = \frac{d\Gamma}{4\pi}\frac{1}{(y_o - y)} \tag{C.28}$$

Plugging Eq. (C.28) into Eq. (C.4) produces the induced angle on the wing at y_o due to a circulation filament $d\Gamma$ at y.

$$\alpha_i(y_o, y) = -\frac{d\Gamma}{4\pi}\frac{1}{(y_o - y)}\frac{1}{V_\infty} \tag{C.29}$$

The downwash angle at y_o induced by the entire trailing vortex sheet is calculated by taking the integral:

$$\alpha_i(y_o) = -\frac{1}{4\pi V_\infty}\int_{-b/2}^{b/2}\frac{d\Gamma/dy}{y_o - y}dy \tag{C.30}$$

Insert Eq. (C.20) into Eq. (C.30) and complete the integration through variable transformation in Fig. C.4b:

$$\alpha_i(y_o) = \frac{\Gamma_o}{2\pi b V_\infty}\int_{-b/2}^{b/2}\frac{y}{(y_o - y)\sqrt{\left(\frac{b}{2}\right)^2 - y^2}}dy \tag{C.31}$$

for

$$y = \frac{b}{2}\cos\theta\ ; \quad y_o = \frac{b}{2}\cos\theta_o\ ; \quad dy = -\frac{b}{2}\sin\theta\ d\theta \tag{C.32}$$

we get

$$\alpha_i(\theta_o) = \frac{\Gamma_o}{2\pi b V_\infty}\int_0^\pi \frac{\cos\theta}{\cos\theta_o - \cos\theta}d\theta \tag{C.33}$$

The integration of $\int_0^\pi \frac{\cos\theta}{\cos\theta_o - \cos\theta}d\theta = -\pi$ can be found in [22 – p. 286] or in [24 – p.92]. Both approaches yielded the same result even though they were carried out differently. Thus the induced angle of attack is:

$$\alpha_i(\theta_o) = -\frac{\Gamma_o}{2bV_\infty} \tag{C.34}$$

The expression for the induced angle in Eq. (C.34) shows that the induced angle of an elliptic wing is constant throughout the wing's span. Now, we write Eq. (C.34) in term of the lift coefficient and the aspect ratio by solving Eq. (C.24) for $\frac{\Gamma_o}{2bV_\infty}$ and substitute this expression into Eq. (C.34). It gives us a new expression for the induced angle of attack:

$$\alpha_i = -\frac{C_L}{\pi AR} \tag{C.35}$$

Comparison between Eq. (C.35) to Eq. (C.18b) indicates that the induced angle correction factor does not exist in case of elliptic wing. The cause of difference is that the induced angle of an arbitrary wing varies across the wing's span while the in the case of elliptic wing, it stays constant. The variation of the induced angle in an arbitrary wing is characterized by φ in which the Fourier series coefficient A_1 and the wing aspect ratio are the key drivers. The following section will describe the variation through the determination of the Fourier series coefficients.

C.5 Fourier's Series Coefficients Determination

The induced velocity that is generated by any arbitrary circulation distribution $\Gamma(y)$ can be calculated by employing the Bio-Savart law. The calculation is depicted in Fig. C.3, which is expressed as an integral in mathematical language.

$$w(y_1) = \frac{1}{4\pi} \int_{-b/2}^{b/2} \frac{\frac{d\Gamma}{dy} dy}{y_1 - y} \tag{C.36}$$

If the circulation is distributed as Eq. (C.7), its spanwise rate of change is determined by differential rule:

$$\frac{d\Gamma}{d\theta} = 4\frac{b}{2} V_\infty \sum_{n=1}^{\infty} n A_n \cos n\theta \tag{C.37}$$

Following by the transformation of the integral in Eq. (C.36), it yields

$$w(\theta_1) = \frac{1}{4\pi} \int_{\pi}^{0} \frac{\frac{d\Gamma}{d\theta} d\theta}{y_1 - y} = \frac{V_\infty}{\pi} \int_0^{\pi} \frac{\sum_{n=1}^{\infty} n A_n \cos n\theta}{\cos\theta - \cos\theta_1} d\theta \tag{C.38}$$

By the method in [24 – p.92], it is shown that

$$\int_0^{\pi} \frac{\cos n\theta}{\cos\theta - \cos\theta_1} d\theta = \pi \frac{\sin n\theta_1}{\sin\theta_1} \tag{C.39}$$

where θ_1 is a constant that represents any arbitrary spanwise location on the lift line of a wing. Thus at any point θ on the wing, a general expression for the induced velocity is given by:

$$w(\theta) = \frac{V_\infty}{\sin\theta}\sum_{n=1}^{\infty} nA_n \sin n\theta \tag{C.40}$$

Now, the Kutta-Joukowski theorem of lift can be applied for the same wing to find the lift that is generated by the same circulation. That is the short form of lift equation given by Eq. (C.6)

$$L = \rho V_\infty b\Gamma(\theta) \tag{C.41}$$

By equating Eq. (C.41) and Eq. (C.11) gives us an alternative expression for the circulation

$$\Gamma(\theta) = \frac{1}{2}V_\infty \frac{S}{b}C_L \tag{C.42}$$

If a particular lift coefficient of the wing is determined as the "finite span" dash line in Fig. C.1, it could alternative be measured by

$$C_L = a_o\alpha_o \tag{C.43}$$

then upon substitution Eq.(C.5) into α_o we obtain

$$\Gamma(\theta) = \frac{1}{2}V_\infty \frac{S}{b}\left(\alpha_a - \frac{w(\theta)}{V_\infty}\right) = \frac{1}{2}V_\infty \frac{S}{b}\left(\alpha_a - \frac{\sum_{n=1}^{\infty} nA_n \sin n\theta}{\sin\theta}\right) \tag{C.44}$$

However, the circulation $\Gamma(\theta)$ is originally defined by Eq. (C.7). Thus from replacing the left hand side of Eq. (C.44) by Eq. (C.7) and carrying out some algebra manipulations, we will find

$$\sum_{n=1}^{\infty} A_n \sin n\theta \left(n\frac{a_o}{4}\frac{S}{b^2} + \sin\theta\right) = \frac{a_o}{4}\frac{S}{b^2}\alpha_a \sin\theta \tag{C.45}$$

by setting

$$\mu = \frac{a_o}{4}\frac{S}{b^2} \qquad \text{or in terms of the aspect ratio} \qquad \mu = \frac{a_o}{4AR} \tag{C.46}$$

we get

$$\sum_{n=1}^{\infty} A_n \sin n\theta \,(n\mu + \sin\theta) = \mu\alpha_a \sin\theta \tag{C.47}$$

Equation (C.47) is called the monoplane wing fundamental equation [24]. It is the tool for determining the Fourier series coefficient A_n. The higher value of n will yield the better approximation of the circulation distribution on the wing. In fact, increasing the value of n is equivalent to decreasing the value of θ. That is to divide a finite wing into many small segments and produce excessive number of data points. Harvesting more data points will help us establish a more accurate fit curve. Of course, the number of computations will also increase. Nonetheless, the value of A_n decreases rapidly as its index increases. A typical set of the first four terms in the series is often recommended for a symmetrical wing about its mid-span. Thus, the common expansion of Eq. (C.47) is in the following form:

$$\frac{A_1}{\alpha_a}\sin\theta(\mu + sin\,\theta) + \frac{A_3}{\alpha_a}\sin 3\theta(3\mu + sin\,\theta) + \frac{A_5}{\alpha_a}\sin 5\theta(5\mu + sin\,\theta) \ldots$$

$$\ldots + \frac{A_7}{\alpha_a} sin\,7\theta(7\mu + sin\,\theta) = \mu sin\,\theta \tag{C.48}$$

where $\theta = \left[\frac{\pi}{8}, \frac{\pi}{4}, \frac{3\pi}{8}, \frac{\pi}{2}\right]$.

Once the coefficient $\frac{A_1}{\alpha_a}$ is determined, the induced angle factor is calculated by using Eq. (C.17). Note that for a particular μ (the combination of the airfoil and the wing geometry), φ can be negative for an arbitrary circulation distribution. The expression of μ in term of wing aspect ratio is only valid for a straight rectangular wing. In this case, for a given aspect ratio μ is a constant. However, for a taper wing μ varies along the wing

span. Therefore, a more general formula of μ is necessary and is derived in the next section.

C.6 Fourier's Series Coefficients of a Tapered Wing

Let consider a rectangular whose airfoil has a chord length c has a wing span of b unit length. The wing platform area is the product of wing span and the airfoil's chord length, $S = bc$. Then μ is written in term of the chord length

$$\mu = \frac{a_o}{4}\frac{c}{b} \tag{C.49}$$

Now consider a taper wing whose taper ratio is the ratio of tip chord length to the mid-span chord length, $= \frac{c_t}{c_r}$, has a wing span b and the mid-span chord (root chord) length c_o. The distinction between the taper wing and the rectangular wing is that the chord length varies along the wing span. The sketch of a typical taper wing and the graphical representation of the local chord's calculation are illustrated in Fig. C.6. At a particular local span position, the wing chord length $c(y)$ is determined by:

$$c(y) = \lambda c_o + x \tag{C.50}$$

The portion x of the local chord length is determined by applying the triangle similarity rule to the upper triangles above the λc_o dash line. The rule states

$$\frac{x}{(1-\lambda)c_o} = \frac{\frac{b}{2} - y}{\frac{b}{2}} \tag{C.51}$$

Using the trigonometric transformation for $y = \frac{b}{2}\cos\theta$ (depicted in Fig. C.4b) and solve Eq. (C.51) for x, we have

$$x = (1 - \lambda)(1 - \cos\theta)c_o \tag{C.52}$$

Substitute x into Eq. (C.50) and simplify the new equation, we obtain

$$c(\theta) = [1 - (1 - \lambda)\cos\theta]c_o \tag{C.53}$$

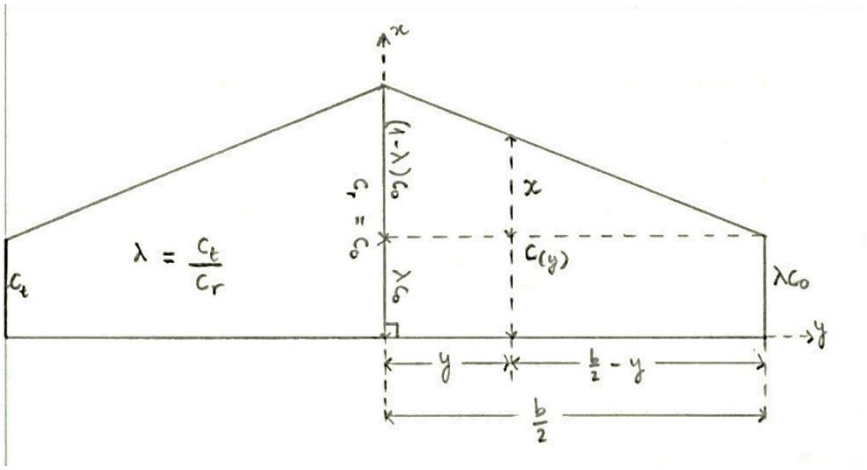

Figure C.6: Taper wing with center chord c_o, span b, and taper ratio λ.

By implementing the formula of local chord into Eq. (C.49), we write μ as a function of span angle θ in the following form:

$$\mu(\theta) = \frac{a_o}{4}\frac{c_o}{b}[1 - (1 - \lambda)\cos\theta] \tag{C.54}$$

and set

$$\mu_o = \frac{a_o}{4}\frac{c_o}{b} \tag{C.55}$$

we get

$$\mu(\theta) = \mu_o[1 - (1 - \lambda)\cos\theta] \tag{C.56}$$

Using the trapezoid area rule, the wing platform area is

$$S = \frac{b}{2}c_o(1 + \lambda) \tag{C.57}$$

Then the wing aspect ratio is

$$AR = \frac{2b}{c_o(1+\lambda)} \tag{C.58}$$

which is the transition to the final formula of μ_0

$$\mu_o = \frac{a_o}{2AR(1+\lambda)} \tag{C.59}$$

As a result, we obtain a general formula for μ in the following form

$$\mu(\theta) = \frac{a_o}{2AR(1+\lambda)}[1-(1-\lambda)\cos\theta] \tag{C.60}$$

Observing Eq. (C.60), we see that when the taper ratio is equal unity, Eq. (C.60) becomes Eq. (C.46). Since Eq. (C.60) works for both rectangular wing and taper wing, it is considered as the general equation of μ. Combining Eq. (C.47) and Eq. (C.60), we can solve for the first four terms of the Fourier series coefficients in the matrix fashion. Let $[\theta_1\ \theta_2\ \theta_3\ \theta_4] = \left[\frac{\pi}{8}\ \frac{\pi}{4}\ \frac{3\pi}{8}\ \frac{\pi}{2}\right]$, then expansion of Eq. (C.47) gives us the following set of four equations:

$$\frac{A_1}{\alpha_a}\sin\theta_1[\mu(\theta_1)+sin\ \theta_1] + \frac{A_3}{\alpha_a}\sin 3\theta_1[3\mu(\theta_1)+sin\ \theta_1] + \frac{A_5}{\alpha_a}\sin 5\theta_1[5\mu(\theta_1)+ \cdots sin\ \theta_1] + \frac{A_7}{\alpha_a}\sin 7\theta_1[7\mu(\theta_1)+sin\ \theta_1] = \mu(\theta_1)sin\ \theta_1 \tag{C.61a}$$

$$\frac{A_1}{\alpha_a}\sin\theta_2[\mu(\theta_2)+sin\ \theta_2] + \frac{A_3}{\alpha_a}\sin 3\theta_2[3\mu(\theta_2)+sin\ \theta_2] + \frac{A_5}{\alpha_a}\sin 5\theta_2[5\mu(\theta_2)+ \cdots sin\ \theta_2] + \frac{A_7}{\alpha_a}\sin 7\theta_2[7\mu(\theta_2)+sin\ \theta_2] = \mu(\theta_2)sin\ \theta_2 \tag{C.61b}$$

$$\frac{A_1}{\alpha_a}\sin\theta_3[\mu(\theta_3)+sin\ \theta_3] + \frac{A_3}{\alpha_a}\sin 3\theta_3[3\mu(\theta_3)+sin\ \theta_3] + \frac{A_5}{\alpha_a}\sin 5\theta_3[5\mu(\theta_3)+ \cdots sin\ \theta_3] + \frac{A_7}{\alpha_a}\sin 7\theta_3[7\mu(\theta_3)+sin\ \theta_3] = \mu(\theta_3)sin\ \theta_3 \tag{C.61c}$$

$$\frac{A_1}{\alpha_a}\sin\theta_4[\mu(\theta_4)+sin\ \theta_4] + \frac{A_3}{\alpha_a}\sin 3\theta_4[3\mu(\theta_4)+sin\ \theta_4] + \frac{A_5}{\alpha_a}\sin 5\theta_4[5\mu(\theta_4)+ \cdots sin\ \theta_4] + \frac{A_7}{\alpha_a}\sin 7\theta_4[7\mu(\theta_4)+sin\ \theta_4] = \mu(\theta_4)sin\ \theta_4 \tag{C.61d}$$

Converting Eqs. (C.61a – d) into a matrix form, it yields

$$\begin{bmatrix} \sin\theta_1[\mu(\theta_1)+sin\,\theta_1] & \cdots & \sin 7\theta_1[7\mu(\theta_1)+sin\,\theta_1] \\ \vdots & \ddots & \vdots \\ \sin\theta_4[\mu(\theta_4)+sin\,\theta_4] & \cdots & \sin 7\theta_4[7\mu(\theta_4)+sin\,\theta_4] \end{bmatrix} \begin{bmatrix} A_1/\alpha_a \\ A_3/\alpha_a \\ A_5/\alpha_a \\ A_7/\alpha_a \end{bmatrix} = \begin{bmatrix} \mu(\theta_1)sin\,\theta_1 \\ \mu(\theta_2)sin\,\theta_2 \\ \mu(\theta_3)sin\,\theta_3 \\ \mu(\theta_4)sin\,\theta_4 \end{bmatrix} \tag{C.62}$$

Hence the solutions are

$$\begin{bmatrix} A_1/\alpha_a \\ A_3/\alpha_a \\ A_5/\alpha_a \\ A_7/\alpha_a \end{bmatrix} = \begin{bmatrix} \sin\theta_1[\mu(\theta_1)+sin\,\theta_1] & \cdots & \sin 7\theta_1[7\mu(\theta_1)+sin\,\theta_1] \\ \vdots & \ddots & \vdots \\ \sin\theta_4[\mu(\theta_4)+sin\,\theta_4] & \cdots & \sin 7\theta_4[7\mu(\theta_4)+sin\,\theta_4] \end{bmatrix}^{-1} \begin{bmatrix} \mu(\theta_1)sin\,\theta_1 \\ \mu(\theta_2)sin\,\theta_2 \\ \mu(\theta_3)sin\,\theta_3 \\ \mu(\theta_4)sin\,\theta_4 \end{bmatrix} \tag{C.63}$$

Most standard airfoils have lift slopes $a_o \approx 2\pi$ per radian, estimated by thin airfoil theory. Fig. C.7 is a sketch of the induced angle factor varying with the taper ratio and the aspect ratio of an airfoil whose lift slope is $a_o = 2\pi$ per radian by using Eq. (C.63) and Eq. (C.17).

The results in Fig. C.7 indicate the taper $\lambda \approx 0.4$ is the common intersection of all wings in regardless of different aspect ratios. This special taper ratio separates the induced angle factors into two distinct trends. For the taper ratios $\lambda > 0.4$, the induced angle factor of the wing jumps to a higher trend as the aspect ratio increases. For a fixed aspect ratio, as the taper ratio is marching from 0.4 toward unity the induced angle factor accelerates to higher values. In this same range $[0.4, 1]$, as the taper ratio approaches unity the increasing rate of the induced angle factor jumps to a higher rate as the aspect ratio increases by one unit. For rectangular wings ($\lambda = 1$) the induced angle factor is the worst for wing with aspect ratio higher than the lift slope. Once the taper ratio begins to drop the induced angle factor begins to be diminished. Therefore, tapered wings are often found in most modern aircraft.

As the taper ratio keeps dropping from unity, when it passes the border line ($\lambda = 0.4$), the induced angle factor keeps decreasing until it reaches the minimum. If the taper ratio

keeps approaching zero, the induce angle factor will go back up. As the aspect ratio increases, the taper ratio where the minimum induced angle factor occurs will move

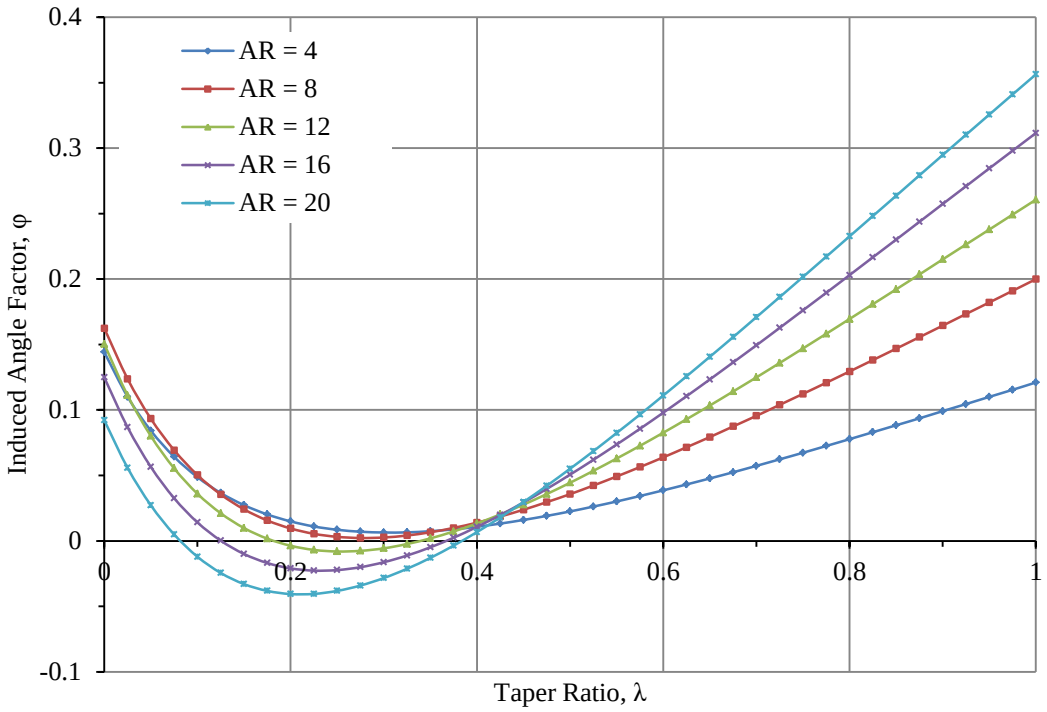

Figure C.7: Induced angle factor of an airfoil with lift slope of 2π per radian.

closer to zero, and the minimum induced angle factor will also drop rapidly. When the aspect ratio is more than 60% higher than the lift slope, the minimum induce angle factor begins to be negative. This is a skeptical point in this thesis because most published works in literature state that the induced angle factor is always small and positive. In fact, this quantity can be negative when $1 + \frac{\pi AR}{a_o} > \frac{\alpha_a}{A_1}$. Moreover, the quantity $\frac{A_1}{\alpha_a}$ is a function of $a_o,\ AR,\ \theta$, and λ. It is not easy to prove the inequality $1 + \frac{\pi AR}{a_o} > \frac{\alpha_a}{A_1}$ mathematically. We will verify this phenomenon with experimental data. We accept this result from this point of the process until the experimental stage.

C.7 Fourier's Series Coefficients of a Twisted Wing

In practice we usually encounter twisted wings in aeronautical design. If one marches along the lifting line of a twisted wing from the center of the wing to either tips of the wing, one would see the absolute angle of incidence varies. Normally, we see most wings have the tip angle of attack smaller than the root angle of attack. A special term to describe this twist fashion is call "wash-out" [24]. In aeroelasticity analysis, engineers usually employ twist, taper, and sweep features to diminish divergence and flutter effects on the wing. For example, the wing of the Cirrus SR22 aircraft has its washout from the quarter span toward both tips. In design a rotor blade for a helicopter, twisting the blade is an important aerodynamic characteristic. Twist must be carefully modeled and designed so that the rotor can achieve its optimal power coefficient and its best noise reduction. For instance, an ideal twist is the state in which the local pitch angle of the rotor's blade is constant and equal to the pitch angle at the tip of the blade. Such twist fashion will ensure a uniform radial inflow across the blade; hence the rotor can reach its optimum hovering power. Therefore, the twist effect must be considered in the estimation of wing lift.

According the method in [24], the twist model of a particular wing can be described by the flowing relation:

$$\alpha_a(\theta) = \alpha_r - \epsilon \cos\theta \tag{C.64}$$

where $\alpha_a(\theta)$ = the local absolute angle of attack

α_r = the absolute angle of attack at mid-span (root)

ϵ = geometric twist angle

θ = the span angle as described in Fig. C.4b

By substituting Eq. (C.64) into Eq. (C.47), we have

$$\sum_{n=1}^{\infty} A_n \sin n\theta \,(n\mu + \sin\theta) = \mu \sin\theta \,(\alpha_r - \epsilon \cos\theta) \tag{C.65}$$

Let denote $\mu_1 = \mu(\theta_1)$, $\mu_2 = \mu(\theta_2)$, and so forth. Then the first fours Fourier coefficients are determined by

$$\begin{bmatrix} A_1 \\ A_3 \\ A_5 \\ A_7 \end{bmatrix} = \begin{bmatrix} \sin\theta_1[\mu_1 + sin\ \theta_1] & \cdots & \sin 7\theta_1[7\mu_1 + sin\ \theta_1] \\ \vdots & \ddots & \vdots \\ \sin\theta_4[\mu_4 + sin\ \theta_4] & \cdots & \sin 7\theta_4[7\mu_4 + sin\ \theta_4] \end{bmatrix}^{-1} \begin{bmatrix} \mu_1 \sin\theta_1\,(\alpha_r - \epsilon\cos\theta_1) \\ \mu_2 \sin\theta_2\,(\alpha_r - \epsilon\cos\theta_2) \\ \mu_3 \sin\theta_3\,(\alpha_r - \epsilon\cos\theta_3) \\ \mu_4 \sin\theta_4\,(\alpha_r - \epsilon\cos\theta_4) \end{bmatrix} \tag{C.66}$$

C.8 Lift-Slope Transformation for High Aspect Ratio Wings in Incompressible Flow

Now we have all the necessary tools; we are ready to answer our question how to transform the lift curve of a two-dimensional airfoil into the lift curve of a three-dimensional wing of that same airfoil. The incidence angles relation can be transformed into the lift-slope relation through the lift coefficient relations in Eq. (C.1) and Eq. (C.2). Rearranging Eq. (C.18a) for the absolute angle of attack formula, we get:

$$\alpha_a = \alpha_o + \frac{C_L}{\pi AR}(1 + \varphi) \tag{C.67}$$

then substitute Eq. (C.1) and Eq. (C.2) for α_o and α_a into Eq. (C.67) respectively, yields

$$\frac{C_L}{a} = \frac{C_L}{a_o} + \frac{C_L}{\pi AR}(1 + \varphi) \tag{C.68}$$

By differentiating Eq. (C.68) with respect to C_L, we get

$$\frac{1}{a} = \frac{1}{a_o} + \frac{1}{\pi AR}(1 + \varphi) \qquad \text{or} \qquad a = \frac{a_o}{1 + \frac{a_o}{\pi AR}(1+\varphi)} \tag{C.69}$$

and by setting

$$\omega = \frac{1}{1+\varphi} \tag{C.70}$$

we have obtained the modification formula for the wing's lift slope as a function of its airfoil's lift slope, the wing's geometry (aspect ratio), and the induced angle correction factor in the following form:

$$a = \frac{a_o}{1 + \frac{a_o}{\pi \omega AR}} \tag{C.71}$$

The limitation of Eq. (C.71) is that it is only valid for the high aspect ratio wings. It does not work well for a wing whose aspect ratio is less than C. Beside the aspect ratio condition, the formula can be applied only for un-swept and untwisted wings in incompressible flows. The corrections for these cases will be discussed in following sections.

C.9 Lift-Slope Transformation for High Aspect Ratio Wings in Subsonic Compressible Flow

When an airfoil travels in the air with a speed greater than Mach 0.3, the air around it will be compressed. When the air density is under compression, it causes the flow to be non-uniform. By using the concept of perturbation potential, aerodynamicists are able to characterize this complicated air dynamic around an airfoil. The Prandtl-Glauert law for transforming a two-dimensional compressible flow into an equivalent incompressible flow [23] can summarized in the following calculation. If a perturbation potential ϕ around an airfoil in a two-dimensional compressible flow at Mach number M_∞ can be written as:

$$\beta^2 \phi_{xx} + \phi_{yy} = 0 \quad \text{where } \beta = \sqrt{1 - M_\infty^2} \tag{C.72}$$

Then the air pressure distributions on the surfaces of the airfoil are given by:

$$C_p = \frac{C_{po}}{\beta} \tag{C.73}$$

where C_{po} is the air pressure distributions on the surfaces of this same airfoil in the incompressible flow. The lift coefficient of the airfoil is the integration of the difference in pressure distributions between the lower surface and the upper surface of the airfoil across the chord line. In the non-dimensional form it is:

$$C_l = \int_0^1 (C_{p_L} - C_{p_U}) d\frac{x}{c} \tag{C.74}$$

Therefore,

$$C_l = \frac{C_{lo}}{\beta} \tag{C.75}$$

hence

$$a_{o,comp} = \frac{1}{\beta} a_o \tag{C.76}$$

where $a_{o,comp}$ is the lift slope of the airfoil in the compressible flow and a_o is the airfoil's lift slope in the incompressible flow. Now, for a high aspect ratio wing in a three-dimensional compressible flow, its lift slope is determined by applying Eq. (C.76) into Eq. (C.71). That is:

$$a_{comp} = \frac{a_{o,comp}}{1 + \frac{a_{o,comp}}{\pi \omega AR}} = \frac{a_o}{\beta + \frac{a_o}{\pi \omega AR}} \tag{C.77}$$

and in term of Mach number

$$a_{comp} = \frac{a_o}{\sqrt{1 - M_\infty^2} + \frac{a_o}{\pi \omega AR}} \tag{C.78}$$

Note that Eq. (C.78) does not work well for an airfoil in transonic flow due to the effect of the critical Mach number phenomenon and the airfoil's surface inclination angle on the pressure distributions. Even though the airfoil is traveling with a subsonic free stream Mach number M_∞, at some point on the surface the local Mach number M can reach

unity. When this phenomenon happens in the flow, the free stream Mach number M_∞ is named as the critical Mach number M_{cr} of the airfoil. The majority airfoils have critical Mach number about 0.6. When the free stream Mach number passes the critical Mach number, there will be a cloud of bubbles accumulated on the upper surface of the airfoil [2 – Fig. 5.25 – p. 295]. In this case the local Mach number outside the cloud is less than 1 and the Mach number inside the cloud is greater than 1. Then the drag suddenly increases drastically. If the free stream Mach number keeps increasing up to a certain limit, shock wave will appear behind the cloud. This limit is called the drag divergence Mach number. When such chaotic flow occurs on the upper surface of an airfoil, the thin airfoil theory no longer guarantees any reliable result. Therefore, experimental data is more useful in estimating the aerodynamic parameters of an airfoil in transonic flow. The curve fit of the lift slope of an airfoil in the transonic flow can be found in [2 – p. 83] and [23 – p. 319].

In addition, the characteristic of the camber line, the maximum thickness, and the angle of attack also affect the limit of the critical Mach number. According the Prandtl – Glauert law, an airfoil with a maximum thickness τ_o is in an $M_{\infty,1} = 0$ flow and another airfoil with the maximum thickness τ is in an $M_{\infty,2} = 0.8$ flow will generate an identical pressure distributions C_p if their maximum thicknesses ratio satisfies

$$\frac{\tau}{\tau_o} = \sqrt{1 - M_{\infty,2}^2} \tag{C.79}$$

Indeed, the experimental data shows that estimation of compressible lift slope given by Eq. (C.78) is good at the free stream Mach number which is experimentally determined by the airfoil's maximum thickness rubric in Table C.1.

For a high aspect ratio wing in supersonic flow, the lift slope is given by the following formula (see [23] for detailed derivation)

$$a_{sup} = \frac{4}{\sqrt{M_\infty^2 - 1}} \tag{C.80}$$

Table C.1: Allowable Free Stream Mach Number Rubric	
Airfoil's maximum thickness	*Allowable free stream Mach number*
$\tau = 18\ \%$	$M_\infty \leq 0.60$
$\tau = 15\ \%$	$M_\infty \leq 0.65$
$\tau = 12\ \%$	$M_\infty \leq 0.80$
$\tau = 9\ \ \%$	$M_\infty \leq 0.86$
$\tau = 6\ \ \%$	$M_\infty \leq 0.87$

C.10 Lift-Slope Transformation for Low Aspect Ratio Wings

For a wing with $AR < 4$, the lifting line theory is no longer feasible. Indeed, in the lifting line theory we assumed that the circulation distribution over the wing varies only in the spanwise direction and the resultant of the lift vectors in chordwise direction ends up along a single line. On the other hand, the wing tip vortices vigorously disturb the flow field over the wing. Thus the assumptions used in the lifting line theory are no longer accurate. Moreover, the lifting surface theory (panel method) provides better solutions. As a result, the transformations of lift slope for high aspect ratio wing are invalid in this case. Instead, the formula obtained from the panel method is applied to wings at low aspect ratios. We do not derive it here. Rather, we borrow it from [2]. For a low aspect ratio wing in incompressible flow, the wing lift slope is given by

$$a = \frac{a_o}{\sqrt{1 + \left(\frac{a_o}{\pi AR}\right)^2} + \frac{a_o}{\pi AR}} \tag{C.81}$$

For a low aspect ratio wing in subsonic compressible flow, the wing lift is determined by

$$a_{comp} = \frac{a_o}{\sqrt{1 - M_\infty^2 + \left(\frac{a_o}{\pi AR}\right)^2} + \frac{a_o}{\pi AR}} \tag{C.82}$$

For the same wing but in supersonic flow, the lift slope is

$$a_{sup} = \frac{4}{\sqrt{M_\infty^2 - 1}}\left(1 - \frac{1}{2AR\sqrt{M_\infty^2 - 1}}\right) \tag{C.83}$$

C.11 Lift-Slope Transformation for Swept Wings

Swept wings are also often encountered in aeronautical designs. Since swept angle helps reducing the lateral effective wind velocity which the wing's airfoil actually sees, it is very useful in attenuating the aeroelastic effects on the wing and increasing the critical Mach number.

From [2], the author suggests that a swept wing can be treated as the low aspect ratio wing except for the airfoil's lift slope is reduced by a factor of $\cos\Lambda_{c/2}$, where $\Lambda_{c/2}$ is the half-chord swept angle of the wing. For a swept wing in the incompressible flow, the lift slope is determined as:

$$a = \frac{a_o \cos\Lambda_{c/2}}{\sqrt{1 + \left(\frac{a_o \cos\Lambda_{c/2}}{\pi AR}\right)^2} + \frac{a_o \cos\Lambda_{c/2}}{\pi AR}} \tag{C.84}$$

For a swept wing in the subsonic compressible flow, the lift slope can be estimated by:

$$a_{comp} = \frac{a_o \cos\Lambda_{c/2}}{\sqrt{1 - M_\infty^2 \cos^2\Lambda_{c/2} + \left(\frac{a_o \cos\Lambda_{c/2}}{\pi AR}\right)^2} + \frac{a_o \cos\Lambda_{c/2}}{\pi AR}} \tag{C.85}$$

For swept wings in supersonic flow, use the charts in [8 – p. 314 – 315]. A brief summary of all lift slope transformations is presented in Table C.2.Once we obtained the lift slope of a finite-span wing, we can estimate the wing lift coefficient for the linear segment of the lift curve by using:

$$C_L = a(\alpha - \alpha_{Lo}) \quad \text{or} \quad C_{L,comp} = a_{comp}(\alpha - \alpha_{Lo}) \tag{C.86}$$

where the lift slope must be in per degree unit.

C.12 Induced Drag

In the two-dimensional flow the lift vector $\vec{L}$ of an airfoil is perpendicular to the flight path and the drag vector $\vec{D}$ is parallel to the flight path. In the three-dimensional flow the lift vector $\vec{L'}$ is perpendicular to the relative wind which is offset from the flight path by the induced angle α_i. When resolving the lift vector $\vec{L'}$ into the flight path coordinate, we see this vector has two components: $\vec{L'} = L\hat{k} + D_i\hat{\imath}$ (see Fig. C.8). The vertical component in the z-direction provides the lifting force for the wing while the horizontal component in the x-direction causes extra drag to the wing. This extra drag is often called the induced drag of a finite aspect ratio wing. Its magnitude is determined by:

$$D_i = L\tan(-\alpha_i) \tag{C.87}$$

Using the definition of the induced angle, we write the induced drag as:

$$D_i = L\frac{w}{V_\infty} \tag{C.88}$$

Substitute the expression of lift from Eq. (C.9) and induced velocity from Eq. (C.40) into Eq. (C.88), we get

$$D_i = \rho b^2 V_\infty^2 \int_0^\pi \sum_{n=1}^{\infty} nA_n^2 \sin^2 n\theta \, d\theta \tag{C.89}$$

The integral $\int_0^\pi \sum_{n=1}^{\infty} nA_n^2 \sin^2 n\theta \, d\theta = \frac{\pi}{2}\sum_{n=1}^{\infty} nA_n^2$. Therefore, the induced drag is written as:

$$D_i = \frac{\pi}{2}\rho b^2 V_\infty^2 \sum_{n=1}^{\infty} nA_n^2 \tag{C.90}$$

However, the induced drag can also be expressed in a different formula such as:

$$D_i = \frac{1}{2}\rho V_\infty^2 S C_{D_i} \tag{C.91}$$

Equating Eq. (C.90) and Eq. (C.91), we have

$$C_{D_i} = \pi \frac{b^2}{S} \sum_{n=1}^{\infty} n A_n^2 \tag{C.92}$$

in terms of the aspect ratio, $AR = \frac{b^2}{S}$

$$C_{D_i} = \pi AR \sum_{n=1}^{\infty} n A_n^2 \tag{C.93}$$

From the lift coefficient formula given by Eq. (C.12), we know that $\pi AR = \frac{C_L}{A_1}$ or equivalent to $\pi AR = \frac{1}{\pi AR} \frac{C_L^2}{A_1^2}$. Substitute the quantity πAR into Eq. (C.93) the induced drag coefficient becomes a function of the lift coefficient, the aspect ratio, and the Fourier coefficients in the form:

$$C_{D_i} = \frac{C_L^2}{\pi AR} \frac{\sum_{n=1}^{\infty} n A_n^2}{A_1^2} \tag{C.94}$$

By setting

$$1 + \delta = \frac{\sum_{n=1}^{\infty} n A_n^2}{A_1^2} \tag{C.95}$$

and

$$\phi = \frac{1}{1 + \delta} \tag{C.96}$$

The induced drag coefficient transforms into its well-known form in literature as:

$$C_{D_i} = \frac{C_L^2}{\pi \phi AR} \tag{C.97}$$

where ϕ is known as the span efficiency factor which ultimately is a function of the Fourier coefficients. The intermediate variable δ is called the induced drag factor. As δ increases, the induced drag coefficient increases. From the definition of the induced drag factor given in Eq. (C.95), δ is always positive.

Table C.2: Lift slope transformations for various types of wings in different flows		
Wing Type	*Flow Category*	*Lift Slope Transformation*
High Aspect Ratio $AR \geq 4$	Incompressible	$a = \frac{a_o}{1 + \frac{a_o}{\pi \omega AR}}$
	Subsonic Compressible	$a_{comp} = \frac{a_o}{\sqrt{1 - M_\infty^2} + \frac{a_o}{\pi \omega AR}}$
	Supersonic	$a_{sup} = \frac{4}{\sqrt{M_\infty^2 - 1}}$
Low Aspect Ratio $AR < 4$	Incompressible	$a = \frac{a_o}{\sqrt{1 + \left(\frac{a_o}{\pi AR}\right)^2} + \frac{a_o}{\pi AR}}$
	Subsonic Compressible	$a_{comp} = \frac{a_o}{\sqrt{1 - M_\infty^2 + \left(\frac{a_o}{\pi AR}\right)^2} + \frac{a_o}{\pi AR}}$
	Supersonic	$a_{sup} = \frac{4}{\sqrt{M_\infty^2 - 1}} \left(1 - \frac{1}{2AR\sqrt{M_\infty^2 - 1}} \right)$
Swept	Incompressible	$a = \frac{a_o \cos \Lambda_{c/2}}{\sqrt{1 + \left(\frac{a_o \cos \Lambda_{c/2}}{\pi AR}\right)^2} + \frac{a_o \cos \Lambda_{c/2}}{\pi AR}}$
	Subsonic Compressible	$a_{comp} = \frac{a_o \cos \Lambda_{c/2}}{\sqrt{1 - M_\infty^2 \cos^2 \Lambda_{c/2} + \left(\frac{a_o \cos \Lambda_{c/2}}{\pi AR}\right)^2} + \frac{a_o \cos \Lambda_{c/2}}{\pi AR}}$
	Supersonic	[8 – p. 314 – 315]
Note: All lift slopes in this table are in per radian unit. Sweep angle $\Lambda_{c/2}$ is the half-chord sweep.		

Thus, the span efficiency factor is always less than 1. For a general finite aspect ratio taper wing, the induced drag factor is indeed a function of the taper ratio and the aspect ratio. Since the Fourier coefficients are determined by the methods described in § C.5

through §C.7, thus these coefficients are the functions of the taper ratio and the aspect ratio. Of course, the induced drag factor is not an exception because it is found by:

$$\delta = \frac{A_1^2 + 3A_3^2 + 5A_5^2 + 7A_7^2}{A_1^2} - 1 \tag{C.98}$$

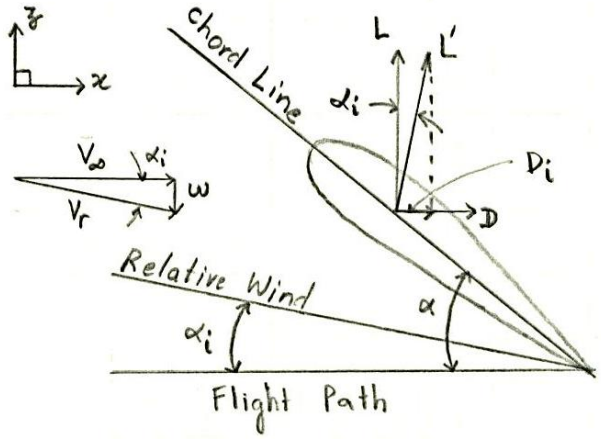

Figure C.8: Induced drag in finite aspect ratio wing.

For a high aspect ratio taper wing with its airfoil's lift slope $a_o = 2\pi$ per radian, the induced drag factor is sketched as the taper ratio varies from zero to unity and the aspect ratio increases from 4 in Fig. C.9. Here, we find δ is a small and positive quantity. The sketch of the induced drag factor in Fig. C.9 indicates the minimum induced drag factor occurs at the taper ratio $\lambda \approx 0.4$ which is common intersection of the induced angle factor in Fig. C.7. Both quantities suggest the delta wing and the rectangular are the worst choices in aircraft design. In contrast, a 40% tapered wing is the most desirable choice in minimizing the induced drag and improving the wing's lift slope. Both Fig. C.7 and Fig. C.9 show that both factors increase as the aspect ratio gets larger.

Logically, one would say that a high aspect ratio wing is not desirable. Nevertheless, the effects of these two factors to the induced angle and the induced drag defined in Eq. (C.69) and Eq. (C.97) respectively are much weaker than the effect of the aspect ratio since they are much smaller than the aspect ratio. In addition, as the aspect ratio gets

higher the increments in both factors is reduced. Therefore, we can improve the aerodynamic efficiency of a wing by increasing the wing's aspect ratio.

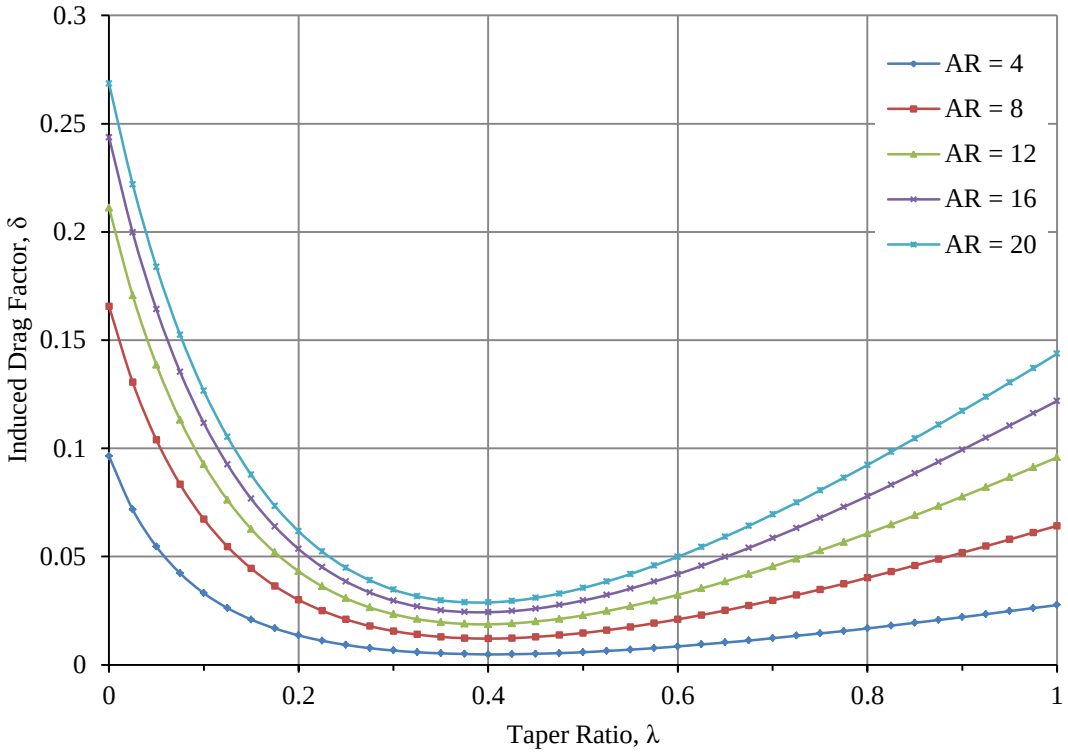

Figure C.9: Induced drag factor of an airfoil with lift slope of 2π per radian.

Once the lift of the finite wing have determined, we can obtain the drag of the wing by the following formula:

$$C_D = C_d + \frac{C_L^2}{\pi \phi AR} \tag{C.99}$$

where C_d is obtain from the airfoil's drag profile in which the drag coefficient is a function of lift coefficient, $C_d = f(C_L)$. According the derivation found in [15 – p.387], we can write the formula for total drag of a symmetrical-airfoil wing as a sum of the parasite drag and the induced drag:

$$C_D = C_{D,o} + \left(r + \frac{1}{\pi\phi AR}\right) C_L^2 \quad \text{(C.100)}$$

where $C_{D,o}$ is the parasite drag which is the drag coefficient at zero lift on the drag profile curve. The constant r does not have any formula; rather it is empirically determined. The author suggests to combine r and ϕ together and denote by e and called it as the Oswald efficiency factor. The factor r was suggested by Oswald to encounter for the drag of the whole body of the vehicle. Unlike ϕ only represents for wing itself and does not include the effects of fuselage and the tails of the vehicle. The Oswald efficiency factor for different types of airplanes were tabulated in [40], as reported in Table C.3.

Table C.3: Empirical values of airplane efficiency factor

Type of airplane	Use values of e varying with "cleanness"	From	To
Flying wing	……..……	0.95	1.00
Cantilever monoplane	……..……	0.85	1.00
Semi-cantilever monoplane	……..……	0.80	0.95
Single bay biplane	……..……	0.75	0.95
Multiple bay biplane	……..……	0.70	0.90

The empirical formulas for estimating the Oswald efficiency factor based on real models, which were mathematically formulated by Cavallo in 1966, are presented [8 – p. 347] in two forms:

- Unswept-Wing Aircraft:

$$e = 1.78(1 - 0.045 \times AR^{0.68}) - 0.64 \quad \text{(C.101)}$$

- Swept-Wing Aircraft:

$$e = 4.61(1 - 0.045 \times AR^{0.68})(\cos \Lambda_{LE})^{0.15} - 3.1 \quad \text{(C.102)}$$

These two equations are only valid for regular aircraft with moderate aspect ratios. For very high aspect ratio vehicles like sailplane, these formulas do not give accurate results. In that case, the formula for ϕ is more appropriate because the wing are much wider and its aerodynamics dominates the effects of fuselage. The second limitation of these

formulas is the leading edge sweep angle must greater than 30 degrees ($\Lambda_{LE} > 30°$). These equations do not quantitatively estimate the effects of the taper ratio, the twist angle, and the low aspect ratio wings.

Thus Eq. (C.100) can be rewritten in a compact form of airplane efficiency factor

$$C_D = C_{D,o} + \frac{C_L^2}{\pi e AR} \tag{C.103}$$

The deviation form of Eq. (C.103) for a camber-airfoil wing is in term of the minimum drag and the lift coefficient at that minimum drag, like:

$$C_D = C_{D,min} + \frac{\left(C_L - C_{L,\min drag}\right)^2}{\pi e AR} \tag{C.104}$$

Since the airplane efficiency factors listed in Table C.3 are similar range of the wing span efficiency factor given by Eq. (C.96), thus to be more precise we will use the value of the span efficiency factor instead of the airplane efficiency factor. Let consider a drag coefficient C_D' whose value is determined by:

$$C_D' = C_d(C_l) + \frac{C_l^2}{\pi e AR} \tag{C.105}$$

Then both $C_{D,o}$ and $C_{D,min}$ are the minimum value of C_D'. The distinction between $C_{D,o}$ and $C_{D,min}$ is the value of the lift coefficient at $C_{D,min}'$. Precisely, we write:

$$\begin{cases} C_{D,o} = C_{D,min}' \;\; at \;\; C_l = 0 \; or \; C_{lo} & for \; symmetrical \; airfoil \\ C_{D,min} = C_{D,min}' \;\; at \;\; C_l = C_{L,\min drag} \neq 0 & for \; camber \; airfoil \end{cases}$$

C.13 Discretization-Interpolation of Lift Curve in Non-linear Regime

The methods for transforming the lift curve are only valid in the linear regime. Therefore, it cannot be applied to the non-linear regime and predict the maximum and minimum lift coefficients. It requires both potential flow and viscous flow to model the stall

characteristic of an airfoil. However, the thin airfoil theory and the wing theory are based only on the potential flow. Thus, the wing theory is inapplicable for transforming the lift curve in the stall angle's neighborhood. In this thesis, we used the interpolation method to estimate the lift characteristic in the non-linear regime.

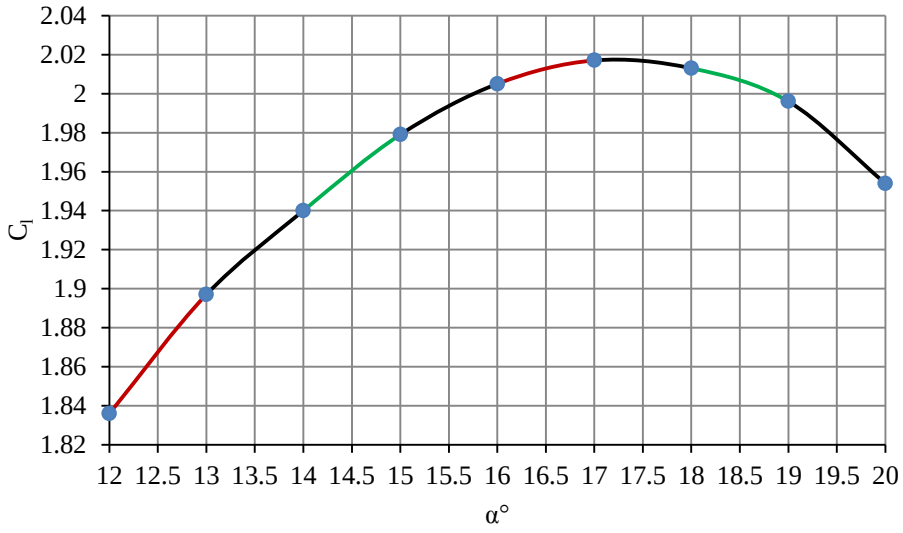

Figure C.10: Non-linear lift curve of NASA MS(1)-0317 airfoil in discrete form.

Let consider the upper non-linear part of the lift curve of the NASA MS1-0317 airfoil that is sketched in Fig. C.10. If we cut the curve into many small finite segments, we would see each segment like a very short straight line. The lift slope of each segment is given by:

$$a_{o_i} = \frac{c_{l_i} - c_{l_{i-1}}}{\alpha_i - \alpha_{i-1}} \tag{C.106}$$

where the super subscript i is the index of each data point on the curve. Then apply the linear transformation to find the wing lift slope a_i which represents the segmental increment in lift from point $(i-1)^{th}$ to point i^{th} on the curve.

Finally, using the finite wing lift slope just found to calculate the lift coefficient at the i^{th} data point by using:

$$C_{L_i} = a_i(\alpha_i - \alpha_{i-1}) + C_{L_{i-1}} \tag{C.107}$$

where $C_{L_{i-1}}$ is the lift coefficient of the previous point. In computing the lift coefficient at the beginning point of the curve, $C_{L_{i-1}}$ is the ending point of the linear line. Incorporating with the linear fit curve gives a complete lift curve of the wing.

C.14 Three-Dimensional Aerodynamics of the MS(1)-0317 Airfoil

A two-dimensional sketch of the NASA MS1-0317 airfoil is shown in Fig. C.11. The two-dimensional lift, moment, and drag profiles of the NASA MS1-0317 airfoil are presented in Fig. C.12, Fig. C.13, and Fig. C.14, respectively.

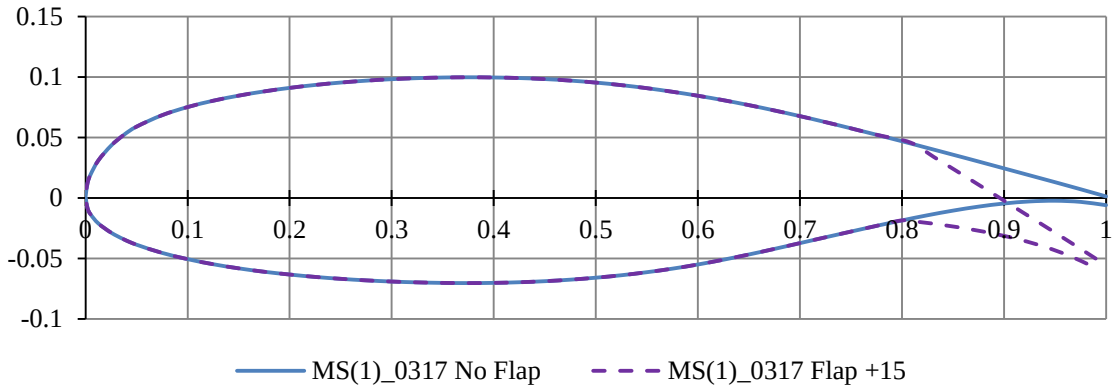

Figure C.11: 2-D sketch of the NASA MS(1)-0317 airfoil.

Having a good understanding on the transformation method, one could see that the conversion is quite simple. For instance, we want to convert the lift curve of the NASA MS1-0317 airfoil in a two-dimensional flow where the free stream Mach number is 0.1 and the Reynolds number is 6 million into a lift curve of the a finite rectangular wing whose aspect ratio is $AR = 6$ and taper ratio is $\lambda = 1$, unsweep, and untwisted in a

similar three-dimensional flow. The two-dimensional lift curve of the airfoil is shown in Fig. C.12. In order to make this conversion, we first need to extract the linear segment of the curve because the transformation is based on the linear relation between the lift coefficient and the geometric angle of attack. The least-square-fit is the best approach for job. The goodness of fit in the method is measured coefficient of determination R^2, where $R^2 = 1$ yields a perfect fit on the data. Three samples of the extraction are shown in Fig. C.15.

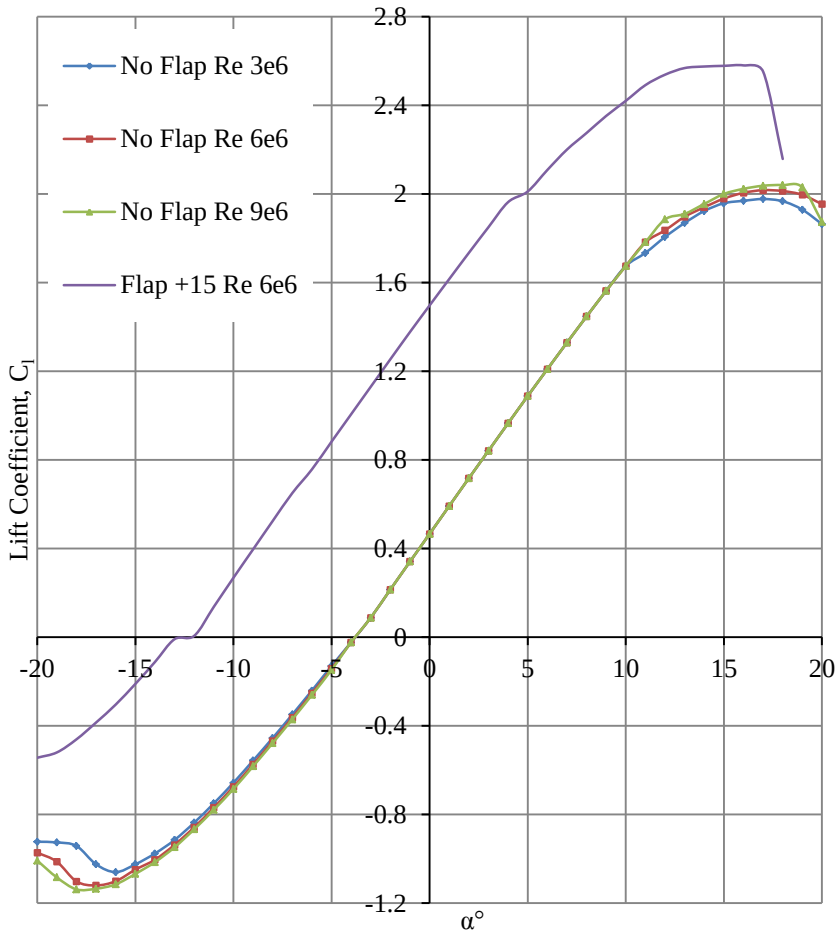

Figure C.12: Lift curve of the NASA MS(1)-0317 airfoil.

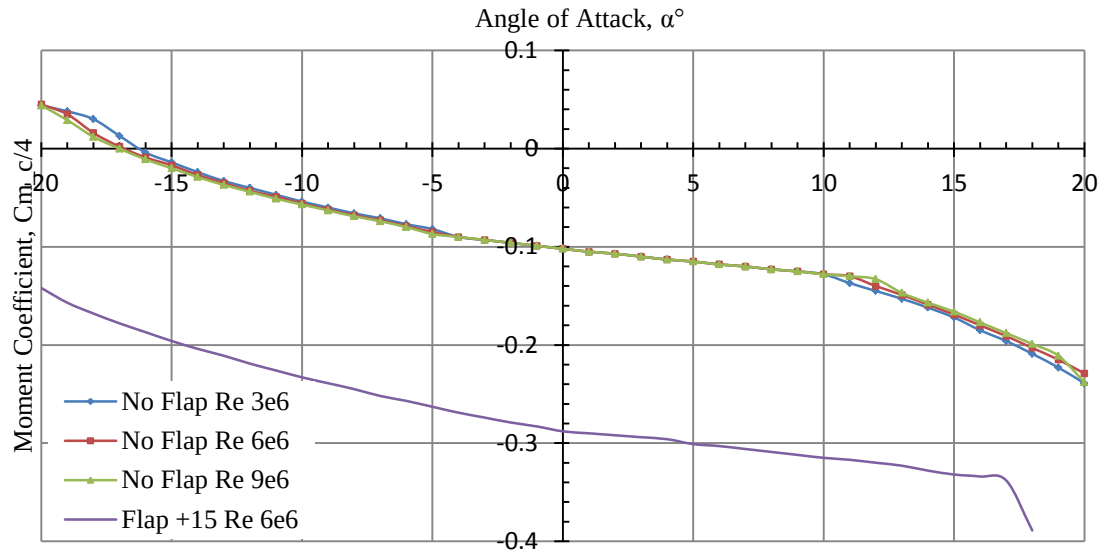

Figure C.13: Quarter-chord moment curve of NASA MS(1)-0317 airfoil.

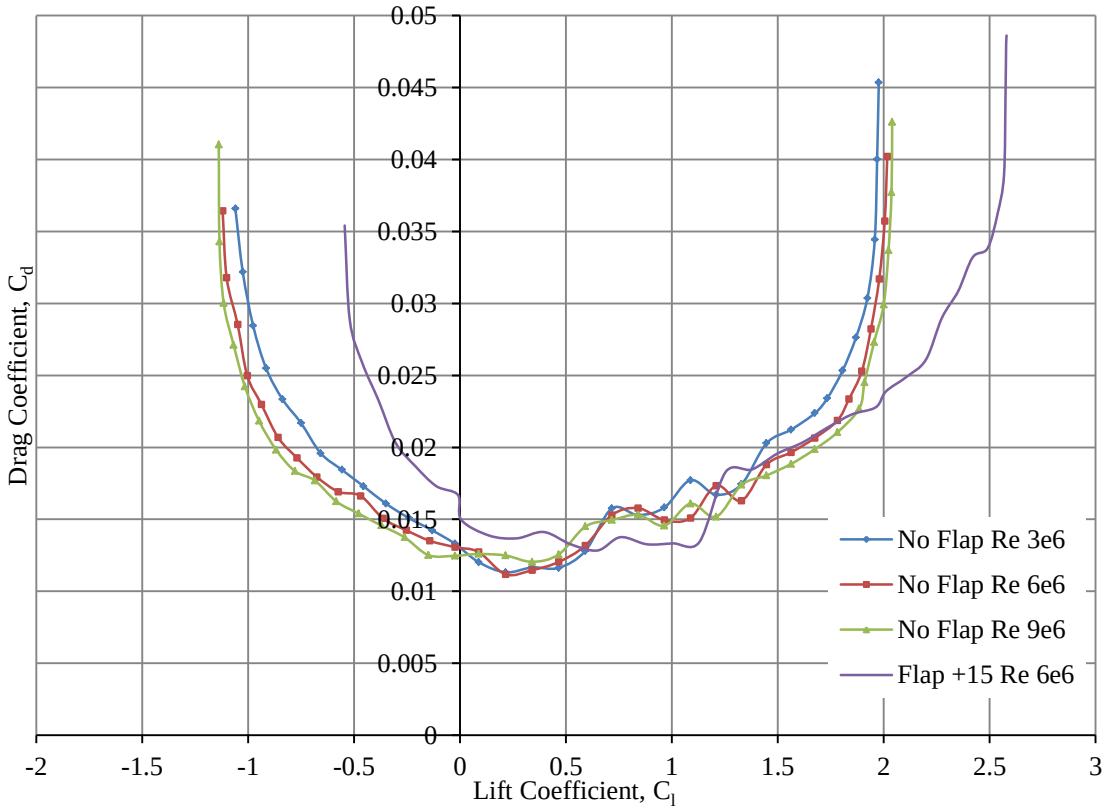

Figure C.14: Drag polar diagram of the NASA MS(1)-0317 airfoil.

The first linear fit in Fig. C.15a represents the linear relation of lift coefficients to geometric angle of attack in a range from minimum lift coefficient to the maximum lift coefficient which is corresponding to the angle of attack range from -17° to 17°. This line has the coefficient of determination $R^2 = 0.9911$. The second fit curve in Fig. C.15b cover a group of data points in the angle of attack range from -5° to 5° and has the coefficient of determination $R^2 = 0.9999$. The third line (Fig. C.15c) has the determination coefficient $R^2 = 0.9998$ to fit all the points in the range of angle of attack from -7° to 11°.

Comparing the goodness of fit among the three lines, obviously line (a) is the worst and line (c) is the best. Line (a) is the worst not because of its lowest coefficient of determination, but also because the fitting includes the non-linear regimes of the lift curve. As a result, its uncertainty increases; and the accuracy of the formula is degraded. In contrast, line (b) has the highest coefficient of determination; it almost perfectly matches all the points in the range. However, it does not represent the whole linear regime of the lift curve due to the limited number of data points. On the other hand, line (c) does a better job in representing the linear regime of the lift curve. It fits almost twice as much as the number of data points in line (b) while it still maintains the coefficient of determination close to that of line (b). Quantitatively, line (c) is one to the ten thousand less accurate than line (b), but it covers 73% more data points than line (b) does. That is why it the best representation of the linear regime. It implies that the best linear fit of the lift curve is the line whose coefficient of determination must be closed to unity and cover a wide range of data points.

As the results, we have obtained the lift line for NASA MS1-0317 airfoil as:

$$C_l = 0.1213\alpha + 0.4698 \tag{C.108}$$

where the lower bound is at (-0.363, -7°); and the upper bound is at (1.782, 11°).

The lift slope

$$a_o = 0.1213\ \frac{1}{deg} = 0.1213\ \frac{1}{deg} \times \frac{180\ deg}{\pi\ rad} \approx 6.95\ \frac{1}{rad}$$

The zero-lift angle of attack

$$\alpha_{Lo} = -\frac{0.4698}{0.1213} \approx -3.873°$$

For rectangular wing, μ is reduced to

$$\mu = \frac{a_o}{4AR} \approx 0.2896$$

Applying the four-span-station approximation: $[\theta_1\ \theta_2\ \theta_3\ \theta_4] = \left[\frac{\pi}{8}\ \frac{\pi}{4}\ \frac{3\pi}{8}\ \frac{\pi}{2}\right]$ to find the first four Fourier coefficients using Eq. (C.63)

$$\begin{bmatrix} A_1/\alpha_a \\ A_3/\alpha_a \\ A_5/\alpha_a \\ A_7/\alpha_a \end{bmatrix} = \begin{bmatrix} 0.2573 & 1.1562 & 1.6913 & 0.9222 \\ 0.7048 & 1.1143 & -1.5239 & -1.9335 \\ 1.1211 & -0.6860 & -0.9077 & 2.7265 \\ 1.2896 & -1.8688 & 2.4480 & -3.0272 \end{bmatrix}^{-1} \begin{bmatrix} 0.1108 \\ 0.2048 \\ 0.2676 \\ 0.2896 \end{bmatrix}$$

Hence, the Fourier coefficients are

$$\begin{bmatrix} A_1/\alpha_a \\ A_3/\alpha_a \\ A_5/\alpha_a \\ A_7/\alpha_a \end{bmatrix} = \begin{bmatrix} 0.2588 \\ 0.0294 \\ 0.0056 \\ 0.0010 \end{bmatrix}$$

When the Fourier coefficients are known, the induced angle factor and the induced drag factors are determined by using Eq. (C.17) and Eq. (C.98), respectively.

$$\varphi = \frac{\alpha_a}{A_1} - \frac{\pi AR}{a_o} - 1 = \frac{1}{0.2588} - \frac{6\pi}{6.95} - 1 \approx 0.152$$

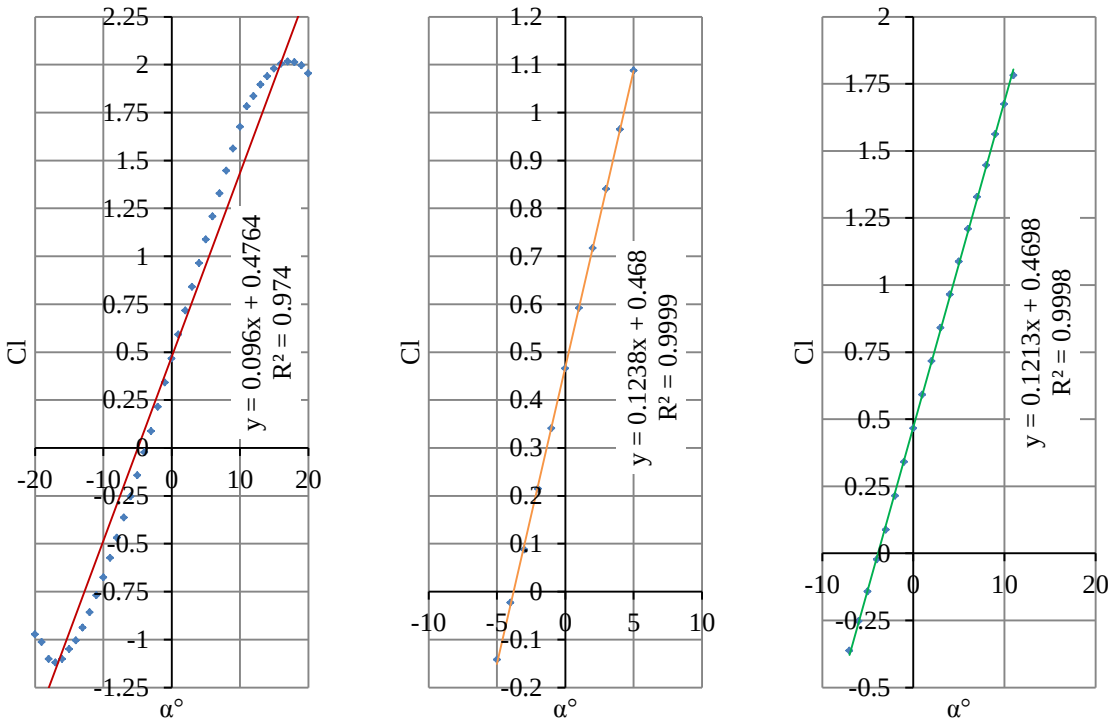

(a) **(b)** **(c)**

Figure C.15: Least square fits of the lift coefficients of the NASA MS1-0317 airfoil in the linear regime.

$$\delta = \frac{A_1^2 + 3A_3^2 + 5A_5^2 + 7A_7^2}{A_1^2} - 1 = \frac{0.2588^2 + 30.0294^2 + 50.0056^2 + 70.001^2}{0.2588^2} - 1 \approx 0.041$$

Follow by the calculations of lift correction factor and span efficiency factor using Eq. (C.70) and Eq. (C.96), respectively:

$$\omega = \frac{1}{1 + \varphi} = \frac{1}{1 + 0.152} \approx 0.8681$$

$$\phi = \frac{1}{1 + \delta} = \frac{1}{1 + 0.041} \approx 0.9606$$

The solutions indicate that the lift correction factor and the Span efficiency factor are not identical as well as the induced angle factor and the induced drag factor are not equal to each other. For a straight wing with high aspect ratio in the incompressible flow, the lift slope transformation is given by:

$$a = \frac{a_o}{1 + \frac{a_o}{\pi \omega AR}} = \frac{6.95}{1 + \frac{6.95}{6\pi \times 0.8681}} \approx 4.8782 \frac{1}{rad} \approx 0.0851 \frac{1}{deg}$$

If we make the assumption that φ is equal to δ, we would find the lift slope is slightly different from the lift slope has found above:

$$a = \frac{a_o}{1 + \frac{a_o}{\pi \phi AR}} = \frac{6.95}{1 + \frac{6.95}{6\pi \times 0.9606}} \approx 5.0223 \frac{1}{rad} \approx 0.0877 \frac{1}{deg}$$

That is about 3% in difference. Indeed, there is a chain of reduction in the difference between the two correction factors. From elementary level, φ is 3.71 times greater than δ, in this particular example. Then in the intermediate level, ϕ is 1.12 times greater than ω. Then both ω and e must multiply with πAR before they are divided by a_o in the denominator of the lift slope transformation formula. At the final level, these fractions are added to 1 before they are used to divide the lift slope. Eventually, there are only 3% left in difference. Therefore, the assumption that φ is equal to δ is used in some textbooks.

Now, we can sketch the lift line in the linear region using Eq. (C.86). The zero-lift angle is determined at -3.873°. However, for simplicity in coding we used the zero-lift angle at -4° because the lift coefficient at this angle of attack is -0.023 which is the zero-closest value on the fit curve. So that the deviated form of Eq. (C.86) is:

$$C_L = a(\alpha - \alpha_{Lo}) + C_{lo} = 0.0851(\alpha + 4°) - 0.023$$

In this relation, the geometric angle of attack is an independent variable. At this point we have an ambiguity in our equation because we do not know where the line will end. At the beginning of the problem, we already determined the boundary of the linear fit curve

at the lower bound and upper bound points. Should we stop marching at the bounding angle of attacks, -7° and 11°? The answer is no because they are not the actual bound of the linear fit curve. In both relations, then angle of attack serves as the independent variable. Instead, the lift coefficient range determines the actual boundaries of the curve. Indeed the lift coefficient range is the official bound of the curve because in our derivation for the lift slope transformation, we have made the assumption that a particular lift coefficient in the linear region can be measured by either Eq. (C.1) or Eq. (C.2). It is absolutely true if we look a Fig. C.1 and imagine that the "Finite Span" dash line move from $C_{L_{lower}} = -0.363$ to $C_{L_{upper}} = 1.782$ on the $C_l - axis$, it will trace out two lift curves as sketched in the figure. Therefore, we will start at the zero-lift angle and march out in both directions until at the lift coefficient has reached both lift boundaries. When reaching both ends, we need to stop and deal with the non-linear part of the curve. The curves are shown in Fig. C.16.

Figure C.17 shows the sketches of the lift profiles of the wing and its airfoil. The result shows the maximum lift of the wing is lower than that of the airfoil and the minimum lift of the wing is higher than that of the airfoil. The stall angle of the wing is larger than the stall of the airfoil. Both curves have the same shape but have different magnitudes whereas the slope of lift curve of the wing is smaller than the slope of the lift curve of the airfoil. If the aspect ratio of the wing increases, its lift curve will move closer to the lift curve of the airfoil.

The curves in Fig. C.18 show what we have predicted. As the aspect ratio gets higher, the change in the lift slope gets smaller. When the aspect ratio goes from 8 to 20 the lift slope improves slowly, while it improves drastically when the aspect ratio goes from 1 to 8. More interestingly, when the aspect ratio is at 8 and 12, the maximum lift coefficient is smaller than the maximum lift coefficient when the aspect ratio is at 3 and 4. The phenomenon is inexplicable. As the aspect ratio increases the stall angle decreases.

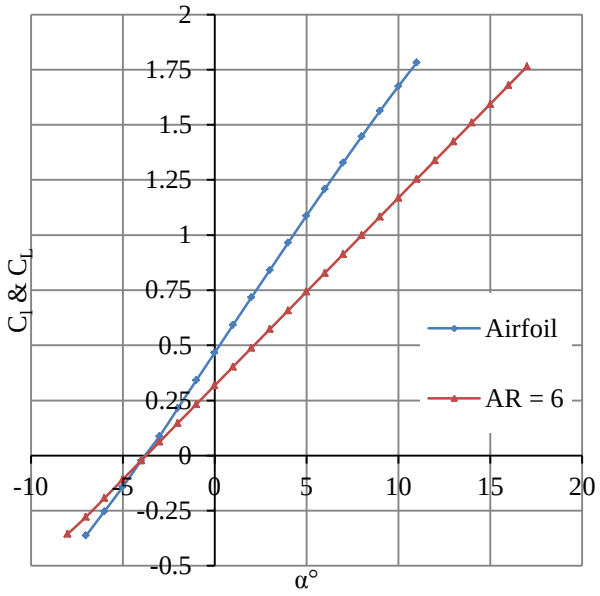

Figure C.16: Linear lift curves of the NASA MS1-0317 wing with $AR = 6$ and its airfoil.

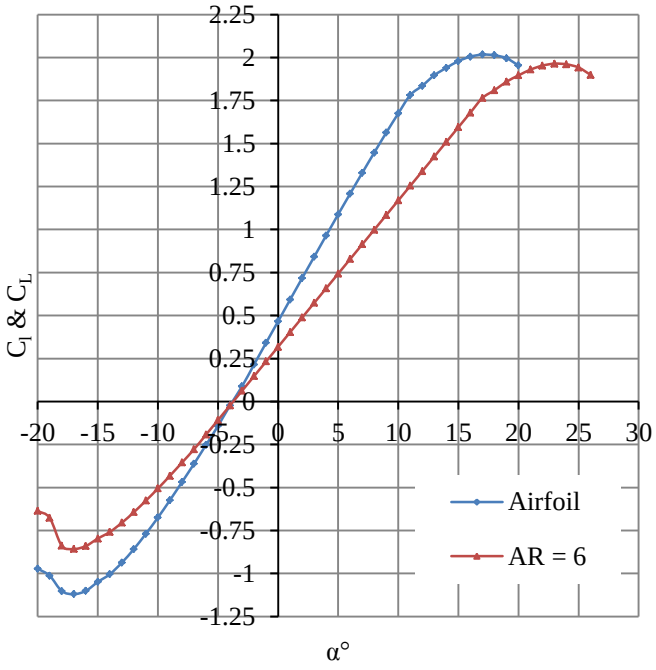

Figure C.17: Complete lift curves of the NASA MS1-0317 wing with $AR = 6$ and its airfoil.

Here we found that the wing at $AR = 1, 2, and\ 3$ will stall at 71°, 40°, and 31°, respectively. It is questionable for a wing to stall at 71° and seems to be unrealistic. It needs to be verified with wind tunnel experiment. Or it could be explained that wings with small aspect ratios behave like a two-dimensional airfoil. Figure C.19 shows the drag polar of the NASA MS1-0317 wing as the aspect ratio varies. Figure C.20 sketches the aerodynamic efficiency of the wing as a function of the lift coefficient.

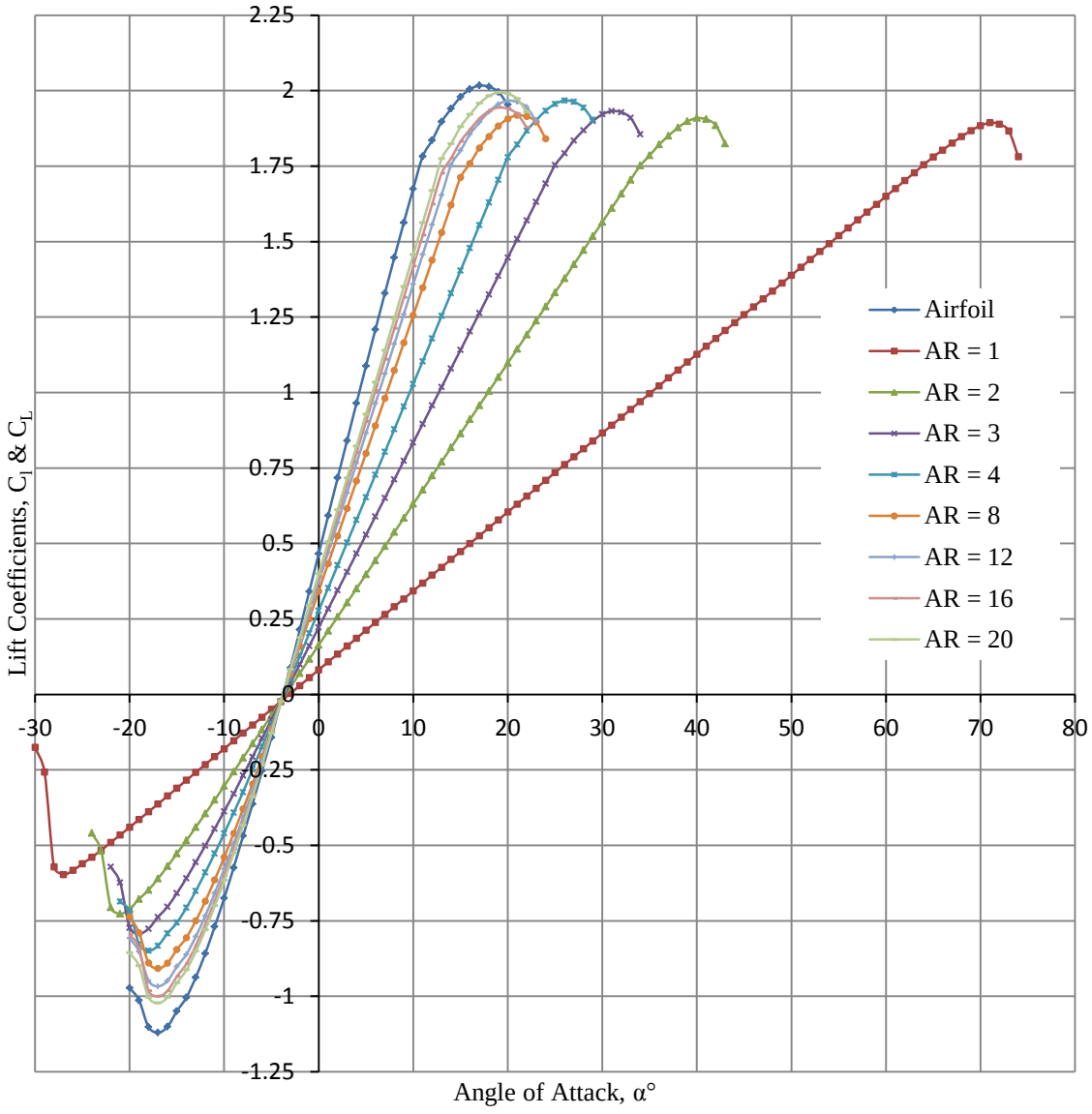

Figure C.18: Lift curve varies as the wing's aspect ratio changes.

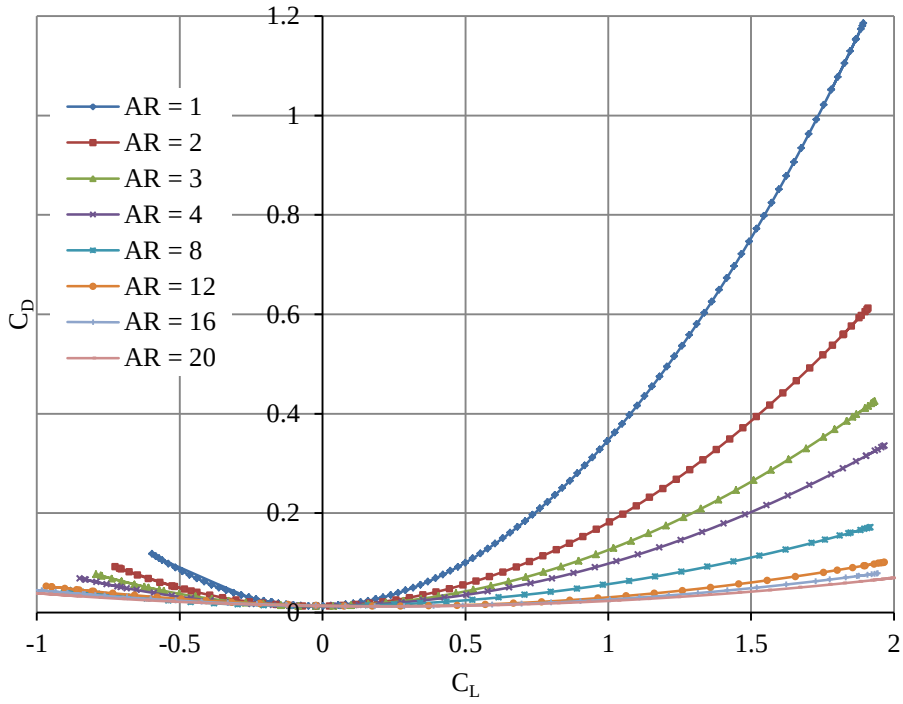

Figure C.19: NASA MS1-0317 Wing drag polar as aspect ratio varies from 1 to 20.

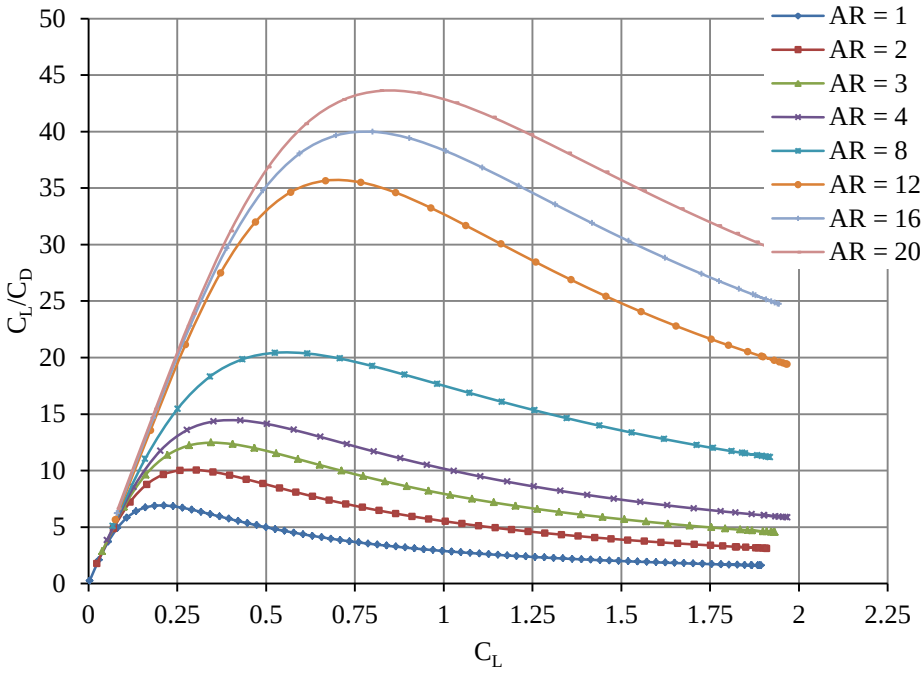

Figure C.20: NASA MS1-0317 Wing's aerodynamic efficiency.

Observing the drag polar in Fig. C.19, once again we see the prominent influence of the aspect ratio on the aerodynamic characteristic of an airfoil. As the aspect ratio increases the drag coefficient of wing decreases. When the aspect ratio is very high, the change in drag is almost unnoticeable. For example, when as spec ratio raises from 12 to 20, the amount reducing in drag is just small portion of the reduced drag as the aspect ratio increases from 1 to 8. Thus having an infinite aspect ratio does not mean the wing can infinitely improve the aerodynamic efficiency. Rather, there is a certain aspect ratio where the efficiency can be improved significantly compare to its neighbors. For instance, the lift-to-drag curves in Fig. C.20 indicate the biggest jump in efficiency between aspect ratio at 8 and 12. When we plotted the curves with a unit step size in increasing the aspect ratio, we found that 11 is the most improvable aspect ratio of the NASA MS1-0317 wing.

C.15 Summary

The transformation of a two-dimensional aerodynamics to a three-dimensional aerodynamics in this chapter has answered our questions on the differences between aerodynamics of an airfoil and the aerodynamics of a finite wing. The lift slope of a finite wing is smaller than the lift slope of an airfoil. The maximum lift coefficient at the stall angle of a finite wing is also smaller than that of an airfoil. The drag coefficient of a finite wing is much higher than the drag coefficient of an airfoil. As a result, the aerodynamic efficient of a finite wing is much smaller than the aerodynamic efficiency of an airfoil. The root cause of these differences is the wing tip vortex. The vortex induces the third dimensional flow in the vertical plane of the wing and decreases the efficiency of the wing. Because of the nature of the flow at high angle attack, the discretization-interpolation method in estimating the lift coefficient in the non-linear regime of the lift curve is not very appropriate. Nonetheless, the result from estimation is very reasonable. Thus we adapt the method in our estimation for the aerodynamic profiles of a finite wing.

Appendix D. Auxiliary Aerodynamic Surfaces

D.1 Introduction

The aerodynamic characteristics determined in §4.5 and Appendix C are considered as the clean parameters. We have seen the increments in lift and drag due to the deployment of flaps during takeoff and landing in Chapter 3. Indeed, the roles of flaps, slats, ailerons, elevators, rudders, and spoilers are very important in designing an aircraft. The ailerons, elevators, and rudders are called the control surfaces. They play crucial roles in control the attitude of an aircraft. The flaps, slats, and spoilers are called auxiliary aerodynamics surfaces. They enhance the aerodynamic forces of the wing to ensure the aircraft can take off and land without requiring a larger wing platform area. In general, these two types of surfaces are called high lift devices.

The history shows most jet-transport aircraft have maximum lift coefficient in a range from 2.028 to 3.38 [25] during landing maneuver. On the other hand, most airfoils have maximum lift coefficients in the neighborhood of 1.5. Therefore, the high maximum lift coefficients of the historical trends in [25] must come from the enhancements of the auxiliary aerodynamic surfaces. The challenge is how to accurately estimate the lift increment and accompanied drag on the wing. The estimations for precise lift and drag increments are difficult at this stage of the design because we have not built the wing model yet. Thus, the accurate estimation for increasing in lift and drag due to auxiliary aerodynamic surfaces is very necessary.

D.2 Typical Auxiliary Aerodynamic Surface System

There are many complicated methods for this type of estimation in literature. A few methods for approximating increments in aerodynamic parameters of an airfoil due to auxiliary aerodynamic surfaces, which are based on many empirically approximated parameters, were presented in [26] and [27]. Nonetheless, these methods still require a number of specific details about the wing's geometry and prior experimental data of the

airfoil to complete the estimation. Such information is not available for us at this stage of the design process. Thus, a highly accurate empirical formula for predicting the maximum lift increment of an airfoil is essential for us at this stage of the process.

A classical method to formulate an empirical formula is based on the experimental data of the subject to be calculated. Fortunately, there are numerous wind-tunnel test results on the lift and drag coefficients due to flap and slat deflections. Riegels [28] summarized the results of wind-tunnel tests on a wide range of airfoils under influence of various high-lift devices in his book called "Aerofoil Sections." From observation on the results, we learn that a particular flap or slat in a certain configuration generates similar influence on different airfoils. Thus, we might use the linearity rule to estimate the increment in aerodynamic parameter of our selected airfoil (Eppler 407) based on these results without having done any wind-tunnel test on the airfoil yet. However, we need to determine the type of high-lift device to be used before carry out the estimation.

At this stage of the design, the high-lift system is completely arbitrary. Therefore, we need to know the influence of different high-lift devices on one single airfoil in order to select the most feasible system for our airfoil. Figure 134 in [29] lists thirty different flaps and slats influence on the Clark Y airfoil. It is noticeable that the multi-element-high-lift system increases the maximum lift higher than the single-element system does. Nevertheless, the multi-element high-lift system is much more complicated and adds more weight to the wing than the single-element system. As a result, it is the best result to have a fairly simple high-lift system that can generate high maximum lift. The weakness of this list is that it does not provide any detail about the high-lift system, the wind-tunnel test conditions, and the geometry of the wing used in the test.

Table 3.2 of [30] contains all the necessary information for us to accomplish this estimation. The table shows fifteen different flap and slat characteristics which were tested on the Clark Y wing rectangular section with the aspect ratio at 6 where the chord length was 10 inches. The wing section was in an incompressible flow at Reynolds number is 609,000, which is equivalent to a flow speed of 80 mph. Relative to the main

airfoil's chord length, the Krueger Flap with 10% chord at the leading edge and the Fowler Flap with 30% chord at the trailing edge are deflected by 40°, and increased the wing's maximum lift coefficient from 1.29 to 3.41. It is the highest maximum lift coefficient in the table. However, the drag coefficient and the angle of attack at maximum lift coefficient are not determined. Therefore, we would not use this high-lift system for our design at this stage due to lack of information.

A similar three-piece enhancement system, which includes a Handley Page Slat and a 40% chord Fowler Flap deflected 40°, stimulates the wing's maximum lift coefficient up to 3.36. It is about 1.5% less than the maximum lift coefficient of the previous enhancement system. However, we know about all other aerodynamic parameters. In addition, the system is not too complicated to design. As a result, we choose this system for our aerodynamic enhancement system. The sketch of the system on the Clark Y airfoil is shown in Fig. D.1 and Fig. D.2. The changes in aerodynamic characteristics of the wing are listed in Table D.1.

Figure D.1: Basic Clark Y airfoil with Fowler flap and Handley Page slat in retracted positions.

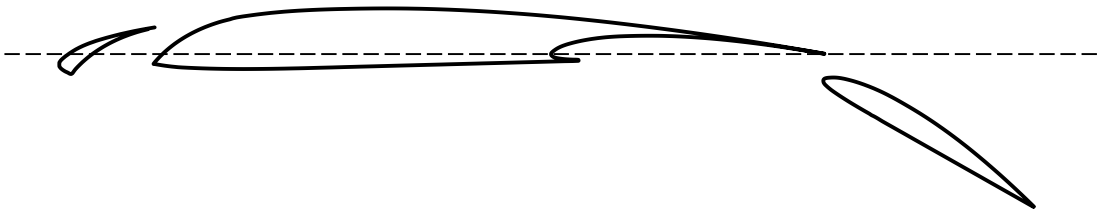

Figure D.2: Basic Clark Y airfoil with Fowler flap and Handley Page slat in extended and deflection positions.

D.3 Fowler Flap

The Fowler flap is defined as the scaled airfoil of the main airfoil. The common scale dimension is the chord length of the main airfoil. Many studies have found that a 40% scale in the chord length of the main airfoil works best for most cases. Both airfoils have their leading edge pivots coincide and the chord lines are parallel. When the flap extends outboard, it increases lifting surface of the wing by the x% scale of the main airfoil. The flap's deflection increases the camber for the main airfoil, which ultimately increases the lift coefficient of the airfoil. The gap between the leading edge of the flap and the trailing edge of the main airfoil is called a slot. When the slot is open, the flap behaves like an individual airfoil. A portion of the airstream under the lower surface of the main airfoil escapes through this slot and delays the flow separation over the upper surface of the flap [29 – p. 205]. The study on the this behavior of the Fowler flap on the Clark Y airfoil [31] shows the size of the slot dictates the aerodynamic characteristics of the flap and hence influence the aerodynamics of the airfoil as well.

Table D.1: Aerodynamic characteristics of Clark Y airfoil with slat and flap

System	C_{Lmax}	α° at C_{Lmax}	L/D at C_{Lmax}	C_{Mac}
Basic Clark Y Airfoil	1.29	15	7.5	-0.085
Handley Page Slat and 0.4c Fowler Flap deflected 40°	3.36	16	3.7	-0.740
Data is obtained from Table 3.2 in [30 – p. 108].				

Figure D.3 depicts the Fowler flap deflection at which it creates a slot behind the trailing edge of the main airfoil. The slot width is the distance between the leading edge of the flap and the trailing edge of the main airfoil. It is positive when the leading edge of the flap is behind the trialing edge of the airfoil. The slot depth is the distance from the chord line of the main airfoil to the tip of the leading edge of the flap. It is positive when the

leading edge of the flap is below the chord line. All distances are measured in percentage of the main airfoil's chord length.

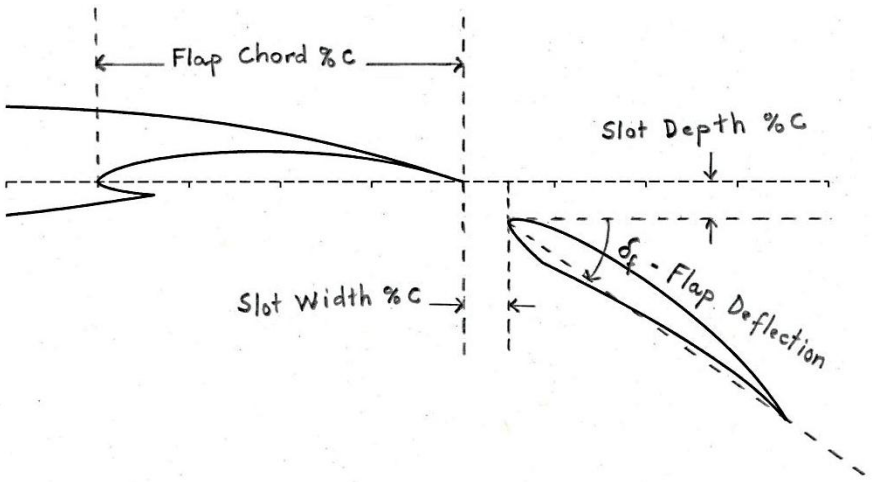

Figure D.3: Fowler flap of the Eppler 407 airfoil at the outboard deflected position.

Weick and Platt [31] made a series of wind-tunnel tests on the same Clark Y wing in the same flow conditions as made in Wenzinger's and Shortal's study [32]. The wing was a rectangular with an aspect ratio of 6, where the wing chord was 10 inches. The wing was submerged into a flow of free-stream speed of 80 mph equivalent to a Reynolds number of 609,000 [31].They found the best position for a 40% chord Fowler flap when it extends to a 0% chord slot width, a 2.5% chord slot depth, and deflects +40° (clockwise rotation). At this optimum position, the flap itself increases the maximum lift coefficient of the wing from 1.27 at 14° angle of attack to 3.17 at 15° angle of attack [31]. Surprisingly, the stall angle of the Clark Y wing under the influence of the flap does not decrease as is predicted in theory. In theory, increasing the camber of an airfoil will decreases the stall angle of that airfoil. In this case, the phenomenon happens in the opposite direction. The explanation must come from the slot as in the discussion above.

D.4 Handley Page Slat

If the flap at the trailing edge of a wing is used to increase lift and causes the reduction in stall angle, the slat is an auxiliary aerodynamic surface at the leading edge of the wing, which is mainly used to balance the stall angle and increase a small portion of lift. Figure D.4 describes a typical Handley Page Slat with a slat width of x% chord, a slat cut-off of y% chord, and a slat chord of z% chord relative to the main airfoil's chord length. Typically, the slat is cut by arc of a radius 20% of the main airfoil's chord length starting from the intersection of cut-off line and the lower surface of the airfoil to the intersection of the slat width line and the upper surface of the airfoil. When the slat is deployed, it can be moved forward and downward in front of leading edge of the airfoil to create a slot. A slot is sized by a slot width, a slot depth, and a slot gap.

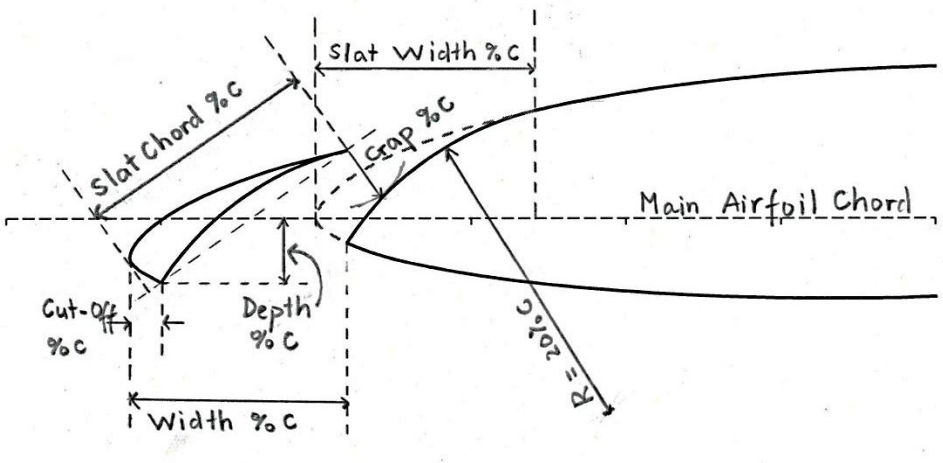

Figure D.4: Handley Page slat of Eppler 407 airfoil at the outboard position.

A slot width is the distance from the cut-off point on the lower surface of the airfoil to the leading edge of the slat. It is always positive. A slat depth is the distance from the main airfoil chord line to the cut-off pivot on the slat. It is positive when the pivot is above the chord line. A slat gap is the distance between the trailing edge of the slat and the cut-off arc on the main airfoil. The slot gap is controlled by rotating the slat about the hinge joint. All distances are measured in percent chord of the main airfoil.

Wenzinger and Shortal investigated the behavior of the Handley Page slat on a rectangular Clark Y wing through a series of wind-tunnel tests. The wing's aspect ratio was 6, where the wing's chord was 10 inches. The air was blown over the wing at a free-stream speed of 80 mph which results in a Reynolds number of 609,000 [32]. The study found the best average slat chord was 14.7% of main airfoil chord. The slat width was 13% and the cut-off was 1.85% within ± 0.01 inch uncertainty. The position of the slat to obtain the highest maximum lift coefficient was found at slot gap of 2%, slot width of 12%, and slot depth of -4%. At this position, the highest maximum lift coefficient was recorded at 1.84 at a corresponding angle of attack of 28°.

On the other hand, the position for the airfoil to stay at high angle of attack for maximum lift coefficient is slightly different. The airfoil can obtain a maximum lift coefficient of 1.6 while maintaining at a corresponding angle of attack of 40°. The position of the slat for the airfoil to achieve these values is located at slot gap of 3%, slot width of 8%, and slot depth of -3.6%. As a result, this position is determined as the optimum position for Handley Page slat on Clark Y wing. The slat increases the stall angle because its slot delays the separation in the flow on the upper surface of the airfoil. A small additional lift is also gained from the increasing in the camber of the airfoil when the slat stays outboard at a certain slot depth. Thus the main application of a slat is to balance the reduction in stall angle caused by a flap.

Table D.2: Sizes and configurations of Fowler flap and Handley Page slat

	Surfaces	*Chord*	*Cut-off*	*Width*	*Depth*	*Rotation*	*Gap*
Surface Size	Flap	40	--	--	--	--	--
	Slat	14.7	1.85	13	--	--	--
Slot Size	Flap	--	--	0	2.5	40°	--
	Slat	--	--	12	4	42°	2
All length measurements are in percentage of main airfoil's chord length (% c).							

Weick and Platt [33] studied the combination of a Fowler flap and a Handley Page slat on the Clark Y wing. The wing's aspect ratio was 6 where the wing's chord length was 10 inches. The flow's Reynold number was 609,000 at the free-stream air speed of 80 mph. The tests were carried out with the sizes and the configurations of the flap and the slat are summarized in Table D.2. At these sizes and configurations, the investigation's results are presented in Table D.3 [33].

D.5 Chord Length Extension Method

In aerodynamics, we know that increasing the camber of an airfoil will increase the lift. The main purpose of deploying these high-lift surfaces is to increase the camber of the airfoil. Thus, if we know the increment of the curvature of the camber of an airfoil, we will know how much lift will be increased. Instead of measuring on lift increment through the increasing in the curvature of the airfoil, we approximate it through the extension of the airfoil's chord length by the surfaces and the deflection of these surfaces.

Table D.3: Aerodynamic characteristics of Clark Y wing equipped with slat and flap

Wing Systems	C_{Lmax}	$\alpha°$ at C_{Lmax}	C_D at C_{Lmax}	C_{Dmin}
Plain Clark Y wing	1.27 ± 0.02	15 ± 1	0.130 ± 0.002	0.016 ± 0.002
Plain wing with Handley Page slat	1.84 ± 0.02	28	0.452 ± 0.002	0.052 ± 0.002
Plain wing with Fowler flap	3.17 ± 0.02	15	0.756 ± 0.002	0.169 ± 0.002
Wing with Fowler flap and Hanley Page slat	3.37 ± 0.02	16	0.904 ± 0.002	0.182 ± 0.002
Data is obtained from report of Weick and Platt, see NACA-TN-459 [33].				

A simple systematic approximation is suggested in [8].The lift increment of a wing can be estimated by function of the lift increment of its airfoil, the ratio of wing area swept out by the span of the auxiliary surface to the total wing's platform area, and the cosine of the sweep angle at the hinge line of the auxiliary surface. The simple empirical equation for estimating the lift increment on a wing due to high-lift surfaces is the following form:

$$\Delta C_{L_{max}} = 0.9\Delta C_{l_{max}} \left(\frac{S_{flapped}}{S_{ref}}\right) \cos \Lambda_{HL} \tag{D.1}$$

Likewise, the change in zero-lift angle of the wing is also estimated by the following empirical equation:

$$\Delta\alpha_{Lo} = \Delta\alpha_{lo} \left(\frac{S_{flapped}}{S_{ref}}\right) \cos \Lambda_{HL} \tag{D.2}$$

The quantities $\Delta C_{l_{max}}$ and $\Delta\alpha_{lo}$ are either obtained from wind-tunnel tests or from Table 12.2 in [8]. The table is attached in Table D.12.

The factor $\frac{c'}{c}$ in Table D.12 is the ratio of the extended chord length of the wing due to an auxiliary surface to the wing's original chord length. Figure D.5 describes the wing's chord length is extended by a slat or a flap. The flapped area $S_{flapped}$ in Eq. (D.1) is defined as the shaded area in Fig. D.6.

In Figure D.6, the hinge lines are only valid for inboard high-lift surfaces. The outboard high-lift surfaces have their hinge lines outside of the wing when they are fully extended. The best position for the hinge is the center of gravity of the high-lift surface. The formula for the hinge-line sweep angle is derived based on the geometry of the wing in Fig. D.7. The sweep angle at any arbitrary line on a wing can be calculated based on the leading-edge sweep angle Λ_{LE}, the taper ratio λ, and the aspect ratio AR of the wing. According to Fig. 3.14, the distance C_{LE} is calculated by the equation:

$$C_{LE} = \frac{b}{2} \tan \Lambda_{LE} \tag{D.3}$$

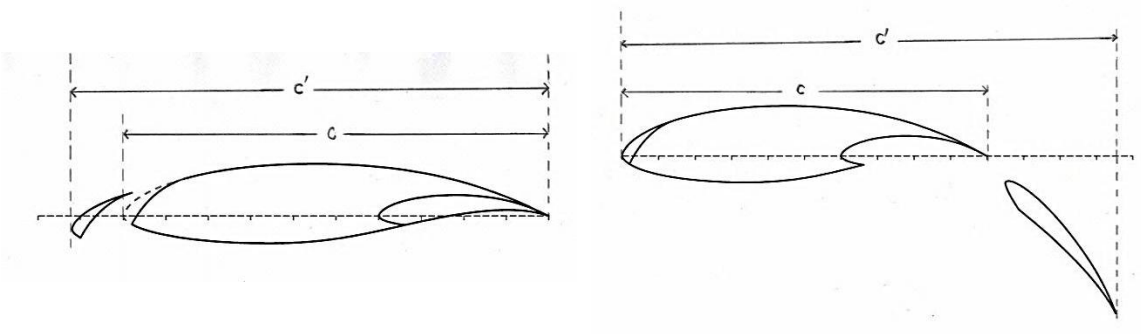

(a) **(b)**

Figure D.5: High-lift surfaces extend the wing's chord: (a) slat extension, (b) flap extension.

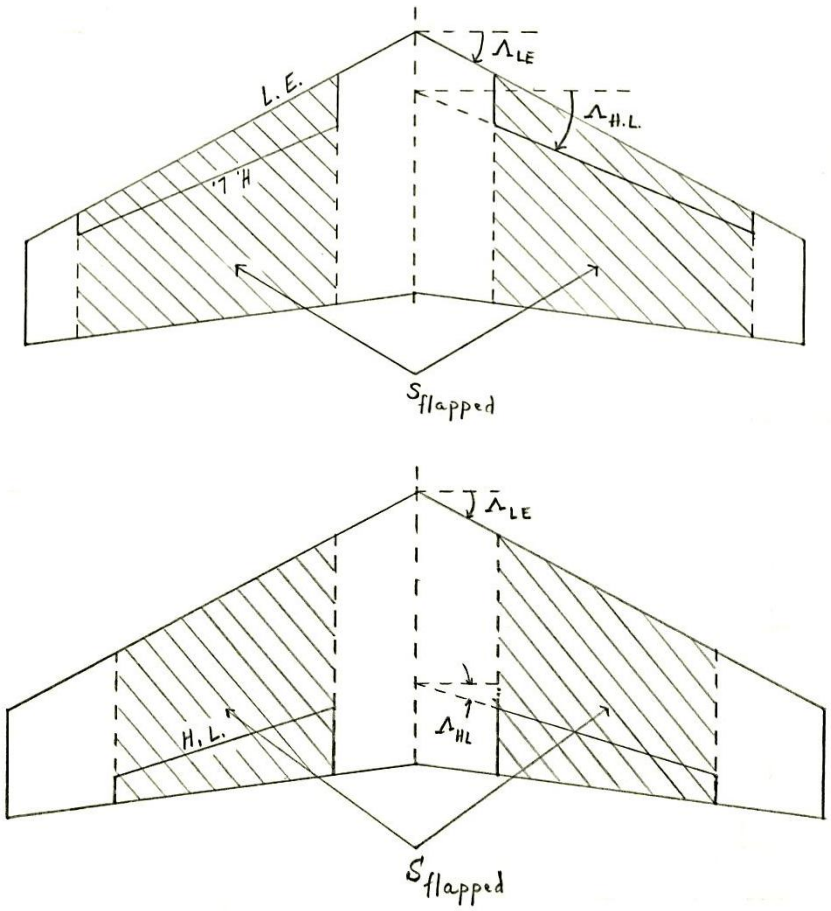

Figure D.6: High-lift surfaces trace out proportional areas on wing platform.

Similarly, the distance $C_{c/n}$ is computed by:

$$C_{c/n} = C_{LE} - \frac{c_r}{n} + \frac{c_t}{n} \tag{D.4}$$

which is equivalent to:

$$C_{c/n} = \frac{b}{2}\tan\Lambda_{LE} - \frac{c_r}{n}(1-\lambda) \tag{D.5}$$

For any line at a distance $\frac{c_r}{n}$ behind the leading-edge of a wing, the tangent of the sweep angle is given by:

$$\tan\Lambda_{c/n} = \frac{C_{c/n}}{b/2} = \tan\Lambda_{LE} - \frac{2}{n}\frac{c_r}{b}(1-\lambda) \tag{D.6}$$

Using the trapezoidal area rule and the definition of the aspect ratio, we find the ratio of the root chord to the wing's span in the following equation:

$$\frac{c_r}{b} = \frac{2}{AR(1+\lambda)} \tag{D.7}$$

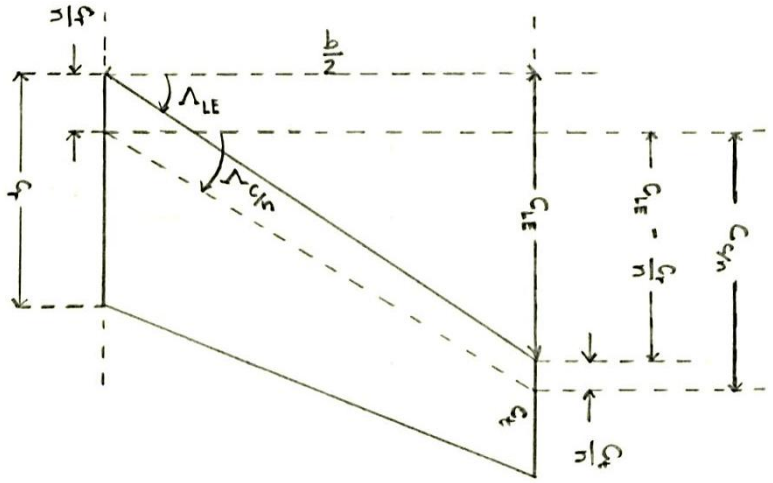

Figure D.7: Sweep angle at an arbitrary line is related to the leading-edge sweep angle.

Substituting Eq. (D.7) into Eq. (D.6), we obtain an equation to convert the leading-edge sweep angle to any arbitrary sweep angle (and vice versa) in the form of:

$$\tan \Lambda_{c/n} = \tan \Lambda_{LE} - \frac{4}{nAR}\left(\frac{1-\lambda}{1+\lambda}\right) \tag{D.8}$$

Table D.4 illustrates the implement of Eq. (D.1) in estimating the lift increments on several airfoils due to the Fowler flap. According to their original reports, theses airfoil models were built in rectangular unswept platforms with full span flaps. Thus, Eq. (D.1) becomes:

$$\Delta C_{L_{max}} = 0.9 \Delta C_{l_{max}} \tag{D.9}$$

Each flap has its c_f chord in percentage of the main airfoil's chord length and was set at the optimum position: fully extended outboard with slot gap at 0% chord, slot depth was varied in each airfoil, and all flaps were deflected to 40° (their optimum configurations). It led to the equation for the flap chord ratio in the following formula:

$$\frac{c'}{c} = \frac{c + c_f \cos 40^\circ}{c} \tag{D.10}$$

Table D.4: Maximum lift increment by Fowler flap estimations

Airfoil	$C_{L_{max}}$	$\alpha^\circ @ C_{L_{max}}$	$C^f_{L_{max}}$	$\alpha^\circ @ C^f_{L_{max}}$	$\Delta C^{exp}_{L_{max}}$	$\frac{C^f_{L_{max}}}{C_{L_{max}}}$	*Source*
Clark Y	1.27	15	3.17	15	1.9	2.5	NACA-TN-419[31]
NACA 23012	1.54	16	3.3	12	1.76	2.1	NACA-TN-808[34]
GA(W) – 1	1.55	16	3.8	10	2.25	2.5	NASA-CR-2443[35]
GA(W) – 2	1.68	15	3.82	9	2.13	2.3	NASA-CR-145139[36]

Table D.4 (continue): $\Delta C_{l_{max}}^{est} = 1.3\, c'/c$								
Airfoil	c_f	δ_f°	c'/c	$\Delta C_{l_{max}}^{est}$	$\Delta C_{L_{max}}^{est}$	$error\ \Delta$	$C_{L_{max}}^{f\_est}$	$error\ C_L$
Clark Y	0.4c	40	1.31	1.7	1.53	-19.6 %	2.8	-11.7 %
NACA 23012	0.3c	40	1.23	1.6	1.45	-17.8 %	3.0	-9.43 %
GA(W) – 1	0.3c	40	1.23	1.6	1.45	-36.1 %	3.24	-21.4 %
GA(W) – 2	0.3c	40	1.23	1.6	1.45	-32.8 %	3.12	-18.4 %

The results in Table D.4 show the method in Eq. (D.1) under-estimates the lift increment on average by 26.5%. The average error on the estimated maximum lift due to flap is 15.2%. We also compare the ratio of lift increment $\frac{C_{L_{max}}^{f}}{C_{L_{max}}}$ (the ratio of maximum lift due to flap deployment to the maximum lift of the plain airfoil) in this illustration. The average lift increment ratio is 2.3:1. If we amend the scale in Table D.12 for Fowler flap to $\Delta C_{l_{max}}^{est} = 1.6\, c'/c$, we under-estimate by 8.3% of the maximum lift increment and 5% of the maximum lift coefficient due to flap, on average.

If we use the linearity rule by applying an increasing factor by 2.3 in maximum lift, we would under-estimate by 1.2% overall. If using the increasing factor by 2.2, the results in maximum lift would be under-estimate by 5.5%. Since this is an early stage estimation of a design, we should consider the under-estimation rather than over-estimation because the under-estimation already includes the safety margin. We will adjust these early stage estimations later in the design process.

Through the comparative study, we will use the amended guideline $\Delta C_{l_{max}}^{est} = 1.6\, c'/c$ in our estimation for lift increment due to Fowler flap using Eq. (D.1). We could use the linear estimation instead of Eq. (D.1). However, the linear estimation does not account the taper wing or the sweep wing and the partial span flap. Table D.5 shows the results of the new correlations.

Table D.5: Correction of $\Delta C_{l_{max}}^{est}$ and linear estimation with correction						
Airfoil	$C_{L_{max}}^{f(1)}$	$error\ C_{L_{max}}^{f(1)}$	$C_{L_{max}}^{f(2)}$	$error\ C_{L_{max}}^{f(2)}$	$C_{L_{max}}^{f(3)}$	$error\ C_{L_{max}}^{f(3)}$
Clark Y	3.17	0 %	2.92	-7.9 %	2.8	-11.9%
NACA 23012	3.34	1.2 %	3.57	8.0 %	3.4	2.7 %
GA(W) – 1	3.35	-12 %	3.57	-6.2 %	3.7	-3.0 %
GA(W) – 2	3.48	-9 %	3.86	1.2 %	4.0	4.2 %
(1): Estimation based on $\Delta C_{l_{max}}^{est} = 1.6\, c_f/c$ (2): Estimation based on $C_{L_{max}}^{f} = 2.3 C_{L_{max}}$ (3): Estimation based on $C_{L_{max}}^{f} = 2.2 C_{L_{max}}$						

Table D.6: Maximum lift increment by Handley Page slat estimations							
Airfoil	$C_{L_{max}}$	$\alpha^{\circ}@\ C_{L_{max}}$	$C_{L_{max}}^{s}$	$\alpha^{\circ}@\ C_{L_{max}}^{s}$	$\Delta C_{L_{max}}^{exp}$	$\frac{C_{L_{max}}^{s}}{C_{L_{max}}}$	*Source*
Clark Y	1.27	15	1.84	28	0.57	1.4	NACA-TR-400[32]
NACA 23012	1.54	16	2.06	27	0.52	1.3	NACA-WRL-261[37]
NACA 64_1A212	1.49	14	1.96	25	0.47	1.3	NACA-TN-1293[38]
NACA 64A010	0.95	10	1.49	20	0.54	1.6	NACA-TN-3129[39]

We made the same estimations for the Handley Page slat using Eq. (D.1). The results are presented in Table D.6. Once again the results under-estimate the lift increments compared to the experimental data. On average, the estimated lift increment is 23.1% less than the experimental result. However, the maximum lift is only 7% less than the maximum lift obtained from the experiments. Within 10% uncertainty, the estimation is a good approximation because the experimental result is not the true value. The only true value is the result obtained from a real flight test. Also, the average maximum lift increment ratio achieved by the slat is 1.4:1.

Table D.6 (continue): $\Delta C_{l_{max}}^{est} = 0.4\, c'/c$							
Airfoil	*Slot Width*	c'/c	$\Delta C_{l_{max}}^{est}$	$\Delta C_{L_{max}}^{est}$	*error* Δ	$C_{L_{max}}^{s\_est}$	*error* C_L
Clark Y	0.1015c	1.1015	0.44	0.39	-30.4 %	1.67	-9.4 %
NACA 23012	0.09c	1.09	0.44	0.39	-24.5 %	1.93	-6.2 %
NACA 64_1A212	0.176c	1.176	0.47	0.42	-10.0 %	1.91	-2.4 %
NACA 64A010	0.09c	1.09	0.44	0.39	-27.3 %	1.34	-7.0 %

Table D.7: Correction of $\Delta C_{l_{max}}^{est}$ and linear estimation						
Airfoil	$\Delta C_{L_{max}}^{est}$	*error* Δ	$C_{L_{max}}^{s(1)}$	*error* $C_{L_{max}}^{s(1)}$	$C_{L_{max}}^{s(2)}$	*error* $C_{L_{max}}^{s(2)}$
Clark Y	0.5	-13.0 %	1.77	-4.0 %	1.78	-3.4 %
NACA 23012	0.49	-5.7 %	2.03	-1.4 %	2.16	4.7 %
NACA 64_1A212	0.53	12.6 %	2.02	3.0 %	2.09	6.4 %
NACA 64A010	0.49	-9.2 %	1.44	-3.3 %	1.33	-10.7 %
(1): Estimation based on $\Delta C_{l_{max}}^{est} = 0.5\, c_s/c$ (2): Estimation based on $C_{L_{max}}^{s} = 1.4 C_{L_{max}}$						

If we adjust the scale for Handley Page slat in Table D.12 to $\Delta C_{l_{max}}^{est} = 0.5\, c'/c$, we will reduce the average error in the maximum lift increment estimation to -3.8% and the average error in maximum lift coefficient is -1.4%. If we use the pure linear estimation based on the average lift increment ratio is 1.4:1, the maximum lift coefficients will be under-approximated by 0.75% on average. The new calculations are shown in Table D.7. For convenience and safety purpose, we will use the method in Eq. (D.1) without any adjustment on the scale for the Handley Page slat, $\Delta C_{l_{max}}^{est} = 0.4\, c'/c$, to estimate the increment in maximum lift coefficient for our wing.

D.6 Minimum Drag Increment Estimation

Analogy with the linear approximation for lift increment, we find the minimum drag increment for the wing due to high-lift surfaces. On average, the minimum drag coefficient increases by a factor of 9.2 due to Fowler flap. If using a factor-of-9.2 scale (multiply by 9.2) for estimating the increase in minimum drag due to Fowler flap, we will over-estimate by 1.8%. In opposite to the lift increment estimation, drag should be over-estimated to include the safety margin.

Let consider an additional 10% margin on a factor-of-9 scale. The actual increased factor for drag due to the Fowler flap is 9.9. A factor-of-10 scale yields a 10.7% over-estimation. And a third of this fator-of-10 scale is about same drag increment factor due to Handley Page slat. Thus, we will use a fator-of-10 scale to estimate the minimum drag due to Fowler flap and factor-of-3.3 scale to estimate the minimum drag due to Handley Page slat. The estimations for drag due to Fowler flap are shown in Table D.8.

Table D.8: Minimum drag increases by Fowler flap

Airfoil	$C_{D_{min}}$	$C^f_{D_{min}}$	$\frac{C^f_{D_{min}}}{C_{D_{min}}}$	$10 \times C_{D_{min}}$	*error*
Clark Y	0.016	0.169	10.6	0.16	-5.3 %
NACA 23012	0.011	0.1	9.5	0.11	4.8 %
GA(W) – 1	0.015	0.11	7.5	0.15	32.5 %
GA(W) – 2	0.016	0.14	9.0	0.16	10.7 %

D.7 Implementation on an Eppler 407 Wing

Now, we are ready to estimate effects of the Fowler flap and the Handley Page slat on an Eppler 407 airfoil. The platform geometry is depicted by the aspect ratio at 5, the taper ratio at 0.4, with 40-degree half-chord swept angle, and a zero-twist angle. Theoretically, the plain wing can achieve a maximum lift coefficient of 1.52 at the corresponding angle

of attack of 19° when the Mach number is 0.1 in a flow of Reynolds number of 6 million. The minimum drag coefficient is 0.0076.

The Fowler flap's chord is 40% the wing chord. It extends outboard and creates a slot with a depth of 2.5% chord and a slot width of 0% chord. The flap is deflected by 40° clockwise. The Handley Page slat has a width of 14% chord, a cut-off by 2% chord, and a 20% cutting-arc radius. These dimensions create a slat with its chord length equal to 15.6% of the main airfoil's chord length. The slat extends outboard and creates a slot which is described by a slot width of 12%, a slot gap of 2%, and a slot depth of 4% in relative to the main airfoil's chord length.

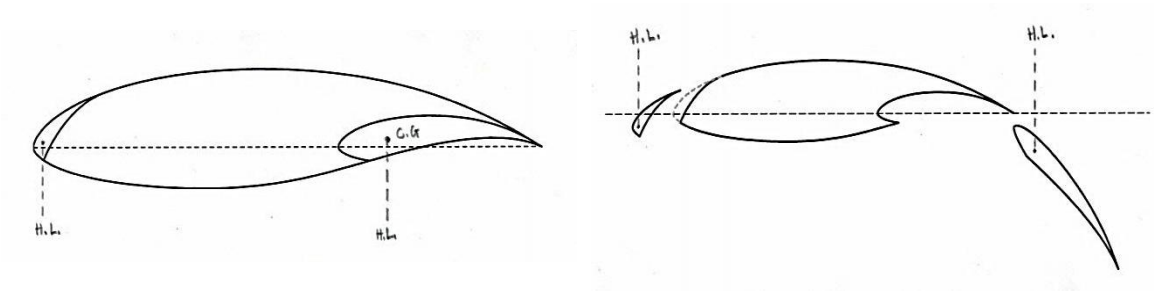

(a) **(b)**

Figure D.8: Hinge line on auxiliary surface: (a) inboard; (b) outboard.

We could assume that the hinge line is at 25% of the flap's chord from the flap's leading edge. When the flap fully extends outboard, the hinge line will be 10 % chord behind the trailing edge because the slot width is 0%. In the case of the slat, the hinge line will be in front of the leading edge. Likewise, the hinge line of the slat will be 8 % in front the leading edge of the wing, whereas the hinge is 2% behind the leading edge of the slat (see Fig. D.8). From knowing the wing's half-chord sweep angle, the aspect ratio, and the taper ratio, we can find the sweep angle at the leading edge by applying Eq. (D.8).

Table D.9: Summary of lift increments for Eppler 407 wing due to flap and slat									
Surface	c'/c	$\Delta C_{l_{max}}^{est}$	$\frac{S_{flapped}}{S_{ref}}$	x_{HL}	Λ_{HL}	$\Delta C_{L_{max}}^{est}$	$\sum \Delta C_{L_{max}}^{est}$	$C_{L_{max}}^{est}$	$\sum C_{L_{max}}^{est}$
Flap	1.31	2.1	0.85	1.1c	32.3°	1.36	1.61	2.88	3.13
Slat	1.1	0.44	0.90	-0.08c	46.1°	0.25		1.77	

The flapped areas can be referenced to the configuration of the Boeing 777-300ER [11] model in Fig. D.9. Base on the sketch, we can make initial estimations of the flapped areas as 90% and 85% of the wing's platform area for the slat and the flap, respectively. The approximated maximum lift coefficients are listed in Table D.9. In the presences of both slat and flap, we will use superposition rule to determine the total maximum lift coefficient. The approximated aerodynamic characteristics of the Eppler 407 wing are summarized in the Table D.10.

Table D.10: Approximated aerodynamic coefficients of the Eppler 407 wing with $AR = 5, \lambda = 0.4, \Lambda_{c/2} = 40°$ in a Flow of $M_\infty = 0.1$ & $Re = 6 \times 10^6$ equipped with the Fowler flap and the Handley Page (H.P.) slat				
Wing System	$C_{L_{max}}$	$\alpha^\circ @\ C_{L_{max}}$	$C_{D_{min}}$	$C_D @\ C_{L_{max}}$
Plain Eppler 407	1.52	19	0.0076	0.136
Plain with Fowler Flap	2.88	--	0.0760	0.622
Plain with H.P. Slat	1.77	--	0.0251	0.240
Fowler Flap and H.P. Slat	3.13	--	0.1011	0.862

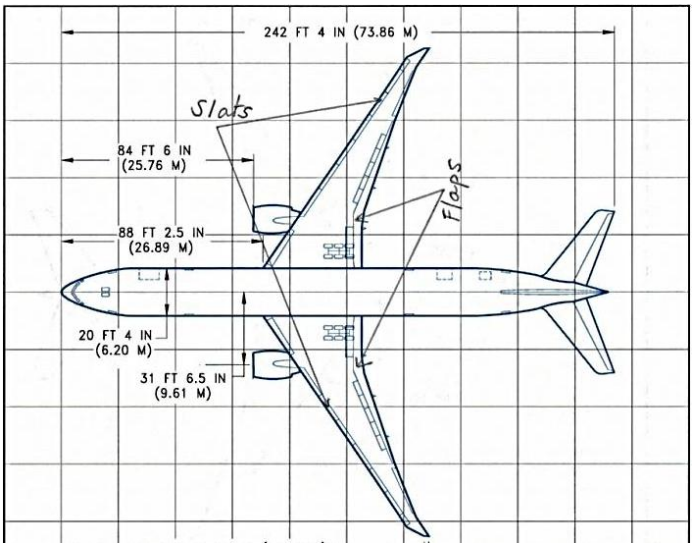

Figure D.9: Top view of Boeing 777-300ER (courtesy to Boeing [11]).

D.8 Summary

In this chapter, we have presented a method to estimate the maximum increment in lift of a wing due to the Fowler flap and the Handley Page slat. The results of these estimations serve as the maximum allowable lift coefficient of the wing because the calculations are based on the optimal extension position of the devices. The robustness of the Fowler flap and Handley Page slat system is illustrated through two features. One is the well-defined sizes of the surfaces. They are the guidelines for us to design the system. Two is the flexibility in the extension of the chord length and the deflection angle of the surfaces.

After verifying the method of the chord length extension with the wind tunnel test results, we found the method is feasible to estimate the lift increment by the high-lift surfaces at this stage of the design. The method is an alternative in measuring the increment of the camber of an airfoil due to flaps or slats. Hence, it measures the increment in lift as well. The method is fairly simple and requires minimal information about the wing which is available at this stage of the design. Through the verification of the method, we have made an adjustment on the empirical constant of the chord extension ratio for the Fowler flap. The empirical increment in two-dimensional lift of an airfoil due to Fowler flap and H.P. slat are shown in Table D.11.

Table D.11: 2-D lift & minimum drag increments by flap and slat		
High-Lift Device	*Fowler Flap*	*Handle Page Slat*
$\Delta C_{l_{max}}$	$1.6\,\frac{c'}{c}$	$0.4\,\frac{c'}{c}$
$C_{D_{min}}^{f/s}$	$10C_{D_{min}}$	$3.3C_{D_{min}}$

Table D.12: Lift increment and change in zero-lift angle of an airfoil due to high-lift devices (original Table 12.2 from [8]).		
High-Lift Device		$\Delta C_{l_{max}}$
Trailing Edge Device	Plain and Split Flap	0.9
	Slotted Flap	1.3
	Fowler Flap	$1.3\,\frac{c'}{c}$
	Double Slotted Flap	$1.6\,\frac{c'}{c}$
	Triple Slotted Flap	$1.9\,\frac{c'}{c}$
Leading Edge Device	Fixed Slot	0.2
	Leading Edge Flap	0.3
	Kreuger Flap	0.3
	Handle Page Slat	$0.4\,\frac{c'}{c}$
Change in Zero-Lift Angle		$\Delta\alpha_{lo}(°)$
	Take-off Flap Configuration	-10
	Landing Flap Configuration	-15

Appendix E. Historical Data of Commercial Aircraft

Table E.1: Empty weight, power plant, thrust per engine, and takeoff gross weight

Aircraft	W_{empty} *(lb)*	*Engine*	*Thrust (lb)*	*TOGW (lb)*
Airbus A300-600	198665	CF6-80C2A5s	61500 (x2)	365745
Airbus A300B2	189400	CF6-50Cs	51000 (x2)	313055
Airbus A300B4	195109	JT9D-9s	53000 (x2)	363760
Airbus A310-200	176683	CF6-80C2A2s	53500 (x2)	313055
Airbus A310-300	179025	CF6-80C2A8s	59000 (x2)	330695
Airbus A318	84600	CF56-5	23800 (x2)	130100
Airbus A319	87930	CFM56-5As	23500 (x2)	141094
Airbus A320-200	92980	CFM56s	27000 (x2)	162040
Airbus A321-100	105605	CFM56s	31000 (x2)	187390
Airbus A321-200	105875	CFM56-5B3s	33000 (x2)	196210
Airbus A330-200	264875	CF6-80E1A2s	67500 (x2)	507050
Airbus A330-300	268675	CF6-80E1A2s	67500 (x2)	467380
Airbus A340-200	277775	CFM56-5C	31200 (x4)	573200
Airbus A340-300	286150	CFM56-5C3	32550 (x4)	573200
Airbus A340-500	375665	Rolls-Royce	53000 (x4)	804675
Airbus A340-600	390220	Rolls-Royce	56000 (x4)	804675
Airbus A380-800	610700	Rolls-Royce	84000 (x4)	1235000
Boeing 707-120B	122533	JT3D-1s	17000 (x4)	257000
Boeing 707-320B	146400	JT3D-3s	19000 (x4)	333600
Boeing 717-200BGW	69830	BR715-A1-30	18500 (x2)	114000
Boeing 717-200hGW	70790	BR715s	21000 (x2)	121000
Boeing 720B	112883	JT3D-3s	18000 (x4)	234000
Boeing 727-100	80602	JT8D-7	14000 (x3)	160000
Boeing 727-200	100000	JT8D-17s	16000 (x3)	209500
Boeing 737-100	57000	JT8D-7	14000 (x2)	110000
Boeing 737-200	60600	JT8D-17S	16000 (x2)	115500
Boeing 737-300	72490	CFM56-3B1	20000 (x2)	124500
Boeing 737-400	76200	CFM56-3B2	22000 (x2)	138500
Boeing 737-500	70510	CFM56-3C1s	20000 (x2)	115500
Boeing 737-600	81800	CFM56-7B18	19500 (x2)	124000
Boeing 737-700	84100	CFM56-7B20S	20600 (x2)	133000
Boeing 737-800	90710	CFM56-7B24s	24200 (x2)	155500

Aircraft	W_{empty} *(lb)*	*Engine*	*Thrust (lb)*	*TOGW (lb)*
Boeing 737-900	93680	CFM56-7B26s	26300 (x2)	164000
Boeing 747-100	358000	JT9D-7A	46950 (x4)	750000
Boeing 747-200	383600	RB211-524D4s	53110 (x4)	833000
Boeing 747-300	383900	JT9D7R4G2	54750 (x4)	775000
	387400	CF6-50E2s	52500 (x4)	785000
	390000	CF6-80C2B1s	56700 (x4)	800000
	392800	RB211524D4s	53110 (x4)	833000
Boeing 747-400	399000	PW-4056	56750 (x4)	800000
	399000	PW-4060s	60000 (x4)	833000
	399000	PW-4062s	62000 (x4)	833000
	398500	CF6-80-C2B1Fs	56750 (x4)	850000
	398500	CF6-80-C2B1F1s	61500 (x4)	850000
	400700	RB-211-524G	58000 (x4)	875000
	400700	RB-211-524G/H-Ts	60000 (x4)	875000
Boeing 747SP	325000	JT9D-7AW	48750 (x4)	700000
	325000	RB211-524Bs	50100 (x4)	700000
	325000	RB211-524Cs	51600 (x4)	700000
	325000	CF6-45A2s	46500 (x4)	700000
Boeing 757-200	127810	RB211-535C	37400 (x2)	240000
	127810	RB211-535E4s	40200 (x2)	240000
	127810	RB211-535E4-Bs	43500 (x2)	240000
	127500	PW2037s	36600 (x2)	250000
	127810	PW2040s	40100 (x2)	250000
	127810	PW2043s	42600 (x2)	250000
Boeing 757-300	142400	RB-211-535E4-B	43100 (x2)	270000
	142110	PW-2043s	43850 (x2)	270000
Boeing 767-200	178400	JT9D7R4D	48000 (x2)	300000
	177500	CF680C2B2s	52500 (x2)	315000
Boeing 767-200ER	186100	PW4056s	56750 (x2)	387000
	186000	CF680C2B4Fs	57900 (x2)	387000
Boeing 767-300	192100	PW-4050s	50000 (x2)	401000
	191700	CF6-80C2B2s	52500 (x2)	387000
Boeing 767-400	227400	PW4062s	63300 (x2)	450000
	227300	CF6-80C2B8Fs	63500 (x2)	450000
Boeing 777-200	306800	GE90-75Bs	77000 (x2)	535000
Boeing 777-300	353600	PW-4098s	98000 (x2)	580000
DC-8-61	148897	JT3D-3B	18000 (x4)	325000

Aircraft	W_{empty} *(lb)*	*Engine*	*Thrust (lb)*	*TOGW (lb)*
DC-8-62	141903	JT3D-3B	18000 (x4)	335000
DC-8-63	153749	JT3D-7s	19000 (x4)	350000
DC-8-73	166500	CFM56-2C5s	22000 (x4)	355000
DC-9-10	49900	JT8D-5	12250 (x2)	90700
DC-9-30	57190	JT8D-17s	16000 (x2)	121000
DC-10-30	267197	CF6-50C2Bs	54000 (x3)	580000
DC-10-40	271062	JT9D-59As	53000 (x3)	572000
Embraer ERJ-170/175	44422	CF34-8E	14000 (x2)	78153
Embraer ERJ-190/195	59744	CF34-10Es	18500 (x2)	103593
Fokker 100	53738	Rolls-Royce	13850 (x2)	95000
Fokker 70	49985	Rolls-Royce	13850 (x2)	81000
Fokker F-28 Fellowship	37400	Rolls-Royce	9900 (x2)	73000
MD-11	286965	CF6-80C2D1F	61500 (x3)	602555
MD-81	77888	JT8D-209	18500 (x2)	140000
MD-87	73274	JT8D-217C	20000 (x2)	140000
MD-88	77976	JT8D-219s	21000 (x2)	149500
MD-90-30	88000	V2525D5	25000 (x2)	156000
MD-90-55	91900	V2528D5s	28000 (x2)	172500

Table E.2: Maximum cruise speed, long range cruise speed, and range			
Aircraft	*Max Cruise Speed (kn)*	*LRC Speed (kn)*	*Range (nmi)*
Airbus A300-600	484	472	3600
Airbus A300B2	495	457	1850
Airbus A300B4	495	457	2900
Airbus A310-200	484	459	3670
Airbus A310-300	484	459	4310
Airbus A318	472 (0.82M, 35K ft)	472	1500
Airbus A319	487 (28,000 ft)	454	1831
Airbus A320-200	487 (28,000 ft)	454	2615
Airbus A321-100	488	447	2300
Airbus A321-200	488	447	2650
Airbus A330-200	475 (33,000 ft)	464	6400
Airbus A330-300	475 (33,000 ft)	464	4500
Airbus A340-200	494	475	7450
Airbus A340-300	494	475	6700
Airbus A340-500	478.5(0.83M, 35K ft)	478.5	8500
Airbus A340-600	478.5(0.83M, 35K ft)	478.5	7500
Airbus A380-800	504.7(0.88M, 43K ft)	487.5(0.85M, 43K ft)	8000
Boeing 707-120B	540	484	4580
Boeing 707-320B	525	478	5000
Boeing 717-200BGW	NA	438	1375
Boeing 717-200hGW	NA	438	2060
Boeing 720B	530	484	4550
Boeing 727-100	518	495	2700
Boeing 727-200	515	467	2400
Boeing 737-100	500	460	1540
Boeing 737-200	500	430	1900
Boeing 737-300	491	429	2685
Boeing 737-400	492	439	2160
Boeing 737-500	492	430	1520
Boeing 737-600	NA	452.5(0.79M, 35K ft)	1340
Boeing 737-700	NA	452.5(0.79M, 35K ft)	1540
Boeing 737-800	NA	452.5(0.79M, 35K ft)	1990
Boeing 737-900	NA	452.5(0.79M, 35K ft)	2060
Boeing 747-100	522	490	4880
Boeing 747-200	530	490	6900

Aircraft	*Max Cruise Speed (kn)*	*LRC Speed (kn)*	*Range (nmi)*
Boeing 747-300	530	490	6300
	530	490	6100
	507	485	6700
	507	485	6250
Boeing 747-400	507	490	7824
	507	490	7824
	507	490	7824
	507	490	7259
	507	490	7259
	507	490	7135
	507	490	7135
Boeing 747SP	540	NA	6650
	540	NA	6650
	540	NA	6650
	540	NA	6650
Boeing 757-200	493	460	2569
	493	460	2569
	493	460	2569
	493	460	2728
	493	460	2728
	493	460	2728
Boeing 757-300	NA	461(0.8M, 35K ft)	3270
	NA	461(0.8M, 35K ft)	3485
Boeing 767-200	493	461	3160
	493	461	3850
Boeing 767-200ER	493	461	6625
	493	461	6670
Boeing 767-300	486	460	4230
	486	460	4260
Boeing 767-400	NA	461(0.8M, 35K ft)	5580
	NA	461(0.8M, 35K ft)	5625
Boeing 777-200	NA	490	5150
Boeing 777-300	NA	482	5720
DC-8-61	521		3256
DC-8-62	521		5210
DC-8-63	521		3907
DC-8-73	479	459	4830

Aircraft	*Max Cruise Speed (kn)*	*LRC Speed (kn)*	*Range (nmi)*
DC-9-10	488	478	570
DC-9-30	490	430	1670
DC-10-30	530	490	4000
DC-10-40	530	490	4050
Embraer ERJ-170/175	481	470 (41K ft)	1800
Embraer ERJ-190/195	481	470 (41K ft)	1800
Fokker 100	456	453	1323
Fokker 70		444(0.77M, 35K ft)	1085
Fokker F-28 Fellowship	455	366	1480
MD-11	510	473	6821
MD-81	500	440	1564
MD-87	500	438	2372
MD-88	500	440	2620
MD-90-30	NA	437	2085
MD-90-55	NA	437	2700

Table E.3: Wing span, wing reference area, passenger count, and class count				
Aircraft	*Wing Span (ft)*	*Wing Area (ft^2)*	*Passenger*	*Class*
Airbus A300-600	147	2798.7	266	2
Airbus A300B2	147	2798.7	250	2
Airbus A300B4	147	2798.7	269	2
Airbus A310-200	144	2357.3	212	2
Airbus A310-300	144	2357.3	218	2
Airbus A318	111	1320	100	1
Airbus A319	111	1317.5	124	2
Airbus A320-200	111	1319.7	150	2
Airbus A321-100	111	1320	186	2
Airbus A321-200	111	1320	186	2
Airbus A330-200	197	3908	293	2
Airbus A330-300	197	3908.4	335	2
Airbus A340-200	197	3908.4	263 (303)	3 (2)
Airbus A340-300	197	3908.4	295	3
Airbus A340-500	209	4704	313	3
Airbus A340-600	209	4704	380	3
Airbus A380-800	261.83	9096	555	3
Boeing 707-120B	130.83	2433	110	2
Boeing 707-320B	145.75	3050	147	2
Boeing 717-200BGW	93.25	1000.7	106	2
Boeing 717-200hGW	93.25	1000.7	106	2
Boeing 720B	130.83	2521	112	2
Boeing 727-100	108	1700	94	2
Boeing 727-200	108	1700	145	2
Boeing 737-100	93	980	100	1
Boeing 737-200	93	980	115	1
Boeing 737-300	94.75	1135	128	2
Boeing 737-400	94.75	1135	146	2
Boeing 737-500	94.75	1135	108	2
Boeing 737-600	112.6	1344	110	2
Boeing 737-700	112.6	1344	126	2
Boeing 737-800	112.6	1344	162	2
Boeing 737-900	112.6	1344	177	2
Boeing 747-100	195.7	5500	385	3
Boeing 747-200	195.7	5500	452	2

Aircraft	*Wing Span (ft)*	*Wing Area (ft^2)*	*Passenger*	*Class*
Boeing 747-300	195.7	5500	400	3
	195.7	5500	400	3
	195.7	5500	400	3
	195.7	5500	400	3
Boeing 747-400	211.4	5825	420	3
	211.4	5825	420	3
	211.4	5825	420	3
	211.4	5825	420	3
	211.4	5825	420	3
	211.4	5825	420	3
	211.4	5825	420	3
Boeing 747SP	195.7	5500	276	2
	195.7	5500	276	2
	195.7	5500	276	2
	195.7	5500	276	2
Boeing 757-200	124.83	1994	186	2
	124.83	1994	186	2
	124.83	1994	186	2
	124.83	1994	186	2
	124.83	1994	186	2
	124.83	1994	186	2
Boeing 757-300	124.83	1994	240	2
	124.83	1994	240	2
Boeing 767-200	156	3050	216	2
	156	3050	216	2
Boeing 767-200ER	156	3050	216	2
	156	3050	216	2
Boeing 767-300	156	3050	269	2
	156	3050	269	2
Boeing 767-400	170.3	3222.5	245	3
	170.3	3222.5	245	3
Boeing 777-200	200	4605	305	3
Boeing 777-300	200	4605	394	3
DC-8-61	142.4	2884	220	1
DC-8-62	148.4	2927	180	1
DC-8-63	148.4	2927	220	1
DC-8-73	148.4	2927	220	1

Aircraft	*Wing Span (ft)*	*Wing Area (ft^2)*	*Passenger*	*Class*
DC-9-10	89.4	934	80	1
DC-9-30	93.4	1000.7	80	1
DC-10-30	165.4	3958	250	1
DC-10-40	165.4	3958	270	1
Embraer ERJ-170/175	85.3	783	70	1
Embraer ERJ-190/195	94.25	996	98	1
Fokker 100	92.2	1006.4	107	1
Fokker 70	92.2	1006.4	70	1
Fokker F-28 Fellowship	82.25	850	65	1
MD-11	169.5	3648	298	3
MD-81	107.83	1209	155	2
MD-87	107.83	1209	130	1
MD-88	107.83	1209	155	2
MD-90-30	107.83	1209	153	2
MD-90-55	107.83	1209	187	2